Hotan Shalibeik

Rare-Earth-Doped Fiber Lasers and Amplifiers

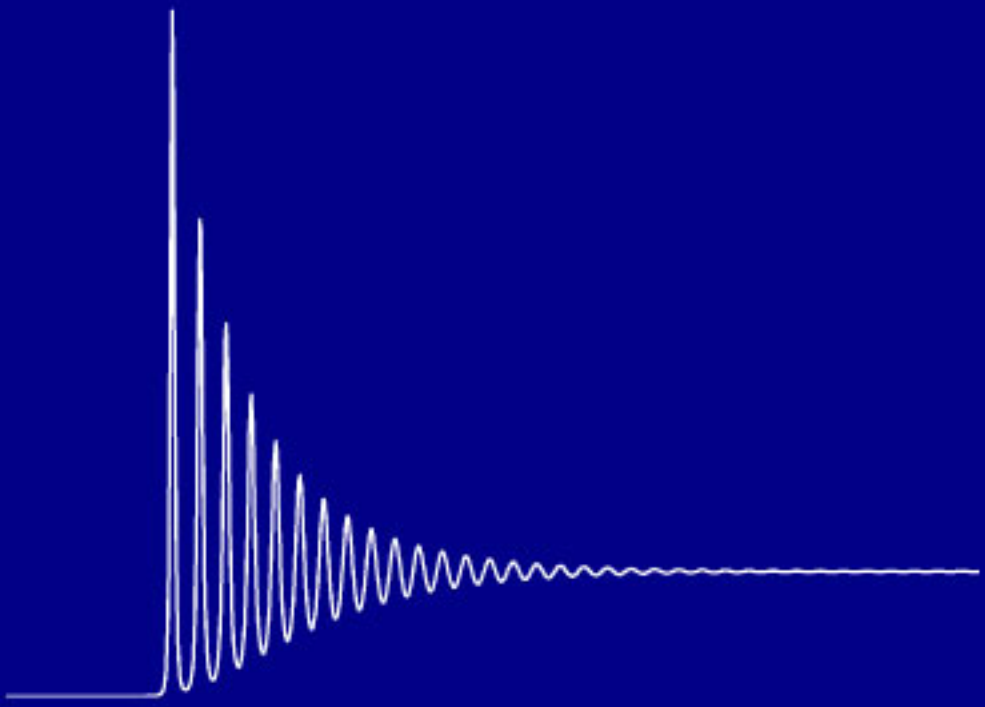

Cuvillier Verlag Göttingen

Rare-Earth-Doped Fiber Lasers and Amplifiers

Von der Fakultät für Elektrotechnik und Informationstechnik
der Technischen Universität Carolo-Wilhelmina zu Braunschweig

zur Erlangung der Würde

eines Doktor-Ingenieurs (Dr.-Ing.)

genehmigte Dissertation

von:	Dipl.-Ing. Hotan Shalibeik
aus:	Teheran

eingereicht am:	03.04.2007
mündliche Prüfung am:	27.04.2007

Referenten:	Prof. Dr.-Ing. Wolfgang Kowalsky Prof. Dr. rer. nat. Andreas Waag

2007

Bibliografische Information der Deutschen Nationalbibliothek
Die Deutsche Nationalbibliothek verzeichnet diese Publikation in der Deutschen Nationalbibliografie; detaillierte bibliografische Daten sind im Internet über http://dnb.ddb.de abrufbar.
1. Aufl. - Göttingen : Cuvillier, 2007
Zugl.: (TU) Braunschweig, Univ., Diss., 2007

978-3-86727-467-8

Nonnenstieg 8, 37075 Göttingen
Telefon: 0551-54724-0
Telefax: 0551-54724-21
www.cuvillier.de

1. Auflage, 2007
Gedruckt auf säurefreiem Papier

978-3-86727-467-8

To My Parents

Acknowledgements

This work is the result of my research as a scientist at the Institute for High-Frequency Technology (IHF) of the Technical University Braunschweig from July 2004 to March 2007. I would like to thank Prof. Dr.-Ing. Wolfgang Kowalsky, the Head of the IHF, for the opportunity to work on two interesting and exciting projects sponsored by the German government and also for getting the opportunity to participate in teaching activities.

Prof. Kowalsky and Dr.-Ing. Dipl.-Phys. Reinhard Caspary, the Head of the research group "Fluoride Glass Fibers and Fiber Lasers", were my academic supervisors. Prof. Kowalsky was able to provide an excellent working atmosphere in the Institute and gave me the possibility to work on different and very interesting research projects during my stay in Braunschweig: First, the characterization of fiber amplifiers by coherent optical frequency-domain reflectometry (OFDR) and, second, spectroscopy of fluoride glasses and simulation of various fiber lasers on which the main part of this thesis is based.

I am very grateful to and will always remember Prof. em. Dr. Ishwar Chandra Goyal from the Indian Institute of Technology in New Delhi, who passed away unexpectedly during his short stay in Braunschweig in the summer of 2006. It was a great pleasure to discuss the theory of the transient behavior of fiber lasers and amplifiers with him. He gave me the idea of the step-by-step algorithm which was successfully applied to simulate different rare-earth-doped fiber lasers.

I am also thankful to Prof. Anderson Stevens Leônidas Gomes from the Universidade Federal de Pernambuco (UFPE) in Recife, Brazil, who saved me from a pitfall in the characterization of thulium-doped fiber amplifiers with OFDR.

I would also like to thank Prof. Dr.-Ing. Jörg Schöbel, the chairman of the Examination Committee and Head of the Microwave group at the Institute as well as the co-examinators Prof. Dr.-Ing. Wolfgang Kowalsky and Prof. Dr. rer. nat. Andreas Waag, the Head of the Institute for Semiconductor Technology at the Technical University Braunschweig.

Dr. Mohammad Saadatfar, a friend I met during my stay at the Australian National University (ANU) in Canberra, Dr. Timo Betcke, my fellow student at the Technical University Hamburg-Harburg (TUHH) during my study time, and Elmar Zander from the Institute of Scientific Computing at the Technical University Braunschweig, gave me interesting ideas and hints in dealing with different numerical methods.

The cooperation with other colleagues in the research group was also very pleasant:
I wish to thank Kathleen Möhring, Dr. Dirk Goebel, Dr.-Ing. Thorsten Buschmann, Dr. Ranjan Sen, Associate Prof. Dr. Li Pei, M.Sc. Siew Kien Mah, Dipl.-Chem. Maike Waldmann, Dr.-Ing. Tomasz Baraniecki, Dr.-Ing. Marcin Kozak, and Dr.-Ing. Sören Hartmann.
There are many reasons why I should be thankful to everyone of them, but I would like to specially thank K. Möhring. She prepared, poured, and polished all the ZBLAN and IBZP glass samples in excellent quality on which the spectroscopy part of this thesis is based. I also appreciate the successful cooperation with cand. el. Arne Behrends and Dipl.-Ing. Patrick Görrn. Their engaged work on their Diploma thesis and Project works embossed my thesis.

The person involved in correcting this work was Dipl.-Ing. M.Sc. Tobias Werth. Despite moving houses from Braunschweig to Aachen and being busy with his own PhD work, he spent many hours in critical proof reading of the manuscript. In record time he gave me many appropriate suggestions to avoid a number of mistakes.

I am also thankful to many colleagues from outside the research group:
The network administrator of the Institute Dipl.-Ing. Marc Blumentritt solved nearly every problem with the network and also with the office and lab computers. Without him many solutions to computer problems would have taken many more hours.
Dipl.-Wi.-Ing. M.Sc. Lars Beckmann was always a helpful hand. The cooperation with Dipl.-Ing. Jens Meyer in holding the lecture "Hochfrequenzübertragungstechnik" and performing the oral exams with the Diploma students is an experience which I will always keep in good remembrance, and, of course, the jogging activities (also with Dr. Guergana Dobreva) after a whole working day. Especially in the winter I preferred to go to the gym, most of the time with M.Sc. Nico Vieweg and Dipl.-Ing. Patrick Görrn.

Last but not least, I am very grateful to my family for their support and encouragement during my whole life. My parents were the persons who supported me most which beyond doubt was a necessary precondition for the success of this work. I will never forget how my sister Helena helped me to move from Hamburg to Braunschweig when I was suffering from an achillorrhexis. She supported and encouraged me in many decisions. I will for sure not only support her in her studies of Pharmacy at the University of Hamburg but also in personal matters like she did.

Hotan Shalibeik
Braunschweig, April 2007

Summary

The goals of this work are, first, to determine different parameters of rare-earth-doped fibers and glasses and, second, to develop a simulation model for rare-earth-doped fiber lasers and amplifiers in order to avoid time consuming and expensive measurements in the laboratory during the development of such devices. The model should be applicable to arbitrary rare earth devices in a variety of configurations and cover their steady-state and transient behavior. Moreover, cross relaxation processes between two different rare earth ions should be taken into account as it is commonly used for better performance of fiber lasers and amplifiers. For the simulation a couple of spectroscopic parameters are needed, which have to be obtained in advance from bulk glasses. Some parameters like the non-radiative transition rates are difficult to obtain and thus an approach is shown to fix these usually unknown values and to consider thermally coupled energy levels.

After a short introduction, which includes general laser theory and an overview of some selected solid-state and semiconductor laser systems, some properties of rare-earth-doped materials and glass hosts are discussed. The focus is Pr^{3+}/Yb^{3+}-doped fluoride glass and the underlying avalanche upconversion process.

Then, a coherent reflectometric technique (C-OFDR) is applied to characterize thulium-doped fluoride fiber amplifiers (TDFAs) operating in the S-band of optical communications. The optimum length of the fluoride fiber and quantities like fiber gain and optimum gain-length ratio are determined for ZBLAN fibers with different thulium concentrations. Furthermore, a frequency transfer function (FTF) method is introduced to extract fluorescent lifetimes of energy levels of arbitrary rare-earth-doped glasses and fibers from phases and/or magnitudes of the measured frequency transfer function. This method is applied to measure lifetimes of the upper laser levels of praseodymium-doped fluoride glasses, namely ZBLAN and IBZP. Some of the glass samples are co-doped with ytterbium. These results are reported together with the investigation of the concentration quenching effect. Moreover, spectroscopic results of Pr^{3+}- and Yb^{3+}-doped ZBLAN glasses are presented and included in the simulation model developed.

Simulations are carried out for Yb^{3+}-, Pr^{3+}- and Pr^{3+}/Yb^{3+}-doped ZBLAN fiber lasers. Their behavior in stationary and dynamic states is investigated for a simple Fabry-Perot setup. The demonstration of the dominant role of the avalanche upconversion process for Pr^{3+}/Yb^{3+}-doped ZBLAN fiber lasers is shown and the turn-on behavior of the above mentioned lasers shows relaxation oscillations typical to solid-state lasers. With the model at hand it is easily possible to simulate any other laser or amplifier configuration as well.

Kurzzusammenfassung

Die Ziele dieser Arbeit sind, erstens, die Bestimmung verschiedener Parameter von Seltenerd-dotierten Fasern und Gläsern, und, zweitens, die Entwicklung eines Simulationsmodells für Seltenerd-dotierte Faserlaser und Faserverstärker, um zeit- und kostenaufwändige Messungen im Labor während der Entwicklung solcher Bauelemente zu vermeiden. Das Modell soll für beliebige Seltenerd-dotierte Bauelemente in verschiedenen Anordnungen anwendbar sein und sowohl das eingeschwungene als auch das transiente Verhalten dieser Bauelemente simulieren. Ferner sollen Kreuzrelaxationsprozesse zwischen zwei unterschiedlichen Seltenerdionen in dem Modell erfasst werden, da diese gewöhnlich genutzt werden, um eine bessere Performance bei Faserlasern und -verstärkern zu erzielen. Einige spektroskopische Parameter werden für die Simulationen benötigt, die man im Voraus anhand spektroskopischer Untersuchungen an Gläsern bestimmen muss. Jedoch gibt es viele Parameter, die nicht oder nur ungenau bestimmt werden können. Dies sind z.B. die nicht-strahlenden Übergangsraten wofür in dieser Arbeit ein neuartiger Ansatz gezeigt wird, um diese Werte konstant zu setzen und zugleich die thermische Verkopplung zwischen benachbarten Energieniveaus zu berücksichtigen.
Nach einer kurzen Einleitung, in der die allgemeine Lasertheorie präsentiert wird und zudem auf ausgewählte Festkörper- und Halbleiterlaser eingegangen wird, werden die Eigenschaften von Seltenerd-dotierten Materialien und Wirtsgläsern beschrieben. Dabei stehen Pr^{3+}/Yb^{3+}-dotierte Fluoridgläser und der Avalanche Aufkonversionsprozess im Vordergrund.
Danach wird die kohärente optische Frequenzbereichsreflektometrie (C-OFDR) eingesetzt, um Thulium-dotierte Fluoridglasfaserverstärker (TDFAs) zu untersuchen. Diese arbeiten im S-Band der optischen Kommunikationstechnik. Die Bestimmung der optimalen Länge der aktiven Faser, der Fasergewinn und das Gewinn-Längenverhältnis werden für verschieden stark Thulium-dotierte ZBLAN Fasern durchgeführt. Des Weiteren wird eine Frequenzübertragungsfunktionsmethode (FTF Methode) vorgestellt, um Fluoreszenzlebensdauern von Energieniveaus willkürlicher Seltenerdelemente aus der Phase und/oder der Amplitude der gemessenen Funktion zu extrahieren. Diese Methode wird eingesetzt, um die Lebensdauern der oberen Laserlevel von Praseodym-dotierten Fluoridgläsern wie ZBLAN und IBZP zu bestimmen. Einige dieser Glasstücke weisen eine Kodotierung mit Ytterbium auf. Die Ergebnisse dieser Untersuchung werden zusammen mit dem beobachteten Konzentrationsquenching näher erläutert. Ferner werden spektroskopische Ergebnisse von Pr^{3+}- und Yb^{3+}-dotieren ZBLAN Gläsern präsentiert und in das entwickelte Simulationsmodell integriert.
Yb^{3+}-, Pr^{3+}- und Pr^{3+}/Yb^{3+}-dotierte ZBLAN Faserlaser werden in dieser Arbeit simuliert. Ihr Verhalten in stationären und dynamischen Zuständen wird für einen einfachen Fabry-Perot Aufbau untersucht. Es wird demonstriert, dass der Avalanche Aufkonversionsprozess bei Pr^{3+}/Yb^{3+}-dotierten ZBLAN Faserlasern dominiert und dass das Einschaltverhalten der oben genannten Laser Relaxationsoszillationen aufweist, die typisch für das dynamische Verhalten von Festkörperlasern sind. Mit dem verfügbaren Modell ist es ohne weiteres möglich jede andere Laser- oder Verstärkerkonfiguration zu simulieren.

Contents

Publications

Some parts of this thesis have already been published or are intended to be published in journal papers and will be presented on conferences as well:

[A1] H. Shalibeik, A. Behrends, M.M. Kozak, W. Kowalsky, and R. Caspary, "Characterization of 1050 nm pumped S-band TDFA with different dopant concentrations by coherent optical frequency-domain reflectometry," IEEE Photonics Technology Letters, vol. 19, no. 4, pp. 188-190, Feb. 2007

[A2] H. Shalibeik, P. Görrn, W. Kowalsky, and R. Caspary, "Frequency transfer function method to measure the fluorescent lifetime of praseodymium-doped fluoride glasses," to be published in IEEE Journal of Quantum Electronics, 2007

[A3] R. Caspary, A. Behrends, H. Shalibeik, M.M. Kozak, and W. Kowalsky, "Coherent optical frequency-domain reflectometry as characterisation tool for S-band TDFAs," in *9th International Conference on Transparent Optical Networks*, ICTON 2007, Rome, Italy, July 1-5, 2007

Introduction

Many applications in industry and life science have initiated the development of laser sources in the visible spectral range. Important biotechnological, pharmaceutical and medical measurement procedures, such as the confocal microscopy and flow cytometry, are based on laser-induced fluorescence detection technologies. Almost all known human life-threatening diseases can be diagnosed by cytology, the study of the properties of single cells, using tunable visible lasers of a few mW power.
For small hand-held full-color displays red, green, and blue lasers emitting less than 1 mW of total optical power will probably be sufficient. Moreover, three laser beams (blue, green, red) are used for exposing photographic paper, films or printing plates. In addition, depending on the spectral sensitivity of the materials used for these colors, upconversion fiber lasers have the potential to replace one or more lasers in the different setups being used today. Further applications of upconversion fiber lasers are in the field of imaging, metrology, sensing and spectroscopy.
Upconversion fiber lasers offer a good alternative to air-cooled ion lasers and frequency-doubled solid-state lasers. Fiber lasers provide high efficiency, reliable operation, and single-mode beam quality with cost effectiveness. Laser transitions of the Pr^{3+} ion are attractive because laser operation at blue, green, orange and red wavelengths can all be obtained using the same pump source when additionally doping the fiber core with Yb^{3+} ions.
Upconversion lasers may provide a useful route to the development of visible lasers pumped by cheap semiconductor lasers operating in the near infrared region of the spectrum. The emission wavelength of a fiber laser can be adjusted by suitable doping with one or several rare earth ions and additionally be modified by varying the glass composition. The inhomogeneous broadened transitions and thus the broad emission spectra of rare earth ions in glasses enable a spectrally wide tuning range of the emission lines of such lasers by means of wavelength selective resonators.
The discovery of fluoride glass in 1974 originated in a new class of active components in the visible range. This is due to a lower phonon energy which implies a smaller contribution to multi-phonon relaxation, hence, increasing the number of metastable excited levels in fluoride glasses compared to silica hosts. Silica fibers incorporating rare earth ions as the active medium are not particularly adequate for visible lasers. Compared with silica fiber lasers, fluoride fiber lasers offer a wider wavelength range. In practice, most low phonon energy glasses are heavy metals of which ZBLAN glass based on zirconium fluoride is the most famous type, followed by IBZP glass based on indium fluoride.

Spatially resolved determination of the fiber gain of thulium-doped ZBLAN fiber is one main issue of this thesis. In this work, the coherent optical frequency-domain reflectometry (C-OFDR) method is applied to characterize 1050 nm laser diode pumped S-band thulium-doped

fluoride fiber amplifiers (TDFAs). With this measurement technique it is possible to determine the optimum length of the active fiber in amplifier applications without destroying the expensive fluoride fiber. Different thulium concentrations of the active ZBLAN fiber are investigated. Strong cross relaxation processes are expected for highly thulium-doped ZBLAN fibers and will explain the efficient operation of this type of fiber amplifier.
Furthermore, a frequency transfer function (FTF) method is introduced to determine fluorescent lifetimes of arbitrary rare-earth-doped glasses and fibers. The fluorescent lifetime of energy levels of rare-earth-doped glasses or fibers provides a valuable information for fiber laser and amplifier applications. Lifetime measurements for the upper energy levels of praseodymium-doped ZBLAN and IBZP glasses are reported and the influence of ytterbium as co-dopant is shown as well. Concentration quenching is expected for highly praseodymium-doped glass samples. In addition, this work summarizes the fundamental spectroscopic properties of triply ionized praseodymium- and ytterbium-doped ZBLAN glasses.
Special attention is given to the simulation of praseodymium-, ytterbium-, and Pr^{3+}/Yb^{3+}-doped ZBLAN fiber lasers emitting in the visible and infrared spectral range. Simulations allow to reduce the costs of experiments. Experience shows that in the design of a rare-earth-doped ZBLAN fiber laser the suppression of competing laser transitions is as important as the support of desired transitions. Thus, a major part of this work will deal with defining a suitable model which is applicable for arbitrary rare-earth-doped fiber lasers and amplifiers in a variety of configurations. The aim is to find a model which covers steady-state and transient behavior of rare earth devices. Simulations will help to understand the processes, which play a role in the lasing or amplification process and finally, they can be used to find the optimum device parameters and predict the performance of the whole system.

This thesis is organized in six chapters. Their contents is briefly summarized below.

Chapter 1: This chapter summarizes the fundamental processes behind laser operation. Absorption, spontaneous and stimulated emission are described as well as the creation of population inversion.

Chapter 2: In this chapter an overview of exemplary solid-state and semiconductor laser systems is provided. Ruby and fiber lasers are presented as examples of solid-state laser systems, and distributed feedback lasers are presented as an example of semiconductor laser systems.

Chapter 3: The most important properties of rare earth host materials which are important in understanding fiber laser operation are discussed in this chapter. Emphasis is put on basic features of fluoride glasses doped with rare earth ions. An overview of ion interactions and the properties of non-radiative transitions is also given. The latter includes multi-phonon processes and energy transfer mechanisms. The avalanche upconversion pumping scheme of Pr^{3+}/Yb^{3+}-doped lasers is discussed in detail. Finally, the relevant transitions

in praseodymium- and ytterbium-doped fluoride glasses are presented.

Chapter 4: The properties of thulium-doped fluoride fibers used for fiber amplifier applications and of praseodymium-doped fluoride glasses for fiber laser applications are thoroughly discussed in this chapter. The active thulium fiber is spatially characterized by C-OFDR. Moreover, a new frequency transfer function (FTF) method is presented and applied to measure the fluorescent lifetimes of the upper laser levels in praseodymium-doped ZBLAN and IBZP glasses, some of them co-doped with ytterbium.
In the last section of this chapter some important spectroscopic parameters of praseodymium in ZBLAN glass are presented which will be used for fiber laser simulation in chapters 5 and 6. Extensions to the methods developed in this chapter are given in appendix A, B, and C.

Chapter 5: The spectroscopic parameters described in the previous chapter are used in this chapter to simulate different fiber lasers. A stationary model for the simulation of arbitrary rare-earth-doped fiber lasers and amplifiers is presented. The model is applicable for a rare earth ion as dopant in lasers and amplifiers and is applied to the simulation of an ytterbium-doped and to red, orange and blue praseodymium-doped ZBLAN fiber lasers. Maxwell-Boltzmann statistics for thermally coupled energy levels is applied in combination with a novel approach to fix the usually unknown values of non-radiative transition rates for the simulations. Furthermore, the model is extended to simulate cross relaxation processes between two different ions in rare-earth-doped devices. Finally, red, orange and blue characteristics of Pr^{3+}/Yb^{3+}-doped ZBLAN fiber lasers are simulated and compared to the results of Pr^{3+}-doped ZBLAN fiber lasers. The dominance of the avalanche upconversion process in case of the former type of laser is proven by this model.

Chapter 6: In this chapter a novel dynamic model for the simulation of arbitrary rare-earth-doped fiber lasers and amplifiers is presented. A model for a single rare earth ion is presented and extended to model energy transfer processes in lasers and amplifiers doped with two rare earth ions. The model uses the same mathematical concept introduced in chapter 5 and is applied to simulate the transient behavior of ytterbium-doped, praseodymium-doped and Pr^{3+}/Yb^{3+}-doped ZBLAN fiber lasers. Relaxation oscillations of the output power have been observed and these results have been evaluated to extract different parameters of the simulated fiber lasers.

1 Laser theory

In this chapter, the fundamental processes behind laser operation are briefly discussed. In 1917, Albert Einstein showed that the process of stimulated emission must exist, but it was not before 1960 that Maiman was able to demonstrate laser action for the first time [1]. A laser consists of three elements: an active medium, a pump, and a resonator. To make a laser oscillator from an amplifier, it is necessary to introduce suitable positive feedback by means of the resonator. Basic principles and the construction of lasers are relatively simple but, on the other hand, a rigorous analysis of laser physics is quite sophisticated. Thus, the approach described here has been simplified to cover basic laser principles while maintaining a concise theory.

1.1 Interaction of radiation with matter

In order to understand laser operation some of the principles which govern the interaction of radiation and matter have to be known. Atomic systems such as atoms, ions, and molecules can exist only in discrete energy states. A change from one energy state to another is called a transition. To simplify the discussion, let us consider an idealized material with merely two energy levels, 1 and 2, having populations of N_1 and N_2, respectively (see Figure 1.1). The total number of atoms in these two levels N_0 is assumed to be constant:

$$N_0 = N_1 + N_2. \tag{1.1}$$

Let us assume that the system is in the lower level E_1. Then, in the presence of photons, it may be excited to the upper level E_2 by absorbing a photon with energy $E_2 - E_1$. This process is called *absorption*. Alternatively, if the system is in the level E_2, it may return to the ground state with the emission of a photon. The energy difference between the levels must be compensated by the emission of radiative energy and is given by the following relation:

$$\Delta E = E_2 - E_1 = \frac{h \cdot c}{\lambda} = h \cdot \nu_{21}, \tag{1.2}$$

where h is Planck's constant, c the speed of light, ν_{21} the optical frequency, and λ the wavelength of the photon. E_2 and E_1 are energy values corresponding to the two discrete energy levels and ΔE represents their energy difference.
The emission process may occur in two ways: A first possibility is the *spontaneous emission* process in which the system drops to the lower level in a completely random way. The second possibility is the *stimulated emission* process in which the system is 'triggered' by the presence of a photon to make the transition. The photon must have the proper energy corresponding to the energy difference between the original state and the lower energy level. The stimulated

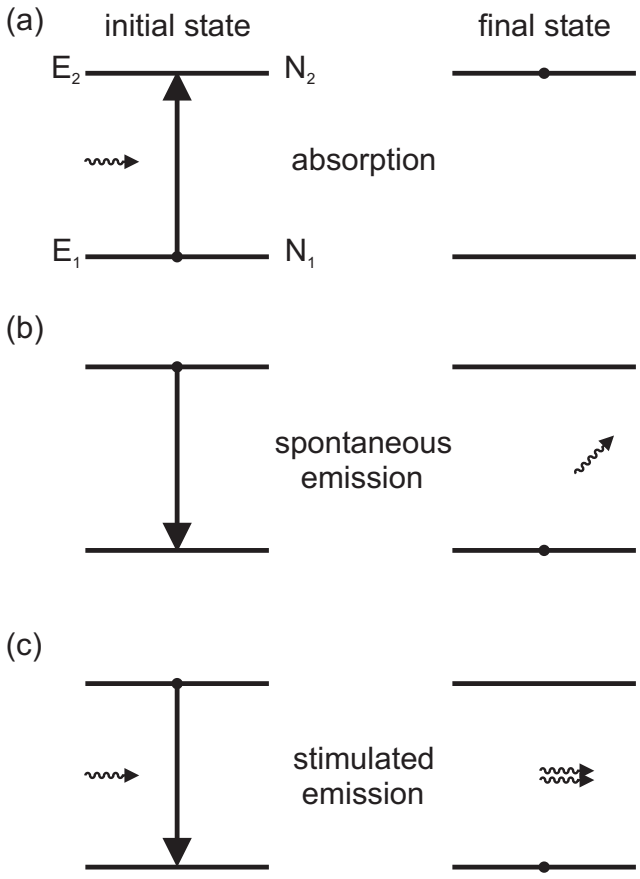

Figure 1.1: Schematic diagram illustrating (a) absorption, (b) spontaneous emission, and (c) stimulated emission

photon has the same frequency, same polarization state, same phase, and it propagates in the same direction as the stimulating photon. This is the fundamental difference between the stimulated and the spontaneous emission processes. In case of the latter one, atoms emit an electromagnetic wave that has no definite phase relation to that emitted by another atom (see Figure 1.1). Furthermore, the wave can be emitted in any direction.
In case of stimulated emission the original radiation is still present, and so the radiation intensity has been amplified. This is the origin of the acronym LASER: *Light Amplification by Stimulated Emission of Radiation*. The three processes are illustrated in Figure 1.1. The horizontal straight lines represent the energy level, the wavy arrows represent photons and the vertical arrows represent the transitions of electrons from one level to another. The black dot indicates the atom state, before (left part of the diagram) and after the transition (right part of the diagram).

1.1.1 Absorption

If a quasi monochromatic electromagnetic wave of frequency ν_{21} passes through an atomic system with energy gap $h \cdot \nu_{21}$, the population of the lower level will be depleted at a rate proportional both to the radiation density $\rho(\nu)$ and to the population N_1 of that level:

$$\frac{\mathrm{d}N_1}{\mathrm{d}t} = -B_{12} \cdot \rho(\nu) \cdot N_1, \tag{1.3}$$

where B_{12} is the coupling constant of radiation and matter for the absorption process (Einstein coefficient). The product $B_{12} \cdot \rho(\nu)$ can be interpreted as the probability per unit frequency that transitions are induced by the electromagnetic field.

1.1.2 Spontaneous emission

After a couple of atoms have been excited to the upper level, the population of the upper level decays spontaneously to the lower level at a rate proportional to the upper level population:

$$\frac{\mathrm{d}N_2}{\mathrm{d}t} = -A_{21} \cdot N_2, \tag{1.4}$$

where A_{21} is the coupling constant for the spontaneous emission process (Einstein coefficient). This coefficient gives the probability for an atom in level 2 to decay spontaneously to the lower level 1 within a unit of time. Spontaneous emission is characterized by the lifetime of the electron in the excited state in which it will spontaneously return to the lower state and radiate the energy difference. This radiative lifetime is related to A_{21} by:

$$\tau_{rad} = \tau_{21} = \frac{1}{A_{21}}. \tag{1.5}$$

In general, the reciprocal transition probability of a process is called its lifetime (see section 4.2).
It is noted that spontaneous radiative emission is merely one of two possible ways for the atom to decay. Decay can also occur in a non-radiative way. In this case the energy difference is delivered in some form of energy other than electromagnetic radiation such as kinetic or internal energy of the surrounding atoms or molecules [2].

1.1.3 Stimulated emission

As has already been mentioned, emission takes place not only spontaneously but also under stimulation. The atom gives a quantum to the radiation field by induced emission:

$$\frac{\mathrm{d}N_2}{\mathrm{d}t} = -B_{21} \cdot \rho(\nu) \cdot N_2, \tag{1.6}$$

where B_{21} is the coupling constant for the stimulated emission process (Einstein coefficient). Combining absorption, spontaneous and stimulated emission, as presented in equations (1.3), (1.4) and (1.6), one can write for the change of the upper and lower level populations in the two-level model:

$$\frac{\mathrm{d}N_1}{\mathrm{d}t} = -\frac{\mathrm{d}N_2}{\mathrm{d}t} = B_{21} \cdot \rho(\nu) \cdot N_2 - B_{12} \cdot \rho(\nu) \cdot N_1 + A_{21} \cdot N_2. \tag{1.7}$$

For a system in thermal equilibrium, the number of transitions per unit time from E_1 to E_2 must be equal to the number of transitions from E_2 to E_1. Hence, one gets:

$$A_{21} \cdot N_2 + B_{21} \cdot \rho(\nu) \cdot N_2 = B_{12} \cdot \rho(\nu) \cdot N_1, \tag{1.8}$$

which means that the sum of the rates for spontaneous and stimulated emission must be equal to the absorption rate in thermal equilibrium. Thus, one obtains for the radiation density

$$\rho(\nu) = \frac{A_{21}/B_{21}}{\frac{B_{12}}{B_{21}}\frac{N_1}{N_2} - 1}. \tag{1.9}$$

The populations of the energy levels 1 and 2 in thermal equilibrium are given by Boltzmann statistics:

$$\frac{N_1}{N_2} = \frac{g_1}{g_2} \exp\left(\frac{\Delta E}{k_B T}\right) = \frac{g_1}{g_2} \exp\left(\frac{h \cdot \nu_{21}}{k_B T}\right), \tag{1.10}$$

where k_B is Boltzmann's constant, T is the absolute temperature of the material in Kelvin and g_j is the degeneracy of level j. Hence, substituting equation (1.10) into (1.9) yields

$$\rho(\nu) = \frac{A_{21}/B_{21}}{\frac{g_1}{g_2}\frac{B_{12}}{B_{21}} \cdot \exp\left(\frac{h \cdot \nu_{21}}{k_B T}\right) - 1}. \tag{1.11}$$

The atom system is considered to be in thermal equilibrium, thus it must give rise to radiation which is identical with blackbody radiation, the density of which was described by Planck:

$$\rho(\nu) = \frac{8\pi h \nu^3}{c_0^3} \frac{1}{\exp\left(\frac{h \cdot \nu}{k_B T}\right) - 1}. \tag{1.12}$$

Comparing equations (1.11) and (1.12), one concludes:

$$\frac{A_{21}}{B_{21}} = \frac{8\pi h \nu^3}{c_0^3} \quad \text{and} \quad B_{21} = \frac{g_1 B_{12}}{g_2}. \tag{1.13}$$

The relation between the A's and B's are known as Einstein's relations, and, as already mentioned above, A_{21}, B_{12} and B_{21} are Einstein coefficients. Equations (1.13) are very important because they show a connection between the described radiation processes which are fundamental for describing laser operation.

The fundamental processes of spontaneous emission, stimulated emission, and absorption is summarized now by describing them in terms of absorbed or emitted photons: In the spontaneous emission process, the atom decays from level 2 to level 1 through the emission of a photon. In the stimulated emission process, the incident photon stimulates the transition $2 \rightarrow 1$, resulting in two photons (the stimulating one and the stimulated one). In the absorption process, the incident photon is simply absorbed to produce the transition $1 \rightarrow 2$. Thus, each stimulated emission process creates a photon, whereas each absorption process annihilates a photon [2].

1.2 Population inversion

At absolute zero temperature, Boltzmann's statistic in equation (1.10) predicts that all atoms will be in ground state. Thermal equilibrium at any temperature requires that a state with a lower energy is more densely populated than a state with a higher energy. Absorption and emission probabilities are always independent of population distribution among the levels. As long as the population of the higher energy level is smaller than that of the lower one, the number of absorption transitions is larger than that of emission transitions. There is an overall attenuation of radiation. If the ratio of atoms in both states is equal to g_2/g_1, the number of emissions becomes equal to the number of absorptions, and the material is transparent for the incident radiation. As soon as the product of the population of the higher level with g_1 becomes larger than the product of the lower level population with g_2, emission processes dominate and the radiation is amplified during its passage through the material. Thus, for achieving laser amplification, the following condition must be fulfilled:

$$N_2 \cdot g_1 > N_1 \cdot g_2, \tag{1.14}$$

i.e. one must create the so-called *population inversion*. A material in which this population inversion can be produced is referred to as an *active medium* [2]. Population inversion is clearly an abnormal situation, it is never observed in thermal equilibrium. In order to obtain it, a source of energy to populate the upper level has to exist. This process is commonly referred to as *pumping*. The point at which the population ratio of both states is equal to g_2/g_1 is called the inversion threshold.
It is impossible to achieve population inversion by optical pumping in an electronic system with only two energy levels. For a simple two-level system with no degeneracy, i.e. $g_1 = g_2$, one sees from equation (1.13) that $B_{21} = B_{12}$ holds. Hence, if atoms are excited into the upper level the probabilities of further absorption or stimulated emission are identical even with very intensive pumping. Thus, the best that can be achieved with a two-level system is equality of population of the two levels. Hence, the material becomes transparent. This situation is often referred to as *two-level saturation*.

As a consequence one must look for materials with more than two energy levels. Laser materials generally have a large number of energy levels, but only three or four of them are directly involved in laser operation. The three-level system is illustrated in Figure 1.2 (a). Initially,

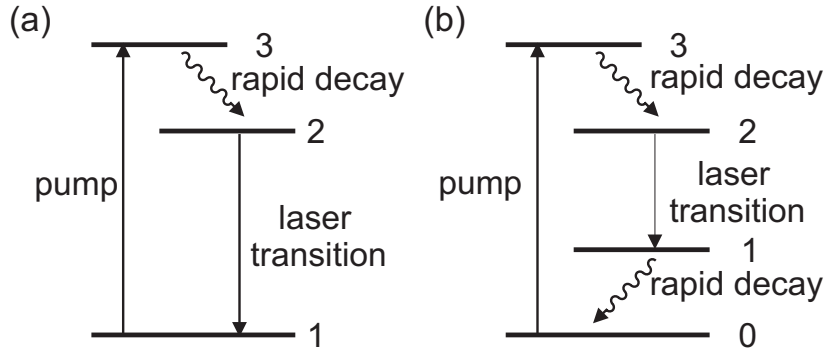

Figure 1.2: Simplified energy level diagram of (a) a three-level and (b) a four-level laser

all atoms of the laser material are in the lowest level 1. An auxiliary radiation pump source excites the atoms. The pump radiation raises an atom from the ground state to the pump band of level 3. Most of the excited atoms are transferred by fast radiationless transitions into the intermediate level 2. In this process the energy lost by the atom is transferred to the lattice and converted to heat. With higher pump power population inversion between levels 2 and 1 is achieved. Finally, the atoms return to the ground level by the emission of a photon. This transition is responsible for the laser action in a *three-level system*. It is important that the rate of radiationless transfers from level 3 to level 2 is fast compared to the other spontaneous transition rates. Therefore, the lifetime of the metastable level 2 should be large. This allows for a large build-up in the number of atoms in level 2. The relatively long lifetime of the metastable level provides a mechanism by which inverted population can be achieved. The main advantage of the three-level system is that atoms are in effect pumped directly from level 1 into the metastable level 2 with only a short break as they pass through level 3. But the three-level system has the drawback that level 1 is the ground level which normally possesses almost all the atoms. To achieve population inversion between levels 2 and 1 in a non-degenerate system, half of all the atoms must be moved to level 2, and so intensive pumping is needed. In a degenerated system, the population ratio g_2/g_1 has to be reached.

Figure 1.2 (b) shows a *four-level laser system*. The pump transition raises atoms from the ground state (now called level 0) to level 3. As in case of the three-level system, the atoms excited in this way will decay fast to level 2. The laser transition proceeds now to the fourth level, terminal level 1, which is situated above the ground state. From here the atoms undergo a rapid non-radiative transition to the ground level guaranteeing continuous-wave (cw) operation. In a true four-level system, the terminal laser level 1 will always be empty, hence

a population inversion of the laser transition between levels 2 and 1 can occur even with a small pump power. Thus, the high pump rate necessary in a three-level system is no longer needed. It should be noted that the term four-level laser is used for any laser whose lower laser level is essentially empty due to the reason that it is many k_BT above the ground level. Even when levels 2 and 3 are the same level, it is called a four-level system despite of having only three levels [2].
In conclusion, three-level systems have higher threshold powers than four-level systems, and thus four-level schemes are to be preferred. However, by a combination of favorable circumstances, it is possible to overcome the disadvantage of the three-level scheme.
The so-called *quasi-three-level laser* has become a very important laser category as well. In this case, the ground level consists of many sublevels, the lower laser level being one of these sublevels. Hence, the scheme in Figure 1.2 (b) can still be applied to a quasi-three-level laser with the understanding that level 1 is a sublevel of the ground level and level 0 is the lowest sublevel of the ground level. If all ground state sublevels are strongly thermally coupled e.g. by some fast non-radiative decay process, then populations of these sublevels are always in thermal equilibrium [2]. If one further assumes that the energy separation between levels 1 and 0 is comparable to k_BT, then there is always some population present in the lower laser level and the laser system behaves in a way that is intermediate between a three- and a four-level laser.

2 Solid-state and semiconductor laser systems

It is very time-consuming to catalog all the laser devices that have been demonstrated to date, especially since the variety of laser materials, laser pumping methods, and laser experimental techniques is almost endless. This chapter gives a brief overview of some selected solid-state and semiconductor lasers. It will not go into detail and thus is not a substitute of a typical lecture book. Ruby lasers and fiber lasers are presented as examples of solid-state laser systems which comprise crystals, glasses and fibers as active medium. Finally, distributed feedback (DFB) lasers are presented as an example of semiconductor laser systems.

2.1 Solid-state lasers

2.1.1 Ruby lasers

The first laser of any type to be operated was the flash-pumped ruby laser demonstrated by Maiman in early 1960 [1]. Ruby (Cr^{3+}:Al_2O_3) is sapphire (Al_2O_3), in which chromium ions (Cr^{3+}) replace a small percentage of the aluminium ions.
Maiman was able to use blue and green wavelengths from the flash lamp to optically pump atoms from the $^4A_2$ ground level of the Cr^{3+} ions in the lattice into the broad $^4F_2$ and $^4F_1$ bands of excited energy levels. Corresponding levels of interest for laser action are shown in Figure 2.1. This was possible by placing a ruby rod (see Figure 2.2) inside a spiral flash lamp

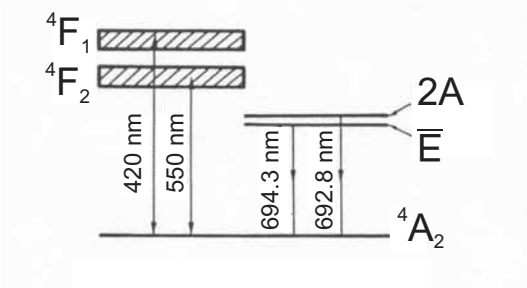

Figure 2.1: Simplified energy level diagram of ruby [2]

filled with xenon and then discharging a high-voltage capacitor through the lamp [3]. In the first ruby lasers, partially transparent metallic silver mirrors were evaporated directly onto the polished ends of the laser rod. Modern lasers often instead use rods with ends cut and polished at Brewster's angle to avoid reflections, with external dielectric mirrors forming the optical cavity. Curved mirrors are used, especially in free space setups, to reduce alignment

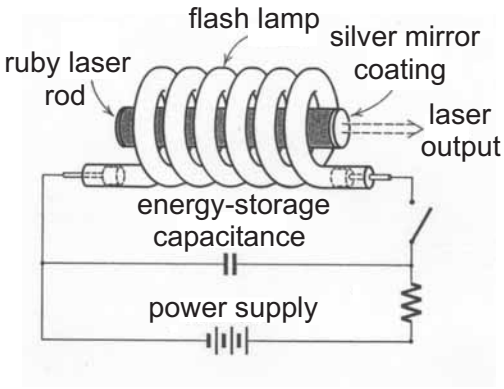

Figure 2.2: Design of the first pulsed ruby laser [3]

tolerances. In ruby, atoms excited into the above mentioned energy levels will relax very rapidly, and with close to 100 % quantum efficiency, down into the comparatively very sharp 2A and $\bar{\text{E}}$ levels, also called ^{2}E levels, lying about 694 nm (representing the well-known red laser transition) above the ground energy level.
However, the ruby laser is a three-level laser system, in which the lower laser level is also the ground energy level. By pumping hard enough, more than half of the Cr^{3+} ions can cycle from the ground level up through the absorption bands, which are responsible for the pink color of the material, and into the highly metastable upper energy laser level with its fluorescent lifetime of about 4.3 ms. Even though a ruby laser is a three-level laser, which is usually very unfavorable compared to a four-level system (see chapter 1), Maiman was able to produce a powerful burst of laser action (multimode operation) from the ruby rod with sufficiently hard pumping.
In a flash-pumped ruby laser, the flash lamp may be connected to a capacitor of about 10 to 100 μF charged to a prebreakdown voltage of roughly 1000 to 1500 V. The lamp itself is then triggered or ionized by a high-voltage pulse, so that it becomes conducting. The capacitor energy then discharges through the lamp with a typical pulse length of 200 μs, peak currents of up to a few hundred amperes and peak electrical power input of 25 to 250 kW [3]. The laser rod may convert the pump light into laser energy with about 1 % efficiency, leading to laser output energies of 50 mJ to 0.5 J per shot and average powers during the pulse of 2.5 to 25 kW [3]. Commercially available ruby lasers use rods that are typically 5 to 20 cm in length [4]. Typical rod diameters range from 5 to 10 mm [2].
The laser action in ruby actually occurs as a series of short *spikes* or relaxation oscillation bursts during the entire pumping time. Relaxation oscillations will be discussed in chapter 6. Ruby can, with some difficulty, be made to oscillate on a cw basis [3]. Ruby lasers are rarely used today and are being replaced by alexandrite (Cr^{3+}:Al_2BeO_4) lasers.

2.1.2 Fiber lasers

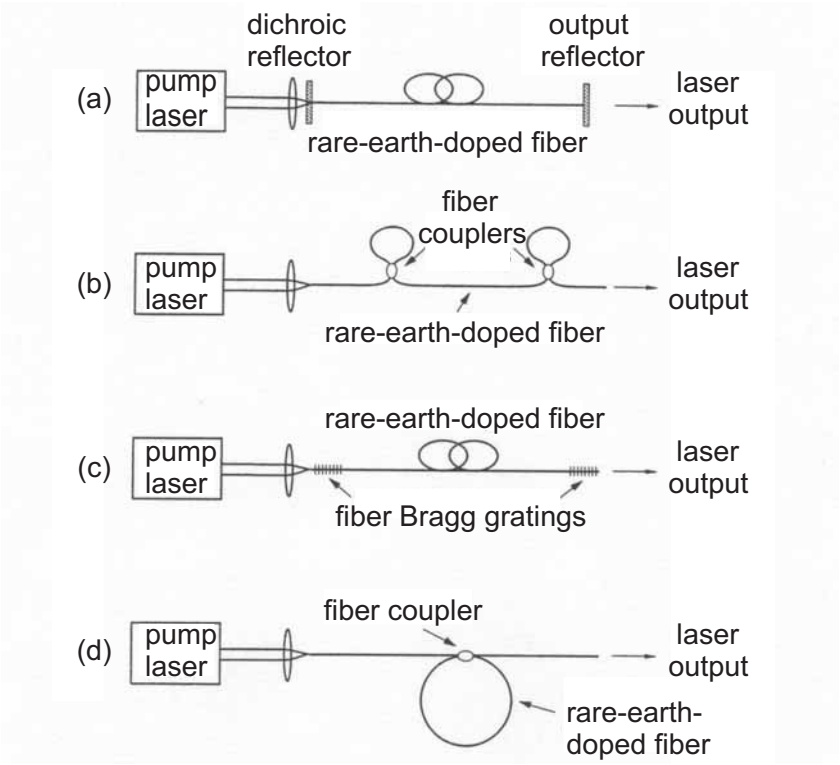

Figure 2.3: Some possible schematics of fiber resonators for a cw fiber laser: (a) Fabry-Perot with dielectric reflectors, (b) Fabry-Perot with all-fiber reflectors, (c) Fabry-Perot with fiber Bragg gratings, and (d) ring configuration [5].

A fiber laser is a solid-state laser in which the active gain medium is the core of an optical fiber doped with rare earth elements such as erbium, praseodymium, ytterbium or thulium. Semiconductor laser diodes are commonly used for pumping fiber lasers. Fiber lasers can have extremely long gain regions and thus a long interaction length of pump and laser field. They can support very high output powers because the fiber's high surface area to volume ratio allows efficient cooling and thus results in very high efficiencies. Its waveguiding properties reduce thermal distortion of the beam. Hence, the beam quality is more or less independent of the output power in contrast to laser diodes.
These interesting properties make them attractive alternatives to other solid-state lasers. Due to the waveguide structure of the fiber the fiber laser setup in general is very simple. Several types of optical resonators have been used in cw rare-earth-doped fiber lasers, each with its own advantages and disadvantages. The most common resonator is the Fabry-Perot resonator

(see Figure 2.3 (a) to (c)). It is typically formed by placing miniature planar dielectric reflectors in intimate contact with the ends of the doped fiber (see Figure 2.3 (a)), which are either polished or cleaved perpendicular to the fiber axis. The pump beam is usually focused into the fiber through the highly reflective mirror, which must be dichroic to transmit the pump [5]. A variation of this design uses dielectric reflectors deposited directly onto the polished fiber ends. In lasers based on a high-gain transition, the dielectric reflectors can be eliminated altogether, and the weak Fresnel reflections at the fiber ends can provide sufficient optical feedback to reach oscillation.
Another form is the all-fiber Fabry-Perot resonator (see Figure 2.3 (b)). The optical feedback is provided by two Sagnac fiber loops, one at each end of the doped fiber. Each Sagnac loop is made of a length of doped fiber closed by a coupler [5]. The coupler can be one of several types of commercial devices, such as a fused fiber coupler.
The simplest setup consists of a rare-earth-doped fiber with fiber Bragg gratings (FBGs) written into the fiber at both ends and acting as laser mirrors (see Figure 2.3 (c)). A pigtailed pump diode is spliced to one fiber end whereas the other end delivers the laser radiation. Such strikingly simple setups without any need of alignment are one reason for the fascination caused by these devices.
Another important fiber laser resonator is the all-fiber ring resonator shown in Figure 2.3 (d). In practice it is easy to fabricate by forming a loop with the doped fiber and a coupler, such as a low-loss fused fiber coupler [5]. The pump light can be injected into the resonator either through the coupler, provided its coupling ratio is close to zero at the pump wavelength, or through an auxiliary wavelength division multiplexed (WDM) coupler placed in the loop. Such a ring laser resonates in both directions and thus has a bidirectional output which yields a conversion efficiency which is only half as high as that of the Fabry-Perot cavity. This limitation can be removed by introducing an optical isolator in the ring, which forces unidirectional operation. As in a Fabry-Perot resonator, in a ring resonator the two counterpropagating signal waves interfere and produce a standing wave. The latter induces spatial hole burning in the fiber gain, which allows the oscillation of several longitudinal cavity modes [5]. Again, an intracavity isolator can eliminate this effect and helps to narrow the laser linewidth. Ring configurations are in fact often used to produce single-mode fiber lasers.
Rare-earth-doped silica fibers with proper resonator design can be operated as single longitudinal mode lasers where the pump beam is launched longitudinally along the fiber length and is guided by the core itself. If it is guided by the inner cladding around its core, it is called a *double-clad fiber laser*. A typical example for the performance of a single-mode fiber laser is a 5 m long Er^{3+}:silica fiber laser operated in Fabry-Perot configuration with a mirror reflectance of 99 % at one end and 4 % (simple Fresnel reflection) at the other end which provides an output of about 8 mW with a semiconductor pump power of 90 mW at 1.46 μm [4].
Doped silica fiber lasers can also function in pulsed Q-switched and mode-locked configurations. At 300 K the above described system behaves as a three-level laser, while at 77 K it behaves as a four-level laser [4]. There is an optimal fiber length for achieving minimum threshold in a three-level system, whereas in a four-level system the threshold power decreases

inversely with the active fiber length [4].
In a conventional single-mode fiber, the transverse dimensions of both pump and laser beams are comparable to the core radius. Thus, both dimensions are 10 to 50 times smaller than corresponding typical values for bulk devices. Hence, for the same values of laser parameters, the threshold power is expected to be by two to three orders of magnitude smaller in a fiber laser compared to a bulk device [2].

2.2 Semiconductor lasers

2.2.1 DFB lasers

Semiconductor lasers show a large variety of applications and have found widespread use as pumps for solid-state lasers. The spontaneous and stimulated emission processes are vastly more efficient in direct bandgap semiconductors than in indirect bandgap semiconductors, thus silicon is not a common material for semiconductor laser diodes.
A laser diode, like many other semiconductor devices, is formed by doping a very thin layer on the surface of a crystal wafer. The crystal is doped to produce an n-type region and a p-type region, one above the other, resulting in a p-n junction. Under suitable conditions, the electron and the hole may coexist in the same area for quite some time (on the order of microseconds) before they recombine. Then a nearby photon with energy equal to the recombination energy can cause recombination by stimulated emission. This generates another photon and means that stimulated emission causes gain in an optical wave (of the correct wavelength) in the injection region. The gain increases as the number of electrons and holes injected across the junction increases.
The distributed feedback (DFB) laser was designed to overcome the spectral shortcomings of a Fabry-Perot laser [6]. It is the industry standard in long-distance fiber-optic links. One obtains much smaller linewidths with DFB lasers than with a Fabry-Perot laser. Figure 2.4 (a) shows the structure of a DFB laser which is very similar to a Fabry-Perot laser. The main difference is the Bragg reflector structure located near the light-emitting active region. The grating is etched close to the p-n junction of the diode to stabilize the lasing wavelength. The Bragg grating acts as a reflective mirror and provides a periodic change in the index of refraction in the waveguide. Each grating period reflects a small amount of light back in the opposite direction. The Bragg grating reflects the light at the wavelength where the grating period is one half of the wavelength of light in the semiconductor material.
At least one facet of a DFB is anti-reflection coated. The DFB laser has a stable wavelength that is set during manufacturing by the pitch of the grating, and can only be tuned slightly with temperature. The small grating dimensions make the device fabrication technology more critical than a Fabry-Perot laser. In fact, the pitch of the grating typically has to be of submicron dimension, e.g. for a 1550 nm InGaAsP laser with an effective refractive index of 3.4, one can calculate a grating pitch of about 0.23 μm. It is thus difficult to make the pitch uniform along the grating length and also constant from one grating to the next. Extra wafer

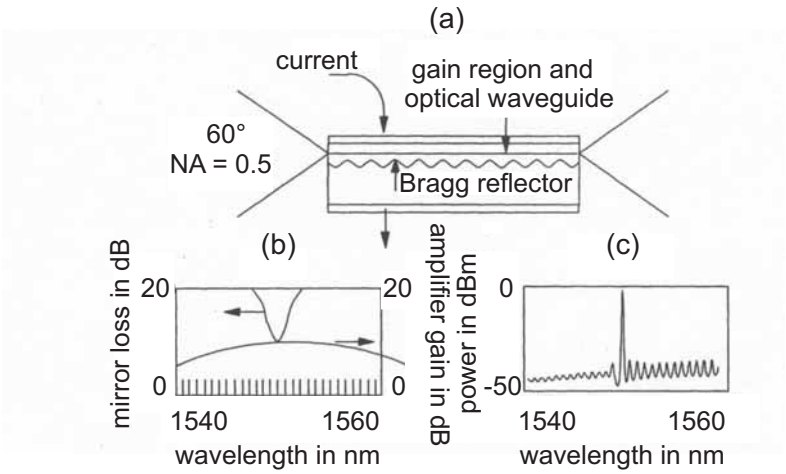

Figure 2.4: (a) Cross-section of a distributed feedback (DFB) laser. (b) Bragg grating reflectivity, amplifier gain, and longitudinal mode location. (c) Power versus wavelength for the DFB laser [6].

processing steps are necessary to etch the Bragg grating into the semiconductor material and to grow new material on top which results in more expensive laser diodes.
The effect of the Bragg grating on the mirror reflectivity shape is shown in Figure 2.4 (b). It shows that the Bragg grating reflection passband is only a few nanometers wide. Only a narrow wavelength range can reach the threshold condition when increasing the current in this laser. All laser power is emitted in a single longitudinal mode due to the frequency-dependent mirror reflectivity. Figure 2.4 (c) shows the single longitudinal mode spectral shape of a DFB laser.

3 Rare earth laser materials

Until here the presence of an ideal active medium was assumed which does not exist in reality. A huge number of laser materials is in use, but in this chapter only the most important properties of rare earth host materials which are important to understand fiber laser operation will be discussed. The basic features will be briefly explained. Emphasis is put on fluoride glasses doped with rare earth ions.

3.1 Rare earth ions and host materials

Rare earth ions are good candidates for active ions in laser materials because they show many absorption and fluorescence transitions in almost every region of the visible and the near-infrared range. Rare earths have other important characteristics in comparison to other optically active ions as well: the wavelengths of their emission and absorption transitions are relatively insensitive to host materials, the lifetimes of metastable states are long and the quantum efficiency tends to be high [5]. These properties lead to an excellent performance of rare earth ions in many optical applications.
The electronic configuration and the effects of the environment determine the electronic energy levels of rare earth ions. For instance, the two 4f electrons of praseodymium ions in the central field interact electrostatically (Coulomb interaction), and as a result their energy level splits into seven levels with different energies such as ^{1}S, ^{3}P, ^{1}D, ^{3}F, ^{1}G, ^{3}H, and ^{1}I. Then, due to spin-orbit coupling, the triplet levels ^{3}H and ^{3}F which show a total spin of $S = 1$ split into three levels such as $^3H_6$, $^3H_5$, $^3H_4$, and $^3F_4$, $^3F_3$, $^3F_2$, whereas the singulett level ^{1}G does not split.
Expressions such as $^3H_6$, $^3H_5$, $^3H_4$ are called term symbols which provide three pieces of information [7]:

- The letter indicates the total orbital angular momentum L defined by the letters S, P, D, F, G, H, I, ... which correspond to $L = 0, 1, 2, 3, 4, 5, 6, \ldots$, respectively.
- The left superscript in the term symbol shows the multiplicity of the terms. This is given by the total spin S, and the multiplicity is $2S + 1$.
- The right subscript in the term symbol is the value of the total angular momentum quantum number J and is given by

$$J = L + S, L + S - 1, \ldots, |L - S|.$$

Russell-Saunders coupling (LS coupling) is most often used to describe the states of lanthanides, and the states are therefore expressed as $^{2S+1}L_J$.

The effect of the structural environment in condensed matter is another important issue. When a many-electron atom is placed in an external field such as a magnetic field or an electric field, the energy levels split. In general, when a magnetic field is applied to ions, the energy levels split into levels whose number depends on the value of the total angular momentum quantum number J. This splitting is called *Zeeman effect*. On the other hand, if an electric field is applied to ions, the splitting is called *Stark effect*.
In glass materials, the electrostatic interaction between the ions and lattice is dominant, so the energy level splitting is due to the Stark effect. The number of Stark levels is $2J + 1$. As a result of the shielding of the 4f electrons, these Stark shifts are quite small, only around a few hundred inverse centimeters. Additionally, the magnitude of the energy split depends on the magnitude of local electrical fields, which varies dependent on their location in the host material. The magnitude of the Stark splitting is slightly different for each individual ion because of the differences in the crystal field surrounding the rare earth ions. Therefore, a group of several Stark levels has a noticeable broadening originating from the site-to-site difference in the Stark level of the individual ions. It is noted that an individual Stark level is not broadened at all.
This broadening is an *inhomogeneous broadening* and originates from the material structure. In addition, the individual Stark levels fluctuate and broaden as a result of the crystal field fluctuations caused by thermal atomic motions. This broadening due to thermal fluctuation is called *homogeneous broadening*. A transition between two Stark levels takes place by the creation or annihilation of a phonon. Lowering the temperature reduces the phonon population and thus causes spectral narrowing. Phonon broadening acts on all of the rare earth ions to a similar degree and is thus homogeneous.
In thermal equilibrium, the energy population of ions shows a Boltzmann distribution, and there is a large difference in the population of the sublevels. The sublevels with lower energy show a higher population. Hence, the absorption spectra shift towards shorter wavelengths and the fluorescence spectra towards longer wavelengths. The absorption and emission of photons in rare earth ions take place between different energy levels, specifically between different Stark levels. The resulting asymmetry of the fluorescence and absorption bands would not occur if all Stark levels were equally populated. The Stark split in glass materials varies dependent on the ion location and the field magnitude. Different condensed materials such as silica glass, fluoride glass and crystals show different spectral characteristics of absorption and emission of rare earth ions due to the different glass matrices and their different Stark split energy levels.

Materials for laser operation should have strong absorption bands and a reasonably high quantum efficiency for the fluorescent transition of interest. Such characteristics are generally shown by solids which contain a small amount of elements in which optical transitions can take place between states of inner, incomplete electron shells. Roughly, solid-state host materials may be grouped in crystalline solids, glasses and fibers. The host must have good optical, mechanical and thermal properties in order to resist the operating conditions of practical

lasers. Desirable properties include hardness, chemical inertness, absence of internal strain and refractive index variation, and ease of fabrication.
For rare-earth-doped crystals, the absorption and emission between Stark components of different levels usually can be observed at room temperature as discrete lines. In contrast, individual Stark transitions for glass hosts cannot be resolved.
Crystalline hosts provide high intensity at nearly discrete wavelengths while glass hosts have lower intensities over a broad, continuous range of wavelengths. This is possible because of the disordered structure of glass. There are site-to-site variations in the local field acting on the laser ions in glasses which cause a range of Stark energy level splitting of about 50 to 100 cm^{-1}. It is in the same order of magnitude as the spacing between individual Stark levels. Thus, optical transitions between Stark levels are not resolved for glasses at room temperature. The resultant inhomogeneously broadened optical transitions between the J states of rare earths may have total effective linewidths of several hundred cm^{-1} and lasing can usually be obtained throughout this inhomogeneously broadened emission band. Therefore, rare earth glass lasers offer some features not readily available in crystalline materials.
Both homogeneous and inhomogeneous processes are responsible for broadening the sharp line structure of the crystal into the broad spectrum seen for the glass. For a homogeneously broadened transition, radiation of a given wavelength will interact with all ions with equal probability. Thus, photons of any suitable pump wavelength will produce the same gain spectrum, and photons of any signal wavelength in the band can saturate it completely. If inhomogeneous broadening dominates, individual sections of the gain spectrum act independently and can be individually addressed by photons of different wavelengths. In a homogeneously broadened system, all the power can be extracted by a signal at any wavelength within the gain spectrum, and signals at different wavelengths can interact with each other by perturbing the gain spectrum. This leads to high efficiency for lasers and power amplifiers. Homogeneous linewidths are more than an order of magnitude larger in glasses than in crystals, and inhomogeneous linewidths are essentially independent of temperature [5]. In the following glasses as host materials will be described in more detail.
Glasses are an important class of host materials for some of the rare earths. The practical advantages compared to crystalline materials are a comparatively easy fabrication and good optical quality. As already mentioned, laser ions placed in glass show a larger fluorescent linewidth than in crystals. On the other hand, glass has a much lower thermal conductivity than most crystalline hosts. In general, if a liquid material is cooled down gradually, it crystallizes, expelling the specific latent heat at a characteristic temperature, that is, the melting temperature. However, dependent on the cooling method some special materials do not crystallize below the melting temperature and their viscosity increases to such a high value that they become solid with a disordered arrangement of atoms, quite like that in the liquid state. Fast cooling is required for glasses. Such a super cooled liquid is called glass. Therefore, glasses have only a short-range order and form a three-dimensional matrix, but lack the uniformity, symmetry, and structure of a crystalline material, and they have no long-range periodicity. Glasses are in a state somewhere between a crystalline solid and a liquid.

Heavy metal fluoride glasses (HMFG), based on zirconium fluoride (ZrF_4) and indium fluoride (InF_3), show interesting properties as rare earth hosts. The most stable HMFG is ZBLAN, made from the fluorides of zirconium, barium, lanthanum, aluminium, and sodium (Zr, Ba, La, Al, and Na) in the stoichiometry 53:20:4:3:20 mol%, respectively. This glass is called a fluorozirconate glass because its major component is Zr. The bonding of HMFG is not covalent but ionic, and weak compared to SiO_2. This is the reason for a wider infrared transparency. At long wavelengths, the transparency of an optical material is limited by the existence of an infrared vibration or the so-called multi-phonon edge.
Materials such as ZBLAN have a high degree of transparency at wavelengths in the 2-5 μm infrared range. By contrast, silica glass is transparent only up to 2 μm, beyond which strong absorption occurs.
Another interesting feature of ZBLAN glass is that it already contains rare earth ions (La^{3+}) as an integral component. La^{3+} can easily be substituted by an alternative rare earth ion without significantly affecting the properties of the glass. Doping up to 10 mol% is possible. In contrast, silica fiber is usually doped with less than 0.1 mol%. If rare earth ions are incorporated in a silica glass network, the SiO_2 is distorted and does not accept the dopant ions well which consequently tend to cluster. Therefore, SiO_2 can incorporate only very small amounts of rare earth dopants before microscopic clustering occurs and ion-ion interactions (see section 3.3) shorten the fluorescent lifetimes.

3.2 Non-radiative relaxation

Non-radiative relaxation caused by multi-phonon emission processes strongly influences the radiative quantum efficiency of the transitions between the 4f states of rare earth ions. These phonons arise from the interaction of the electronic levels of the rare earth with vibrations of the host lattice. If electronic states are spaced so closely that they can be bridged by a small number of phonons, the transition will occur rapidly. This leads to thermal occupation of levels above the ground state or metastable states if the separations are on the order of thermal energy. The ion undergoes a non-radiative transition to a lower electronic state through the emission of multiple phonons. If the non-radiative relaxation rate of a specific level is comparable to its radiative transmission rate, the efficiency of the luminescent process originating in that level is degraded. The lattice vibrations are quantized as phonons having excitation energies determined by the masses of the constituent ions and the binding energies between the ions.
The probability of such a transition decreases strongly with an increasing number of phonons needed. In materials with low phonon energy (LPE), the number of phonons required to bridge an energy gap is large, leading to a low multi-phonon relaxation rate because the multi-phonon relaxation probability depends approximately exponential on the energy gap between levels and decreases with decreasing temperature [5].
For a given energy difference the multi-phonon relaxation rate in silicate glass is always larger

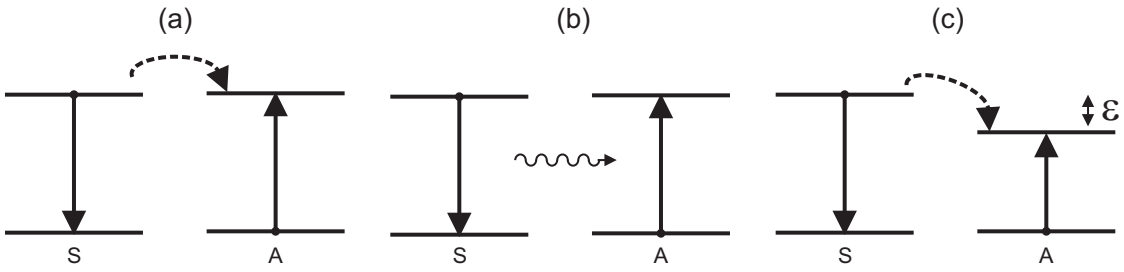

Figure 3.1: Ion-ion energy transfer mechanisms from a sensitizer (S) to an activator (A): (a) resonant energy transfer, (b) radiative transfer, (c) energy transfer assisted by phonons

than in fluoride glass. These large differences originate mainly from the difference in phonon energies of the host glasses. The strong covalent bonds of silicate glasses result in a higher phonon energy (1100 cm^{-1}) compared to the weaker ionic bonds of fluoride glasses which lead to a much lower phonon energy (580 cm^{-1}). Owing to this lower phonon energy, more metastable levels are available in fluoride glasses. Therefore, many transitions that are laser-inactive in silicate glass can be active in fluoride glass. In silica the multi-phonon relaxation rate is so high that any ion arriving in an upper level will undergo multi-phonon emission before having a chance to show fluorescence. Only when the energy gap to the next lower level is larger than 4000-5000 cm^{-1} may a level in silica become fluorescent to a significant degree. By contrast, in fluoride glasses, where the phonon energy is smaller, an energy gap of only 2000-3000 cm^{-1} is needed before significant fluorescence decreasing occurs. In conclusion, this difference in multi-phonon relaxation yields a better quantum efficiency for fluoride glasses compared to silica.

3.3 Ion-ion interaction

In the preceding discussions only isolated ions have been considered. When the dopant density of rare earth ions is increased, a level will be reached where the mean ion separation is sufficiently small to allow for a spatial migration of the excitation from one rare earth ion to a neighboring ion. Such an excitation transfer can be used to enhance the pumping of a laser transition and, thus, to increase lasing efficiency. However, there are also situations where the presence of multi-ion phenomena can weaken the laser performance. In the following, different ion-ion interaction processes will be described in detail.

3.3.1 Energy transfer

The simplest case of energy transfer involves the transfer of energy from an excited ion to a nearby ion in its ground state without gain or loss of energy in a two-ion system as a whole. This is known as *resonant energy transfer* and is illustrated in Figure 3.1 (a). The activator

ion (A) receives energy from a nearby sensitizer ion (S). Also, *non-resonant energy transfer* can occur where the difference in energies between the initial and final ionic states is made up by the assistance of a photon or a phonon [8]. In the first case, one ion emits a photon which is then reabsorbed by another ion (see Figure 3.1 (b)). If the transition energies for the ions involved are not equal, absorption or emission of phonons becomes necessary in order to conserve energy. This process is schematically shown in Figure 3.1 (c).
If energy transfer between two different kinds of ions takes place, the type of ion that is optically excited is referred to as the *donor*, and the one that receives the excitation is called the *acceptor*. The process can occur in a single step in which the particular donor ion that absorbs the pump photon transfers its energy to a nearby acceptor. If the donor concentration is high enough, another mechanism can occur: the migration of the excitation among the strong coupled donor ions (donor-donor transfer). This proceeds until the excitation reaches a donor which is close enough to an acceptor to complete the final step of the transfer process. This mechanism is commonly used for sensitizing materials by using a large donor concentration (e.g. Yb^{3+}) in order to absorb the optical excitation and to transfer it to the activator (e.g. Pr^{3+}) if the latter has weekly or poorly placed absorption bands [5].
Processes which convert long-wave radiation into short-wave radiation by multi-photon mechanisms are called *upconversion processes*. The high values of pump intensity in a conventional single-mode fiber available from laser pumping enables a considerable fraction of the ground-state population to be raised to some upper level of the active ion. Under this condition, a second pump photon of the same or different wavelength can thus raise this population to a still higher energy level. From this level, laser action can take place to a lower energy level, so that the energy of the emitted photon is actually higher than each pump photon energy.
A laser working on such a scheme is referred to as an *upconversion laser* [2]. While such schemes, where two or more pump photons of equal or different wavelength are used, work with bulk media, they are much more practical with fiber lasers exploiting fiber materials of a special kind. In silica fibers, in fact, the main limitations to this upconversion scheme stem from non-radiative decay (see section 3.2) of the energy levels involved which usually occurs by multi-phonon deactivation. The probability of such a decay is a very strong function of the number of phonons that must be emitted in the process [2]. In this case the relevant phonon energy is the maximum energy in the phonon spectrum of the host material, since the non-radiative decay rate increases strongly for a given transition with increasing phonon energy values. A substantial reduction in the non-radiative decay is obtained by using host materials with LPE. Among the materials that can be fabricated into fibers, the most widely used one consists of a mixture of heavy-metal fluorides such as ZBLAN.
As examples, when pumped by three photons of the same wavelength ($\lambda = 1120 - 1150$ nm), ZBLAN fibers doped with Tm^{3+} have produced a very efficient upconversion laser in the blue ($\lambda = 480$ nm), giving output powers in excess of 200 mW [2]. When pumped by two photons at about 1020 nm and 835 nm, ZBLAN fibers doped with Pr^{3+} have produced laser action on several transitions from blue to red ($\lambda = 491, 520, 605, 635$ nm), giving e.g. as high as approximately 20 mW output power in the blue. More details in case of the Pr^{3+}-doped fiber

laser are discussed later.
Rare earth ions can be optically excited to several discrete energy states, each of which has a finite lifetime before decay to a lower energy state occurs. Therefore, energies of absorbed photons are added in the energy level scheme of a rare earth ion resulting in the population of a higher excited state than could be reached by one-photon absorption. The finite lifetimes can be usefully employed to allow for further interactions, e.g. the energy transfer to, or the absorption of a second photon. The general energy scheme related to the successive absorption of two photons is shown in Figure 3.2 (a). If a photon of wavelength λ_1 has an energy in resonance with the transition from the ground state 1 to the excited state 2, it is absorbed. This process is termed *ground state absorption (GSA)*. After that, an incident photon with an energy resonant with the transition from state 2 to the higher excited state 3 may be absorbed by the previously excited ion. This process is known as *excited state absorption (ESA)*. It leads to an ion reaching a higher excited state. Again, the ion may be excited to a metastable level or to undergo a decay to a lower level. Because of the broadening of rare earth ion transitions in glass at room temperature, overlapping GSA and ESA spectra are quite common. This may lead to a case, where only one pump wavelength is necessary ($\lambda_1 = \lambda_2$).
In rare-earth-doped crystals, on the other hand, rare earth absorption spectra are significantly less broadened, and it is much less likely that the GSA and ESA spectra overlap. Thus, it is necessary to use two pump laser wavelengths, one resonant with the GSA transition and the other resonant with the ESA transition. Energy transfer can also occur between ions where both the sensitizer and activator ions are in one of their excited states. This allows for a possible fluorescence at a higher frequency than that of the excitation beam which is typical for upconversion processes.
The different types of the energy transfer upconversion are illustrated in Figure 3.2 (b)-(f). In Figure 3.2 (b) the energy transfer between the sensitizer in its excited state and the activator in its ground state is presented. The activator is promoted to its excited state 2. Then ESA occurs from state 2 of the acceptor ion and is promoted to the higher excited state 3. This pumping process has an advantage: compared to pure ESA for most cases only one pump beam is necessary.
The next process shown in Figure 3.2 (c) is called *successive energy transfer*. In this case, only the sensitizer ion may absorb photons. After that, the activator ion is promoted to its excited state 2 by a first energy transfer, and then it is promoted to its excited state 3 by a second energy transfer. Figure 3.2 (d) depicts schematically the case which might be named *cross relaxation upconversion*. Indeed, *cross relaxation* usually refers to all types of energy transfers occurring between identical ions. If the sensitizer and the activator are identical ions, photons are absorbed both by the sensitizer and by the activator leading to these two ions reaching their excited state 2. Then, an energy transfer promotes the activator ion to its state 3 while the sensitizer goes down to a lower energy state. For the three cases (b), (c), and (d), further energy transfers from the sensitizer to the activator may occur and populate higher energy levels of the activator [9].

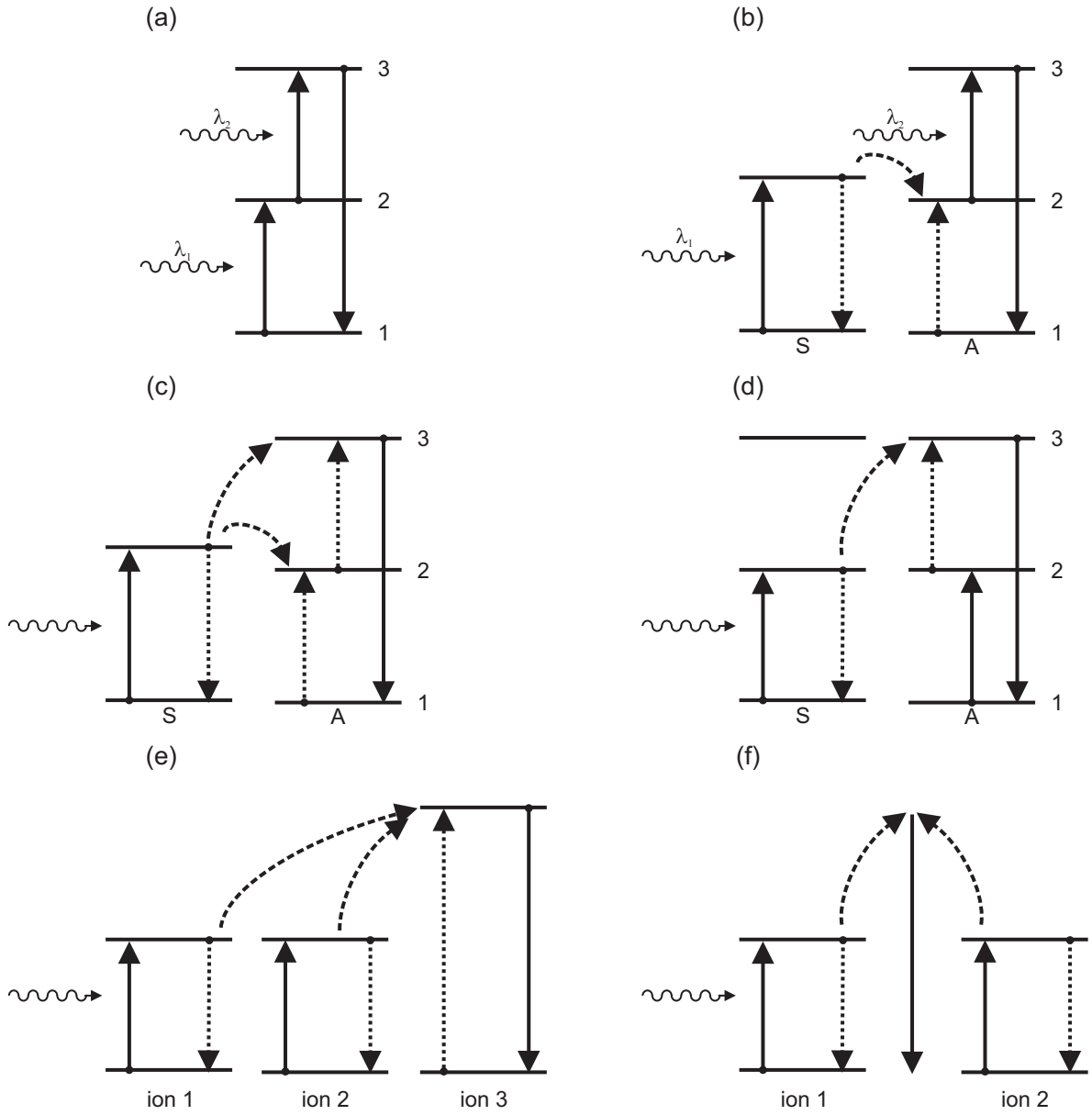

Figure 3.2: Schematic illustration of upconversion excitation mechanisms: (a) two-step absorption, (b) energy transfer followed by ESA, (c) successive energy transfers, (d) cross relaxation upconversion, (e) cooperative sensitization, (f) cooperative luminescence [9]

If more than one center is involved in the elementary process of sensitization or luminescence, one may speak of *cooperative effects*. Figure 3.2 (e) shows the case of *cooperative sensitization*. Here, the energy accumulated by two excited ions is transferred to another ion which

reaches a higher excited state from which it can relax to the ground state. When the process starts, ions 1 and 2 are in their excited states and ion 3 is in its ground state. The final state is reached when ions 1 and 2 are in their ground states and ion 3 is in its excited state. Conservation of energy requires that the photon emitted by ion 3 must carry the cumulated energy of the two photons absorbed by ions 1 and 2. If two excited interacting ions cause in a single process the emission of a photon, one speaks of *cooperative luminescence* shown in Figure 3.2 (f).

3.3.2 Photon avalanche

The phenomenon called *photon avalanche* is shown in Figure 3.3. This is an unconventional

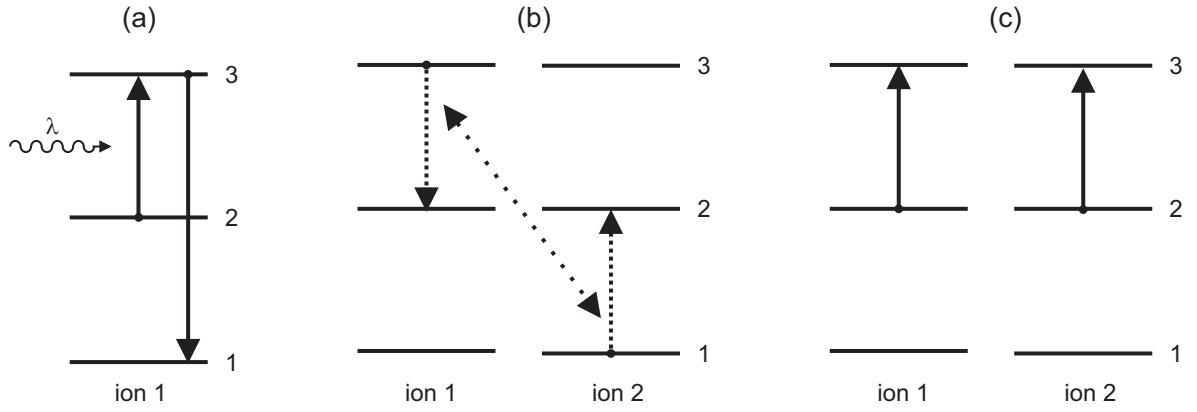

Figure 3.3: Energy scheme for the simplest photon avalanche process [9]

pumping mechanism because it may lead to strong upconverted emissions from level 3 without any resonant GSA. The pump wavelength is only resonant between a metastable state 2 and a higher energy level 3 (see Figure 3.3 (a)). This is the first characteristic of the photon avalanche process.
As all ions are initially in the ground state 1 (no thermal population of level 2), the effect of the pump is at minimum. If an ion is promoted to the metastable state 2, it may be further excited to level 3 by absorption of a pump photon, regardless of the mechanism of population of this state. Then, the cross relaxation excites this ion as well as one of its neighbors to the metastable level 2 (Figure 3.3 (b)). Now two ions are available for further ESA of the pump light (Figure 3.3 (c)). In the following, by the same feeding process, four ions will be in this metastable state. Thus, this process causes doubling of the population of level 2, and the number of ions in this level grows like an avalanche. Another characteristic feature of an avalanche process is an excitation power threshold which clearly separates two different regimes. Below the threshold, the intensity of the upconverted fluorescence is weak and the doped material is transparent to the pump. Above the threshold, the fluorescence increases

by some orders of magnitude and the pump light is strongly absorbed. It is a so-called *self-induced absorption* [9]. In addition, when the pump light is turned on, fluorescence builds up slowly on a time scale that is much longer than any of the lifetimes of the metastable states. Therefore, there is a noticeable delay between the onset of the pump power and the maximum of the fluorescence. It was found that with increasing pump intensity this delay decreases.

In the remaining part of this chapter, it is focused on the upconversion pumping process in praseodymium-doped fluoride glasses since the simulation models which will be developed in chapters 5 and 6, will be applied to simulate the behavior of praseodymium-doped fiber lasers.

3.3.3 Upconversion pumping process in Pr^{3+}-doped glass

In a conventional optically pumped laser, the photon energy of pump light is higher than that of the laser photons, and the absorption of one photon by an active ion is sufficient to excite the upper laser level. Upconversion lasers represent a class of optically pumped lasers that operate at wavelengths shorter than that of the pump laser. But, on the other hand, more than one pump photon is required to provide sufficient energy for the excitation of one laser ion. Using this non-linear excitation process, such lasers can convert infrared pump radiation from semiconductor diode lasers to a visible laser output. The operation of a number of such upconversion lasers has been demonstrated using rare earth ions doped into crystals and glasses. Upconversion lasers can potentially provide practical all-solid state sources with output wavelengths from the ultraviolet to the infrared [10]. As already mentioned, lifetimes for many levels in fluoride glasses are longer than in other glass hosts, and this offers the possibility for realizing upconversion lasers. The longer lifetimes allow for a greater probability for two-photon (or more) absorption, e.g. IR to UV lasers become more feasible.

Praseodymium is a very interesting dopant ion because it offers laser transitions in the blue, green, orange, and red using the same pumping scheme. Emission in the visible occurs with transitions originating from the $^3P_0$, $^3P_1$, and $^1I_6$ levels as shown in Figure 3.4. For simplicity, and because of the quasi perfect energy match between the levels $^3P_1$ and $^1I_6$, these two levels will be collectively referred to as $^3P_1$ level in further discussions, and all of the three levels ($^3P_0$, $^3P_1$, and $^1I_6$) will be addressed as ^3P_J. Owing to the small energy difference of about 600 cm^{-1} between $^3P_0$ and $^3P_1$ [11], these levels are thermally coupled following Boltzmann's distribution law, so that the population of $^3P_1$ is 5 % of the population of $^3P_0$ at room temperature. The lifetime of the ^3P_J manifold of Pr^{3+} in ZBLAN has been reported to be in the range of 39-47 μs dependent on ion concentration [12]. Hence, one can treat it as a metastable level. In contrast to ZBLAN, the level $^3P_0$ is not metastable in silica because of non-radiative emission. However, a weak fluorescence from this level has been observed [13].

In Figure 3.5, an emission spectrum of a ZBLAN glass sample doped with 3 mol% Pr^{3+} is shown together with the transitions responsible for the fluorescent bands. It was measured by Baraniecki [14]. The glass sample was pumped by the 458 nm line from an argon ion laser corresponding to absorption into the $^3P_1$ level. The $^3P_0$ level is also populated due to non-

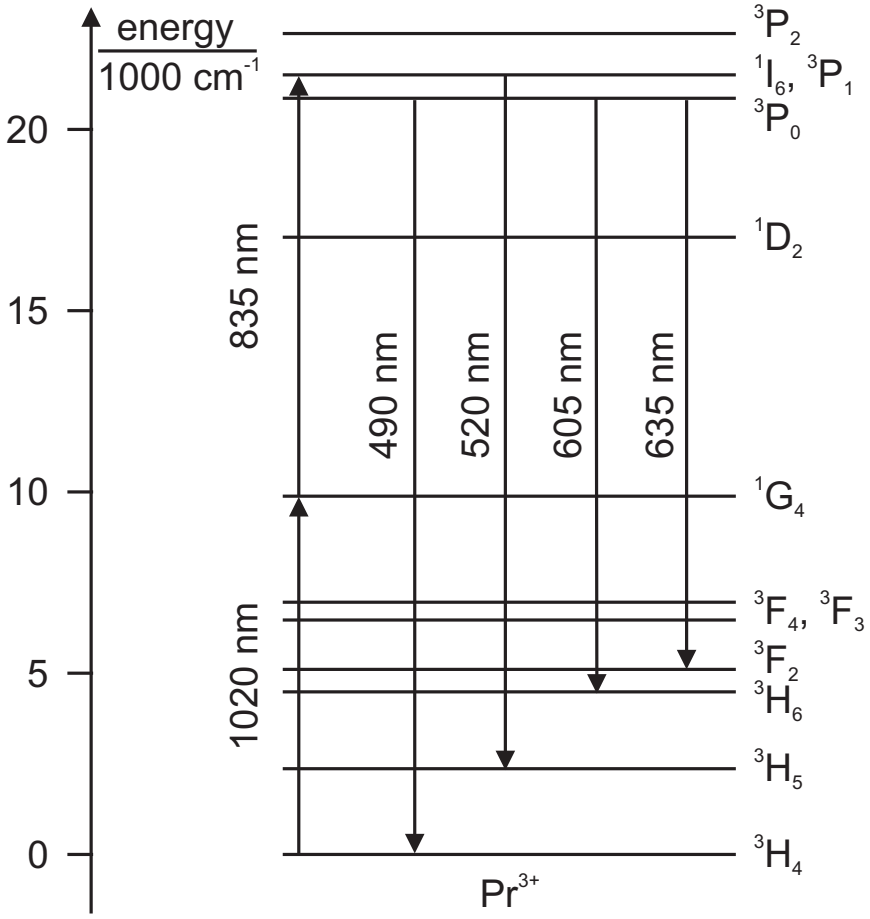

Figure 3.4: Energy level diagram for Pr^{3+}- doped ZBLAN glass with laser transitions

radiative transition from the $^3P_1$ level. The 490, 605, 635 nm transitions all originate from the $^3P_0$ level and terminate in the $^3H_4$, $^3H_6$, and $^3F_2$ levels, respectively (see Figure 3.4). The 520 nm transition originates from the $^3P_1$ level and terminates in the $^3H_5$ state. Despite the fact that at room temperature only about 5 % of the population of the $^3P_1$- and $^3P_0$-coupled manifold resides in the $^3P_1$ level, the $^3P_1 \rightarrow {}^3H_5$ transition dominates the $^3P_0 \rightarrow {}^3H_5$ transition, centered at about 540 nm, because the latter is nominally forbidden and, therefore, much weaker [5, 15]. Each emission from $^3P_0$ is accompanied by the corresponding blue-shifted emission from $^3P_1$. The $^3P_1 \rightarrow {}^3F_2$ emission may be present under the tail of the $^3P_0 \rightarrow {}^3H_6$ band [11]. All these terminal levels lie close together, and therefore, they depopulate rapidly to the ground state by non-radiative relaxations. The radiative branching ratio from $^3P_0$ to $^1D_2$ is very low (a few percent at most), and hardly any of the visible emissions from Pr^{3+}-doped glass originates from $^1D_2$ if an argon ion laser is used for excitation [12].

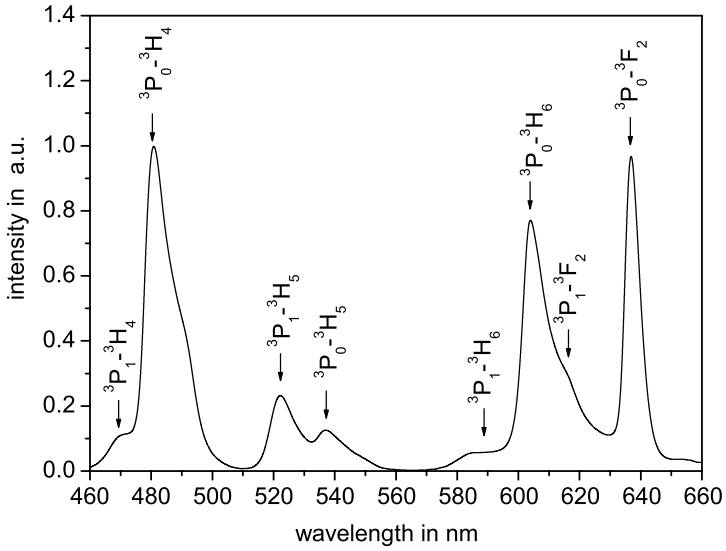

Figure 3.5: Fluorescence spectrum of Pr^{3+} in ZBLAN under excitation at 458 nm [14]

For population of the ^3P_J levels the upconversion processes can also be used. Two-step absorption is an interesting alternative to an argon ion laser pump. It is not possible to pump these high levels by a single infrared pump source, because the energy levels are not suitably placed. An upconversion process is realized through two infrared excitations at different wavelengths, as shown in Figure 3.4. The pump light at 1020 nm excites the ions from the ground state to an intermediate level, $^1G_4$. This is a metastable level with a lifetime of about 100 μs [16]. This time span is long enough for further excitation of these ions to the upper levels $^1I_6$, $^3P_1$ and $^3P_0$, by absorbing photons at about 835 to 845 nm, the latter level by a successive non-radiative relaxation [17, 18]. 96 % of the oscillator strengths in these ESA steps resides in the $^1G_4 \rightarrow {}^1I_6$ transition [15, 19]. Finally, the Pr^{3+} ion decays from levels ^3P_J to other levels of lower energies emitting light at various wavelengths. The great attraction of pumping at infrared wavelengths is that high power laser diodes are available, and so it is possible to construct an efficient and compact laser. The described pumping scheme is again ineffective in silica glass due to the small energy gap between $^1G_4$ and the next closest level $^3F_4$ ($\Delta E \approx 2800$ cm^{-1} [20]) and also due to large phonon energy. The $^1G_4$ level in silica is strongly depopulated by multi-phonon relaxation. On the other hand, the transition $^1G_4 \rightarrow {}^3H_5$ is of particular importance for optical telecommunications. Praseodymium-doped fiber amplifiers working at 1.3 μm utilize this transition [21, 22], and only host glasses with LPE such as fluoride glasses assure proper operation of this amplifier. Therefore, the amplifier based on silica glass shows poor efficiency.

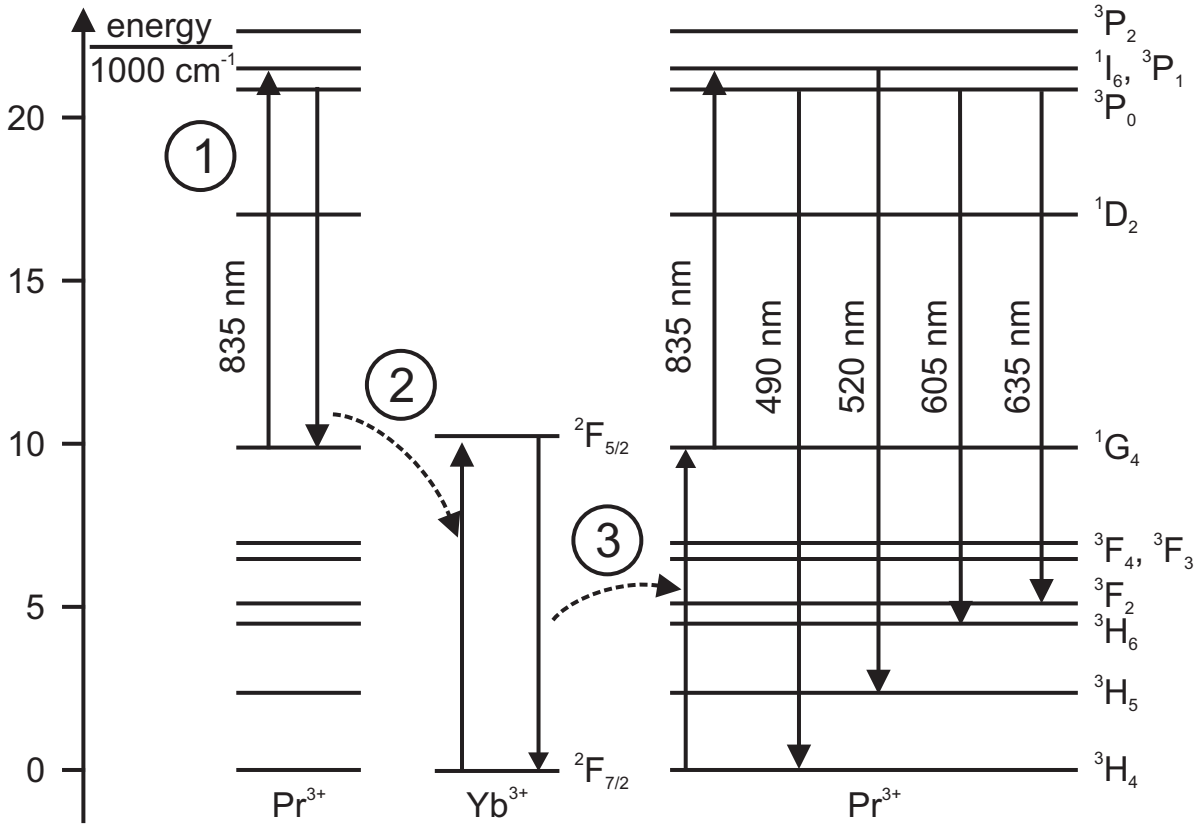

Figure 3.6: Photon avalanche upconversion in Pr^{3+}/Yb^{3+} co-doped ZBLAN glass [23, 24]

It is possible to obtain laser transition from the ^3P_J levels by pumping only at one wavelength, but in this case the glass sample has to be co-doped with a sensitizer ion. Ytterbium is often used as a sensitizer for other rare-earth-doped lasers because of several useful properties. It has a very broad energy level which absorbs strongly in the region covered by high power GaAs laser diodes. The broad absorption band permits a wide pump wavelength range for activating Yb^{3+}. This has a great practical importance, because a sophisticated temperature control of laser diodes to suppress frequency changes is not needed. The Yb^{3+} ion has only one energy level above the ground state (see Figure 3.6). Consequently, it neither suffers from unwanted upconversion due to energy transfer within its own system nor from ESA. The broad excited state overlaps with a range of energy levels in other rare earths where direct diode pumping is not possible. Thus, coupled with the long lifetime of its single excited state (1.7 ms in ZBLAN [25]), Yb^{3+} is a good sensitizer for transferring energy to nearly matched levels in other ions [26]. Isolated Yb^{3+} ions cannot transfer their energy, which is therefore lost. The Yb^{3+} concentration has to be relatively high to ensure a high probability of proximity to a

Pr^{3+} ion. The energy of Yb^{3+} can now migrate (by energy transfer) to a Pr^{3+} ion. Usually, a sufficiently high concentration of Yb^{3+} to obtain an efficient energy transfer is 2 mol% [27]. Several pumping paths are possible to excite the Pr^{3+} ion from the ground state to ^3P_J levels by co-doping it with Yb^{3+} ions. The most efficient and most probable pumping path for upconversion processes in Pr^{3+}/Yb^{3+}-doped ZBLAN fibers is illustrated in Figure 3.6. It is the photon avalanche upconversion which shows three steps. The three steps of the excitation process are marked by numbers. At the beginning a pump photon is absorbed by an excited Pr^{3+} ion (e.g. the excitation can be thermal), and this ion is promoted from an intermediate state $^1G_4$ to the group of levels ^3P_J (step 1). This ESA is followed by a cross relaxation from the Pr^{3+} ion to a nearby Yb^{3+} ion, raising the Yb^{3+} ion into an excited state and leaving Pr^{3+} in the intermediate level (step 2):

$$Pr^{3+} \quad (^3P_J), \quad Yb^{3+} \quad (^2F_{7/2}) \rightarrow Pr^{3+} \quad (^1G_4), \quad Yb^{3+} \quad (^2F_{5/2}).$$

Subsequently, the Yb^{3+} ion can transfer its energy to another Pr^{3+} ion nearby, the Yb^{3+} relaxes to its ground state exciting a Pr^{3+} ion from its ground state to the intermediate level (step 3):

$$Yb^{3+} \quad (^2F_{5/2}), \quad Pr^{3+} \quad (^3H_4) \rightarrow Yb^{3+} \quad (^2F_{7/2}), \quad Pr^{3+} \quad (^1G_4).$$

This excitation closes the pumping cycle in the Pr^{3+}/Yb^{3+} system. After each cycle, the number of ions excited to the $^1G_4$ state of Pr^{3+} doubles. Therefore, this pumping scheme is called an avalanche process [28, 29].
Because the typical dopant concentrations of Pr^{3+} and Yb^{3+} ions used in visible laser applications are about 0.3 mol% and 2 mol%, respectively, it is unlikely that any given Yb^{3+} ion will be located near two Pr^{3+} ions, assuming the doping to be spatially uniform. Generally, the energy from an excited Yb^{3+} ion may migrate through one or more nearby Yb^{3+} ions until an Yb^{3+} ion that lies near a Pr^{3+} ion is excited, at which point an Yb^{3+}-Pr^{3+} interaction can take place [5].
Although the photon avalanche upconversion process seems to be a very complicated one and thus less probable, there are many indications that, in reality, this is the dominant process in a Pr^{3+}/Yb^{3+}-doped glass among the alternative processes presented in literature. An important argument is the existence of a critical pump power. After reaching a threshold pump power, a considerably intense fluorescence is observed, and this is a typical feature of an avalanche process. Additionally, a self-induced absorption has also been observed [30]. Simulations, which have been carried out, have confirmed a dominant role of the photon avalanche upconversion in the pumping process of such fiber lasers based on ZBLAN.

4 Parameters of rare-earth-doped fibers and glasses

Some properties of thulium-doped fluoride fibers used for fiber amplifier applications and of praseodymium-doped fluoride glasses for fiber laser applications are thoroughly discussed in this chapter. The active thulium fiber is spatially characterized by a reflectometric method called *optical frequency-domain reflectometry (OFDR)*. In a following section a *frequency transfer function (FTF) method* is presented and used to measure the fluorescent lifetimes of praseodymium-doped fluoride glasses, some of them co-doped with ytterbium. In the last section some important spectroscopic parameters of praseodymium in ZBLAN glass are presented. These parameters will be used for fiber laser simulation in chapters 5 and 6.

4.1 C-OFDR for investigation of TDFAs

This section deals with coherent optical frequency-domain reflectometry (C-OFDR) for characterization of 1050 nm laser diode pumped S-band thulium-doped fluoride fiber amplifiers (TDFAs).
For this purpose, a fiberoptic measurement setup based on silica has been realized. Spatially resolved determination of the fiber gain of thulium-doped ZBLAN fibers has been the main focus of this work. With this property it is possible to judge about the optimum length of the active fiber in amplifier applications.
First, the energy level diagram of thulium in ZBLAN glass is presented. Then the TDFA operation principle and the TDFA setup are briefly discussed. Further, some reflectometric measurement procedures are introduced with an emphasis on C-OFDR. Moreover, applications of C-OFDR are briefly discussed. The impact of phase noise and Rayleigh backscattering (RBS) is investigated analytically and compared to measurement results. A rule of thumb for detecting RBS levels for TDFA investigations in the presence of phase noise is derived. The analytical derivation for these limitations of measurement sensitivity are rather lengthy, so that the detailed derivation has been shifted to appendix A. Furthermore, measurement results concerning TDFA characterization with 2000 ppm and 5000 ppm thulium-doped ZBLAN fibers by C-OFDR are presented. Finally, the results are briefly summarized.

4.1.1 TDFA operation principle

Fiber amplifiers play a key role in optical communications due to their ability to amplify signals without conversion of optical to electrical signals. The success of erbium-doped fiber amplifiers (EDFAs) and the ever-increasing demand for bandwidth in wavelength division multiplexed (WDM) optical telecommunication systems are leading the research toward extending the transmission bands from the conventional C-band (from 1530 to 1560 nm) to other wavelength ranges. One of the most promising candidates is the thulium-doped fiber

amplifier (TDFA) based on fluoride fiber operating in the S-band (from 1450 - 1530 nm). This type of optical amplifier is more difficult to optimize compared to EDFAs which work as 3-level amplifiers. The complexity of the TDFA is caused by the number of energy levels which are involved in the amplification process. TDFAs pumped at 1050 nm work as four-level amplifiers, and besides the ground state absorption (GSA) and emission cross-sections, there are also some excited state absorption (ESA) transitions, which are important for the operation [31].
The basic TDFA operation principle and its setup will be presented in the following:
The properties of fiber amplifiers depend, on one hand, on the dopant ion and, on the other hand, on the interaction of the dopant with the host material. In case of TDFAs, thulium ions are used as dopant of the active fiber. Figure 4.1 shows the part of the energy level diagram of thulium ions in ZBLAN which is relevant for amplifier operation. In addition, typical low concentration fluorescent lifetimes of relevant energy levels are indicated. The arrows represent the allowed transitions with the equivalent wavelengths which are emitted (arrows in downward direction) or absorbed (arrows in upward direction). By absorbing pump power thulium ions are excited to higher energy levels until population inversion (see section 1.2) necessary for signal amplification is reached. It is important to note that most ions have to be excited to the $^3H_4$ state due to the reason that the $^3H_4 \rightarrow {}^3F_4$ transition is responsible for signal amplification with a center wavelength of 1470 nm.
The LPE fluorozirconate glass ZBLAN shows a significant advantage compared to silica: Non-radiative phonon transitions between neighboring energy levels become less probable and thus the fluorescent lifetimes of excited states increase. Hence, it becomes more efficient to pump from excited states to higher energy levels. Since the phonon energy of glass depends on the atomic binding (see section 3.2), the mechanical and thermal stability decreases with decreasing phonon energy. Thus, it is more difficult to handle fluoride fibers and therefore TDFAs than to handle EDFAs which are based on silica. TDFAs based on silica have also been realized [32] but, as expected, they are less efficient than TDFAs based on fluoride fiber hosts.
A simple TDFA setup with one pump laser diode is illustrated in Figure 4.2. To achieve a high power density in the fiber core, a ZBLAN fiber with a high numerical aperture (NA) is used. Due to different mode field diameters in fluoride and silica fibers, it would come to high losses when directly connected to each other. To minimize these losses, a high NA (HNA) silica fiber is used which is connected by means of a glue splice [33] to the fluoride fiber. The other end of the HNA fiber is connected to silica fiber by means of a thermally-diffused expanded core (TEC) splice. A low-loss connection between two different silica fibers with different NA is easily achieved by means of the TEC technique which is usually applied to silica fibers whose core is doped with germanium. Due to the high temperatures when splicing, germanium starts to diffuse from the core to the cladding and thus changes the refractive index of the cladding. Hence, the core is expanded and the losses are minimized due to mode field matching of both fibers [33].
In contrast to EDFAs which are simple three-level systems, TDFAs cannot be uniquely clas-

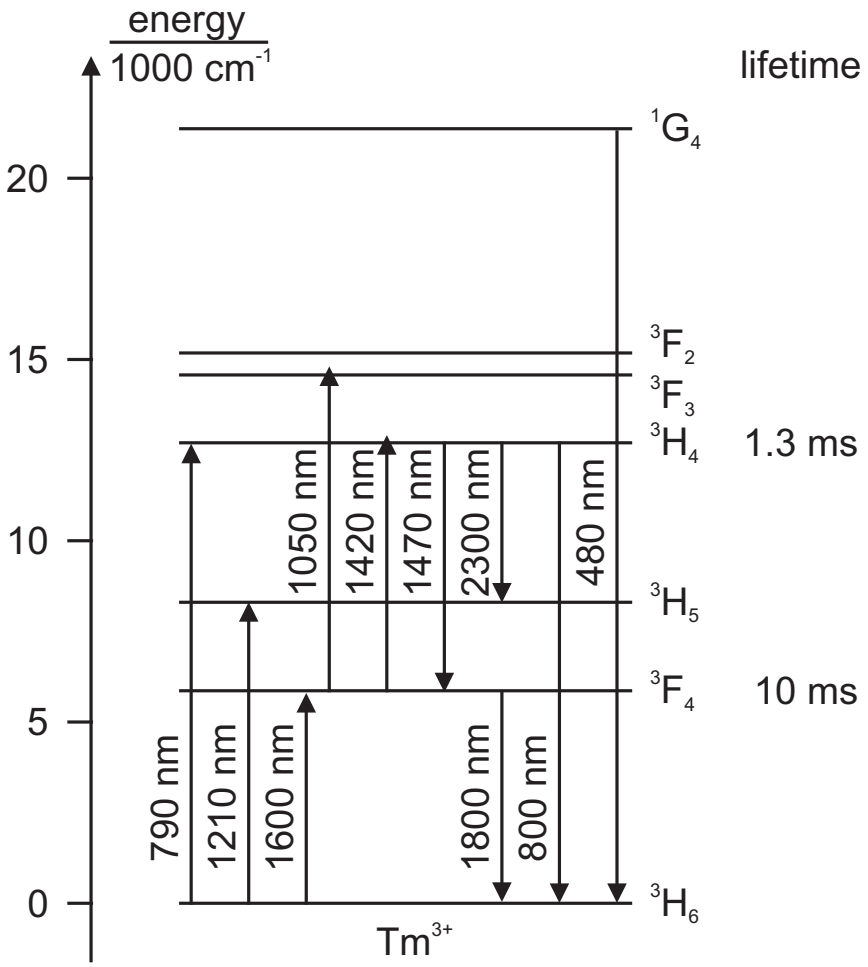

Figure 4.1: Energy level diagram of Tm^{3+}:ZBLAN. The low concentration lifetime of the $^3F_4$ and $^3H_4$ levels is also indicated.

sified. To achieve the highest possible gain different pump configurations with one or two pump laser diodes have been investigated according to literature. For a pump wavelength of 790 nm the TDFA behavior corresponds to a four-level system which is transparent for the signal wavelength when the pump is switched off. Only with the addition of an additional pump wavelength population inversion can be achieved when pumping with 790 nm since the fluorescent lifetime of the $^3F_4$ level is very high (10 ms) leading to ground state depletion. Therefore, another pump has to be available for the absorption of the excited $^3F_4$ state to reach the $^3H_4$ state. If only directly pumped from the ground state to the amplifying $^3H_4$ state with 790 nm, the fiber would absorb the signal and thus lead to an additional attenuation [34].

1420 or 1050 nm can be chosen as an additional pump where 1050 nm should be preferred

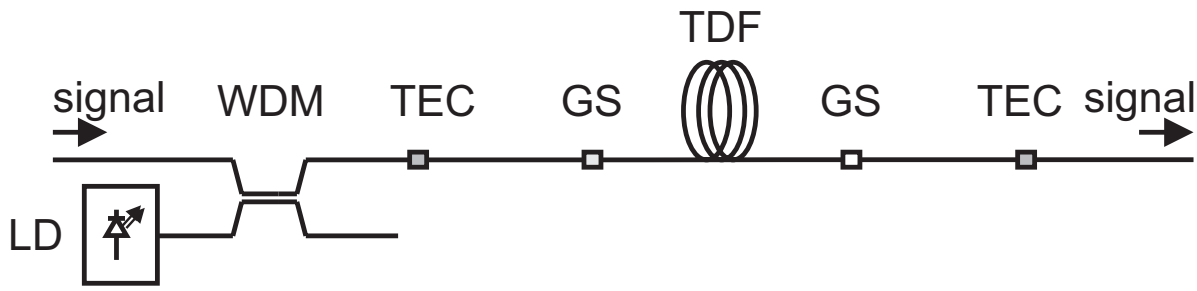

Figure 4.2: Simple TDFA setup with one pump laser diode (LD). The other abbreviations are: TDF: thulium-doped fiber, WDM: WDM coupler, TEC: TEC splice, and GS: glue splice.

due to the larger absorption cross section at this wavelength which requires a shorter fiber length with lower total pump power to achieve the same gain [35]. As an alternative, thulium can exclusively be pumped by 1050 nm. In this case, the ions are excited to the $^3H_5$ level and then relax by a non-radiative transition to the $^3F_4$ state. After absorption of another pump photon the ions are directed again by non-radiative relaxation to the desired $^3H_4$ state. Unfortunately, the GSA at this wavelength is not resonant and thus high pump power is necessary to achieve reasonable gain.
An improvement is achieved with TDFAs doped with a high thulium concentration due to cross relaxation processes (see section 3.3). Assuming a populated energy level $^3F_4$, e.g. by a simple thermal excitation, then a photon may be absorbed with a pump wavelength of 1050 nm and the ion reaches the state $^3F_{2,3}$. After non-radiative relaxation it reaches the $^3H_4$ state which is responsible for amplification. If now the thulium ion relaxes back to the $^3F_4$ state, then the radiated energy will be adopted from the ground state due to the smaller geometrical distance to another thulium ion and thus this ion reaches the $^3F_4$ state as well. Hence, the energy transfer leads to the excitation of ions to the first excited state and therefore to a more efficient pump at 1050 nm which is due to the fact that ESA of the first excited state is larger than GSA [36].

4.1.2 Reflectometric measurement procedures

Fiber cables can have a length of several hundreds of kilometers and there exists the necessity to detect impurities or defects, such as fiber breaks, by means of special measurement procedures [37].

In *optical time-domain reflectometry (OTDR)* short pulses (in the range of 10 ns to 10 μs) of a light source are coupled into the device under test (DUT) and the reflected light is detected over time. In addition to measurements of the reflected pulses, from which size and deflection determine strength and location of the reflection, one can also detect the backscattered light and therefore calculate fiber attenuation.

With this incoherent method, very long fiber distances can be examined with a spatial resolution of about 1 m given by the pulse width.

The increasing use of fiber and integrated optical components in the sector of optical communication technology causes the necessity to examine these components by means of reflectometric methods with a high spatial resolution in the micrometer range [38]. This serves for localizing unwanted reflections but also makes the characterization of fiber-optic grating structures possible [39, 40]. These grating structures are used e.g. as narrow band filters, add/drop multiplexers and sensors. The knowledge of these structure properties improves the fabrication process dramatically [41].

The OTDR can be improved with regard to spatial resolution and sensitivity by means of a local oscillator (LO) which converts the reflected light down (*heterodyne OTDR*), but to achieve a resolution in the micrometer range one needs a very complex measurement setup [42].
Alternatively, measurement procedures exist which offer high sensitivities and high spatial resolution by means of a relatively simple setup: *optical coherence-domain reflectometry (OCDR)* also known as *optical low coherence reflectometry (OLCR)* and OFDR [43, 44]. All these methods are based on interferometers in contrast to the OTDR principle.

OCDR/OLCR, also called *white light interferometer*, uses a broad band source in cw operation. The reflected light from the DUT is superimposed with light from the reference arm that consists of a movable mirror. The movement of the mirror results in configurations for which the separation distance of source and reference mirror is equal to the separation distance of source and reflection location in the DUT. For such a mirror position x, one can determine reflection strength from the size of the interference signal.
The high source bandwidth is equivalent to a small coherence length which means that light interferes for mirror positions near the position x, but the interference signal becomes weaker with increasing distance to this position. So spatial resolution is dependent on the source bandwidth while measurement range is determined by the maximum possible deflection of the mirror. Moreover, high demands with regard to mirror movement exist.
OLCR was applied for RBS level measurements by Sorin in 1992 [45] and by Takada in 1997 to determine the gain of erbium-doped waveguides [46].

C-OFDR was for the first time introduced by Eickhoff and Ulrich in 1981 [47]. In OFDR there is no need for movable parts, except for the tunable laser source with its external cavity. Here, the optical frequency of the light source is tuned and the reflected light from the DUT is superimposed with light from the LO arm which now consists of a fixed mirror.
OFDR needs a narrow band source since the coherence length determines the measurement range whereas spatial resolution is dependent on the swept frequency range. The demand for a narrow band source which should be linearly tunable in time over a broad frequency range has limited the practical use of OFDR, when it was first developed, but due to the availability

of suitable sources nowadays, it has become a powerful measurement procedure.

4.1.3 Applications of OFDR

OFDR can be used for fiber Bragg grating (FBG) dispersion measurements and active control during FBG fabrication [39]. The complex reflectivity of FBGs can be measured by OFDR. By applying an inverse scattering algorithm, the complex coupling coefficient $\kappa(z)$ of FBGs is reconstructed [40]. The knowledge of the coupling coefficient is important in analyzing FBG writing techniques [41].
In principle, reflectometric measurements yield desired information about the spatial structure of optical waveguides, whereas transmission measurements do not contain this information. In reflectometry applications, inner coupling and perturbation locations of planar waveguide components (e.g. weak reflecting coupling locations between fibers and planar waveguides) are localized and quantified by means of OFDR.
Determination of polarization mode dispersion (PMD) and chromatic dispersion (CD) properties of optical devices by means of OFDR is shown in [48].
Recently, tunable fiber lasers have been realized as a laser source for coherent OFDR [49, 50]. They show a coherence length of 210 km in air and it is possible to achieve a measurement range of 95 km [50] which is the highest reported value so far. Furthermore, OFDR based on a mode-locked fiber laser has also been reported in literature [51]. The exotic setup realized with this pulsed source shows a measurement range of only a few centimeters and a dynamic range of about 50 dB.
Another possible application of OFDR is the so-called optical frequency-domain imaging (OFDI) which is used in coherence tomography [52]. It is an interferometric imaging method very similar to the OFDR technique.
Moreover, OFDR is used to characterize fiber amplifiers such as EDFAs and TDFAs. For TDFA design, knowledge of the gain distribution within the active fiber is of great value. For the first time, the distributed gain along highly thulium-doped fibers has been measured with high-resolution reflectometry [53]. The C-OFDR is a non-destructive and non-invasive method well matched to this task due to its dynamic range, spatial resolution and measurement range. Using thulium-doped fibers with different Tm^{3+}-dopant concentrations, precise measurements of RBS levels are shown for obtaining the optimum gain-length ratio for S-band TDFA pumped by 1050 nm laser diodes.
In addition, it is shown that experimental results concerning RBS and phase noise floor levels inherent to C-OFDR are in accordance with analytical results.

4.1.4 OFDR measurement principle and setup

The C-OFDR measurement principle which will be described in this section is only applicable for coherent light sources and for spatially coherent interferometers. The device under test (DUT) is considered to be non-dispersive. The goal of an OFDR measurement is to deter-

mine the respective position and reflectivity of the DUT with high spatial resolution and high sensitivity.

C-OFDR achieves a spatial resolution in the micrometer range by using the given spectral properties of the light source properly. This measurement method needs a relatively uncomplicated setup. The OFDR setup used is illustrated in Figure 4.3 with a single-wavelength pumped TDFA as DUT. The Rayleigh backscattering (RBS) levels of the TDFA should be detected in order to make a suitable statement about the optimum active fiber length.

A diode laser in cw operation is used as light source whose optical frequency ν is tuned almost

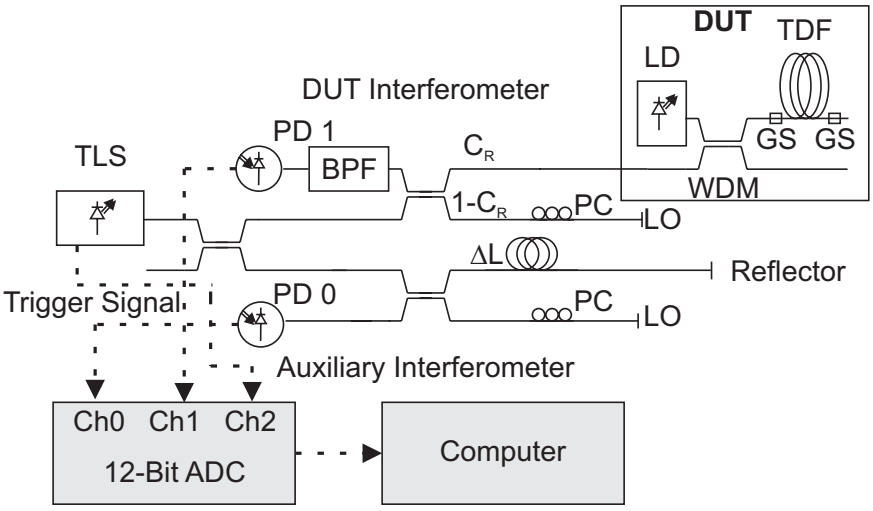

Figure 4.3: Experimental C-OFDR setup for S-band TDFA characterization. The abbreviations are: TLS: tunable laser source, LD: pump laser diode, PD: InGaAs photodiode, LO: reflector acting as local oscillator, TDF: thulium-doped fiber, WDM: WDM coupler, BPF: bandpass filter, ADC: analog-digital-converter card, PC: polarization controller, and GS: glue splice.

linearly in time, but in fact the laser sweep is nonlinear. This tunable laser source (TLS) is narrow band in optical frequency and hence has a high coherence length (GN Nettest Tunics Reference ES). The setup contains two all-fiber Michelson interferometers (a DUT and an auxiliary interferometer). The DUT is placed in one arm of the Michelson interferometer (DUT interferometer). This DUT interferometer serves for the measurement of the complex reflection spectrum of a given measurement object (DUT). The auxiliary interferometer [54, 55] is used to compensate for nonlinearities of the laser sweep. It serves for determining the time-domain behavior of the optical instantaneous frequency $\nu(t)$ of the TLS and has a fixed arm-difference length of ΔL. Hence, the nonlinear laser sweep is corrected in order to get a spatial resolution in the micrometer range. The limitation of sweep reproducibility of the TLS and its effects on OFDR analysis are described in detail in [48].

With this setup polarization resolved measurements can be performed. This is reasonable since

the C-OFDR principle extremely depends on polarization of light. A polarization controller is used in the LO arms of both Michelson interferometers in order to match the polarization state of the DUT arm and to guarantee constructive interference [56, 57].
The OFDR detection principle corresponds to the heterodyne detection: The frequency-tuned light is coupled into the DUT with an arbitrary state of polarization (SOP) and the back-scattered light from the DUT is superimposed with light from the LO reflector which is a well-known reflector such as a gold tipped fiber end face with a reflectivity of almost 100 % in the S-band or a Fresnel reflector (straight fiber end or FC/PC connector) with a reflectivity of 4 % (glass-air interface). In the setup used a Fresnel reflector in each interferometer acts as LO.
In order to automatize the measurement one can use the polarization diversity receiver (PDR) concept [6]. The signal of the DUT interferometer is split into two orthogonal SOPs by means of a polarization beam splitter (PBS) and two detectors in the DUT interferometer. However, since only two detectors had been available, one for each interferometer, manual polarization controllers (OZ Optics FPC-100) have been used.
By tuning the optical frequency of the TLS [1] linearly in time, difference frequencies, so called *beat frequencies*, arise in the interference signal at the detector due to interference between light form the DUT and LO arm of the Michelson interferometer. The beat frequencies are determined by the time delay differences of the light waves from the DUT and LO arm of the interferometer and also by the frequency sweep rate γ of the TLS. Dependent on the sweep rate and on the arm-difference length ΔL of the interferometer, beat frequencies on the order of several hundred kHz can arise in the setup used. Their behavior can be well detected through the measurement bandwidth of the low noise InGaAs detectors (New Focus 2011).
Sampling both detector signals (an analog digital converter, ADC, with a maximum of 10 MSamples/s is used in the setup, NI PCI 6115) and performing an FFT (fast Fourier transform) of the sampled detector signal, this yields the amplitude spectrum. Each single peak, the so called *signature*, at given beat frequencies, corresponds to one reflection location in the DUT.
The amplitude of the regarded beat frequency is proportional to the amplitude reflection factor of the reflection location in the DUT. Data acquisition and evaluation is done by means of a personal computer. The TLS trigger signal sent to the ADC guarantees synchronized data acquisition.
All couplers used are self-made 3 dB couplers except the DUT coupler (see Figure 4.3, where C_R denotes the coupled part of light into the DUT arm) which shows a 80:20 coupling ratio. In a Michelson interferometer a 3 dB coupler is normally most adequate but due to technological problems the production of such fused fiber couplers led to higher insertion losses than couplers with different coupling ratios. Pump and signal lasers are coupled together by a self-made WDM coupler which couples 99 % of the signal wavelength (1471 nm) and 90 % of the pump wavelength (1050 nm) to the active fiber.

[1] In fact, the optical *wavelength* of the TLS is tuned almost linearly in time.

The bandpass filter (BPF) with a bandwidth of 12 nm around 1471 nm (AFOP SpectraMux) has only been used when measuring RBS levels. The BPF is used to avoid detector saturation and to filter out a major part of the amplified spontaneous emission (ASE) light, thus decreasing background noise [34]. It is important to note that only under certain circumstances the Rayleigh backscattering dominates the phase noise inherent to the C-OFDR technique [58] (see section 4.1.5). Thus, the measurement parameters must be carefully chosen.

Now, let us focus on two important properties of OFDR: spatial resolution and measurement range.

Spatial resolution

There are two definitions for spatial resolution: the *one-point* and the *two-point* spatial resolution. One-point spatial resolution is the accuracy for which the location of a discrete reflector can be obtained while two-point spatial resolution denotes the minimum distance of two reflection locations which can be distinguished from each other in the evaluated signal (given by the full width at half maximum, FWHM, of the respective signatures).
The two-point spatial resolution is inversely proportional to the width of the signatures, i.e. inversely proportional to the swept frequency range $\Delta\nu = \nu_{max} - \nu_{min}$ of the TLS [6].
The one-point spatial resolution principally depends on data acquisition and evaluation algorithm. Data acquisition of the measurement data by means of an ADC leads to discrete digital signals which can be used for further signal processing. The ADC converts analog signals of the photodiode into digital signals. Inverse FFT (IFFT) is performed on the measurement data. More precisely, discrete FFT (DFFT) is performed which means that resulting data points are located at equidistant sampling points of the Fourier transform.
It is noted that when regarding a global maximum of the discrete sinc $(\sin(\pi x)/\pi x)$ signature, which arises due to the finite swept frequency range instead of a Dirac signature that would arise in case of an unlimited swept frequency range, this can possibly lead to an absolute difference between real and evaluated reflection location since the sampling points may lie at a slightly different position. A remedy is to increase the number of data points for the FFT. Hence, the distance Δz between adjacent points of the Fourier transform will decrease and therefore the sinc signatures in the OFDR spectrum will be finer resolved.

The two-point spatial resolution for OFDR measurements is derived in appendix A, equation (A.14). It depends on the swept wavelength range $\Delta\lambda$ of the TLS:

$$\Delta z \approx 0.88 \frac{\lambda_0^2}{2 \cdot n_g \cdot \Delta\lambda}, \tag{4.1}$$

where λ_0 is the center wavelength and n_g the group index of the medium ($n_g = 1.467$ for SiO_2 fibers at 1550 nm). Two adjacent reflection locations can be separated from each other, if the maxima of both sinc signatures can be clearly identified.

Measurement range

The measurement range is the maximum distance for which reflection locations can be recognized in the OFDR spectrum. Since OFDR is based on coherent superposition of two light waves, OFDR analysis is only possible when the path difference between LO arm and the reflection location in the DUT arm is smaller than approximately half the coherence length of the light source.
The coherence length L_c of a laser source in the fiber is given by:

$$L_c = \frac{c_0}{n_g \cdot \pi \cdot \Delta\nu_{source}}, \tag{4.2}$$

where $\Delta\nu_{source}$ is the laser linewidth.
The coherence time τ_c is therefore given by

$$\tau_c = \frac{L_c}{c} = \frac{L_c \cdot n_g}{c_0} = \frac{1}{\pi \cdot \Delta\nu_{source}}, \tag{4.3}$$

where n_g is the group index of the medium used (here silica), c and c_0 are the speed of light in medium and vacuum, respectively.
The TLS used shows a linewidth of $\Delta\nu_{source} = 150$ kHz. With a group index $n_g = 1.467$ for silica (SiO_2) and $c_0 = 3 \cdot 10^8$ m/s one receives from formulae (4.2) and (4.3) a coherence length L_c of about 434 m and a coherence time τ_c of about 2.12 μs, respectively.
The maximum distance to the reflection location z_{max} is determined by the maximum beat frequency f_{max} of the detector signal and is given by

$$z_{max} = \frac{c_0 \cdot f_{max}}{2 \cdot \gamma \cdot n_g}. \tag{4.4}$$

With $\gamma \approx \sigma \cdot \frac{c_0}{\lambda_0^2}$, where γ denotes the frequency sweep rate of the TLS $\gamma = \mathrm{d}\nu/\mathrm{d}t$ and $\sigma = \mathrm{d}\lambda/\mathrm{d}t$ the wavelength sweep rate, one obtains:

$$z_{max} = \frac{\lambda_0^2 \cdot f_{max}}{2 \cdot \sigma \cdot n_g}. \tag{4.5}$$

Shannon's sampling theorem states that a signal can be discretized uniquely, when the sampling frequency f_s is at least two times larger than the maximum appearing frequency component f_{max} of the signal (Nyquist frequency $f_N = f_{max}$). The maximum sampling frequency $f_{s,max}$ is determined by the ADC to 10 MHz while f_{max} is determined by the path difference of the LO and the furthest reflection location in the DUT including possible multipath reflections and, of course, by the detector bandwidth.
If reflection locations exist in larger distances with corresponding beat frequencies f_m covered

by the detector bandwidth, one has to suppress these frequency components by means of a low pass filter in the detector electronics in order to prevent *aliasing*.
Typical measurement times for discrete reflectors are on the order of one second and for RBS level measurements the measurement time even decreases to hundreds of milliseconds since the swept wavelength range is only a few nanometers. It should be emphasized that for a highly coherent light source, the sampling rate limits the measurement range. An increased sampling rate increases the measurement range and does *not* improve spatial resolution.

The mathematical basics for C-OFDR are in detail presented in [43, 48, 59] and thus it is resigned to give a description here. It should be emphasized that a moderate signal processing scheme is needed especially in case of detecting RBS levels for amplifier characterization. This is very important because, first, one wants to obtain a reduced data set which can be comfortably used in further evaluation steps and, second, the influence of noise has to be minimized. This is not the scope of this thesis and thus the interested reader is referred to [48] and to [60].
Moreover, formation causes of artifacts (artificial signatures) appearing in the OFDR spectrum are described in detail in [48]. These artifacts make a distinction between real and artificial signatures more difficult and may corrupt signal information. However, the artifacts which appeared in the TDFA measurements can be explained easily. This will be done when the OFDR spectra of the RBS levels is presented (see section 4.1.6).
More details about the C-OFDR technique can be found in [54–56] and references therein.

4.1.5 Analysis of different noise sources

In this section, the limitation of measurement sensitivity due to phase noise and Rayleigh backscattering (RBS) is analytically described. In case of phase noise the analytical results are also compared to experimental results when strong reflectors such as self-made gold tipped fiber end faces are measured. The experimental results concerning RBS are shown in section 4.1.6. Phase noise has been observed to be the dominant noise source in the OFDR setup used when measuring discrete or distributed reflectors. One is interested in detecting RBS levels to be able to determine the optimum fiber length of TDFAs. Thus, a rule of thumb for which RBS can be detected in the presence of phase noise will be derived. Since all these mathematical derivations are lengthy, the end results are only presented and the interested reader is referred to appendix A for a detailed derivation.
In the following, formulae for the minimum detectable reflection strength due to phase noise and RBS will be indicated: Reflections which are stronger than those calculated levels can be recognized in the OFDR spectrum. It is worth noting that due to attenuation and backscattering losses in the DUT arm of the DUT interferometer, one will observe weaker signals. Therefore, the real reflection factor must be several dB stronger than the indicated minimum reflection strength $R_{\min}$, in order to recognize a reflection in presence of noise. It is not the

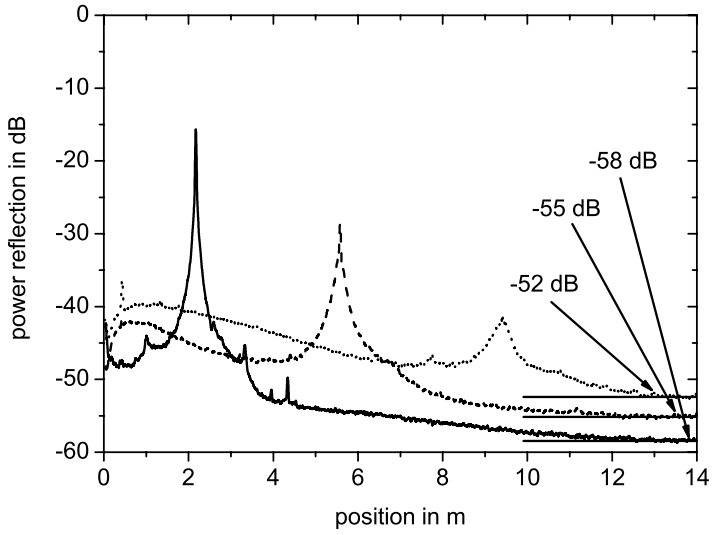

Figure 4.4: Reflected power of a gold tipped fiber end face for different arm-difference lengths versus position along fiber length. Solid, dashed, and dotted lines represent 2.2 m, 5.6 m and 9.4 m arm-difference length, respectively.

aim to present an exact agreement between experimental and analytical results. This is rather impossible since the different noise sources that show an impact on dynamic range are hardly separable from one another. Furthermore, the calculations present a simplified approach, for instance the couplers, splices and connectors are assumed to be lossless. However, the comparison of experimental to analytical results aims on bringing these results in accordance with each other.

Dependent on the reflection strength and arm-difference length, dynamic range varies between 50 dB and about 80 dB for discrete reflections where phase noise limits sensitivity. Experimental results concerning the reflected power of a self-made gold tipped fiber end face versus position along fiber length are shown in Figure 4.4. The measurements have been performed with different arm-difference lengths of the DUT interferometer (the bandpass filter, BPF, has been left out in the setup used). In analogy to the calculations in [58], applied to the setup used, the minimum detectable reflection strength due to phase noise can be calculated by

$$R_{\min}^{\Phi} \approx \frac{8}{C_R \cdot (1 - C_R)} \cdot \frac{R_0}{R_{LO}} \cdot \frac{\tau_0^2}{\tau_c} \cdot \Delta f, \tag{4.6}$$

where C_R, R_0/R_{LO}, τ_0 and τ_c denote the coupled part of light into the DUT arm (here 80 %), the ratio of the power reflectivities of the DUT and LO arms (here 25), the time delay to the reflection location (given by the position of the reflection in the DUT arm of the DUT interfe-

rometer) and the coherence time of the laser source (here 2.12 μs), respectively. Δf indicates the frequency resolution given by the inverse measurement time. In these measurements Δf amounts to about 0.8 Hz corresponding to an effective measurement time of 1.25 seconds. Regarding the measurements, the minimum detectable phase noise level can be calculated to be -67 dB, -59 dB and -54 dB for 2.2 m, 5.6 m and 9.4 m arm-difference length, respectively. These calculated values are in accordance with the experiments (see indicated values in Fig. 4.4). All measurements shown in Figure 4.4 have been calibrated with the reflection of the first gold tipped fiber end face at 2.2 m. Thus, the first signature at 2.2 m should show a maximum value of 0 dB which is obviously not the case. This is due to data reduction which had been performed and as already explained in section 4.1.4 the impact of data reduction on OFDR analysis is not the scope of this thesis and thus the interested reader is referred to [48] and to [60]. Nevertheless, it has been taken care that absolute values are obtained, i.e. the values for measurement sensitivity and dynamic range are not corrupted by data reduction.
Furthermore, it has to be noted that the reflected power values shown in Fig. 4.4 indicate the noise floor level at the end of the measurement range. It is worth noting that disturbances from other noise sources and especially from the detector unit are at minimum at the end of the measurement range. Moreover, it must be emphasized that the measurement range is not limited by the DUT (here the gold tipped fiber end face) as this quantity is independent of the DUT (see section 4.1.4). The noise floor levels can be compared at the position of the strongest reflection to obtain an exact value for the phase noise (see also appendix A). However, separation of the impacts of phase noise and other noise sources, which predominantly occur at the beginning of the measurement range, on dynamic range is hardly possible. For the reason explained above and due to the fact that the measurement range is longer than needed, it has thus been chosen to compare the noise floor levels at the end of the measurement range. This is not only easily practicable but also reasonable since formula (4.6) neglects the actual sinc^2 behavior of phase noise (see equation (A.19) which shows that R^{Φ}_{min} is a function of frequency). The noise floor level due to phase noise depends on the reflector strength and on the reflector location. However, for the measurements presented the value of the noise floor at the end of the measurement range hardly changes and thus the more simplified expression in equation (4.6) is used. A strong reflection increases noise floor not only in close proximity to the reflection but also in the whole measurement range. So dynamic range and measurement sensitivity, respectively, in case of phase noise are fully given by the strongest reflection in the measurement range. The noise floor level is given by formula (4.6) which also indicates that with a decreasing reflection strength R_0 of the DUT the dynamic range would increase and thus improve sensitivity.
For $C_{\mathrm{R}} = 0.5$ (3 dB coupler) the term $C_R \cdot (1 - C_R)$ shows a maximum and thus equation (4.6) indicates a decrease of the noise floor. However, couplers with different coupling ratios have been tried (see also section 4.1.4) and the best performance for the detection of RBS levels has been achieved with a coupler which showed a coupling ratio of 80:20 which corresponds to $C_{\mathrm{R}} = 0.8$.
Rayleigh backscattering (RBS) is a decisive parameter for the characterization of fiber am-

fiber	dopant concentration in ppm	NA	α_s in $\frac{1}{m}$	$\frac{\omega_0}{a}$ @ 1471 nm	V @ 1471 nm	S in 10^{-3}
A	2000	0.26	0.076	1.006	2.776	5.79
B	5000	0.25	0.083	1.006	2.776	5.36

Table 4.1: Parameters of the investigated active fibers of the TDFAs

plifiers. It is due to scattering of light on inhomogeneities of the fiber (differential refractive index differences). Thus, a small portion of the signal power is reflected continuously and in opposite direction to the propagation direction. To determine the fiber gain of the active fiber, this backscattered power must be larger than any other noise contribution.
The average RBS reflectivity is given by [58]:

$$R_{RBS} = S \cdot \alpha_S \cdot \Delta z, \tag{4.7}$$

where S, α_S and Δz denote capture fraction, loss constant and spatial resolution, respectively. In case of fiber B (see table 4.1), S can be calculated [61] to be $5.36 \cdot 10^{-3}$ which leads to an average RBS level of -71 dB. Appendix A shows that equation (4.7) is equivalent to the minimum detectable reflection strength due to RBS in the Michelson setup used (cp. equation (A.29)).

The parameters of the investigated active fibers of the TDFAs are shown in table 4.1. Both fiber types are home-made fibers with 2000 ppm and 5000 ppm thulium concentration. The fiber core refractive index amounts to $n_1 = 1.497$ [33].
The fibers of type A are 8.2 m and 5 m long with 2000 ppm Tm^{3+} concentration, a numerical aperture (NA) of 0.26, core diameter 2.5 μm, 125 μm cladding diameter, and a background loss of 0.33 dB/m at 1.4 μm. The fibers of type B are 1.85 m and 0.93 m long with 5000 ppm Tm^{3+} concentration, an NA of 0.25, core diameter 2.6 μm, 125 μm cladding diameter, and a background loss of 0.36 dB/m at 1.4 μm.
The capture fraction S of a single-mode fiber depends on the fiber properties and can be calculated by [61]:

$$S = \frac{3}{2} \cdot \frac{\frac{n_1^2 - n_2^2}{n_1^2}}{\left(\frac{\omega_0}{a}\right)^2 \cdot V^2}, \tag{4.8}$$

with the refractive indices n_1 and n_2 of fiber core and cladding, respectively. ω_0 is the mode field diameter, a is the core radius and V denotes the normalized frequency which is given by [62]

$$V = \frac{2\pi}{\lambda} \cdot a \cdot \sqrt{n_1^2 - n_2^2} = k \cdot a \cdot \mathrm{NA}. \tag{4.9}$$

k is the wavenumber and the ratio of the mode field diameter to the core diameter is given by the so-called *Marcuse approximation* to [61, 62]:

$$\frac{\omega_0}{a} \approx 0.65 + 1.619 \cdot V^{-1.5} + 2.879 \cdot V^{-6}. \tag{4.10}$$

To guarantee that RBS levels may be observable in the presence of phase noise, a rule of thumb can be derived by just demanding that the minimum detectable reflection strength of RBS must be equal or larger than that of phase noise. Equating both expressions (see equations (A.29) and (4.6)) and after some simple mathematical steps, the maximum arm-difference length of the DUT interferometer for which RBS levels may be observable in the presence of phase noise is derived:

$$\Delta L \leq \frac{\lambda_0 \cdot c_0}{8 \cdot n_g} \cdot \sqrt{\frac{R_{\mathrm{LO}}}{R_0} \cdot \frac{S \cdot \alpha_{\mathrm{S}} \cdot \tau_c}{\sigma \cdot n_{\mathrm{g}}} \cdot C_{\mathrm{R}} \left(1 - C_{\mathrm{R}}\right)}. \tag{4.11}$$

All parameters in equation (4.11) have already been defined above. For the distributed reflectivity in case of RBS an effective reflection factor has been assumed, as also described in appendix A. This means that RBS is treated like a discrete (or local) reflection which is a reasonable interpretation since an effective reflection factor has been introduced. It goes without saying that the sweep speed σ is proportional to the swept wavelength range $\Delta\lambda$ according to $\Delta\lambda = \sigma \cdot T_{\mathrm{S}}$, where T_{S} denotes the measurement time, i.e. the sweep time. Formula (4.11) shows that for a given fiber, a given TLS and a center wavelength which usually is chosen to be the wavelength of maximum gain of the amplifier (1471 nm in case of the investigated TDFAs), several other parameters must be carefully chosen: The coupling ratio C_{R}, the wavelength sweep speed σ and the ratio of LO reflectivity to signal reflectivity R_{LO}/R_0. According to equation (4.11) a gold tipped fiber end face as an LO would lead to a larger arm-difference length than a Fresnel reflector but since only a limited number of them had been available Fresnel reflectors have been used. Moreover, according to equation (4.6) a strong reflector such as a gold tipped fiber end face acting as LO would also improve measurement sensitivity by decreasing phase noise floor. However, for a very large arm-difference length, a coupling factor of $C_{\mathrm{R}} = 0.5$ would be preferable but all measurements have been done with a C_{R} of 0.8, i.e. 80 % of the input power has been coupled to the TDFA. As already mentioned, this coupling factor delivered the best performance when measuring RBS levels.
Nevertheless, condition (4.11) could still be fulfilled which is shown in Figure 4.5. It illustrates the maximum arm-difference length for different reflection strengths and for the fibers used as a function of sweep speed. For both investigated types of fibers (see table 4.1) no significant difference has been observed by these calculations and thus only for one type of fiber these plots are shown. As already described, the thulium-doped fluoride fibers are connected to silica fibers by means of glue splices. In the worst case, there is an air gap between both fibers, and thus there will be a maximum reflection of $R_0 = -14$ dB corresponding to a Fresnel reflection (see Figure 4.5). As explained before, in the calculations all reflections including the RBS reflection have been assumed to show discrete values. In practice, discrete reflections superimpose with RBS, which represents distributed reflections, and the sum of discrete and distributed reflections is detected. The calculated RBS levels lie in the range of about -70 dB which in some of the experiments have been observed as well. These experiments are discussed

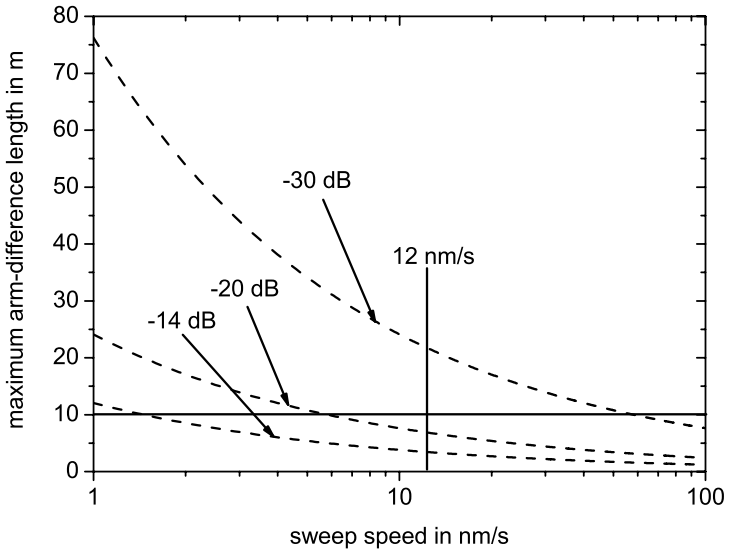

Figure 4.5: Calculation of the maximum arm-difference length for which RBS is dominant to phase noise as a function of sweep speed. The reflection strength R_0 is the varying parameter. Typical values for sweep speed and arm-difference length are indicated as solid lines.

in detail in [60]. However, since there are many other reflections in the setup, such as from TEC or glue splices, these reflections will superimpose to the RBS levels. Hence, in most of the experiments carried out noise floor values up to -40 dB have been observed. Thus, the calculations shown in Figure 4.5 are shown for -30 dB, -20 dB and for the worst-case scenario of -14 dB. For a RBS level between -30 dB to -70 dB even larger arm-difference lengths can be expected (see equation (4.11)) and thus these traces are not shown in Figure 4.5.
According to the graphs shown, the smallest possible sweep speed of 1 nm/s should be chosen. However, the TLS used shows a minimum achievable sweep speed of roughly 12 nm/s, The active fiber lengths of the TDFAs are up to 8.2 m long in case of fiber A and up to 2 m in case of fiber B. Thus, for a sweep speed $\sigma = 12$ nm/s and reflection strengths of the glue splices which are significantly smaller than Fresnel reflections, RBS will be dominant compared to phase noise.
For silica fibers the capture fraction is on the order of $1.2 \cdot 10^{-3}$ and the loss constant amounts to $4 \cdot 10^{-5}$ m^{-1} [6, 62]. If one chooses a sweep speed of 10 nm/s and a wavelength range of 1 nm, the RBS noise level would amount about -104 dB and would be smaller than the phase noise floor level which has been observed in the experiments. Hence, the dynamic range observed in the setup used is insufficient to detect RBS levels of silica. The main limitation is the TLS used which works well in the S-band but it does not cover the center wavelength of EDFAs working in the C-band.

4.1.6 Measurement results for TDFAs characterized by OFDR

The pumping schemes of TDFAs are very different to EDFAs. In contrast to EDFAs, single and dual pump wavelength schemes are of interest. Amplification with one pump wavelength is more effective than a dual-wavelength pumping scheme using a highly concentrated thulium fiber which leads to a very high internal efficiency TDFA [36, 63]. As is well known, 1050 nm pumping alone requires higher power to provide amplification due to the very low GSA.

A critical parameter in the optimization of doped fiber amplifiers is the choice of fiber length, which mainly depends on pump power and pump wavelength. Another critical parameter is the dopant concentration of the active fiber. The cut-back method to determine the optimum fiber length experimentally is not very appropriate because of the high price of ZBLAN (ZrF_4-BaF_2-LaF_3-AlF_3-NaF)-based Tm^{3+}-doped fibers.
C-OFDR as a non-destructive and highly sensitive reflectometric technique is a powerful tool for spatially resolved gain measurements and for obtaining the optimum gain-length ratio of fiber amplifiers.
Spatially resolved gain measurements have already been performed in the C-band for EDFAs [64–66], for L-band EDFAs [67] and in the S-band for TDFAs with fluoride fibers doped either with 2000 ppm or 2500 ppm Tm^{3+} concentration [34, 35, 68, 69]. Several TDFA pumping schemes have already been investigated but there is still the need to investigate further pumping schemes (like the one recently proposed in [70]) and especially fibers with a much higher dopant concentration since they turned out to be much more efficient [36].
Besides the destructive cut-back method, the only non-invasive way is the possibility of using numerical models for TDFA characterization [71, 72] which is not always the best solution due to the simplicity or the lack of accurateness of the underlying models.
In this section, the results for single-pumped TDFA with ZBLAN fibers of 2000 ppm Tm^{3+} concentration are compared to the results with ZBLAN fibers of 5000 ppm Tm^{3+} concentration. The optimum gain-length ratio for each configuration is determined. This is the first time that highly doped TDFAs are investigated with C-OFDR.
The measurements are done within a wavelength range of about 3.5 nm around 1471 nm and the sweep speed has been approximately 12 nm/s. The maximum detectable range of the measurements, determined by the laser linewidth (150 kHz) is about 434 m, much larger than the range of the measurements. In most of the experiments a sampling rate of 500 kHz has been used. The pump laser for the TDFA is a commercially available laser diode (Lumics, Berlin) emitting up to 330 mW at 1050 nm. The maximum pump power has been limited to about 210 mW (corresponding to 170 mW after the WDM coupler) to avoid possible damage to the doped fiber module and other optical components.
Four TDFAs consisting of self-made ZBLAN fibers with different parameters are characterized [36, 53]. The parameters of the fibers used have already been described in section 4.1.5. The first fiber of type A, which is 8.2 m long, is spliced from one end with a commercial silica fiber pigtail and the other end is an open fiber end, whereas the first fiber of type B (1.85 m

long) and the second fiber of each type (5 m long fiber of type A and 0.93 m long fiber of type B) are spliced at both ends with commercial silica fiber pigtails using the glue splice technique described in [73].
The first result is shown in Figure 4.6 with all parameters. This figure displays the reflected

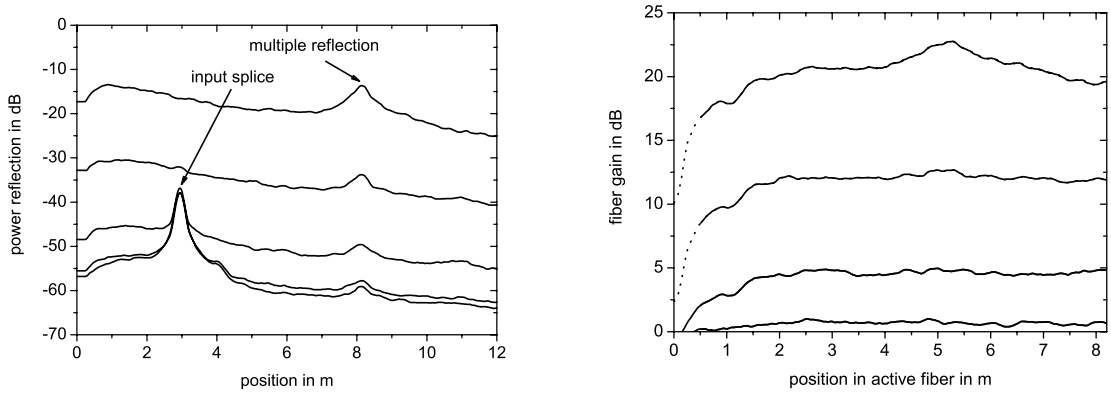

Figure 4.6: First fiber of type A: Reflected power versus position along fiber length (left) and calculated fiber gain as a function of position in the active fiber (right) for different pump powers of the 1050 nm laser diode. The traces are plotted from bottom to top for increasing pump power: left: no pump power, 26, 66, 140 and 170 mW, and right: 26, 66, 140 and 170 mW.

power against position along the fiber and the calculated fiber gain over position in the active fiber for the 8.2 m long fiber, respectively. The gain distribution in Figure 4.6 has been directly calculated by subtracting the respective backscattered signals along the fiber (in logarithmic scale) from the value at the same position for no input power and dividing by two, to account for the double-pass round trip of the signal along the active fiber [53, 68]. All gain curves, which will be presented in the following, should be zero at the beginning of the active fiber. In most cases this is not valid and can be explained by the superposition of the backscattered signal with the backward ASE white beat noise, masking the distributed gain results at the beginning of the active fiber. It is noted that a calibration is not necessary to obtain the exact gain values. However, a calibration has been performed for all measurements shown in this work. Larger values than 0 dB are possible since the RBS levels increase for increasing pump power and all OFDR traces shown in the same plot have been calibrated with the reflection of a gold tipped fiber end face measurement. From the shape of the OFDR trace one can also determine whether the fiber length is optimized or not.
There are several additional signatures in Figure 4.6 which are due to the interference between the reflections of one glue splice and the open fiber end in the same interferometer arm and not with the LO. Signal wavelength and signal power are kept constant in all measurements to 1471 nm and -2 dBm (0.63 mW), respectively. In the left part of Figure 4.6 the input

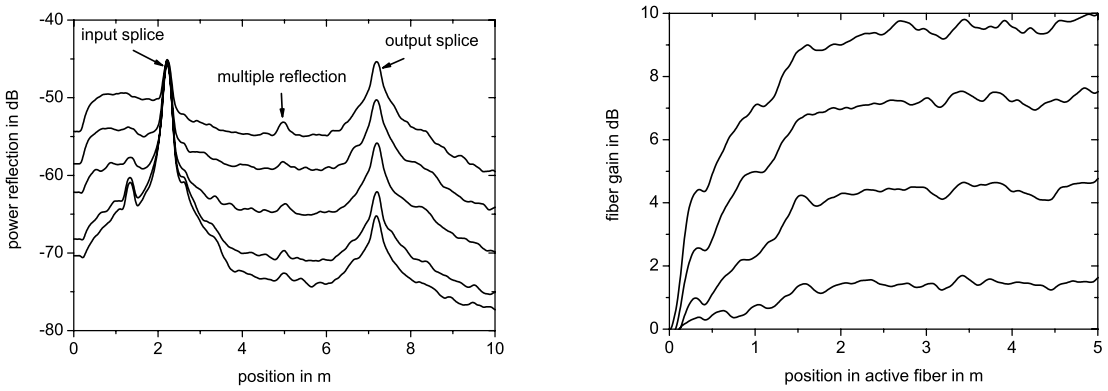

Figure 4.7: Second fiber of type A: Reflected power versus position along fiber length (left) and calculated fiber gain as a function of position in the active fiber (right) for different pump powers of the 1050 nm laser diode. The traces are plotted from bottom to top for increasing pump power: left: no pump power, 26, 66, 105 and 140 mW, and right: 26, 66, 105 and 140 mW.

splice is indicated. The signatures at 8.2 m are due to multiple reflection between the input splice and the open fiber end. Since the active fiber length amounts about 8.2 m, one can see a weak reflection at about 11 m which is due to the reflection at the open fiber end.
Due to the high accuracy of the C-OFDR technique used, these measurements are reliable and even the multiple reflections within the active fiber region located between both active fiber end reflections do not have a strong impact on the fiber gain results which are depicted in the right part of Figure 4.6. It shows the accumulated gain along the fiber for increasing pump power. From the gain traces one sees that the gain slope is increasing at the beginning of the fiber and saturating even at smaller pump powers at a position of about 2 m for fiber A (see Figure 4.6). This indicates that the fiber is longer than the optimum length. A maximum gain of roughly 20 dB has been achieved and the optimum length is 2 m which leads to a gain-length ratio of 10 dB/m for the 2000 ppm fiber. The RBS noise floor values observed during all experiments, when the pump laser had been switched off, are in accordance with the work of Mussi *et al.* [74].
The results of the second thulium fiber of type A are shown in Figure 4.7. It is about 5 m long and shows a concentration of 2000 ppm. One can recognize the signatures for input and output splice at 2.2 m and 7.2 m, respectively. Thus, a weak artifact is observed at about 5 m. The behavior of the fiber gain is similar to the one shown in Figure 4.6 but the maximum gain only amounts to 10 dB. The reason is that in this case the maximum power has been limited to 140 mW and thus compared to the 8.2 m long fiber of type A for the same pump power, both experiments are in excellent agreement. There, for the same pump power a gain value of roughly 12 dB has been achieved. The discrepancy of 2 dB can be explained by the use of glue splices. Their properties change with increasing powers and with time [33].

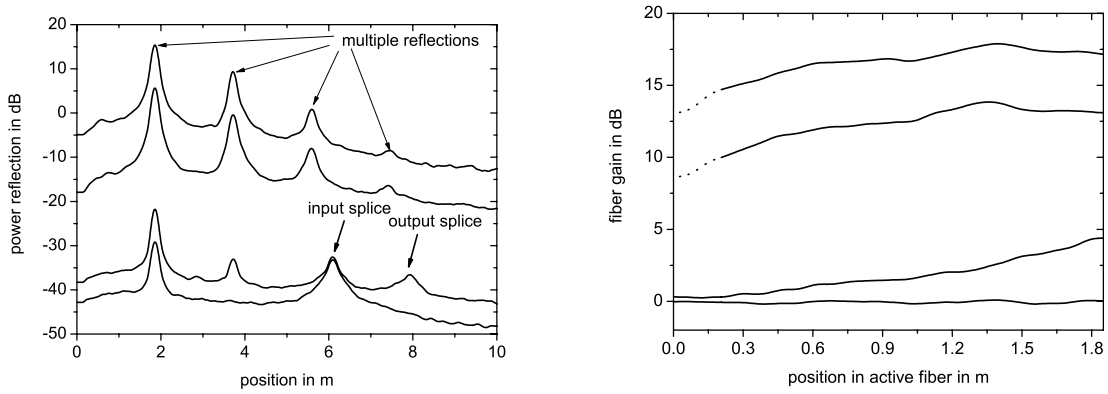

Figure 4.8: First fiber of type B: Reflected power versus position along fiber length (left) and calculated fiber gain as a function of position in the active fiber (right) for different pump powers of the 1050 nm laser diode. The traces are plotted from bottom to top for increasing pump power: left: no pump power, 105, 140 and 170 mW, and right: 26, 105, 140 and 170 mW.

Now, the fibers of type B will be investigated. They show a higher thulium concentration than the fibers of type A. In the left part of Figure 4.8 input and output splice can clearly be identified for pump powers less than 105 mW. Above this level the RBS reflectivity increases, so that these signatures cannot be observed any more. The number of detectable multiple reflection signatures (located at multiples of 1.85 m) increases with the power level. The input splice and output splice signatures can be seen at positions of 6.1 m and 7.95 m, respectively. The right part of Figure 4.8 shows the result for the 1.85 m long fiber of type B with 5000 ppm Tm^{3+} concentration. In this case a maximum gain of about 16 dB is obtained. It is more difficult to determine the optimum fiber length for this fiber. Assuming that the optimum concentration-length product amounts 4000 ppm · m like for the fibers of type A, one could estimate an optimum length of 80 cm for the fibers of type B. This would lead to a gain-length ratio of 20 dB/m for the first fiber of type B, proving that with a higher dopant concentration the gain-length ratio increases. The maximum gain will be reached at higher wavelengths [36, 63]. The fact that the fiber gain is not saturating in case of pumping fiber B with powers up to 105 mW supports the observation that the power threshold value for energy transfer between thulium ions lies between 105 to 140 mW [36]. Rapid increase of fiber gain is reached after passing the threshold power of 105 mW (avalanche effect). Then, the level $^3F_4$ is strongly populated due to cross relaxation and finally a resonant ESA with succeeding non-radiative relaxation takes place to the $^3H_4$ level which is responsible for the amplifier gain. Below the threshold power the weak GSA at the pump wavelength causes only a small fiber gain.

The results for the 0.93 m long active fiber of type B are shown in Figure 4.9. The active fiber length is 93 cm long [36] with 5000 ppm Tm^{3+} concentration. It has been spliced at

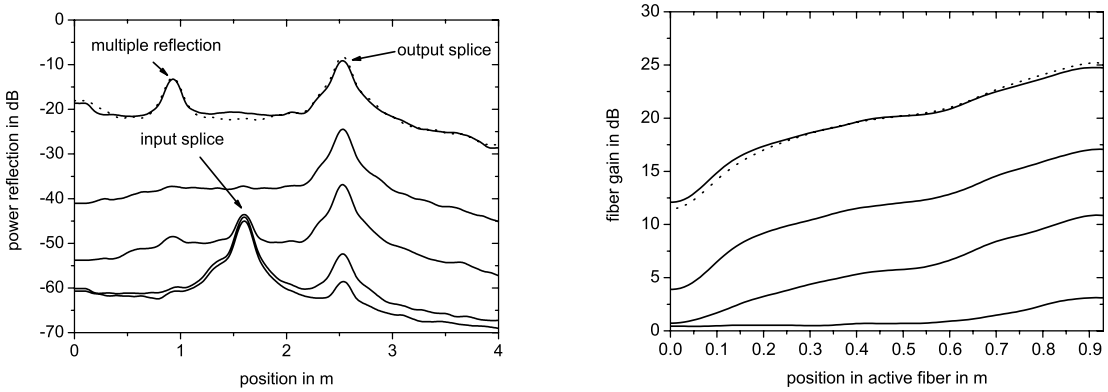

Figure 4.9: Second fiber of type B: Reflected power versus position along fiber length (left) and calculated fiber gain as a function of position in the active fiber (right) for different pump powers of the 1050 nm laser diode. The traces are plotted from bottom to top for increasing pump power: left: no pump power, 26, 67, 105, 141 and 173 mW (dotted line), and right: 26, 67, 105, 141 and 173 mW (dotted line).

both ends with commercial silica fiber pigtails using glue splices.
The input and output glue splice signatures are at a position of 1.6 m and 2.53 m, respectively, which leads to a multiple reflection at 0.93 m.
The right part of Figure 4.9 shows the accumulated gain along the active fiber for increasing pump power. From these curves one sees that the fiber gain increases continuously up to the fiber end. A maximum gain of 25 dB has been achieved which leads to a gain-length ratio of about 27 dB/m (this time it has been assumed that the actual fiber length is equal to the optimum length). For pump powers larger than 140 mW the gain level remains almost unchanged indicating that a complete population inversion along the active fiber length has already been reached for 140 mW.
In Figures 4.6, 4.8 and 4.9 all gain curves should be zero at the beginning of the active fiber (like in Figure 4.7). Obviously, and as already explained, this is not the case and can be explained by the superposition of the backscattered signal with the backward ASE white beat noise, masking the distributed gain results at the beginning of the active fiber [65, 68]. According to the pump powers used here, fibers A and B could be shortened to 2 m respectively 80 cm (except for the 0.93 m long fiber where the fiber gain did not saturate along the position) while keeping at least the same gain and concentration-length product in this pumping scheme. In case of the 1.85 m long active fiber the assumed optimum length of 80 cm is in good agreement with the experiment although artifacts (due to multiple reflections between both glue splices) cause that the fiber gain still increases after about 90 cm.

4.1.7 Summary

OFDR measurements on RBS levels give physical insights into the amplification process of fiber amplifiers for a given pump power, pumping scheme and active fiber used. In EDFAs it is well known that the signal wavelength lies in a transition from the ground state to the first excited state, thus being absorbed in the absence of pump power, whereas in TDFAs the amplifying levels occur between excited states and thus no signal absorption exists in the absence of pumping. In case of EDFAs for no pump power the gain decreases due to GSA (see for instance [64, 65]) which is not the case for TDFAs as can be seen from the measurements. The C-OFDR technique has been used to obtain information about the gain-length ratio for S-band TDFA pumped by 1050 nm laser diodes which is the most efficient wavelength for single-wavelength pumped TDFAs [35, 36]. In this section, RBS levels of ZBLAN based fluoride fibers with strongly different dopant concentrations and different fiber lengths are compared to each other. Up to 20 dB amplifier small-signal gain has been achieved from this single-wavelength scheme for the 2000 ppm fiber, in good agreement with the work of Gomes *et al.* (see [34] and [68]). The gain-length ratio for this fiber amounts to 10 dB/m and for the highly 5000 ppm Tm^{3+}-doped fiber it amounts to 20 dB/m assuming the same optimum concentration-length product.
The influence of the BPF on RBS level measurements is relatively small. To suppress the ASE even more and thus to achieve even better results one needs a filter which has a narrower wavelength band with cut-off wavelengths corresponding to the start and stop wavelengths of the TLS sweep. It would be more informative to achieve spatially resolved gain measurements over a broad wavelength range. For this purpose one would need a narrow but tunable bandpass filter which is expensive.
An alternative, mentioned by many researchers, to achieve that the fiber gain is 0 dB at the beginning of the active fiber would be to interpolate the gain curves to the origin of the diagrams. This has not been done since the author does not want to corrupt the gain traces calculated from the OFDR spectra. To the author's opinion this is not a real alternative because in many cases the gain traces would be corrupted. Moreover, a certain amount of reflection from the glue splices is necessary to determine the beginning of the active fiber in the OFDR spectrum. Thus, an ideal splice with almost no reflection is not desirable despite of reducing the signal losses and improving the pump incoupling into the active fiber.
From various measurements [36] it has been concluded that the active fiber length of the self-made highly thulium-doped fiber amplifiers must be in the range between 80 cm and 1 m. For a fiber length of 93 cm [36], the amplifier small-signal gain amounts to 25 dB in this single-wavelength scheme which has been the maximum value determined by the experiments. This led to a gain-length ratio of about 27 dB/m. Actual numbers depend on experimental conditions such as pump power, signal power, and particularly splice losses.
Higher gain is expected for longer wavelengths [36, 75]. The fiber gain does not saturate for low pump powers which is due to the threshold power of energy transfer between thulium ions in such highly doped fibers [36, 53].

Comparing both types of fibers it can be concluded that the 5000 ppm fiber offers higher gain and a larger gain-length ratio. In addition, it offers similar gain values like the 2000 ppm fiber for less pump power. Besides the advantage of needing only one pump laser diode to achieve a high internal efficiency with a highly doped fiber, the economic advantage of the 5000 ppm fiber lies in the fact that a shorter fiber length represents a significant total amplifier cost reduction.
Theoretical calculations for the RBS levels and for the phase noise levels when measuring strong reflectors are in accordance with the experiments. In principle, OFDR measurement sensitivity is quantum limited (i.e. limited by shot noise of the detector) [43]. In the setup used, the noise level for discrete reflectors is given by phase noise and in case of fiber amplifiers it has been possible to achieve that RBS dominates phase noise.
Phase noise can be clearly improved using shorter connection fibers in the setup. But this is only possible to a certain degree because of the tuning nonlinearity of the laser which may corrupt the reflection information due to broadened spectra before laser-sweep correction [48]. Moreover, the possibility to investigate different glass hosts for TDFAs, different pumping schemes and different dopant concentrations with the C-OFDR technique is not extensively investigated yet. According to literature, the most promising pumping scheme for standard application of TDFAs seems to be the dual wavelength pumping scheme with 800 nm and 1050 nm [76]. Nevertheless, there is the need to optimize TDFAs for its application in the S-band. Especially the glue splice technique has to be optimized or an alternative splicing method, which is more reliable and efficient, has to be found. Thus, the author believes that in the near future much more research work will be seen in this field.

4.2 FTF method to measure fluorescent lifetimes of Pr^{3+}-doped fluoride glasses

The fluorescent lifetime of energy levels of rare-earth-doped glasses or fibers provides a valuable information for fiber laser and amplifier applications. Lifetime measurements for the upper energy levels of praseodymium-doped fluoride glasses are reported and the influence of ytterbium as co-dopant is shown as well. A frequency transfer function (FTF) method [77] is introduced to determine fluorescent lifetimes of arbitrary rare-earth-doped glasses and fibers. The FTF method is applied to the case of praseodymium-doped glasses co-doped with ytterbium. Lifetimes between 17 μs to 46 μs in case of praseodymium concentrations of less than 0.1 mol% have been measured.

4.2.1 Introduction

Knowledge of spectroscopic properties of rare earth ions doped in glasses or fibers is mandatory for predicting the characteristics of fiber lasers and amplifiers. In addition, it is necessary to understand the limitations of device efficiency. For fiber laser applications the lifetime of the upper laser levels ^3P_J of the praseodymium ion is of highest interest. Ohishi optimized

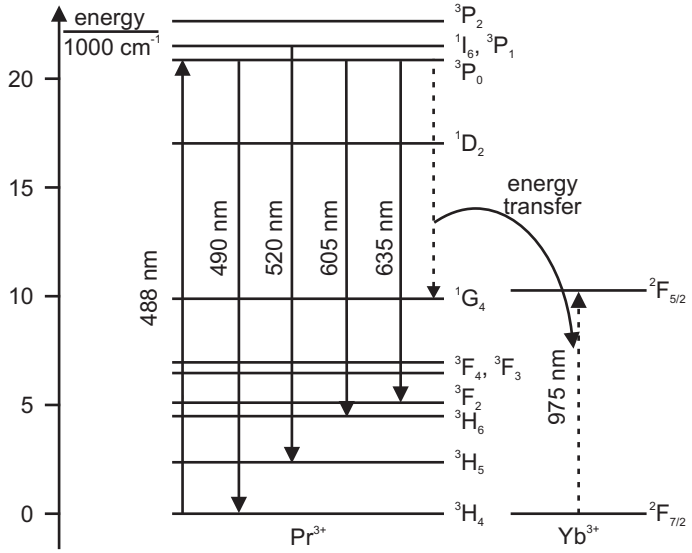

Figure 4.10: Energy level diagram of Pr^{3+} and Yb^{3+} in the transmission window of ZBLAN together with the red, orange, green and blue transitions of Pr^{3+}. A possible energy transfer process between both ions is indicated with an arrow. The $^3P_0$ level of Pr^{3+} is pumped with a wavelength of 488 nm while Yb^{3+} may be pumped with a wavelength of 975 nm.

praseodymium-doped fiber amplifiers with regard to concentration [78]. He performed lifetime measurements on the $^1G_4$ level and obtained a value of about 110 μs for less than 1000 ppm concentration. The energy level diagrams of praseodymium (Pr^{3+}) and ytterbium (Yb^{3+}) in the fluorozirconate glass ZBLAN together with a possible energy transfer process are displayed in Figure 4.10.

In [79] lifetime measurements were performed for Pr^{3+}/Yb^{3+}-doped fluoride fiber. The influence of Yb^{3+} on the lifetime of Pr^{3+} energy levels was investigated and it was shown that a co-doping with Yb^{3+} is advantageous due to energy transfer and a shift of the pump wavelength towards lower wavelengths where more laser diodes were available in 1991 [79]. Energy transfer is well possible due to spectral overlap of the Yb^{3+} emission cross section with Pr^{3+} absorption cross section.

Lifetime measurements for the $^1G_4$ level in fluoride fibers were also investigated in [80–83] and for other glass hosts in [84]. Concentration quenching was observed and it was concluded that for Pr^{3+}-doped glasses the concentration should be less than 500 ppm to avoid cross relaxation processes [81]. For quantitative values, the reader is referred to the cited references. The measured lifetime is influenced not only by the dopant concentration but also by temperature [12, 85–87]. In this section lifetime measurements at room temperature will be reported. In [88] the energy transfer process between Pr^{3+} and Yb^{3+} in ZBLAN glass is explained in detail. The fluorescent lifetimes of the most relevant energy levels of Pr^{3+} and Yb^{3+} are listed there. Alcala also presented lifetimes of the $^3P_0$, $^1D_2$ and $^1G_4$ levels [89]. Lifetime measure-

ments of the upper energy levels of Pr^{3+}-doped fluoride glasses [90] were e.g. presented in [91] and of the $^1D_2$ level in [92].
In this section, the fluorescent lifetimes of the upper energy levels in Pr^{3+}-doped fluoride glasses are reported. First, the temperature dependence of fluorescent lifetimes is summarized, then, the influence of the $^1G_4$ lifetime on the energy transfer processes between Pr^{3+} and Yb^{3+} and the optimum dopant concentration as reported in literature are indicated. Moreover, an FTF method is presented to determine fluorescent lifetimes from energy levels of arbitrary rare-earth-doped glasses and fibers. Further, the FTF of praseodymium-doped glasses is measured and the lifetimes of the upper energy levels are extracted from the complex FTF by fitting the recorded phase. Furthermore, alternatives are shown to extract fluorescent lifetimes by either the recorded magnitude or the complex FTF itself. Since these alternatives are not applied on praseodymium, this part is shifted to appendix B. Finally, the impact of ytterbium as co-dopant on the fluorescent lifetimes of praseodymium in IBZP (a fluoroindate glass) and in ZBLAN (a fluorozirconate glass) is investigated.

4.2.2 Temperature dependence of the fluorescent lifetimes

As the temperature increases, the measured lifetimes are also seen to increase slowly [85]. This phenomenon is used in temperature sensors based on Pr^{3+}-doped ZBLAN glass. This behavior which is opposite to the one corresponding to multi-phonon decays, can be understood as due to thermal population of the $^3P_1$ and $^1I_6$ levels at high temperatures and to the different decay probabilities of these levels as compared with that of $^3P_0$ [93]. Nguyen reported that there is a critical concentration of 6900 ppm [94] at which the fluorescent lifetime is independent of temperature. The fluorescent lifetime increases with temperature at dopant levels below this critical level, and decreases with temperature at dopant levels higher than this critical level. The increase of the lifetime with growing temperature was also observed for an Yb^{3+}-doped fluorophosphate glass [95].
There is also an influence of the temperature on the emission intensity. The analysis of this phenomenon in Pr^{3+}/Yb^{3+}-doped ZBLAN, pumped at 960 nm, is reported in [87]. The intensity of the upconversion emission first increases with temperature, reaches a maximum value, and then decreases. This indicates that the energy transfer probability among Pr^{3+} ions depends on temperature and supports the assumption that under infrared excitation it is a phonon-assisted energy transfer process.
The increase of emission intensity in Pr^{3+}-doped ZBLAN glass with increasing temperature is due to an increase in the probability of the non-resonant multi-phonon process which is involved in the transfer of electron-excitation energy among the activator ions. This results in populating the highly excited levels of the activator. However, an increase in the temperature also causes both an increase in the probability of multi-phonon relaxation transitions and an increase of processes involved in the reverse transfer of electron excitation energy among the activator ions which depletes the radiative levels of the activator. As a result of the combined competitive action of such processes, a maximum value of the intensity is obtained at a certain

temperature. The intensity value drops with further increase of the temperature [96].

4.2.3 Lifetimes of the $^1G_4$ level and optimum dopant concentration

The $^1G_4$ level plays an important role in the upconversion pumping process of the Pr^{3+}/Yb^{3+} system (see section 3.3.3). The transition from $^1G_4$ to $^3H_5$ is of great interest because of the possibility of realizing fiber based amplifiers for the 1.3 μm telecommunication window. The dependence of the $^1G_4$ lifetime in ZBLAN on the Pr^{3+} concentration was reported in [97]. According to [97] the fluorescent lifetime decreases noticeably at concentrations of more than 0.1 mol%. At lower concentrations, the fluorescent lifetime remains constant at 110 μs within measurement errors. This result indicates that the $^1G_4$ level is quenched at concentrations of more than 0.1 mol% similar to the case of the ^3P_J transitions. Remillieux reported that a slight reduction of the lifetime of the $^1G_4$ level is also observed in the 0.02 to 0.1 mol% concentration range [98] which suggests that there are still some interacting Pr^{3+} ions degrading the lifetime. Pr^{3+} ions become isolated from each other at concentrations below 0.02 mol%.
In [79] the Pr^{3+} and Yb^{3+} lifetime dependence on Yb^{3+} concentrations for the $^1G_4 \rightarrow {}^3H_5$ fluorescence of Pr^{3+} and the $^2F_{5/2} \rightarrow {}^2F_{7/2}$ fluorescence of Yb^{3+} in ZBLAN was shown. The Pr^{3+} concentration remained constant (0.3 mol%) and that of Yb^{3+} changed from 0.1 to 2 mol%. The fluorescent lifetime was determined as the first e-folding time of the fluorescence decay curve. The lifetime of Pr^{3+} increased and that of Yb^{3+} decreased with an increase of Yb^{3+} concentration. The energy transfer efficiency in the Pr^{3+} (0.3 mol%) and Yb^{3+} (0.2 mol%) system was estimated from a fluorescent lifetime measurement of Yb^{3+} [99] to be 22 %, a result which is apparently due to the low concentration of Yb^{3+} employed. The energy transfer from Yb^{3+} to Pr^{3+} increases to about 56 % if 0.3 mol% Pr^{3+} is co-doped with 2 mol% Yb^{3+} [82]. Hence, the pumping efficiency can be improved by optimizing the concentrations of Pr^{3+} and Yb^{3+} ions in the glass host.
Forward transfer of energy from Yb^{3+} to Pr^{3+} is relatively likely while back transfer of energy from Pr^{3+} to Yb^{3+} is relatively unlikely, mainly as a consequence of the short lifetime of the $^1G_4$ level. The Pr^{3+} ion concentration, if doped alone, should not be more than 0.1 mol% due to concentration quenching. However, if Yb^{3+} ions are added, the energy transfer rate from Yb^{3+} to Pr^{3+} follows an increase of Pr^{3+} effective lifetime. The increase of energy transfer rate compensates absorbability reduction due to Pr^{3+} ion concentration quenching. This shows that it is possible to increase the concentration of Pr^{3+} [100].
A linear dependence of the fluorescence emitted by the Pr^{3+} ions by increasing Yb^{3+} concentration was observed. For Yb^{3+} contents larger than 1.5 mol% a deviation from the linear behavior is observed. The fluorescence intensities increase slower and reach some saturation. All these results reported in literature suggest that the optimum dopant concentration for Pr^{3+}/Yb^{3+} fiber laser applications is 0.3 mol% of Pr^{3+} with 2 mol% Yb^{3+}.

4.2.4 FTF method

The fluorescent lifetime is a very important parameter and a key to the qualitative understanding of laser properties. Detailed measurements of the fluorescence from excited energy levels can provide information on the relative importance of ion-ion interactions such as upconversion and quenching processes. The decay of the population in a given energy level drops exponentially with a time constant equal to the lifetime. For every excited energy level radiative transitions, multi-phonon relaxation and energy transfer occur simultaneously and, thus, the total lifetime is given by:

$$\tau = \frac{1}{A_{rad} + W_{mp} + W_{et}}, \tag{4.12}$$

where A_{rad}, W_{mp} and W_{et} denote radiative relaxation, multi-phonon (non-radiative) and energy transfer transition rates, respectively. The quantum yield η is defined as the radiative portion of the total relaxation rate of a given energy level:

$$\eta = \tau \cdot A_{rad}. \tag{4.13}$$

η is an important property for laser and amplifier applications.
To sum up, there are several ways for the population to decay. The total probability of the decay is equal to the sum of the individual probabilities for each path. The total lifetime for a given rare earth level τ is given by the following relation:

$$\frac{1}{\tau} = \frac{1}{\tau_{rad}} + \frac{1}{\tau_{mp}} + \frac{1}{\tau_{et}}, \tag{4.14}$$

where τ_{rad} is the radiative lifetime, τ_{mp} is the non-radiative lifetime and τ_{et} represents the energy transfer processes. For low dopant concentrations the energy transfer transition rates W_{et} are low and constant. Therefore, it only plays an important role in case of highly rare-earth-doped glasses. Large energy gaps between energy levels result in negligible multi-phonon transition rates. Thus, the measured lifetime is in fact the radiative lifetime τ_{rad} which is determined by the fluorescence from the excited level to all the levels below it. It can also be calculated with the help of Judd-Ofelt analysis [101, 102]. In case of praseodymium some authors proposed that the Judd-Ofelt analysis has to be slightly modified [103–105] to yield more accurate results. These authors proposed the modification because they got negative values for the Judd-Ofelt parameters in contradiction to their definition. The lower success of the Judd-Ofelt theory for praseodymium is mainly caused by the three ^{3}P levels [105]. All in all, the modifications were not very successful and satisfying, and finally it was found [106] that with a new assignment the linear optimization problem to obtain the Judd-Ofelt parameters produces better results than all modifications [15]. Nevertheless, the modified theory with their unrealistic large values are still in use.
In the non-radiative process, the deactivating process from the excited rare earth energy level

is accompanied by the emission of one or several phonons. In case of the thermally coupled upper energy levels of praseodymium, it has been determined that each level leads to the same lifetime when separating the different transitions by means of a prism. As has already been explained, the multi-phonon relaxation is a temperature dependent process which is weaker in fluoride glass than in silica due to the low phonon energies.
The lifetime τ in the upper laser level may be measured simply by monitoring the decaying fluorescence from a glass sample pumped by a chopped laser beam. The only requirement is that the pump light has to be turned on a sufficiently long time for a significant ratio of the rare earth to be excited. This ensures a realistic fluorescence level for the measurement. Ideally, the pump light should then be turned off completely, and the fluorescence intensity would then decay exponentially according to $\exp(-t/\tau)$, where t denotes the time. However, in practice the pump will always have a given decay time. Therefore, dependent on the requirements of accuracy and the involved lifetime, different choppers may be used. If the lifetime is very long (e.g. around 10 ms) realistic lifetime estimates may be obtained by using a mechanical chopper, recording the decay curve by means of a digital oscilloscope and applying an exponential fit (classical method). When a mechanical chopper is used to modulate a laser beam, which shows a Gaussian intensity distribution, the rise and fall time of the modulation should ideally be much faster than the fluorescent lifetime. If the pump has to be turned off much faster like in case of praseodymium, an acousto-optical modulator (AOM) may be used instead of a mechanical chopper.
A frequency-domain method has been applied instead of the classical time-domain method. The method is applicable not only to rare-earth-doped glasses and fibers but also to transition-metal-doped samples as it was done for Cr^{3+} in [107]. It is based on the same principle like the method described in [108]. Morel presented a simple method for measuring the fluorescent lifetime of rare-earth-doped fibers by recording the FTF and by fitting the measured curves. He applied the method to neodymium and thulium but did not give a thorough theoretical formulation for an arbitrary number of N transitions. Let us start with a simple two-level model and then generalize the model for N transitions:
A simple two-level model is assumed and absorption, spontaneous and stimulated emission (cf. section 1.1) are combined. Thus, one can write for the change of the upper and lower level populations N_2 and N_1:

$$\frac{\mathrm{d}N_1}{\mathrm{dt}} = -\frac{\mathrm{d}N_2}{\mathrm{dt}} = B_{21} \cdot \rho(\nu) \cdot N_2 - B_{12} \cdot \rho(\nu) \cdot N_1 + A_{21} \cdot N_2, \tag{4.15}$$

where $\rho(\nu)$ is the frequency dependent radiation density, B_{21} is the Einstein coefficient for the stimulated emission process, B_{12} is the Einstein coefficient of radiation and matter for the absorption process and A_{21} is the Einstein coefficient for an atom in level 2 to decay spontaneously to the lower level 1. The radiative lifetime is connected with A_{21} by the relation

$$\tau = \tau_{rad} = \tau_{21} = \frac{1}{A_{21}}. \tag{4.16}$$

The change of the upper level population N_2 is described by equation (4.15). If one takes equation (4.16) into account and ignores the stimulated emission, one obtains the following equation:

$$\frac{\mathrm{d}N_1}{\mathrm{dt}} = -\frac{\mathrm{d}N_2}{\mathrm{dt}} = -B_{12} \cdot \rho(\nu) \cdot N_1 + \frac{N_2}{\tau}. \tag{4.17}$$

The population density of a specific level is proportional to the energy E accumulated in it. Hence, equation (4.17) can be interpreted as:

$$\frac{\mathrm{d}E}{\mathrm{dt}} = p_{abs} - \frac{E}{\tau}, \tag{4.18}$$

where p_{abs} is the absorbed power and E/τ indicates the emitted power. The difference corresponds to a temporal change of the energy accumulated. The absorption probability and the quantum efficiency are considered to be constants. Consequently, for the pump power $p(t)$ supplied and for the emitted power $s(t)$ the following relations are valid:

$$p(t) \propto p_{abs}, \tag{4.19}$$

and

$$s(t) \propto \frac{E(t)}{\tau}. \tag{4.20}$$

The sample is excited until the time $t = 0$. Then the pump beam is blocked and the fluorescence decays with the time constant τ. The measurement of the lifetimes for the praseodymium-doped glasses in time-domain had been hardly possible, as has already been explained above. Thus the measurements have been performed in frequency-domain. For the fluorescence measurements a lock-in amplifier (LIA) has been used and the phase of the complex FTF has been measured. A way how to use the phase to determine the lifetime is shown. In appendix B, an alternative way how one can extract the lifetimes from the complex FTF or its magnitude is shown as well.

In case of recording the phase of the FTF a phase θ_p at the pump wavelength and a phase θ_s at the signal wavelength have to be measured for different modulation frequencies f. The knowledge of differences between these two phases permits to calculate the fluorescent lifetimes as will be shown in the following:

For the calculation a Fourier transform is used to transform the input and output as a function of time to the frequency-domain where the same inputs and outputs are seen as function of frequency. Assuming a linear time independent (LTI) system, the complex FTF links these frequency dependent signals to one another. Further assumptions are that one cannot detect any pump power at the signal wavelength with the maximum fluorescence intensity and that the temporal behavior of the detector is identical for pump and signal wavelength. The latter assumption would not distort the phases since the rise time of the detector used is on the order of 0.2 μs and thus at least one order of magnitude smaller than the lifetimes which should be measured. The Fourier transforms of the pump power $p(t)$ and the emitted power

$s(t)$ are $P(j\omega)$ and $S(j\omega)$, respectively. There exists exactly one complex transfer function $H(j\omega)$ which is the Fourier transform of the real causal impulse response $h(t)$. $H(j\omega)$ defines the ratio of signal to pump power in frequency-domain:

$$H(j\omega) = \frac{S(j\omega)}{P(j\omega)}. \tag{4.21}$$

Hence, the complex transfer function is determined only by the spontaneous emission and not by the setup itself. For the Fourier transform of equation (4.18), one obtains:

$$j\omega \cdot E(j\omega) = P_{abs}(j\omega) - \frac{E(j\omega)}{\tau}. \tag{4.22}$$

Now, assumptions (4.19) and (4.20) have to be taken into account which yields:

$$\frac{\frac{E(j\omega)}{\tau}}{P_{abs}(j\omega)} = C \cdot \frac{S(j\omega)}{P(j\omega)}, \tag{4.23}$$

with a constant factor C. Application of equations (4.21) and (4.22) leads to

$$C \cdot H(j\omega) = \frac{1}{1 + j\omega \cdot \tau}. \tag{4.24}$$

The unknown constant C in this relation for the complex FTF shows only an influence on the magnitude but not on the phase. Hence, it is assumed to be equal to one for finding a relation for the phases whereas in appendix B.1 it will be taken into account again.
The complex FTF of the system for one lifetime ($H_1(j\omega) = H(j\omega)$, $\tau_1 = \tau$) is:

$$H_1(j\omega) = \frac{1}{1 + j\omega \cdot \tau_1}. \tag{4.25}$$

With the knowledge of this complex transfer function one can take the inverse Fourier transform to find a general solution in time-domain. The impulse response $h_1(t)$ normalized to $h_1(0) = 1$ is given by

$$h_1(t) = \exp\left(-\frac{t}{\tau_1}\right). \tag{4.26}$$

The phase $\theta_1(\omega)$ of the first order LTI system is the argument of the complex FTF:

$$\theta_1(\omega) = \arg\left\{H_1(j\omega)\right\} = -\arctan\left(\omega \cdot \tau_1\right), \tag{4.27}$$

where the angular frequency ω equals $2\pi \cdot f$ with f as modulation frequency.
The interesting phase is the difference between the measured signal phase θ_s and the measured pump phase θ_p at different modulation frequencies f:

$$\theta_1(f) = \theta_s(f) - \theta_p(f). \tag{4.28}$$

The phase $\theta_1(f)$ converges to $-\pi/2$ for modulation frequencies $f \to \infty$. At the position $\omega \cdot \tau = 1$ the phase reaches the value $-\pi/4$ and thus the maximum modulation frequency should be on the order of $1/(2\pi\tau)$. Fluorescent lifetimes of some 10 μs have been expected which makes modulation frequencies on the order of some kHz necessary. This is not possible with a mechanical chopper and thus an AOM has been used to modulate the pump power. It enables modulation frequencies up to the MHz range. The result of a phase measurement

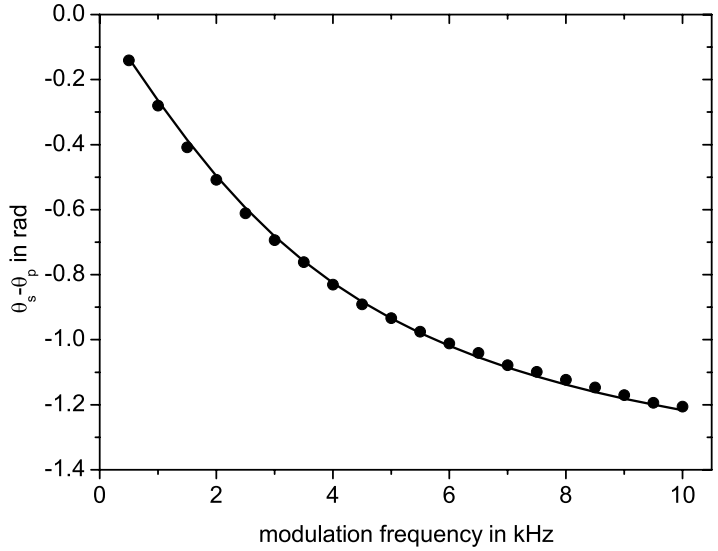

Figure 4.11: Phase difference versus modulation frequency for a 0.1 mol% Pr^{3+}:IBZP glass. The circled points represent measurements and the straight line is a fit to equation (4.27).

for a 0.1 mol% praseodymium-doped glass sample is shown in Figure 4.11 as circled points. The straight line is a fit to the function (4.27) and yields a lifetime of 43.1 μs with a mean uncertainty of $\pm$ 0.28 μs. As can be seen, measurement result and fit show excellent agreement.

Generalization to N transitions

Now, the method introduced in this section will be generalized to an arbitrary number of N transitions [107]. The Fourier relation between the input pump signal and the emitted output powers from N transitions is depicted in a block diagram (see Figure 4.12). Let us assume that there are N transitions which are involved in the emission. Each transition is weighted by a real factor a_i. It should be noted that not the exact values of the a_i are of importance for the phase of the FTF but their ratio. In conclusion, one of the a_i can be fixed to a certain value. Each transition shows a lifetime τ_i which means that when considering N

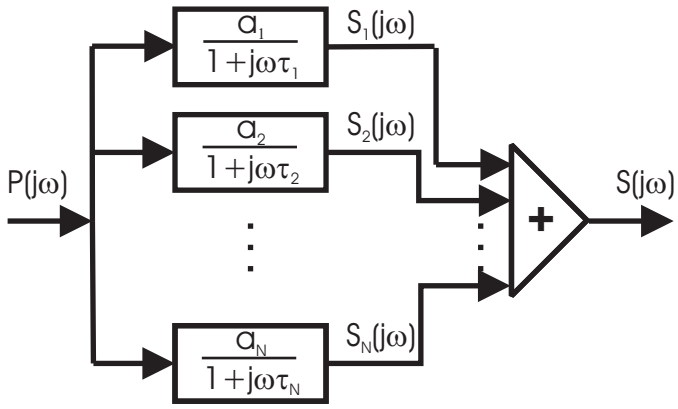

Figure 4.12: Block diagram for a system showing N transitions

transitions one has $2N - 1$ fit parameter.
The FTF for a single transition $\tilde{H}_i(j\omega)$ is still given by the Fourier relation:

$$\tilde{H}_i(j\omega) = \frac{S_i(j\omega)}{P(j\omega)} = \frac{a_i}{1 + j\omega \cdot \tau_i}. \tag{4.29}$$

It is assumed that each transition faces the same pump power and that the total emission $S(j\omega)$ is the superposition of the emitted powers from the single transitions. Thus, the FTF of the total system $H_N(j\omega)$ is the sum of the partial FTFs $\tilde{H}_i(j\omega)$:

$$H_N(j\omega) = \frac{S(j\omega)}{P(j\omega)} = \frac{\sum_{i=1}^{N} S_i(j\omega)}{P(j\omega)} = \sum_{i=1}^{N} \tilde{H}_i(j\omega). \tag{4.30}$$

Finally, one obtains:

$$H_N(j\omega) = \sum_{i=1}^{N} \frac{a_i}{1 + j\omega \cdot \tau_i}. \tag{4.31}$$

The time response when switching the pump power off at $t = 0$ can be calculated by an inverse Fourier transform:

$$g(t) = \frac{1}{\sum_{i=1}^{N} a_i} \left(\sum_{i=1}^{N} a_i \cdot \exp\left(-t/\tau_i\right) \right). \tag{4.32}$$

For the FTF of the total system the argument $\theta_N(\omega)$ has to be calculated by using the relation

$$\theta_N(\omega) = \arg\left\{H_N(j\omega)\right\} = \arg\left\{ \sum_{i=1}^{N} \frac{a_i}{1 + j\omega \cdot \tau_i} \right\}. \tag{4.33}$$

From equation (4.33) one obtains after some straight-forward calculation steps:

$$\boxed{\theta_N(\omega) = -\arctan\left(\frac{\omega \sum_{i=1}^{N}\left(a_i\tau_i \prod_{j=1,j\neq i}^{N}\left(1+(\omega\tau_j)^2\right)\right)}{\sum_{i=1}^{N}\left(a_i \prod_{j=1,j\neq i}^{N}\left(1+(\omega\tau_j)^2\right)\right)}\right)}. \tag{4.34}$$

This function has to be used as a fit function for the phase of the measured FTF in case of arbitrary N transitions. From this function one can already see that a change of a_i by a constant factor has no influence on $\theta_N(\omega)$ which means that its absolute value contains no information. In the case $N = 1$, i.e. in case of only one relevant lifetime, formula (4.34) simplifies to formula (4.27) and the factor a_1 disappears. This is the reason why the factor C (C comprises the factors a_1) has been previously assumed to be equal to one.
It is important to note that increasing the number of fit parameters in case of N expected lifetimes to e.g. $N + 1$ parameter does not improve the fit but leads to a worse convergence. In some cases this may lead to negative values of a_i and τ_i or to unexpectedly large values which is physically not meaningful.
The spontaneous emission from an excited state i with the lifetime τ_i shows the ratio p_i on the total emission:

$$p_i = \frac{a_i}{\sum_{i=1}^{N} a_i}. \tag{4.35}$$

One can consider p_i as the probability of the appearance of τ_i. This factor is proportional to the Boltzmann distribution of the occupation numbers from the respective Stark levels.

The influence of pump power

One of the assumptions is that there is no detectable pump power at the signal wavelength. This assumption may be invalid when pump and signal wavelength are close to each other. Even with adequate filters this assumption might not hold any more. As one can imagine in fibers both, pump and signal, propagate in the core and thus are hardly to separate. An alternative formula for the phase (the magnitude will be considered in appendix B) is now given in which the influence of pump power at the signal wavelength is considered:
If one assumes a superposition of the pump power at the signal wavelength, the phase of the total system will change. Especially in case of increasing modulation frequencies the pump influence increases and affects the phase at the signal wavelength. Thus, a new model is needed which considers the influence of the pump:
The power at the pump wavelength is considered to be the input of the system. The ability to measure this phase is a necessary precondition to determine the exact phase. Still assuming an LTI system, one concludes that part of the input goes to the system output without any phase deviation. This leads to an additional summand a_0 in the new FTF $H_N^{wp}(j\omega)$ where the index wp (with pump) indicates the consideration of the pump:

$$H_N^{wp}(j\omega) = \frac{A(j\omega)}{P(j\omega)} = a_0 + H_N(j\omega) = a_0 + \sum_{i=1}^{N} \frac{a_i}{1 + j\omega \cdot \tau_i}. \tag{4.36}$$

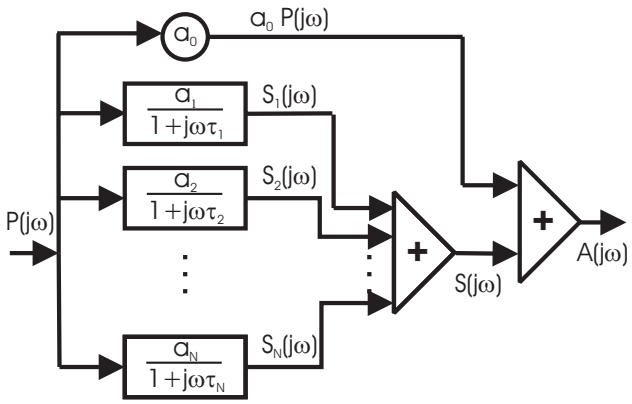

Figure 4.13: Extended model to account for the impact of pump power at the signal wavelength

The new output variable is defined as $A(j\omega) = a_0 \cdot P(j\omega) + S(j\omega)$ due to the power detected at the signal wavelength. Hence, the output power cannot be considered as spontaneously emitted power any more.

An illustration of the extended model is depicted in Figure 4.13. The arrangement of the arm with a_0 outside of the inner sum has an additional reason: The factor a_0 is not comparable with the factors a_i for $i \geq 1$ due to its physical meaning. But still this notation is very favorable which will be seen in the following.

The magnitude of a_0 depends on the pump power at the signal wavelength and its ratio to the other a_i depends on quantum efficiency and absorption probability. Moreover, equation (4.35) is still valid independent of a_0.

In this context the normalized output signal $g(t)$ shows a temporal behavior after $t = 0$ which corresponds to equation (4.32). Switching the pump off leads to a decrease of this function with a ratio $a_0/(\sum_{i=1}^{N} a_i)$. In analogy to the derivation of the phase for N transitions, the phase of the complex FTF under pump consideration can be calculated to be:

$$\boxed{\theta_N^{wp}(\omega) = -\arctan\left(\frac{\omega \sum_{i=1}^{N}\left(a_i\tau_i \prod_{j=1,j\neq i}^{N}\left(1+(\omega\tau_j)^2\right)\right)}{\sum_{i=0}^{N}\left(a_i \prod_{j=1,j\neq i}^{N}\left(1+(\omega\tau_j)^2\right)\right)}\right)}. \tag{4.37}$$

Formula (4.37) is similar to formula (4.34) except for the start index of the sum in the denominator of the argument of the arctan function. For $a_0 = 0$ equation (4.37) is equal to (4.34). The factor a_0 should decrease with increasing modulation frequencies in accordance with the a_i.

4.2.5 Experimental setup

Lifetime measurements of praseodymium-doped ZBLAN and IBZP glasses have been performed using the setup shown in Figure 4.14. The same fluorescence spectrometer can be

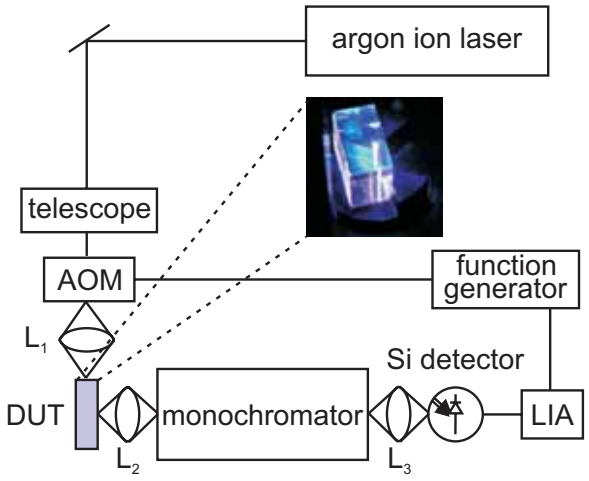

Figure 4.14: Setup of the fluorescence spectrometer for lifetime measurements. The abbreviations are: AOM: acousto-optic modulator, LIA: lock-in amplifier, and DUT: device under test.

used to measure rare-earth-doped fibers. In case of fibers one needs an adjusting element for the incoupling of the free space beam into the fiber core.
The lifetimes of the thermally coupled energy levels $^3P_2$, $^1I_6$, $^3P_1$ and $^3P_0$ of the praseodymium ion have been measured. The $^1I_6$ and $^3P_1$ levels have a considerable overlap in the ground state absorption (GSA) cross section and can be simply referred to as the $^3P_1$ state. The $^3P_0$ level has been pumped with 488 nm argon ion laser light (see energy level diagram in Figure 4.10). The argon laser emits several lines simultaneously. The 488 nm line has been separated which is one of its strongest lines.
Before entering the acousto-optic modulator (AOM) the pump beam is collimated and focused by means of a telescope. The setup differs from the classical setup in the way that an AOM is used instead of a mechanical chopper to modulate the pump signal and thus the excitation. The AOM from Isomet has a fall time of only 2.2 ns which has been four orders of magnitude shorter than the expected lifetime. The reason for using the AOM instead of a mechanical chopper is that a lifetime on the order of some tens of microseconds is expected according to literature values. For the measurement it is of general importance to take care of the AOM frequency and the spot size of the pump beam in the AOM place.
Before entering the monochromator, the pump beam is introduced into the AOM which is located directly in front of the glass sample (device under test (DUT)) to modulate the pump signal and thus the excitation. Besides, the AOM also serves for synchronizing the lock-in amplifier (LIA). In the setup used, the AOM position has been aligned to obtain maximum power in the first order and the modulated beam is used to excite glass samples.
A function generator is used to provide a rectangular modulation function with an amplitude of 5 V which is needed for the AOM driver to modulate an RF signal which then has been applied to the AOM. In a first order approximation, the AOM thus acts like a grating in

transmission. After diffraction the first order has been separated since it contains the largest optical power difference (largest contrast) between turn-off and turn-on state of the pump laser.
The pump beam is focused onto the glass sample by a lens L_1 and the sample is pumped from the top. Hence, the source of the fluorescent light is a glass sample pumped by a laser focused into the sample. It is a cylinder with Gaussian intensity distribution across the diameter. The diameter of the cylinder is considered to be constant across the full length as shown in the attached photograph in Figure 4.14. This is a good approximation if the pump laser is only moderately focused. The light emitted from this cylinder is then collected by another lens L_2, and is imaged onto the entrance slit of a monochromator (Photon Technology International, PTI 01-001). The monochromator is of the Czerny-Turner type with one grating. The monochromator acts as a bandpass filter suppressing large parts of the background noise. The collimating mirrors in the monochromator have a diameter of 50 mm and a focal length of 200 mm. The bandwidth $\Delta\lambda$ of the monochromator is proportional to the slit width w_m and proportional to the inverse focal length f_l of the monochromator mirror and the inverse grating number g (inverse line distance):

$$\Delta\lambda = \frac{w_m}{n \cdot g \cdot f_l}, \tag{4.38}$$

where n is the diffraction order of the beam reflected by the grating. The manufacturer of the monochromator specifies the instrument limit to be reached at a slid width of 0.125 mm. Below this value equation (4.38) is invalid.
The Blaze wavelength of the grating inside the monochromator is 750 nm and the grating showed a number of 1200 lines/mm. The lens L_3 is used to image the exit slit of the monochromator onto the Si detector. The diameter of the detecting area of the Si detector amounts 5 mm. The detected fluorescence signal is then amplified by a transimpedance amplifier and finally the complex FTF measured with the LIA (Signal Recovery Model 5210). Instead of recording the decay curves of the fluorescence by means of a digital storage oscilloscope and exponential fitting as in the classical method, the FTF is recorded by means of an LIA. The LIA can recover signals in the presence of a large noise background and raises the signal-to-noise ratio (SNR). The lifetimes have been measured for the wavelength with maximum fluorescence intensity which is 635 nm (red transition). For comparison the lifetimes for the orange (605 nm), blue (520 nm) and green (490 nm) transitions have also been measured but no significant differences in the measured lifetimes to the lifetime of the red transition have been found. This is due to the thermal coupling of the ^3P_J levels at room temperature. Comparing the position of the maximum fluorescence intensities for ZBLAN and IBZP glasses no significant discrepancy has been observed.
To minimize the probability of a systematic error each glass sample is measured at least three times and used to obtain an arithmetic average value for the lifetimes. All lifetime measurements presented here have been performed at room temperature for two heavy metal fluoride glass compositions (ZBLAN and IBZP) developed and investigated at the Institute. They are

representatives of low phonon energy (LPE) glasses and their names are acronyms built from the first letters of their main components. ZBLAN is based on zirconium fluoride whereas IBZP is based on indium fluoride.

4.2.6 Fabrication of fluoride glasses

To investigate the energy transfer processes in fluoride glasses lifetime measurements have been performed for glasses with different praseodymium and ytterbium concentrations (see table 4.2). The glass samples investigated are Pr^{3+}-doped fluoride glasses, some of them co-doped with Yb^{3+}. The geometrical dimensions of the glass samples used for the lifetime measurements have been measured three times (uncertainty is $\pm$ 0.1 mm) and the arithmetic mean values are collected in table 4.2 along with the actual molar dopant concentration p. The basic composition of both glasses in mol% is as follows:

- ZBLAN:
  53 ZrF_4 - 20 BaF_2 - (3.875-x) LaF_3 - 3 AlF_3 - 17 NaF - 0.125 InF_3 - 2.5 PbF_2 - x PrF_3,

- IBZP:
  (28-x) InF_3 - 14 BaF_2 - 20 ZnF_2 - 16 PbF_2 - 5 YF_3 - 7 AlF_3 - 2 LiF - 8 NaF - x PrF_3.

For the praseodymium doping and ytterbium co-doping, LaF_3 is exchanged by PrF_3 and YbF_3 in case of ZBLAN. In IBZP glass InF_3 is replaced by PrF_3 and YbF_3. The glasses have been prepared by melting ultra pure powders in a platinum crucible under dry nitrogen atmosphere ($H_2O < 1$ ppm) 30 min at 800 °C followed by 30 min at 900 °C for refining. Nitrogen atmosphere ensures an absence of contaminations like e.g. water, hydrogen and hydroxyl radical in the melt. After casting the melt has been poured into a brass mold which is preheated to 260 °C. The glass sample is then cooled down slowly to room temperature. Finally, the samples are polished with diamond paste resulting in high optical quality. Some samples are only polished from four sides, thus not all geometrical dimensions could be measured (see table 4.2). The opposite surfaces are not exactly parallel in order to avoid interference effects. The polished bulk glasses are homogeneous and without crystals or bubbles. The samples are stable under ambient atmosphere including room temperature and did not show any visible alteration of the surface. These compounds show very good optical quality and are very stable against atmospheric moisture. The fluoroindate glass IBZP is characterized by a lower value of phonon energy (about 510 cm^{-1}) than conventional fluorozirconate glasses such as ZBLAN (about 580 cm^{-1}). Thus, fluoroindate glasses are more transparent in the infrared than fluorozirconates and are candidates for the design of efficient fiber lasers and amplifiers. It is obvious that energy transfer becomes significant with increasing dopant concentration. This phenomenon will be explained in the next section.

sample	p mol%	A mm	B mm	C mm
Pr^{3+}:ZBLAN				
Z958	1.050	8.30	11.65	19.30
Z1107	0.191	7.95	14.30	18.80
Z1109	3.000	7.95	14.05	18.80
Z1118	0.112	8.10	15.10	18.50
Z1159	0.220	7.70	14.10	16.70
Z1606	0.010	8.20	17.20	19.90
Z1607	0.030	9.50	17.60	17.60
Z1608	0.300	9.40	18.00	18.20
Z1612	2.000	9.14	16.66	21.12
Z1613	0.500	8.73	17.89	20.55
Pr^{3+}:IBZP				
I546	0.100	8.80	14.55	n.p.
I549	0.300	8.70	14.10	n.p.
I550	1.000	8.95	13.05	15.80
I553	3.000	9.10	12.10	15.70
I555	3.000	9.00	15.00	17.20
I732	0.010	9.00	16.10	18.10
I733	0.030	9.70	15.50	18.50
Pr^{3+}:ZBLAN co-doped with 2 mol% Yb^{3+}				
Z1283	0.300	8.85	16.00	n.p.
Z1473	0.010	7.73	15.23	15.00
Z1474	0.030	8.78	15.30	19.00
Z1475	0.050	8.80	15.95	18.00
Z1615	1.000	8.74	17.94	21.66
Pr^{3+}:IBZP co-doped with 2 mol% Yb^{3+}				
I734	0.010	8.64	15.59	17.35
I735	0.050	8.31	17.54	17.37
I736	0.010	5.95	15.15	24.48
I737	0.050	6.42	16.00	20.18
Pr^{3+}:ZBLAN co-doped with 1 mol% Yb^{3+}				
Z1282	0.300	8.82	15.95	18.15
Z1614	1.000	8.72	17.40	22.35
Z1617	0.010	7.53	17.10	21.30
Z1618	0.050	8.48	16.71	22.95

Table 4.2: Dopant concentrations and dimensions of the glass samples used for lifetime experiments. The dimensions are mean values of three measurements and their uncertainty is ± 0.10 mm (n.p. indicates that the sample is 'not polished').

4.2.7 Concentration quenching

Energy transfer processes which are negligible in glasses with low rare earth ion concentration become more important above a certain dopant ion density. Interactions between two dopant ions (see also section 3.3) are caused by dipole-dipole coupling [109] and two main types of energy transfer processes can be distinguished. One of them is resonant energy transfer between ions of the same dopant and another one is cross relaxation between different dopants. All glass samples investigated here are doped with praseodymium ions and some of them contain ytterbium ions as co-dopant. Thus, both types of energy transfer processes are expected to be observable here. The main consequence of the first process is *concentration quenching*. Increasing the dopant concentration leads to clustering and the critical dopant concentration has been found to be energy level dependent according to literature. Above the critical value the distance between dopant ions is lower which is achieved when the condition

$$W_{et} = A_{rad} + W_{mp} \tag{4.39}$$

is satisfied.
Praseodymium concentration in the investigated glass samples varied from 0.01 to 3 mol%. Afterwards, the lifetimes measured for the red transition $^3P_0 \rightarrow {}^3F_2$ have been fitted using the function

$$\tau_i = \frac{1}{a + b \cdot c_{\text{ion}}^2}, \tag{4.40}$$

where τ_i is the lifetime of the i^{th} energy level, a and b are fit parameters, where a must be on the order of the radiative transition rate (especially for low ion concentrations). c_{ion} is the ion fraction (in mol%, here for PrF_3). The fact that the ion fraction appears quadratic in equation (4.40) is due to interaction between donator and acceptor ion [110]. Expression (4.40) is based on dipole-dipole interaction [109] and can be used to fit the experimental results.

4.2.8 Results and discussion

For each ZBLAN and IBZP glass sample three lifetime measurements have been performed in order to minimize the uncertainties caused by measurement errors. All measurements have been performed at room temperature. The measurement results in conjunction with a fit of these results to equation (4.40) are shown in Figure 4.15. It shows the results from the samples listed in table 4.2. All measurement points are illustrated with their uncertainty which is quite low in all cases showing that the introduced method is highly accurate. The measured lifetimes in both glasses show similar characteristics. As expected, the measured lifetime, which is the result of radiative, non-radiative and energy transfer processes, is larger in ZBLAN compared to IBZP, due to the difference in the multi-phonon energies of both glass types. The difference in the lifetimes for the $^3P_0$ level is relatively small (up to 2 μs within measurement accuracy). The influence of the energy transfer can be observed for higher concentrations, which can be clearly seen in Figure 4.15 in form of a decay of the fit curves.

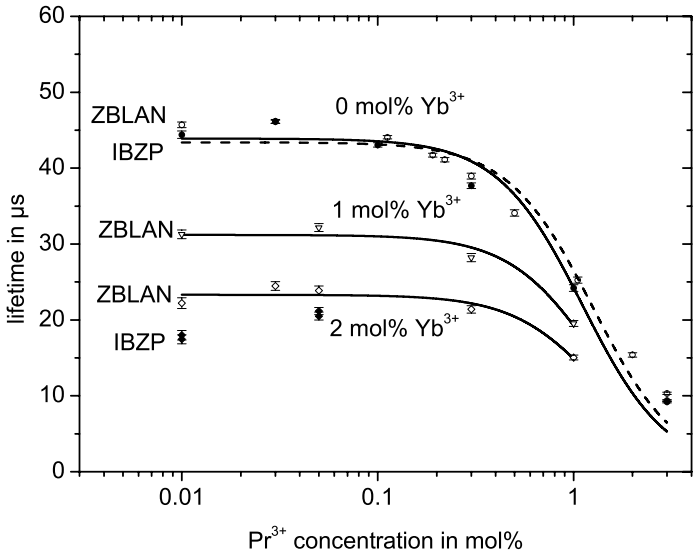

Figure 4.15: Lifetime of the upper energy levels of Pr^{3+} in ZBLAN and IBZP glasses as a function of Pr^{3+} concentration. The circled points represent purely Pr^{3+}-doped glass samples whereas the triangular and diamond points represent 1 mol% and 2 mol% Yb^{3+} used as co-dopant, respectively. In addition, a fit of the lifetime results for the upper four traces to equation (4.40) is shown. Solid and dashed lines are fits for ZBLAN and IBZP glass, respectively.

Because of the high praseodymium concentration, the dipole-dipole interactions depending on the distance between the dopant ions in the host glass become significant which leads to a shortening of the lifetimes. The critical dopant concentration, defined as 10 % reduction of the lifetime, has been found to be approximately 0.1 mol%. With increasing Yb^{3+} concentration the lifetimes become smaller showing that Yb^{3+} additionally quenches the lifetime of Pr^{3+}.
One can deduce the energy transfer efficiency from Pr^{3+} to Yb^{3+} in ZBLAN from the ratio of the upper level lifetimes for a concentration of 0.3 mol% Pr^{3+} typical for Pr^{3+}/Yb^{3+}-doped ZBLAN fiber laser applications. The efficiency increases to 38 % when increasing the Yb^{3+} concentration to 1 mol%. By increasing the Yb^{3+} concentration to 2 mol% the energy transfer efficiency increases to 82 % compared to the purely Pr^{3+}-doped ZBLAN glass. The value of 82 % obtained by these experiments is not in agreement with the value of 56 % indicated in [82]. The difference might be due to different glass compositions and measurement techniques. However, the results indicated here show a large increase in efficiency when doping the Pr^{3+}-doped ZBLAN glass additionally with 2 mol% Yb^{3+}.
The fit of the upper four traces (solid and dashed lines) to equation (4.40) is also shown in Figure 4.15. As can be seen measurement and its fit are in good agreement.
Using the method introduced in section 4.2.4, it has been possible to determine the lifetime of

the $^3P_0$ level for different dopant concentrations in ZBLAN and IBZP glasses. The lifetimes presented have been measured for the red emission line which corresponds to the $^3P_0 \rightarrow {}^3F_2$ transition.
The results obtained are comparable to others reported in the literature [12, 89, 98, 111]. Orange and blue transitions have been used to determine the lifetimes as well. These measurements delivered the same results as for the red transition (a prism has been used to select the desired argon laser line and the monochromator has been adjusted for the respective emission wavelength). In addition, the green transition has been used to determine the lifetime of the $^3P_1$ level and, in this case, the results show again the same values as for the $^3P_0$ level. The reason for this lies in the fact that the upper energy levels (especially the neighbored $^3P_1$ and $^3P_0$ levels) of the triply ionized praseodymium ion are strongly thermally coupled at room temperature. The lifetimes for ZBLAN and IBZP glass are very similar but the lifetime of IBZP is a little shorter. The lifetime depends on the content of Pr^{3+} ions. An increase of the dopant concentration from 0.1 mol% to 1 mol% reduces the lifetime by half. This plays an essential role for selecting the dopant concentration in a laser design. In that context the fluorescent lifetimes should be taken into account.
For both host glasses, the lifetime dependence on concentration is very similar and the traces run nearly parallel. The shortening of the lifetime with increasing dopant concentration is known as concentration quenching. Quenching can also arise from the fact that, in high concentration samples, the excitation can migrate from one ion to another one and thus shows a higher probability of encountering a quenching center where a local phonon or deformation can deactivate the excitation. This is obviously the case for the co-doping with ytterbium ions. Quenching mainly arises due to ion interaction (see also section 3.3.3) between Pr^{3+} ions described in detail in [112]. An ion in the excited state interacts with another neighboring ion in the ground state with the result that both ions end up in some intermediate states, thereby quenching the fluorescence from the excited state. For ion concentrations which are sufficiently low and thus in case of negligible ion-ion interaction, the measured lifetimes should follow directly from the sum of the radiative and non-radiative rates and should be independent of dopant concentration. A low concentration of 0.1 mol% Pr^{3+} is reported as boundary concentration [113] because above, quenching is usually observed. This is also observed by the experiments performed. Consequently, all glass samples used are subject to quenching. It has been determined that in glass samples with concentrations below 0.1 mol% quenching is not that significant and thus dopant concentration does not influence the lifetime.

4.2.9 Summary

The total lifetime of the energy levels is one of the parameters characterizing the host-dopant system. For a low dopant concentration it is determined by the radiative lifetime. However, for higher concentrations energy transfer processes and multi-phonon relaxation strongly influence the total lifetime leading to its shortening. In this section, an FTF method has been introduced to measure fluorescent lifetimes of rare-earth-doped glasses and fibers. The method

has been applied to measure the phase of the complex FTF. Alternatives, like extracting the lifetimes from the measured amplitude of the complex FTF are presented in appendix B.
In addition, the lifetimes of the upper energy levels of praseodymium in fluoride glasses have been measured and the influence of ytterbium ions as co-dopant has been investigated. Lifetimes in the range between 9 μs to 46 μs dependent on the Pr^{3+} concentration have been observed. The critical dopant concentration leading to concentration quenching is found to be approximately 0.1 mol%. Below it the lifetimes of purely Pr^{3+}-doped glasses remained almost constant to about 45 μs. Increasing the concentration to 3 mol% led to lifetimes of less than 10 μs. Yb^{3+} as co-dopant leads to an additional decrease of the lifetime. The critical dopant concentration seems to remain unchanged to 0.1 mol% Pr^{3+} concentration independent of the Yb^{3+} concentration. In case of 1 and 2 mol% Yb^{3+} concentration the lifetimes of Pr^{3+} are in the range of 15 to 32 μs. Furthermore, the results indicated here show in case of ZBLAN a large increase in efficiency when doping the Pr^{3+}-doped ZBLAN glass additionally with Yb^{3+}. For a 0.3 mol% Pr^{3+}-doped ZBLAN glass an addition of 1 mol% Yb^{3+} leads to an increase of 38 % in energy transfer efficiency. By increasing the Yb^{3+} concentration to 2 mol% efficiency increases to 82 %.
The measurements have been performed for two glass types and it has been the author's goal to find whether the IBZP or the ZBLAN glass is a more suitable host for praseodymium-doped fiber lasers operating in the visible range. It can be concluded that it is not expected that IBZP glass is a much better host glass for praseodymium-doped fiber lasers than the usual ZBLAN glass regarding the lifetimes measured for the upper levels. Concentration quenching when measuring the lifetime of the ^3P_J levels of praseodymium-doped fluorozirconate and fluoroindate glasses has been observed.

4.3 Further spectroscopic parameters of Pr^{3+}-doped ZBLAN glasses

Laser and amplifier performance depends strongly on the absorption and emission properties of the dopant in the host glass system. Hence, measuring these properties is helpful for finding an optimum host glass. However, praseodymium-doped ZBLAN and IBZP glasses showed similar behavior in their fluorescent lifetimes. Besides, it had not been possible to draw fluoride fibers from the IBZP preform which could be used for fiber laser or amplifier design. Thus, in this section the absorbtion and emission cross sections of praseodymium-doped ZBLAN glasses are presented which will be used as input parameters for the simulation models in chapters 5 and 6. All spectroscopic measurements presented here were performed at room temperature.

4.3.1 Spectral behavior of the refractive index

The refractive index spectrum is an important quantity of a glass material. The changes in refractive indices can be fitted using the Cauchy formula [110]. However, for the simulations in chapters 5 and 6, the Cauchy fit does not play a big role as long as one is interested in

qualitative and not quantitative analysis. Hence, a mean refractive index has been assumed in the respective wavelength region for the laser simulations which will be carried out in chapters 5 and 6. Nevertheless, the measurement results which are presented here make use of the Cauchy fit.

4.3.2 Intrinsic losses of fluoride glasses

The transmission bandwidth of the glass matrix is one of the basic spectroscopic parameters, which supports information about the characteristic attenuation of the glass and its UV and IR absorption edges. It is obvious, that a decrease in the phonon energy, which is the case in IBZP compared to ZBLAN, causes a red shift in the IR absorption edge.
The basic attenuation curve of any glass sample follows the simplified relation [62]:

$$\alpha = A \cdot \exp\left(\frac{a}{\lambda}\right) + \frac{B}{\lambda^4} + C \cdot \exp\left(-\frac{c}{\lambda}\right), \tag{4.41}$$

where A, a, B, C, and c are the material parameters and λ is the wavelength. The first term in the equation corresponds to the absorption caused by electron transitions from the valence band to the conduction band, which occurs for highly energetic excitations (in the UV range). The second term describes the attenuation due to the Rayleigh backscattering, and it is present in the whole transparency band. The third term formalizes the absorption due to matrix vibration in the glass sample. Since IBZP is supposed to have lower phonon energy, one can expect that this glass is transparent for longer wavelengths compared to ZBLAN.
Furthermore, a constant attenuation for the laser simulation over the respective wavelength region has been assumed. The assumed attenuation losses cover intrinsic as well as extrinsic losses and have been measured for praseodymium-doped ZBLAN fibers in [14].

4.3.3 Transition cross section

Cross sections quantify the ability of an ion to absorb and emit light. The cross section of a particular transition between two states of an ion represents the probability for that transition to occur with the concurrent emission or absorption of light. Given two states, 1 and 2, with respective energies E_1 and E_2 ($E_2 > E_1$), the transition probability for the absorption of a photon of energy $E_2 - E_1$ is proportional to the cross section σ_{12} and that for the emission of a photon is proportional to the emission cross section σ_{21}. The dimension of the cross section is an area. The absorption cross section can be thought of as a sort of target area that can intercept a light flux by catching the photons that flow through it. The emission probability has an analogous interpretation. It should be noted that the emission and absorption probabilities are proportional to the light intensity, not to its power. The smaller the area on which the light is concentrated, the higher the probability for emission or absorption of light [8].
For two non-degenerate states 1 and 2, the absorption and emission cross sections will be equal: $\sigma_{12} = \sigma_{21}$. Complications arise in case of rare earth ions in solids because the absorption and emission cross sections are different. The reason for this lies in the fact that, in case

of rare earth ions, these two states are in reality a set of Stark sublevels.
The spectral shape of measured emission and absorption cross sections for transitions between two manifolds will be different since they depend on thermal population in the various sublevels. The difference between physical and measured cross sections must be emphasized within this context. In the latter a convolution occurs in the way that some transitions might not be separated uniquely. This depends on Boltzmann probability of the population of the respective energy levels. The cross sections that are derived from an experiment yield the effective spectral absorption and emission strength for a given transition of an ion. They are usually needed to actually model and predict the performance of a laser or an amplifier. The key issue is how to correctly extract the emission and absorption cross section from measured absorption and fluorescence spectra.
Absorption and emission of light in a degenerate two-level system will be examined, where level 1 has degeneracy g_1 and level 2 has degeneracy g_2. The transition lines have a finite linewidth and are characterized by a normalized lineshape function $g_{ij}(\nu)$. The absorption cross section at a frequency ν for a broadened line is defined as [8]:

$$\sigma_{12}(\nu) = \frac{h \cdot \nu \cdot n}{c_0} \cdot B_{12} \cdot g_{12}(\nu) = \frac{h}{\lambda} \cdot B_{12} \cdot g_{12}(\nu), \tag{4.42}$$

where B_{12} is the coupling constant of radiation and matter for the absorption process (Einstein coefficient) and n is the refractive index of the medium. A similar definition for the emission cross section is:

$$\sigma_{21}(\nu) = \frac{h \cdot \nu \cdot n}{c_0} \cdot B_{21} \cdot g_{21}(\nu) = \frac{h}{\lambda} \cdot B_{21} \cdot g_{21}(\nu), \tag{4.43}$$

where B_{21} is the coupling constant for the stimulated emission process (Einstein coefficient). The transition lineshape function $g_{ij}(\nu)$ (i and j represent energy levels) is normalized by:

$$\int g_{ij}(\nu)\mathrm{d}\nu = 1, \tag{4.44}$$

where the integral spans the full spectrum of the transition line.
Furthermore, if one inserts equation (1.13) into (4.42) and (4.43), one gets formulae called the *Fuchtbauer-Ladenburg equations* [15]. Thus the absorption and emission cross sections may be written as follows:

$$\sigma_{12}(\nu) = \frac{g_2}{g_1} \cdot \frac{\lambda_0^2}{8\pi \cdot n^2} \cdot A_{21} \cdot g_{12}(\nu), \tag{4.45}$$

and

$$\sigma_{21}(\nu) = \frac{c_0^2}{8\pi \cdot n^2 \cdot \nu_0^2} \cdot A_{21} \cdot g_{21}(\nu). \tag{4.46}$$

The peak wavelength and frequency of the transition are λ_0 and ν_0, respectively. This last equation allows a normalized emission spectrum $g_{21}(\nu)$ to be scaled to the spectral emission cross section by using the calculated emission rate A_{21}. This is very important, because

absolute emission spectra are difficult to obtain. The analogue equation for the GSA cross section is less useful, since the GSA cross section, in contradiction to ESA cross section, can be measured exactly by spectral attenuation measurement in a known length of material.
The McCumber theory provides another method of transformation between the absorption and emission cross section. This is the main difference to the Fuchtbauer-Ladenburg equations where the spontaneous emission cross section is linked to the stimulated emission cross section by only a constant factor (see expressions in chapter 1). The key assumption needed by the McCumber theory is that the time required to establish thermal equilibrium within each manifold is shorter compared to the lifetime of that manifold. The McCumber theory to determine ESA cross sections from emission spectroscopy will be explained in more detail in the following.
In principle, emission spectra of most electronic transitions of a rare earth ion can be obtained if a suitable pump source is available. Measurements of ESAs are considerably more difficult. Thus, it would be a great help to be able to calculate ESA cross sections from the appropriate emission spectra.
McCumber calculated these cross sections accounting for the position and occupation probability due to Boltzmann statistics for each Stark level [114, 115]. His result is

$$\sigma_{abs}(\lambda) = \sigma_{emi}(\lambda) \cdot \exp\left(\frac{\frac{h \cdot c_0}{\lambda} - \overline{\Delta E}}{k_B T}\right), \tag{4.47}$$

where k_B is Boltzmann's constant, T the absolute temperature, and $\overline{\Delta E}$ the free net energy required for an excitation from one Stark level of one multiplet to a Stark level of another multiplet.
The McCumber theory is mainly used to calculate the emission cross section in erbium-doped glasses. In case of other rare earth ions it is likely that the relative magnitude of emission and absorption cross sections might become heavily over- or under-estimated. Additionally, negative values for the cross sections may arise due to rounding errors of the exponential function. These values must be clipped to zero for fiber laser simulations (see chapters 5 and 6) as they are usually very small. The relation between energy E and wavenumber k is given by

$$E = h \cdot \nu = h \cdot \frac{c_0}{\lambda} = h \cdot c_0 \cdot k,$$

where c_0 and h are the speed of light in vacuum and Planck's constant, respectively. One finds the following equation for the ratio of energy change ΔE and the photon energy $k_B \cdot T$:

$$\frac{\Delta E}{k_B \cdot T} = \frac{h \cdot c_0}{k_B \cdot T} \cdot \Delta k,$$

which is quite useful in spectroscopic relations.
The oscillator strength of a transition is proportional to the area below the appropriate

absorption line and is given by

$$f_{ij} = \frac{4\pi \cdot \epsilon_0}{e^2} \cdot \frac{m_e \cdot c_0^2}{\pi \cdot \lambda_0^2} \int \sigma_{ij}(\lambda) \mathrm{d}\lambda, \tag{4.48}$$

with the dielectric constant ϵ_0, the electron mass m_e, the speed of light in vacuum c_0 and the electron charge e. Unfortunately, there is some confusion in the literature about this equation which appears in several forms. Connected with the area below the absorption line is the center wavelength λ_0 which divides the area into two equal parts.
The integrated intensities of transitions of rare earth ions can also be obtained using the Judd-Ofelt theory [101, 102]. The intensity of a transition between two states is often characterized by its oscillator strength. The electric dipole contribution to the oscillator strength f_{ed} for a transition between levels i and j is given in the Judd-Ofelt theory as [105]:

$$f_{ed} = \frac{8\pi^2 m_e \nu \chi_{ed}}{3h(2J_i+1)} \sum_{\lambda=2,4,6} \Omega_\lambda \left| \langle i \| \mathbf{U}^{(\lambda)} \| f \rangle \right|^2 , \tag{4.49}$$

where m_e is the electron mass, ν is the frequency of the transition, h is Planck's constant and J_i is the quantum number of the total angular momentum of the initial state. The dielectric correction factor χ_{ed} is $n(n^2+2)^2/9$ for spontaneous emissions and $(n^2+2)^2/9n$ for absorptions and stimulated emissions, where n is the refractive index of the host material. The second factor in the sum besides the Judd-Ofelt parameter is the squared reduced matrix element of the unit tensor operator $U^{(\lambda)}$ of rank λ between the initial state i and the final state f.
The three terms $\langle i \| \mathbf{U}^{(\lambda)} \| f \rangle$ are the reduced matrix elements calculated in the intermediate coupling approximation. The Judd-Ofelt parameters Ω_2, Ω_4 and Ω_6 are material parameters. They parameterize the oscillator strength for the transition between various multiplets and are usually calculated to provide the best fit to the experimental data obtained by GSA. The whole procedure is described in [15]. These three parameters are then used to calculate the electric dipole oscillator strength between any states and lead, for instance, to the values of ESAs or stimulated emission cross sections. Except for the case of the so-called hypersensitive transitions, this is a good phenomenological model. The Judd-Ofelt analysis is accurate to about 10 to 15 %, although errors on the order of 50 % have been found in certain cases.
From the oscillator strength one can calculate the transition rates for a spontaneous radiative transition from an initial manifold i to a final manifold j using the following equation [103]:

$$A_{ij} = \frac{2\pi\nu^2 e^2}{\epsilon_0 m_e c_0^3} f_{ij}. \tag{4.50}$$

It is noted that f_{ed} is labeled as f_{ij} within this context. The radiative lifetime of an excited level i is given by the sum of all transition probabilities:

$$\tau_{i,rad} = \frac{1}{\sum_j A_{ij}}. \tag{4.51}$$

The luminescence branching ratios β_{ij} are calculated for the transition $i \rightarrow j$ with the following formula:

$$\beta_{ij} = \frac{A_{ij}}{\sum_j A_{ij}} = A_{ij} \cdot \tau_{i,rad}, \tag{4.52}$$

which indicates relative intensities of transition from an excited level to all terminated levels. The sum over all possible channels must be $\sum_j \beta_{ij} = 1$. The branching ratio has an important influence on the performance of a device based on a particular transition. It has a significant effect on the threshold of a laser.

Although the Judd-Ofelt theory is successful for most rare-earth-doped materials, it is well known that its application to Pr^{3+} suffers from several problems. First, large deviations between calculation and experimental data are observed in literature, and a difficulty to fit the $^3H_4 \rightarrow {}^3P_2$ hypersensitive transition is noticed. Moreover, a negative Ω_2 is sometimes obtained, a case which is impossible within the framework of the Judd-Ofelt theory [106]. This problem has already been explained above and the solution is a new assignment in the linear optimization problem to obtain the Judd-Ofelt parameters [15].

4.3.4 GSA measurements

After presenting theoretical issues, results of spectroscopic investigations for Pr^{3+}-doped ZBLAN glasses are presented. The measurement setup and the principle are in detail described in [15]. In the following only the basic issues are described.
Regardless of the spectrometer used, the absorption measurement has to be done in two steps. First, the reference spectrum $I_0(\lambda)$ without a sample has to be measured. This step allows to determine the spectral characteristics of the light source and of all other optical components in the setup. In the second step, the spectrum $I(\lambda)$ with the glass sample inserted has to be obtained. Using these two measurements the transmission of the sample may be calculated by:

$$T(\lambda) = \frac{I(\lambda)}{I_0(\lambda)}. \tag{4.53}$$

The absolute attenuation spectrum is given by:

$$\alpha_{\text{abs}}(\lambda) = -\ln\left(T(\lambda)\right) = \ln\left(\frac{I_0(\lambda)}{I(\lambda)}\right). \tag{4.54}$$

The measurements of the glass samples include not only the raw absorption spectra, but also an attenuation caused by the host glass and Fresnel reflections from both surfaces of the glass. Since one is only interested in the rare earth dopant and not in the properties of the glass host a baseline correction of each spectrum has to be performed [15]. First, each spectrum has to be split into pieces, each containing an individual absorption line or a group of overlapping

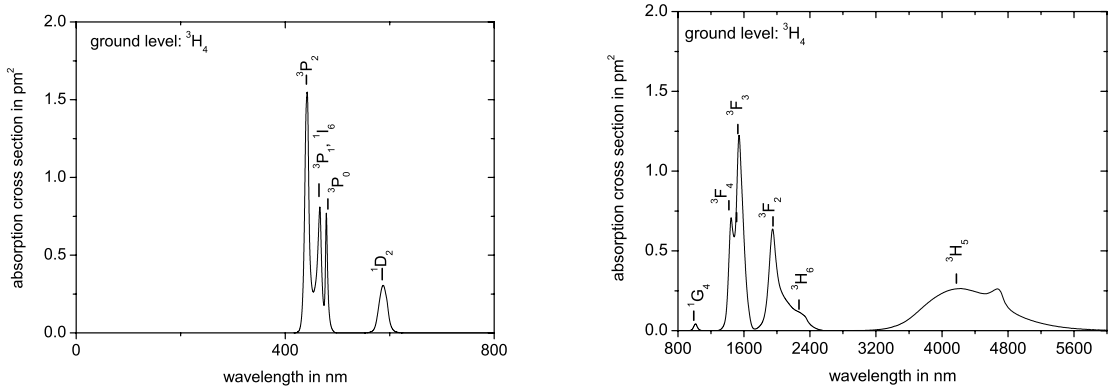

Figure 4.16: Spectrum of the ground state absorption cross section for Pr^{3+}:ZBLAN [15]

lines. Then the baseline correction has to be done. In the next step, the absorption cross section has to be estimated from the corrected spectra using the following equation [15]:

$$\sigma_{\mathrm{abs}}(\lambda) = \frac{\alpha_{\mathrm{abs}}(\lambda)}{l \cdot \gamma \cdot c_{mol}}, \tag{4.55}$$

where l is the length of the sample and c_{mol} the molar concentration. The conversion factor γ is given by:

$$\gamma = \frac{\rho \cdot N_A}{M}, \tag{4.56}$$

where ρ is the mass density, N_A is Avogadro's constant and M the molar mass of the glass composition.
Results of spectroscopic measurements are in general presented in wavenumbers k scaled in cm^{-1}. A wavelength in nm can be converted into a wavenumber by:

$$k \quad \text{in cm}^{-1} = \frac{10^7}{\lambda \quad \text{in nm}}. \tag{4.57}$$

Thus, the wavenumber is the inverse of the wavelength. All measurement results are shown in wavelengths here since for fiber laser and amplifier simulations the wavelength is used for parametrization. However, it should be noted that also wavenumbers or optical frequencies may be used for parametrization without changing the simulation models in chapters 5 and 6. The results of the calculation [15] of the absorption cross section from the ground level $^3H_4$ to higher levels are shown in Figure 4.16. The $^1G_4$ level is the pump level of the praseodymium-doped fiber amplifier operating at 1.3 μm, and this weak absorption is one of the major problems of this amplifier [21]. The transition to level $^3H_5$ shows two peaks which are related to three groups of Stark levels [15]. Level $^3H_6$ shows no separate peak, because the $^3F_2$ line

is larger. The reason for this lies in the oscillator strength assigned to the $^3H_6$ level which is a factor of 3.8 smaller than that assigned to the $^3F_2$ level [15]. There are three particularly interesting absorption peaks grouped near 450 nm (22200 cm^{-1}) which correspond to the $^3P_2$, $^3P_1$, $^1I_6$ and $^3P_0$ multiplets. This broad and strong absorption band absorbs the blue part of the visible spectrum, and it plays an important role for a blue laser line. In addition, it leads to the dark green color of praseodymium-doped glass samples. The $^3P_1$ and $^1I_6$ levels have a considerable overlap and thus it is hardly possible to split these two levels. They can be simply referred to as the $^3P_1$ state. The absorption band position and its relative intensities agree with previous reports on Pr^{3+} ions in other fluoride glasses [90].
It is noted that before inserting these results into the simulation model, all absorption lines which include at least two transitions have been well separated using multiple Gauss fits. The whole procedure is described in detail in appendix C.

4.3.5 ESA measurements

In the previous section, the absorption from the ground state (GSA) has been discussed, but an ESA in the Pr^{3+} laser system is also of interest. This is an undesirable process if the signal light is absorbed from the upper level instead of being amplified, whereas it is a desirable process if used for stepwise pumping of the upper level. In the investigated case, the absorption from the excited state $^1G_4$ to the ^3P_J levels plays an important role in the avalanche upconversion pumping process (see section 3.3.3), and it is only concentrated on this transition. ESA spectra are usually obtained using a pump-probe technique in which the transmission of a tunable probe beam is monitored while the upper level population is modulated by chopping the pump beam. The authors in [19] proposed a new technique. In order to determine the ESA spectrum, the fluorescence from $^3P_0$ to $^1G_4$ as well as the fluorescence from the thermally populated $^3P_1$ and $^1I_6$ levels was measured around 900 nm. The $^3P_0$ level was pumped with 488 nm argon laser light.
The McCumber theory (see section 4.3.3) was then used to calculate the ESA spectrum from the measured fluorescence, and the results of this procedure are shown in Figure 4.17. The ESA spectrum shows a peak at a wavelength of 842 nm which is in good agreement to reports of 835 nm in [17] and 845 nm in [23] as the optimum wavelength for upconversion pumping in visible Pr^{3+}:ZBLAN lasers. This method may determine ESA band profiles more reliably than absolute magnitudes.
In [14] the optimum pump wavelength was found around 840 nm. However, there it was also reported that pump wavelength changes from 830 nm to 850 nm cause intensity deviations of only about 10 %. A pump wavelength of 835 nm has been taken for the laser simulations in chapters 5 and 6, as this value is often mentioned as optimum pump wavelength for Pr^{3+}/Yb^{3+}:ZBLAN fiber lasers.

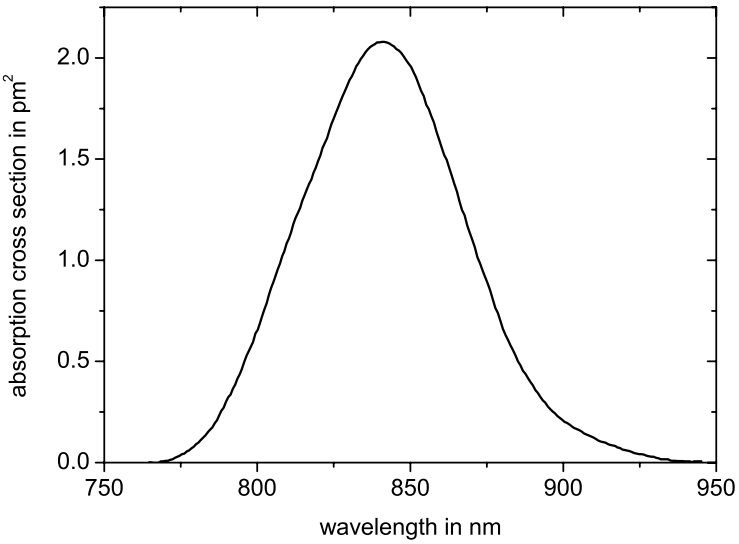

Figure 4.17: ESA cross section spectrum for the $^1G_4 \rightarrow ^3P_J$ transition [19]

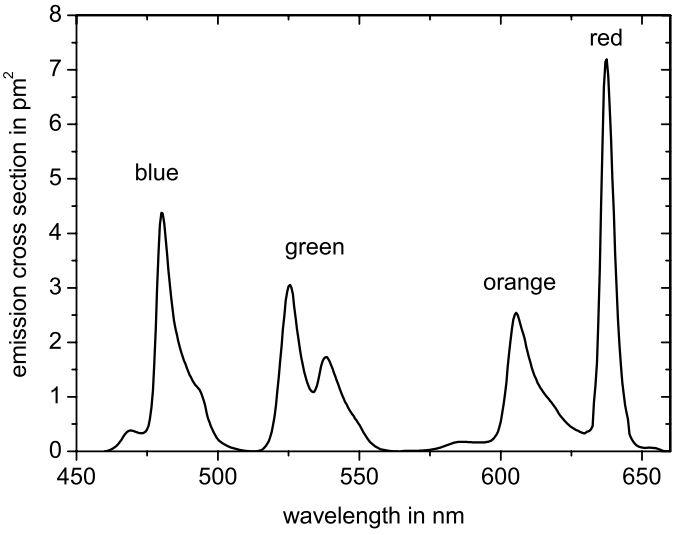

Figure 4.18: Spectrum of the emission cross section for Pr^{3+}/Yb^{3+}:ZBLAN [14]

4.3.6 Emission measurements

The knowledge of possible emission lines is of great importance for designing laser systems. For emission measurements, a fluorescence spectrometer has been used, whose setup is quite

similar to the lifetime measurement setup shown in Figure 4.14. The setup and the measurement principle are described in detail in [14, 15]. In this section, the results of these measurements are shown which will be used as input parameters for the laser simulation models that will be developed in the next two chapters. Before doing this the basic principle is briefly discussed.
Emission spectroscopy is somewhat more difficult than absorption measurements. Instead of absorption measurements, fluorescence spectroscopy delivers unscaled intensity spectra. The drawback of such a one-way measurement is the fact that spectral responses of all optical parts are contained in the measurement results. In reality, the spectrum measured $I_M(\lambda)$ is the real spectrum $I_R(\lambda)$ multiplied by some transition function $T(\lambda)$:

$$I_M(\lambda) = I_R(\lambda) \cdot T(\lambda). \tag{4.58}$$

The transition function describes the spectral characteristics of all optical elements used in the setup. In order to obtain the real spectrum, one has to divide the spectrum measured by $T(\lambda)$. However, first one has to know this function. To determine it, one needs a calibrated light source, e.g. a light source with a well known spectral characteristic $I_{CR}(\lambda)$. The calibrated light source is used instead of the fluorescent glass sample, and the spectrum of this light source $I_{CM}(\lambda)$ is measured. Knowing these two spectra, one can determine $T(\lambda)$ by

$$T(\lambda) = \frac{I_{CM}(\lambda)}{I_{CR}(\lambda)}. \tag{4.59}$$

Hence, one can obtain a correct fluorescence spectrum from the glass sample measured. A 100 W halogen lamp HLX 64342 from OSRAM has been used, driven with 6.3 A from a stabilized current source. The spectral response $I_{CR}(\lambda)$ of this lamp has been measured in the German Institute of Standards (PTB) [14]. Sources like the halogen lamp have blackbody-like emission spectra, and the spectral intensity of such a radiation source is given by

$$I(\lambda) = \frac{A}{\lambda^5} \cdot \frac{1}{\exp\left(\frac{h \cdot c}{\lambda \cdot k_B \cdot T}\right) - 1}, \tag{4.60}$$

where k_B is Boltzmann's constant. This expression has been used to fit $I_{CR}(\lambda)$ with the fit parameters A and T. Since one knows the real $I_{CR}(\lambda)$ and the measured $I_{CM}(\lambda)$ spectrum of the calibrated lamp, $T(\lambda)$ can be calculated using equation (4.59). Thus, one is able to determine the correct fluorescence spectrum $I_R(\lambda)$ by dividing the spectrum measured $I_M(\lambda)$ with the assigned transition function $T(\lambda)$.
Even corrected emission spectra are still relative spectra, because a sample emits in all directions in contrast to absorption measurements where the intensity of a transmitted radiation beam is measured. Therefore, the Fuchtbauer-Ladenburg equation (4.46) has been used in conjunction with the calculated radiative spontaneous emission rate A_{21} to scale the measured lineshape $g_{21}(k)$ of a transition to a cross section spectrum [15]:

$$\sigma_{21}(k) = \frac{1}{8\pi \cdot c_0 \cdot k_{cm}^2 \cdot n^2} \cdot A_{21} \cdot g_{21}(k). \tag{4.61}$$

In equation (4.46), the frequency ν has been replaced by the wavenumber $k = \nu/c_0$, and the lineshape $g_{21}(k)$, due to the different normalization $\int g_{21}(k)\mathrm{d}k = 1$, has the dimension of an inverse wavenumber in contrast to $g_{21}(\nu)$. Therefore, a factor c_0 is introduced. In appendix C, the Ladenburg-Fuchtbauer equation is indicated when transforming from frequency- or wavenumber-domain to wavelength-domain. The center of mass wavenumber k_{cm} divides the area into two equal parts:

$$\int_{-\infty}^{k_{cm}} g_{21}\mathrm{d}k = \int_{k_{cm}}^{\infty} g_{21}\mathrm{d}k. \tag{4.62}$$

The refractive index n has to be taken from a Cauchy fit (see section 4.3.1). The values of the radiative spontaneous emission rate A_{21} for particular transitions have been taken from [15]. The measurement results are shown in Figure 4.18.
The emission wavelengths and emission cross section values are comparable with previous reports on Pr^{3+} ions in fluoride glasses [24, 116, 117]. Fluorescence properties and emission cross sections of Pr^{3+}-doped glasses were quite often presented in literature [22, 89, 91, 116–121]. Bayer presented time-resolved emission spectroscopy of Pr^{3+}-doped fluoride glasses [122]. The emission cross sections obtained are large and indicate that the Pr^{3+}-doped ZBLAN glass is a good laser material in the visible region. The fluorescence properties of Pr^{3+}-doped fluoride glasses are dependent on the glass composition. The red line in ZBLAN glass is clearly dominant, and consequently, the red laser is simple to excite. Nevertheless, laser mirrors have to be selected very carefully if a laser emission other then red is required. The mirrors should have a reflection as small as possible in the red range.
It is noted that before inserting these results into the simulation model, all emission lines which include at least two transition have been well separated using multiple Gauss fits. The whole procedure is in detail described in appendix C.

4.4 Summary

In this chapter some properties of thulium-doped fluoride fibers used for fiber amplifier applications and of praseodymium-doped fluoride glasses for fiber laser applications have been discussed in detail. The active thulium fiber has been spatially characterized by C-OFDR. Then an *FTF method* has been presented and used to measure the fluorescent lifetimes of praseodymium-doped fluoride glasses. Some of these fluoride glasses have been co-doped with ytterbium. In the last section some important spectroscopic parameters of Pr^{3+} in ZBLAN glass have been presented. These parameters will be used for fiber laser simulation in chapters 5 and 6.

5 Stationary model for rare-earth-doped fiber lasers and amplifiers

In the last chapter parameters of rare-earth-doped fibers and glasses have been determined with several different measurement techniques. Now, the author has arrived at the final steps of his work and uses the results of spectroscopic investigations of rare-earth-doped glasses to simulate fiber lasers in stationary and transient states with the possibility to include energy transfer processes between two different rare earth ions. The goal of these two final chapters is to provide a simple simulation model which is applicable for arbitrary rare-earth-doped fiber lasers and amplifiers in a variety of configurations.
In this chapter, a stationary model for the simulation of arbitrary rare-earth-doped fiber lasers and amplifiers [15] is presented. The model is applicable for a rare earth ion as dopant in lasers and amplifiers. Maxwell-Boltzmann statistics for thermally coupled energy levels is applied in combination with a novel approach to fix the usually unknown values of non-radiative transition rates for the simulations. The model is applied to the simulation of an ytterbium-doped and a praseodymium-doped fiber laser in order to optimize the output power of both lasers.
Moreover, the model is extended to simulate energy transfer processes in rare-earth-doped devices co-doped with different rare earth ions. The model is applicable for arbitrary lasers and amplifiers in steady-state and cross relaxation between two different rare earth ions is taken into account. Finally, red, orange and blue laser characteristics of a Pr^{3+}/Yb^{3+}-doped ZBLAN fiber laser are simulated. The laser is optimized with regard to output power and a comparison to the simulated Pr^{3+}-doped fiber laser is performed.

5.1 Introduction

Simulations are an important step in the laser and amplifier development process. They allow to reduce the costs of experiments and help to create devices fulfilling the initial requirements of the developer or customer. In some cases, the information about advisable fiber parameters (like rare earth doping, core diameter or numerical aperture) gathered from simulations can be used as a feedback in the fiber manufacturing process. On the other hand, different aspects of laser and amplifier performance and the way how they influence laser or amplifier operation could be explained by simulation results.
Several numerical rare-earth-doped fiber laser and amplifier models have already been presented in literature [72, 123–129], mostly for thulium-, erbium- or praseodymium-doped fiber amplifiers (TDFA, EDFA or PDFA) or lasers (TDFL, EDFL or PDFL) based on silica and fluoride glasses, respectively. The model in [123] is a simplified monochromatic model of a four-level TDFA simulating stationary and transient states. [124] also presents a model for

the stationary and dynamic simulation of TDFAs but it merely considers three energy levels. Runge-Kutta methods are used to find a numerical solution. In [126] four theoretical models for EDFLs based on silica are presented, all assuming only a few energy levels and some significant simplifications. For the erbium-doped fiber amplifier (EDFA) it was shown that the best match between measurement and simulation can be achieved by applying the Giles model [127], which provides a full spectral solution. The propagation equations are integrated back and forth along the fiber until the solution converges. It provides a highly accurate solution of the rate equations (assuming a two-level system), but it takes longer computing time and thus this model is to be used for very accurate calculations only. A three-level model for the cw operation of EDFLs in ring configuration was given in [128] using an iterative Runge-Kutta method to find a solution. Karasek presented a model for a tunable PDFL in ring configuration which considers four energy levels [129]. The iterative solution is found by the modified Euler method.

Most numerical models presented in the literature are based on rate and gain equations but they significantly differ in their complexity. For some models the gain equations are replaced by propagation or complex field equations. To shorten the computing time, some models neglect the amplified spontaneous emission (ASE) or do not consider the excited state absorption (ESA). Morkel showed a model for a two-level EDFA under consideration of ESA [130]. Nevertheless, simulation results based on such a simplified model cannot fully describe the somehow complex operation of rare-earth-doped fiber lasers or amplifiers.

On the other hand, many analytical models have been developed to find analytical expressions for gain and noise in case of amplifiers, or for threshold power, output power and slope efficiency in case of fiber lasers [18, 131–133], all applying in case of specific rare earth ions and considering a maximum of four relevant energy levels. An analytical model for a three-level ytterbium-doped fiber amplifier was developed in 2002 [134] with several simplifying assumptions. Selvakennedy developed a very simple two-level model for transient and stationary states of EDFLs in ring configuration [135]. The solution was found by relaxation methods. It is an easy and quick model due to the fact that only a few parameters such as attenuation or gain are needed.

None of the models found in the literature comprise thermally coupled energy levels. In all cases many energy levels of the rare earth ions in their respective glass hosts have been neglected. All in all, none of these publications presented general numerical models for arbitrary rare-earth-doped fiber lasers and amplifiers. Many assumptions have been made and some of these models have been too simplified to accurately simulate specific features of lasers or amplifiers. Analytical models and general theory for two-, three- and four-level amplifiers and lasers have quite often been presented in the literature [136–140]. Barnard gave analytical expressions for three- and four-level devices in Fabry-Perot and ring configuration under several assumptions [140]. These expressions are invalid for arbitrary rare-earth-doped fiber lasers or amplifiers but only for a few rare earth ions such as erbium, neodymium, thulium, praseodymium and ytterbium [140].

Recently, Calo presented an interesting approach to simulate photonic crystal EDFAs [141].

He used genetic algorithms as an alternative to rate and gain equations. However, this approach seems to be too sophisticated, especially when trying to formulate a model for arbitrary rare-earth-doped fiber lasers and amplifiers.
The goal of this chapter is to present a simple numerical model which can be applied to arbitrary rare earth ions to simulate lasers and amplifiers in a variety of configurations. It considers the effect of thermally coupled energy levels by a novel approach to fix the values of non-radiative transitions.
Another advantage of the model is that pump, signal, and ESA wavelength do not have to be modeled separately. Instead, only pump powers and wavelength range have to be provided before the simulation starts.
It is obvious, that the performance of lasers and amplifiers depends on the parameters of passive components to a certain degree . They can slightly modify the gain spectrum or change the output signal power, but the lasing respectively amplification occurs in the active fiber. Therefore the core of the model, which will be presented here, is a mathematical description of the rare-earth-doped fiber, only.
This chapter starts with a section about general fiber laser and amplifier operation to make the practical and theoretical background clear. Then the simulation parameters needed are summarized. Moreover, an approach for fixing the usually unknown non-radiative transition rates and taking into account Maxwell-Boltzmann statistics for thermally coupled energy levels is given in section 5.3.2. The discrete mathematical notation for the numerical model and the simulation algorithm will be presented in sections 5.4.1 and 5.4.2. Finally, in sections 5.5.1 and 5.5.2 the simulation model developed is applied to an ytterbium-doped and a praseodymium-doped ZBLAN fiber laser. Both lasers are optimized with regard to output power and their characteristics are discussed.
Before proceeding with modeling energy transfer processes, the first part of this chapter is shortly summarized.

5.2 Fiber laser and amplifier operation

For the sake of clarity, let us concentrate on lasers. Amplifiers are in fact not significantly different to model except that they amplify the signal wavelength which is typically combined by means of wavelength division multiplexed (WDM) couplers with the pump wavelength and, more important, show no feedback mechanism.
Moreover, let us concentrate on the very simple Fabry-Perot setup shown in Figure 5.1. It can be used in the laboratory for cw fiber lasers. Like every laser it consists of three fundamental parts. The first part is the power source which is a pump laser because fiber lasers belong to the class of optically pumped solid state lasers. The second part is the active medium storing pump energy in a metastable state, which may be used for stimulated emission. In a fiber laser, this is the core of the fiber doped with rare earth ions. The remaining third part of a laser is the feedback mechanism to support the process of stimulated emission for which two mirrors are used as is usual in most types of lasers. In the setup shown in Figure 5.1 the

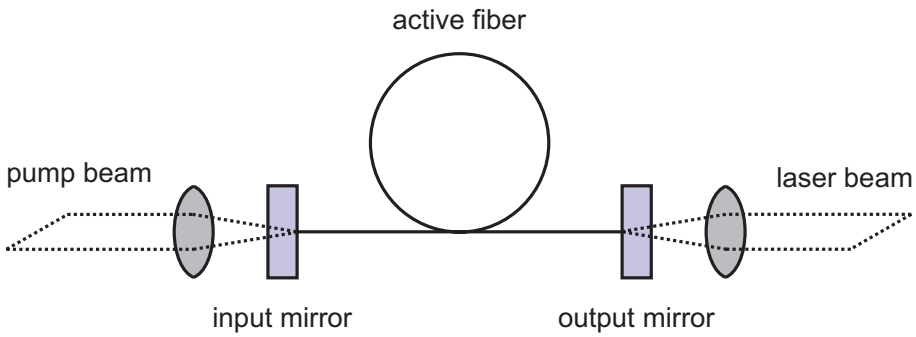

Figure 5.1: Basic free space setup of a fiber laser

mirrors must be dielectric mirrors where the input mirror should be highly transparent for the pump beam and the output mirror partly transparent for the laser beam. Since the laser resonator is a waveguide structure, the mirrors are just flat dielectric coatings placed at the fiber ends with physical contact to the fiber.
The laser process is based on stimulated emissions in the active material which provides gain at the laser wavelength. If the mirror feedback exceeds the losses inside the optical amplifier, it is immediately driven to the nonlinear large signal regime where the amplification process saturates at a level according to the pump power delivered. The part of the radiation which is exceeding the losses in the resonator may be coupled out as the laser beam which is highly coherent due to the inherent coherence of the stimulated emission. Corresponding to this simple principle of laser operation a mathematical description of fundamental importance can be found [15]:

$$\pm\frac{\mathrm{d}n_i}{\mathrm{dt}} = \sigma(\lambda)\cdot n_i \cdot \Phi(\lambda) = \pm\frac{1}{n_I}\cdot\frac{\mathrm{d}\Phi(\lambda)}{\mathrm{dx}}, \tag{5.1}$$

n_i being the relative occupation number of energy level i in the active material, n_I the density of dopant ions, $\Phi(\lambda)$ the photon flux at the wavelength λ, and $\sigma(\lambda)$ the emission or absorption cross section, where the cross section is the coupling constant of the interaction between radiation and matter. The variables x and t refer to position along the fiber axis and time, respectively. Depending on the choice of signs and the type of cross section used, this double equation describes the fundamental process of absorption and stimulated emission in laser materials. The left part (matter) can be expanded into a system of rate equations and the right part (radiation) into the gain equations.
As a more general expansion to the rate equation of level i in segment p for an unlimited system of states the following expression will be used [15]

$$\frac{\mathrm{d}n_i}{\mathrm{dt}} = \sum_j \left[A_{ji} + W_{ji} + \int f(\lambda)\cdot\left(\phi^+(\lambda,x) + \phi^-(\lambda,x)\right)\cdot\sigma_{ji}(\lambda)\,\mathrm{d}\lambda\right]\cdot n_j(x)$$

$$-\sum_j \left[A_{ij} + W_{ij} + \int f(\lambda) \cdot \left(\phi^+(\lambda, x) + \phi^-(\lambda, x) \right) \cdot \sigma_{ij}(\lambda) \, \mathrm{d}\lambda \right] \cdot n_i(x), \tag{5.2}$$

which is straightforward but needs some explanations. The equation is describing the temporal development of the relative occupation number n_i of level i and consists of two sums running over all levels j of the dopant ion. The first sum contains all contributions from transitions ending in level i and the second sum the contributions from all transitions starting from level i. The only difference between both sums is the order of i and j. Since the terms of the first sum lead to an increasing occupation number whereas the terms of the second sum reduce it, the sums appear with a positive and a negative sign, respectively. A_{ij} is the radiative emission rate of level i to j, whereas W_{ij} denotes the non-radiative emissions mainly due to multi-phonon emission and may be calculated directly or from the measured lifetime of level i using appropriate equations (see section 4.2). The integrals are the interaction terms due to absorption and stimulated emission from equation (5.1) with some modifications. The flux of photons is replaced by its spectral counterpart $\phi = \frac{\mathrm{d}\Phi}{\mathrm{d}\lambda}$ and separated in two parts ϕ^+ and ϕ^- where the sign denotes the direction of propagation. The positive sign stands for the flux co-directional to the pump beam and the negative sign for the opposite direction. The position variable along the fiber is x and the integral over λ spans the full absorption or emission line.

Until now the field of electromagnetic radiation has been treated like a swarm of floating photons but it is well-known that this description does not cover all of its properties. The Maxwell equations describe the wave character of this field. In this description the fundamental mode of electromagnetic radiation guided by the core of a single-mode fiber, which is a cylindric waveguide, is the so-called LP_{01} mode with a lateral intensity profile. In case of a weakly guiding fiber it is well approximated by the Gauss function [142]. Part of this wave extends into the cladding of the fiber and is thus unaffected by the dopant ions in the core. The factor $f(\lambda)$ in equation (5.2) contains the fraction of the total lateral intensity integral, which is interacting with the doped fiber core. In case of a single-mode fiber the intensity profile is fixed by the geometry of the fiber and not disturbed by partial interaction with the cladding. In the multi-mode regime the situation is much more difficult. However, the fraction of the guided radiation extending into the cladding can be expected to be relatively small in case of a multi-mode fiber.

For a system of N energy levels N rate equations (equation (5.2)) exist, one for each level, but they are linearly dependent as each equation is determined by all others. This can be immediately seen when writing down the equations for a concrete case. Mathematically speaking, the N-dimensional linear system of rate equations has rank $N-1$. To obtain a system of linear equations with full rank, which is solvable for n_i in the stationary case where $\frac{\mathrm{d}n_i}{dt} = 0$ for all n_i, one of the equations is replaced by the following, which obviously is a necessary condition fixing the relative occupation numbers [15]:

$$\sum_i n_i(x) = 1. \tag{5.3}$$

The right-hand side of equation (5.1) is expanded into a second set of differential equations. There exist two gain equations, one for each direction [15]:

$$\pm\frac{\mathrm{d}\phi^{\pm}(\lambda,x)}{\mathrm{dx}} = w(\lambda)\cdot n_{\mathrm{I}}\cdot\sum_{ij}A_{ij}\cdot g_{ij}(\lambda)\,\mathrm{d}\lambda\cdot n_i(x) + f(\lambda)\sum_{ij}\mathrm{sign}(i-j)\cdot\sigma_{ij}(\lambda)\cdot n_I\cdot n_i(x)\cdot\phi^{\pm}(\lambda,x)-\alpha(\lambda)\cdot\phi^{\pm}(\lambda,x)\,. \quad (5.4)$$

The first term of equation (5.4) describes the contribution of the spontaneous emission to the radiation field. In that term $g_{ij}(\lambda)$ is the lineshape function normalized according to $\int g_{ij}(\lambda)\,\mathrm{d}\lambda = 1$ and $w(\lambda)$ the fraction of the total spontaneous emission, which is guided by the fiber core. Spontaneous emission occurs in all directions with the same intensity, but if the angle between the direction of a photon and the fiber is too large, it will leave the core. The second term in equation (5.4) takes into account absorption and stimulated emission processes whereas the sign of the appropriate contribution is given by the sign of $i-j$. Finally, the fiber always shows a certain amount of background losses summarized by $\alpha(\lambda)$, defined by $\phi(x)=\phi_0\cdot\exp(-\alpha\cdot x)$, where α is usually wavelength dependent.
At both fiber ends of the Fabry-Perot setup shown in Figure 5.1, i.e. at $x=0$ and $x=L$ (where L denotes the active fiber length), the mirrors reflect the co- and counter-propagating photon fluxes into each other. The case is considered where the active fiber is bidirectionally pumped. Denoting the reflectivity of input and output mirror by $R^{in}(\lambda)$ and $R^{out}(\lambda)$, one obtains the following boundary conditions [15]:

$$\begin{aligned}\phi^{+}(\lambda,0) &= R^{in}(\lambda)\cdot\phi^{-}(\lambda,0)+T^{in}(\lambda)\cdot\phi^{fw}_{pump}(\lambda) \quad \text{and}\\ \phi^{-}(\lambda,L) &= R^{out}(\lambda)\cdot\phi^{+}(\lambda,L)+T^{out}(\lambda)\cdot\phi^{bw}_{pump}(\lambda)\,,\end{aligned} \quad (5.5)$$

where the flux of pump photons pumping from the left side $\phi^{fw}_{pump}(\lambda)$ (index fw stands for forward) and from the right side $\phi^{bw}_{pump}(\lambda)$ (index bw stands for backward) with transmission factor $T^{in}(\lambda)$ and $T^{out}(\lambda)$ for input and output mirror have already been included.
The rate equations (5.2) and (5.3) together with the gain equations (5.4) and the boundary conditions (5.5) represent a complex system of coupled ordinary differential equations which can only be solved numerically. It is worth noting that by changing the boundary conditions (5.5), any other laser configuration or any fiber amplifier configuration can easily be modeled as well. If several different fibers are spliced together forming the resonator, the mode-field diameter mismatches have to be introduced into the boundary conditions. In section 5.4.2, an algorithm solving this set of equations in the stationary case is discussed, i.e. $\frac{\mathrm{d}n_i}{\mathrm{dt}}=0$ for all i, to simulate cw fiber lasers and amplifiers.

5.3 Parameters for the simulation

5.3.1 Basic parameters

Before proceeding with the detailed mathematical formulation of the numerical model, let us first summarize all required parameters.
In the first group, the geometrical and optical parameters of the active fiber are collected. They include the fiber length L of the active fiber, its numerical aperture NA, core diameter d_{core}, fiber attenuation or background losses $\alpha(\lambda)$, and rare earth ion concentration c_{mol}. The complement of these parameters are spectroscopic data assigned as ground-state (GSA) and excited-state absorption (ESA) as well as emission cross sections (σ_{GSA}, σ_{ESA} and σ_{Emi}). The radiative emission rates of level i to j, A_{ij}, and the non-radiative emission rates, W_{ij}, are the last parameters in this second group. Finally, the number of energy levels considered in the calculations and the number of fiber segments in which the equations should be solved describe the general parameters of the model. Almost each of the previously described parameters can be measured. The radiative transition rates A_{ij} and other radiative properties of triply ionized praseodymium, erbium and thulium ions in ZBLAN (ZrF_4-BaF_2-LaF_3-AlF_3-NaF) glass have been calculated by Caspary [15]. Due to the fact that values for most non-radiative transition rates are difficult to obtain an approach to fix these values is given in section 5.3.2. Besides any mentioned quantities, the absolute temperature T is an additional parameter.
It is important to note that $f(\lambda)$, $g_{ij}(\lambda)$ and $w(\lambda)$ are dimensionless quantities. The definitions of $f(\lambda)$ and $w(\lambda)$ are given in section 5.4.3, whereas $g_{ij}(\lambda)$ has already been defined in section 5.2.
In order to transform the molar concentration used in glass technology to the ion density n_I, which is the quantity of physical relevance and allows comparison of different glasses, the mass density $\rho = \frac{m}{V}$ of the glass is required:

$$n_I = \gamma \cdot c_{mol} = \frac{\rho N_A}{M} \cdot c_{mol},$$

where N_A is Avogadro's constant and M the molar mass. For the self-made ZBLAN and IBZP (InF_3-BaF_2-ZnF_2-SrF_2-PbF_2-YF_3-AlF_3-LiF-NaF) glasses a molar mass of $M_{\mathrm{ZBLAN}} = 142.41$ g/mol and $M_{\mathrm{IBZP}} = 137.97$ g/mol, and a mass density of $\rho_{\mathrm{ZBLAN}} = 4.33$ g/cm^3 and $\rho_{\mathrm{IBZP}} = 5.2$ g/cm^3 was found, respectively. All values are in good agreement with literature values.
Some time ago, large series of density measurements have been carried out at the Institute [110] and the conversion factor

$$\gamma_{\mathrm{ZBLAN}} = (1.84 \pm 0.02) \cdot 10^{20} \quad \frac{\text{ions cm}^{-3}}{\text{mol\%}}$$

for ZBLAN glass had been found. In case of IBZP glass, a conversion factor of

$$\gamma_{\mathrm{IBZP}} = (2.27 \pm 0.02) \cdot 10^{20} \quad \frac{\text{ions cm}^{-3}}{\text{mol\%}}$$

had been found.

5.3.2 Maxwell-Boltzmann statistics for thermally coupled energy levels

Non-radiative transition rates are the most uncertain spectroscopic parameters. For changing their electronic state, rare earth ions in solids do not necessarily absorb or emit photons. They can undergo a variety of non-radiative transitions. The most important ones are multi-phonon transitions affecting single ions and energy transfer processes between two ions. In principle, both effects may be investigated separately, as energy transfer is negligible at low dopant concentrations and multi-phonon transitions are vanishing at low temperatures and can be neglected for transitions with large energy gaps.
The interaction of f-electrons with vibration modes of the glass matrix allows excited electronic levels to relax by exciting vibrations of the glass network. Unlike the situation in crystals, these vibrations are spatially localized because of the absence of translational invariance in vitreous materials. Nevertheless, the quantized modes are commonly called phonons.
For small energy gaps on the order of $k_B T$, with Boltzmann's constant k_B and the temperature T, the transitions occur very fast in upward and downward directions leading to thermalization of the involved electronic levels. This especially happens for the Stark levels inside M_J-multiplets. In cases where some J-levels are closely located it is important to know the relative occupation numbers of the corresponding states.
In the following we will develop an expression, introduced by Reinhard Caspary, which allows to include the thermal distribution of the relative occupation numbers across neighboring J-levels in a natural way into the framework of the fiber laser simulation shown in the following sub-section. The basic idea is that the distribution of occupation numbers in thermal equilibrium, as given by the Boltzmann equation, is established by non-radiative transitions between all energy levels. However, for each energy level only the next neighbors are of relevance, since the transition rates show an exponential dependency on the size of the energy gap which they are bridging. Therefore we start with the following rate equation of energy level i in thermal equilibrium:

$$\frac{\mathrm{d}n_i}{\mathrm{dt}} = W_{i-1,i} n_{i-1} - W_{i,i-1} n_i - W_{i,i+1} n_i + W_{i+1,i} n_{i+1} = 0,$$

where n_i is the relative occupation number of level i and W_{ij} the non-radiative transition rate from level i to level j. The final occupation numbers are given by the Boltzmann equation

$$\frac{n_i}{n_0} = \frac{g_i}{g_0} \cdot \exp\left(-\beta k_i\right), \tag{5.6}$$

where $g_i = 2J_i + 1$ is the statistical weight of level i, $k_i = 1/\lambda$ the wavenumber of level i and $\beta = \frac{h \cdot c_0}{k_B \cdot T}$ the usual Boltzmann factor. When we insert equation (5.6) into the rate equation of energy level i in thermal equilibrium, we get the expression

$$\left[W_{i-1,i} g_{i-1} \cdot \exp\left(-\beta k_{i-1}\right) - W_{i,i-1} g_i \cdot \exp\left(-\beta k_i\right)\right] -$$

$$[W_{i,i+1}g_i \cdot \exp(-\beta k_i) - W_{i+1,i}g_{i+1} \cdot \exp(-\beta k_{i+1})] = 0,$$

which contains two equivalent terms in brackets. The second term is built by applying the substitution $i \rightarrow i+1$ to the first term. For the lowest and for the highest energy level obviously only one of these terms is existing and the equations for all energy levels share one of these terms with each of the two next levels. Therefore the last equation can only be fulfilled for all levels, if each individual term vanishes:

$$W_{i,i+1}g_i \cdot \exp(-\beta k_i) - W_{i+1,i}g_{i+1} \cdot \exp(-\beta k_{i+1}) = 0.$$

Energy gaps larger than the maximum phonon energy $E_{max} = h \cdot \nu_{max}$ must be bridged by more than one phonon, hence the name multi-phonon transition. These transitions proceed predominantly in the downward direction and lead to high non-radiative relaxation rates for small energy gaps which only need a couple of phonons for the transition. The maximum phonon energy is 1100 cm^{-1} for silica glass, 580 cm^{-1} for ZBLAN and 510 cm^{-1} for IBZP glass.
The transition rate $W_{i,i-1}$ of the downward transition in the last equation is replaced by the usual equation for such relaxation rates based on Layne's phenomenological model [143]. The exponent of this equation contains the energy gap between the lowest Stark level of the upper M_J-multiplet and the highest Stark level of the lower M_J-multiplet, but we want to use the center of mass energies k_i. Therefore we introduce the mean distance k_{Stark} between the lowest and highest Stark level in one multiplet and get therefore

$$W_{i+1,i} = C \cdot \exp(-\delta \cdot (k_{i+1} - k_i - k_{Stark})). \tag{5.7}$$

The values of the parameters C and δ are usually found by a comparison of the measured lifetimes of energy levels with the calculated radiative lifetimes. For ZBLAN glass at room temperature (300 K), [110] reports the values $C = 1.99 \cdot 10^5$ s^{-1} and $\delta = 2.11 \cdot 10^{-5}$ m.
When we insert equation (5.7) into the previous equation, we get the expression

$$W_{i,i+1}g_i \cdot \exp(-\beta k_i) - Cg_{i+1} \exp(-\beta k_{i+1} - \delta(k_{i+1} - k_i - k_{Stark})) = 0,$$

which can easily be solved for $W_{i,i+1}$:

$$W_{i,i+1} = C \cdot \frac{g_{i+1}}{g_i} \cdot \exp(-\beta(k_{i+1} - k_i) - \delta(k_{i+1} - k_i - k_{Stark})). \tag{5.8}$$

Now we are ready to combine the equations (5.7) and (5.8) to a general expression for any non-radiative transition rate W_{ij}:

$$W_{ij} = \begin{cases} C \cdot \exp(-\delta(k_i - k_j - k_{Stark})) & \text{for } j = i-1, \\ C \cdot \frac{g_j}{g_i} \exp(-\beta(k_j - k_i) - \delta(k_j - k_i - k_{Stark})) & \text{for } j = i+1, \\ 0 & \text{otherwise.} \end{cases} \tag{5.9}$$

The derivation of expression (5.9) assures that including this equation into the fiber laser simulation leads to a correct thermalization of closely located energy levels according to the Boltzmann distribution.
Now, since all input parameters are given, a mathematical description is introduced in order to find the required output variables such as the relative occupation numbers n_i and the forward and backward photon fluxes $\Phi^+(\lambda)$ and $\Phi^-(\lambda)$.

5.4 Numerical simulation model

5.4.1 Model description

The model simulates the stationary case of an arbitrary laser or amplifier system in a rare-earth-doped fiber and is based on powers rather than complex field components, like the model of Duclos [125] for an upconversion TDFL, and thus does not account for longitudinal modes or phenomena such as spacial holeburning effects. Spectral holeburning effects are not considered either since the homogenous linewidth of a transition is not taken into account.
Since the laser and amplifier are simulated numerically, the general equations describing its performance (see section 5.2) have to be given in their discrete form and one has to find an algorithm to solve the resulting equations. The calculations have to be performed in three dimensions: energy levels, wavelengths, and spatial position. In other words, the active fiber is divided into m segments (see Figure 5.2), for which the occupation numbers of energy levels are calculated and the change in absorption and/or emission is evaluated. It is important to note that the indices i and j are used for the energy level which is already a discrete value, λ is the index corresponding to wavelength of the radiation field and x denotes the position along the active fiber for which the index p is used. The fiber has to be split in certain pieces which do not necessarily need to be of equal length. Since cw fiber lasers and amplifiers are of interest in this context, no change in the occupation number n of any energy level i is assumed, which corresponds to $\frac{\mathrm{d}n_i}{\mathrm{dt}} = 0$, i.e. $\mathrm{dt} \to \infty$.

When converting the integral in the rate equations (5.2) to a sum, it seems convenient to introduce the plain photon flux [15]

$$\Phi(\lambda) = \int_{\lambda}^{\lambda+\mathrm{d}\lambda} \phi\left(\lambda'\right) \mathrm{d}\lambda',$$

which is defined as the number of photons per unit area and per unit time interval. This leads to the following discrete form of the rate equation of level i in fiber segment p [15]:

$$\begin{aligned}\frac{\mathrm{d}n_i}{\mathrm{dt}} = 0 = &\sum_j \left[A_{ji} + W_{ji} + \sum_\lambda f_\lambda \cdot \left(\Phi^+_{\lambda p} + \Phi^-_{\lambda p+1}\right) \cdot \sigma_{ji\lambda}\right] \cdot n_{jp} \\ &- \sum_j \left[A_{ij} + W_{ij} + \sum_\lambda f_\lambda \cdot \left(\Phi^+_{\lambda p} + \Phi^-_{\lambda p+1}\right) \cdot \sigma_{ij\lambda}\right] \cdot n_{ip}, \end{aligned} \tag{5.10}$$

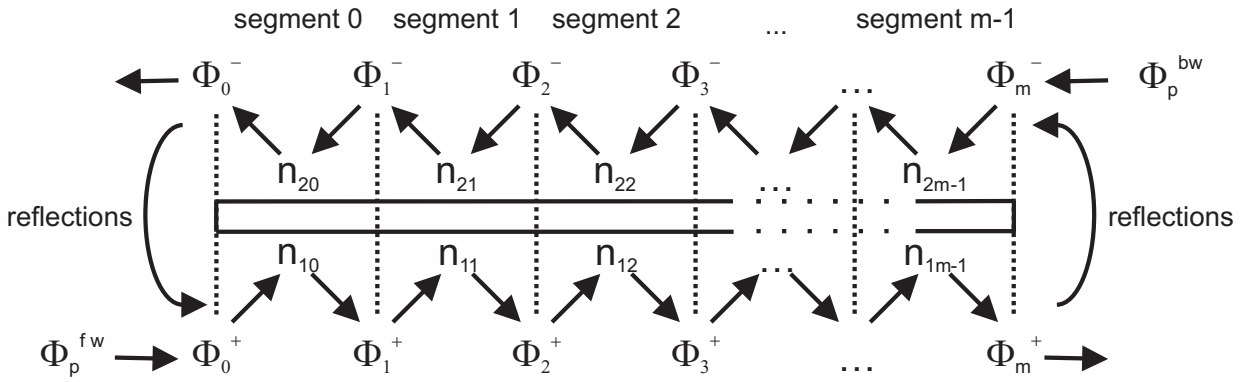

Figure 5.2: The active fiber is divided into m segments. The first index of the occupation numbers n_{ip} denotes the energy levels (here for a two-level system) whereas the second index stands for the fiber segments. Φ_p^{fw} and Φ_p^{bw} represent forward and backward pump photon fluxes, respectively. The illustrated schematic can also be extracted from [15].

where the index $p+1$ of Φ^- should be noted. It is necessary since the photon flux between the fiber segments $p-1$ and p is denoted by $\Phi^{\pm}_{\lambda p}$. Thus $\Phi^{-}_{\lambda p}$ is the flux leaving the segment p towards segment $p-1$ (see Figure 5.2). To further simplify the form of this equation, the matrix B^{sp}_{ij} (index sp stands for spontaneous emission) is introduced by the definition [15]

$$B^{sp}_{ij} = \begin{cases} -\sum_{j'} \left(A_{ij'} + W_{ij'}\right) & \text{if } j = i \text{ and} \\ A_{ji} + W_{ji} & \text{otherwise,} \end{cases} \tag{5.11}$$

and the analog definition of the matrix $B^{st}_{ij\lambda}$ for the terms of absorption and stimulated emission (index st) [15]

$$B^{st}_{ij\lambda} = \begin{cases} -f_\lambda \cdot \sum_{j'} \sigma_{ij'\lambda} & \text{if } j = i \text{ and} \\ f_\lambda \cdot \sigma_{ji\lambda} & \text{otherwise.} \end{cases} \tag{5.12}$$

All elements of both matrices above are given before the actual simulation starts and are therefore calculated outside the simulation kernel.
Let us assume now that one already knows the value of the photon fluxes into segment p and define the matrix B_{ijp} by [15]

$$\boxed{B_{ijp} = \begin{cases} 1 & \text{for } i = 0 \text{ and} \\ B^{sp}_{ij} + \sum_\lambda B^{st}_{ij\lambda} \cdot \left(\Phi^{+}_{\lambda p} + \Phi^{-}_{\lambda p+1}\right) & \text{otherwise,} \end{cases}} \tag{5.13}$$

then the rate equations in the fiber segment p build a set of linear equations, which is solved by matrix inversion to get the relative occupation numbers (all in the range between 0 and

1) of all energy levels in the fiber segment. The appropriate equation for level i is [15]

$$\boxed{\sum_j B_{ijp} \cdot n_{jp} = \begin{cases} 1 & \text{for } i = 0 \text{ and} \\ 0 & \text{otherwise,} \end{cases}} \tag{5.14}$$

and the special treatment of $i = 0$ includes equation (5.3).
Solving the rate equations one obtains the relative occupation of the energy levels, which are the input values for the gain equations (5.4). Now the photon flux traveling from left to the right can be written down in a discrete form [15]:

$$\frac{\Phi^+_{\lambda p+1} - \Phi^+_{\lambda p}}{\Delta x_p} = w_\lambda \cdot n_I \cdot \sum_{ij} A_{ij} \cdot g_{ij\lambda} \cdot n_{ip} + f_\lambda \sum_{ij} \text{sign}\,(i-j) \cdot \sigma_{ij\lambda} \cdot n_I \cdot n_{ip} \cdot \Phi^+_{\lambda p} - \alpha_\lambda \cdot \Phi^+_{\lambda p}, \tag{5.15}$$

and in the opposite direction [15]

$$\frac{\Phi^-_{\lambda p} - \Phi^-_{\lambda p+1}}{\Delta x_p} = w_\lambda \cdot n_I \cdot \sum_{ij} A_{ij} \cdot g_{ij\lambda} \cdot n_{ip} + f_\lambda \sum_{ij} \text{sign}\,(i-j) \cdot \sigma_{ij\lambda} \cdot n_I \cdot n_{ip} \cdot \Phi^-_{\lambda p+1} - \alpha_\lambda \cdot \Phi^-_{\lambda p+1}, \tag{5.16}$$

where Δx_p is the fiber segment's length and $g_{ij\lambda}$ the normalized lineshape function defined by $\sum_\lambda g_{ij\lambda} = 1$.
Again, some matrices containing all data known before the simulation starts are defined. From the term of spontaneous emission (index sp) one defines [15]

$$G^{sp}_{\lambda pi} = n_I \cdot w_\lambda \cdot \Delta x_p \cdot \sum_j A_{ij} \cdot g_{ij\lambda}, \tag{5.17}$$

from the term of absorption and stimulated emission (index st) [15]

$$G^{st}_{\lambda pi} = n_I \cdot f_\lambda \cdot \Delta x_p \cdot \sum_j \text{sign}\,(i-j) \cdot \sigma_{ij\lambda}, \tag{5.18}$$

and from the term of the background losses (index att) [15]

$$G^{att}_{\lambda p} = -\alpha_\lambda \cdot \Delta x_p \quad \text{for } \alpha_\lambda > 0. \tag{5.19}$$

As soon as one knows the values of the relative occupation numbers n_{ip} in segment p, one can calculate the two new matrices [15]

$$\boxed{\begin{aligned} G^{(1)}_{\lambda p} &= \sum_i G^{sp}_{\lambda pi} \cdot n_{ip} \quad \text{and} \\ G^{(2)}_{\lambda p} &= 1 + \sum_i G^{st}_{\lambda pi} \cdot n_{ip} + G^{att}_{\lambda p}, \end{aligned}} \tag{5.20}$$

which again simplify the expression of the gain equation. To account for undamped oscillations in the photon fluxes between successive iterations and thus to improve convergence, a denominator for the matrix $G^{(2)}_{\lambda p}$ in equations (5.20) can be introduced. This term may look like $1 + q_{damp} \cdot (Q - Q_{max})$, where q_{damp} is a dimensionless damping factor usually larger than 1, and the factors Q and Q_{max} define the break criterion for the simulation kernel which will be explained below in more detail. With this term it would follow that if Q equals Q_{max} the matrix $G^{(2)}_{\lambda p}$ would remain unchanged.
The photon flux leaving segment p in the direction of the pump beam and in the opposite direction can now be calculated by [15]

$$\boxed{\begin{aligned} \Phi^{+}_{\lambda p+1} &= G^{(1)}_{\lambda p} + G^{(2)}_{\lambda p} \cdot \Phi^{+}_{\lambda p} \quad \text{and} \\ \Phi^{-}_{\lambda p} &= G^{(1)}_{\lambda p} + G^{(2)}_{\lambda p} \cdot \Phi^{-}_{\lambda p+1}. \end{aligned}} \tag{5.21}$$

Obviously, the gain equations are solved by the finite difference method (FDM).
According to equation (5.5) the fluxes are partially reflected by the mirrors at the fiber ends and fluxes $\Phi^{fw}_{\lambda,pump}$ and $\Phi^{bw}_{\lambda,pump}$ of pump photons are added from both ends, which leads to the equations [15]

$$\boxed{\begin{aligned} \Phi^{+}_{\lambda 0} &= R^{in}_{\lambda} \cdot \Phi^{-}_{\lambda 0} + T^{in}_{\lambda} \cdot \Phi^{fw}_{\lambda,pump} \quad \text{and} \\ \Phi^{-}_{\lambda m} &= R^{out}_{\lambda} \cdot \Phi^{+}_{\lambda m} + T^{out}_{\lambda} \cdot \Phi^{bw}_{\lambda,pump}, \end{aligned}} \tag{5.22}$$

if the number of fiber segments is m. The equation converting power values P to photon fluxes Φ and vice-versa is

$$\Phi = \frac{P}{h \cdot \nu \cdot A_{core}},$$

where h is Planck's constant, ν the optical frequency and $A_{core} = \pi \cdot \frac{d^2_{core}}{4}$ is the area of the fiber core. With $\nu = \frac{c_0}{\lambda}$ this equation leads to

$$\Phi = \frac{P \cdot \lambda}{h \cdot c_0 \cdot A_{core}}, \tag{5.23}$$

where c_0 is the speed of light in vacuum.

5.4.2 Simulation algorithm

The boxed expressions above are all equations needed for the simulation kernel and the way in which the equations have been developed already suggests the structure of a suitable algorithm (see Figure 5.3 for the pseudo-code description) which can be used. It starts with the values of all fluxes set to zero except the pump fluxes entering the segments 0 and $m-1$. It is assumed that all upper energy states are unpopulated i.e. only the ground state is completely populated in the beginning. The forward propagating pump flux entering segment 0 is used to calculate

initial conditions:

$$\Phi^{\pm}_{\lambda p} = 0$$
$$\Phi^{+}_{\lambda 0} = T^{in}_{\lambda} \cdot \Phi^{fw}_{\lambda,pump}$$
$$\Phi^{-}_{\lambda m} = T^{out}_{\lambda} \cdot \Phi^{bw}_{\lambda,pump}$$
$$n_{jp} = 0 \quad \text{for} \quad j > 0$$
$$n_{0p} = 1$$

repeat

for $p = 0$ **to** $m-1$

calculate n_{jp} (5.13), (5.14)

calculate $\Phi^{+}_{\lambda p+1}$ (5.20), (5.21)

$$\Phi^{-}_{\lambda m} = R^{out}_{\lambda} \cdot \Phi^{+}_{\lambda m} + T^{out}_{\lambda} \cdot \Phi^{bw}_{\lambda,pump} \quad (5.22)$$

for $p = m-1$ **to** 0

calculate n_{jp} (5.13), (5.14)

calculate $\Phi^{-}_{\lambda p}$ (5.20), (5.21)

$$\Phi^{+}_{\lambda 0} = R^{in}_{\lambda} \cdot \Phi^{-}_{\lambda 0} + T^{in}_{\lambda} \cdot \Phi^{fw}_{\lambda,pump} \quad (5.22)$$

until converged

$$\Phi^{out,fw}_{\lambda} = T^{out}_{\lambda} \cdot \Phi^{+}_{\lambda m}$$
$$\Phi^{out,bw}_{\lambda} = T^{in}_{\lambda} \cdot \Phi^{-}_{\lambda 0}$$

Figure 5.3: Algorithm of the simulation kernel in pseudo-code with the appropriate equations indicated [15]

the values of the relative occupation numbers of all energy levels in fiber segment 0 by solving the linear set of rate equations (5.14). Taking these occupation numbers, equations (5.21) give the increased or decreased flux of photons to the next segment 1, where again at first the occupation numbers and then the new photon fluxes are calculated. In this way the algorithm proceeds until the output end of the fiber is reached. At that point equations (5.22) give the part of the photon flux reflected from the output mirror as the initial value of the backward flux added by the backward propagating pump flux. In the same way one now proceeds in the opposite direction of the fiber, from the last segment back to the first. Having arrived there, equations (5.22) are used again to calculate the reflected photon flux and add the flux from the pump laser. After the first loop the new values of $\Phi^{+}_{\lambda 0}$ will be quite different from the initial ones, but after a couple of iterations these values usually converge to the stationary case. For the break criterion the value [15]

$$Q = \max_{\lambda} \left(\frac{\left| \Phi^{+}_{\lambda 0} - \Phi^{0}_{\lambda} \right|}{\frac{\Phi^{+}_{\lambda 0} + \Phi^{0}_{\lambda}}{2}} \right) \leq Q_{max}, \quad (5.24)$$

is defined where the nominator gives the absolute deviation between Φ^{0}_{λ} and $\Phi^{+}_{\lambda 0}$ and the denominator gives the arithmetic mean value of both fluxes. Φ^{0}_{λ} is the vector $\Phi^{+}_{\lambda 0}$ from the last iteration. The iteration loop is left when Q falls below a certain defined value Q_{max}.

Of course, any other suitable definition for the break criterion can be used as well e.g. the geometric instead of the arithmetic mean value in the denominator of Q.
All operations in the simulation kernel are usual matrix operations such as multiplication, addition, and inversion, which are carried out at high speed by usual program libraries. Most of the computing time is consumed by matrix operations. Usual simulation runs need about 100 iterations if the pump power is well above threshold power, and with 200 wavelengths, 10 fiber segments, and $Q_{max} = 10^{-3}$ this takes less than a minute even on low-end computers [15].
In cases where the laser wavelength is already known, using this single value increases computing speed significantly. On the other hand, when a fine grid of wavelengths is offered, the simulation automatically pins to the maximum gain position. However, it should be remembered that the model does not take into account the homogeneous line width of a transition and the respective spectral holeburning effects are not simulated either. A number of 10 fiber segments turned out to be suitable in most cases but care must be taken that the pump power is not absorbed completely in the first segment, otherwise errors caused by the discrete treatment of the continuous fiber cause unrecoverable errors in the calculated photon flux which often lead to undamped oscillations in successive iterations. To reduce the oscillations the introduction of a damping factor q_{damp} in the denominator of the matrix $G^{(2)}_{\lambda p}$ has been proposed. Even when the length of the fiber segments is chosen to be short enough, it happens that equations (5.21) give negative values at certain wavelengths due to rounding errors. Hence, these negative values must be clipped to zero to avoid unstable behavior.

5.4.3 Further remarks

Obviously, the term for spontaneous emission in the gain equations (5.21) is not really necessary above laser threshold but it is still useful as it produces a constant seed of photon flux at all wavelengths at a reasonable power level. If this term is omitted, these seed values must be given together with the pump fluxes before the beginning of the iteration loop, otherwise the laser will not start lasing. As a rough approximation of the factor w_λ in this term, which is the probability for a spontaneously emitted photon to be guided by the fiber core, the following derivation is done:
Let Ω be the solid angle spanned by the acceptance angle of the fiber with given NA. It is defined as

$$\Omega = \int_0^{2\pi} \int_0^{\beta} \sin\vartheta \mathrm{d}\vartheta \mathrm{d}\zeta,$$

where β is the maximum angle for light guided by the fiber and given by the numerical aperture $\mathrm{NA} = \sin\beta$. One knows that w_λ is the ratio between Ω and the full solid angle 4π and thus one obtains [15]

$$w_\lambda = \frac{\Omega}{4\pi} = \frac{1}{2} \cdot (1 - \cos(\arcsin(\mathrm{NA}))) . \tag{5.25}$$

Although the concept of an acceptance angle is normally used for multi-mode fibers only it provides a reasonable approximation in case of a single-mode fiber. However, an exact value is not needed anyway. Hence, alternatively, the capture fraction S for single-mode fibers, which has been introduced in chapter 4 (see equation (4.8)), can be used as w_λ.
Of more importance is the confinement factor f_λ in the terms of absorption and spontaneous emission, which is the fraction of the radiation field affected by the fiber core. In case of a single-mode fiber, [144] gives the expression

$$f_\lambda = \left(\frac{W}{V}\right)^2 \cdot \left(1 + \left(\frac{J_0(U)}{J_1(U)}\right)^2\right), \tag{5.26}$$

with the V-number of a fiber $V = \frac{\pi \cdot d_{core}}{\lambda} \cdot \mathrm{NA}$ [142], and the parameters W and U given by $W = 1.1428 \cdot V - 0.9960$ and $U = V^2 - W^2$, respectively. Equation (5.26) contains Bessel functions $J_q(x)$ of order $q = 0$ and $q = 1$, respectively. In the multi-mode regime with V-numbers larger than 2.405 this equation is invalid and quickly reaches unreasonable values above 1. A general calculation of f_λ in the multi-mode case seems to be very cumbersome because it depends on the relative intensity carried in the different radiation modes, which depends on a variety of conditions. However, the value is expected to be relatively large in multi-mode fibers and thus equation (5.26) is used for all wavelengths, but all values exceeding 1 are clipped to $f_\lambda = 1$.
Extensive use of the simulation program showed no problems with numerical stability of the algorithm as long as the fiber segments are chosen to be short enough and the background loss α_λ was set to a nonzero and positive value. It turned out that this attenuation term in the gain equations (5.21) effectively damps the small rounding errors occurring in every numerical calculation, which in certain cases led to photon fluxes slightly increasing with each iteration step without limits when α_λ was omitted. Even very small values of α_λ have been found to assure the numerical stability of the algorithm in all simulations carried out.
In the modeling of semiconductor lasers the algorithms currently used for steady-state analysis are based on the fixed point method [145]. The coupled solution method (CSM) which is one of two possible algorithms is analog to the method the author uses due to the fact that coupled ordinary differential equations such as the rate and gain equations have been found which describe rare-earth-doped fiber laser and amplifier operation. According to Sujecki [145] this method is more stable than the alternative separate solution method (SSM) but diverges for power values near threshold and can converge very slowly when performing multi-wavelength analysis. However, by using appropriate techniques rapid convergence to the solution can be achieved if CSM is used [145].

5.5 Fiber laser simulation

As already described above, the goal of this thesis is to provide a numerical model for arbitrary lasers and amplifiers. To improve a fiber laser or amplifier setup, one has to compare

simulations with measurements. In the literature there are many experimental results but, to the best of the author's knowledge, none of them present all data which are really necessary to simulate their quantitative behavior. Furthermore, a comparison of simulations with experimental results is powerful once the device setup is ready to use in the laboratory. Hence, one could optimize the parameters by directly comparing simulations to experiments. However, due to lack of knowledge of the necessary input parameters and boundary conditions of the work of other researchers, it will not be the goal of this thesis to achieve a quantitative agreement with literature. Instead, examples of typical fiber lasers will be shown. It is the author's goal to show the applicability of the model to different rare-earth-doped fiber lasers and to optimize these lasers with regard to output power.

5.5.1 Yb^{3+}-doped fiber laser

The goal is to simulate an ytterbium-doped cw fiber laser with Fabry-Perot cavity as shown in Figure 5.1. It consists of two laser mirrors where the left mirror shows full reflectivity for the signal wavelength. The reflectivity of the right mirror has been varied to find the maximum output power. Both mirrors are assumed to be fully transparent for the pump wavelength. The configuration is pumped from the left side with a pump power of 200 mW directly into the active fiber core. The pump wavelength is 975 nm.
In this simulation the two levels $^2F_{7/2}$ and $^2F_{5/2}$ of ytterbium-doped ZBLAN glass have been considered, thus Stark splitting has been neglected. Although for this simple two-level system a simplification of the equations given in section 5.4.1 is achievable, it is not done here. The aim of all examples is to show the application of the described simulation model.

The GSA cross section of ytterbium in ZBLAN glass used in the simulation had been measured by Caspary at room temperature [15]. The respective emission cross section of this two-level system has been calculated using formula (4.47) of McCumber with a wavenumber difference Δk of 10345 cm^{-1} [15]. Both cross sections are plotted in Figure 5.4. The GSA cross section shows a sharp peak at 975 nm with a broad foot part. The emission cross section and lifetimes of Yb^{3+} energy levels in different host glasses were also reported in [146].
Ytterbium is mostly used in high power fiber lasers and also used in fiber lasers at 1020 nm to pump PDFAs for signals at 1.3 μm. The wavelength of the ytterbium transition fits perfectly to usual laser diodes used to pump EDFAs at 980 nm. Used as a co-dopant to another rare earth ion, the existence of only two energy levels is an important advantage, because the ytterbium concentration may be quite high without disturbing the transitions of the other rare earth ion at different wavelengths. On the other hand, this high concentration ensures effective energy transfer to appropriate energy levels of the second dopant as e.g. in case of Pr^{3+}/Yb^{3+}-doped ZBLAN fiber lasers which will be simulated in section 5.7.
The value of the radiative transition rate from the excited level $^2F_{5/2}$ to the ground level $^2F_{7/2}$ has been taken to be $A_{21} = 1000\ s^{-1}$ in accordance with [88, 146].
The Yb^{3+}:ZBLAN fiber shows the following parameters: an NA of 0.2, a core diameter of 3 μm, a length of 80 cm and background losses of 2 dB/km. The simulations showed that

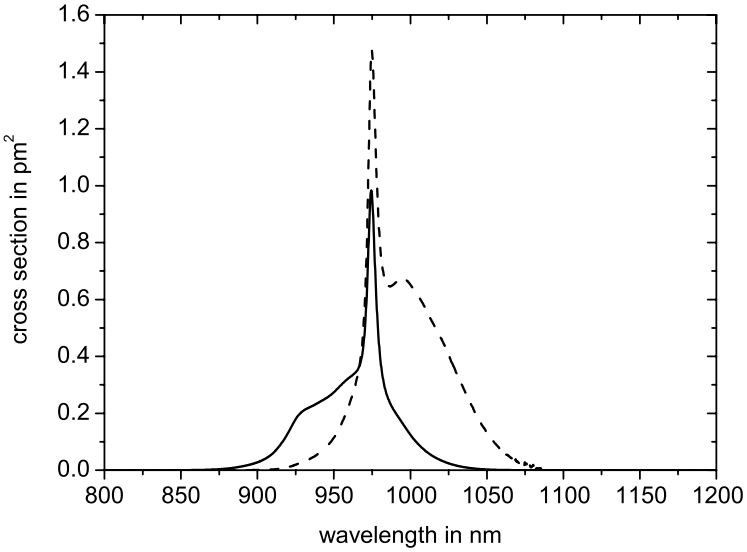

Figure 5.4: Spectrum of the measured absorption cross section (solid line) and calculated emission cross section (dashed line) of Yb^{3+}:ZBLAN

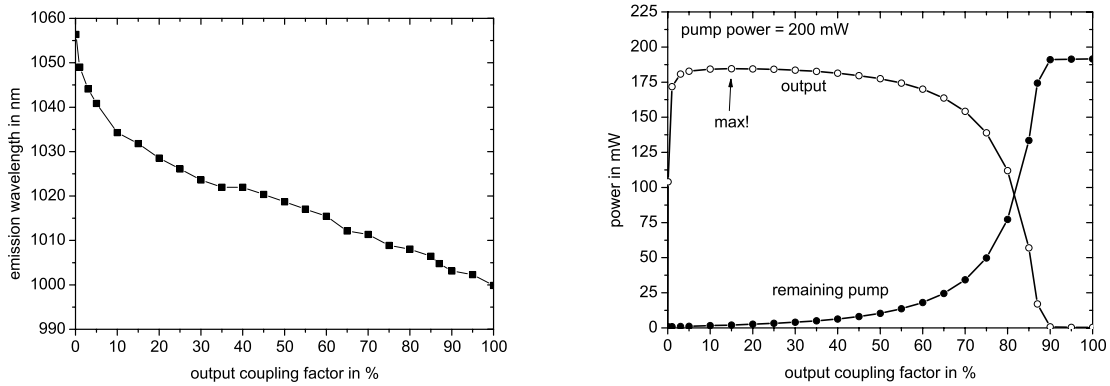

Figure 5.5: Emission wavelength versus output coupling factor (left), and, output and remaining pump power at the right fiber end versus output coupling factor (right) for the simulated Yb^{3+}-doped ZBLAN fiber laser

the output power of the Yb^{3+}-doped ZBLAN fiber laser is quite insensitive with regard to fiber length. A fiber length of 80 cm results in more than 90 % pump absorbtion for the

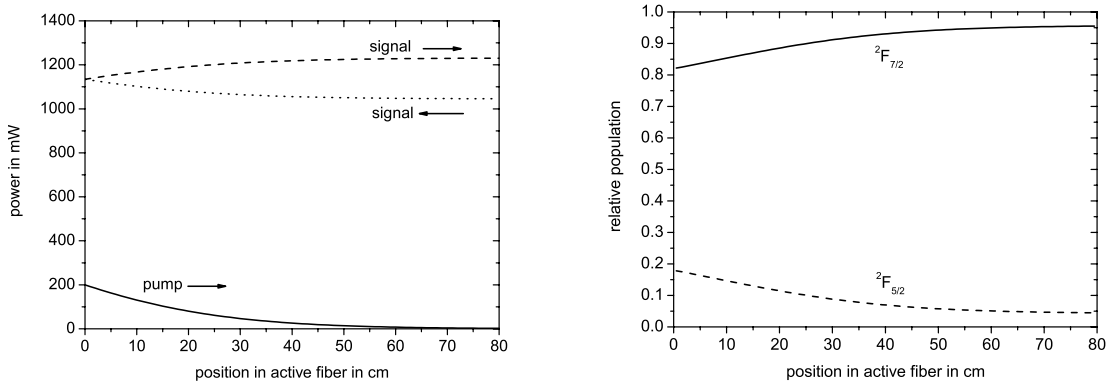

Figure 5.6: Pump power (solid line) and signal powers in forward (dashed line) and backward (dotted line) direction along the position in the active fiber (left) and relative population of the ground level $^2F_{7/2}$ (solid line) and the excited level $^2F_{5/2}$ (dashed line) along the position in the active fiber (right)

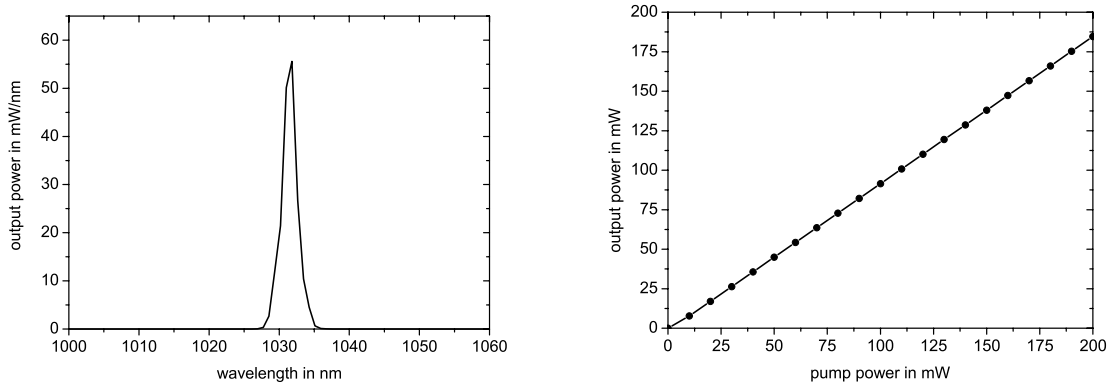

Figure 5.7: Spectral output power at right fiber end for a pump power of 200 mW (left) and laser characteristics of the simulated Yb^{3+}-doped ZBLAN fiber laser (right)

above mentioned pump power and leads to maximum output power. The fiber core is doped with a concentration of 1000 ppm of ytterbium ions which corresponds to an ion density n_I of about $1.84 \cdot 10^{25}$ ions/m^3. The fiber is split into 80 pieces of equal length (fiber segment's length $\Delta x_p = 1$ cm). The simulations have been carried out in the wavelength range between 845 nm to 1090 nm and with a precision of $Q_{max} = 10^{-2}$.
As can be seen in the left part of Figure 5.5 the emission wavelength decreases from about 1060 nm to about 1000 nm for increasing output coupling factor i.e. decreasing mirror reflectivity. This behavior can be explained by the existence of the broad emission cross section

of Yb^{3+}:ZBLAN (see Figure 5.4). The ratio of the absorption cross section spectrum to the emission cross section spectrum causes this behavior, which is typical for three-level lasers. Deviations from a linear trace are due to small fluctuations in the emission cross section spectrum. In the right part of Figure 5.5 the remaining pump power and the output power are plotted against the output coupling factor showing that for increasing output coupling factor pump power absorbtion decreases significantly. The maximum output power of 184.6 mW is reached for 15 % output coupling and the emission wavelength is about 1032 nm. Only 2.1 mW of the pump power is left at the right fiber end. To sum up, a mirror reflectivity of 85 % leads to maximum output power and thus is used for all following calculations.
The signal and pump powers are plotted in the left part of Figure 5.6. As shown in this figure, the pump power is nearly completely absorbed at the right fiber end. Forward and backward photon fluxes both increase as they propagate along the fiber due to the reason that a certain interaction length is needed in any laser configuration. The large values of the signal powers are typical for Yb^{3+}-doped fiber lasers.
Furthermore, it can be seen in the right part of Figure 5.6 that total population inversion (see section 1.2) is never achieved for emission along the whole fiber, although it is usually mentioned as the criterion for laser action. However, population inversion is reached if the spectrum of Stark levels is taken into account instead of the total occupation numbers of the two levels shown. The wavelength of such a two-level laser is shifted towards longer wavelengths in the emission lineshape and, as has already been described in chapter 1, the product of occupation number and cross section must be taken as laser criterion.
The spectral output power is shown in the left part of Figure 5.7. The simulation pins out to an emission wavelength of about 1032 nm for which a maximum power of -12 dBm/nm has reached the right fiber end. A value of 184.6 mW is obtained for the maximum output power. The output power value in relation to the pump power inserted in the active fiber core underlines the high power conversion efficiency (PCE) of ytterbium-doped fiber lasers (around 92 % in this case).
Finally, the laser characteristic is shown in the right part of Figure 5.7. It must be emphasized that the output power is plotted over the pump power which has already reached the resonator i.e. the active fiber. The threshold power and slope efficiency can be extracted by a linear fit of the characteristics to be 1.4 mW and 93 %, respectively.
Of course, the optimum fiber length and mirror reflectivity also depend on pump power, and the case evaluated here is only an example of the large range of investigations possible with the described simulation model.

5.5.2 Pr^{3+}-doped fiber laser

A praseodymium-doped cw fiber laser with Fabry-Perot cavity emitting in different colors is simulated in this section. The parameters of the praseodymium-doped ZBLAN fiber used are specified by Le Verre Fluore: core diameter of 2.8 μm, an NA of 0.23 and a concentration of 3000 ppm of praseodymium ions in the active fiber core corresponding to an ion density n_I

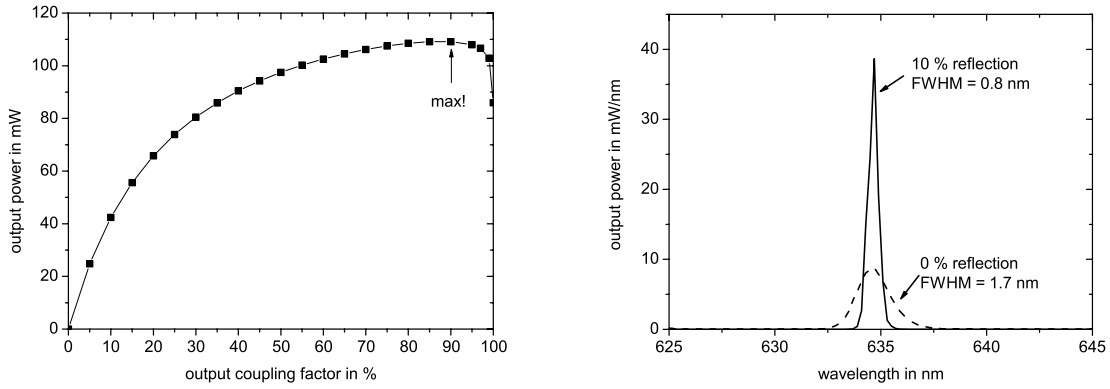

Figure 5.8: Output power at the right fiber end versus output coupling factor (left), and, spectral output power at right fiber end for a pump power of 120 mW and 100 mW at 835 and 1020 nm, respectively (right). The spectral output power is plotted for a mirror reflectivity of 10 % where maximum output power is obtained and for no reflection where a superfluorescence source is present. The full-width-at-half-maximum (FWHM) for both cases is also indicated in the graph.

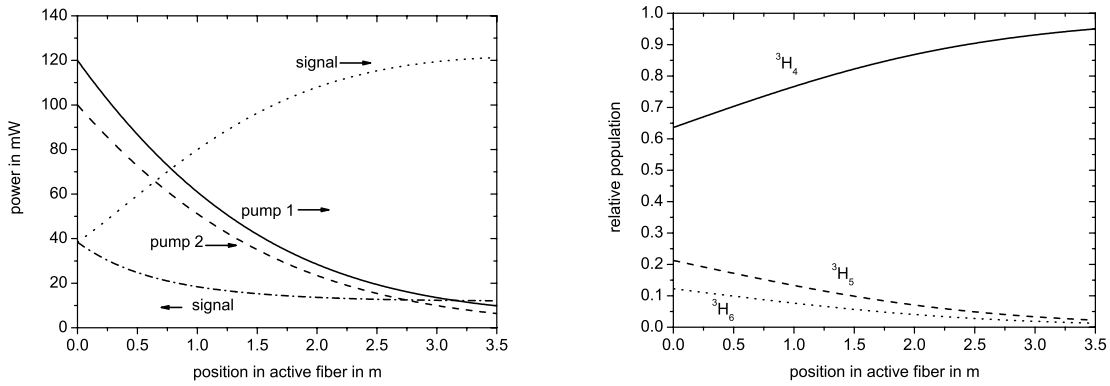

Figure 5.9: Pump powers (solid and dashed lines) and signal powers in forward (dotted line) and backward (dash-dotted line) direction (left), and, relative population (right) of the ground level $^3H_4$ (solid line) and the excited levels $^3H_5$ (dashed line) and $^3H_6$ (dotted line) along the position in the active fiber for the simulated red Pr^{3+}-doped ZBLAN fiber laser

of about $5.52 \cdot 10^{25}$ ions/m^3. The actual attenuation of the fiber is about 0.1 dB/m.
In all simulations which have been carried out in this section and in section 5.7 the fiber segment's length has been chosen to be $\Delta x_p = 1$ cm. To speed up the simulations only the wavelengths of interest for the red, orange, green and blue lasers have been selected and all calculations have been carried out with a precision of $Q_{max} = 15 \cdot 10^{-2}$. The praseodymium-

doped ZBLAN fiber laser consists of two laser mirrors where the input mirror shows 100 % reflectivity for the emission wavelength. The output mirror reflectivity is varied to find the optimum output coupling with regard to maximum output power. Both mirrors are assumed to be fully transparent for the pump wavelengths. The configuration is pumped from the left side with a pump power of 120 mW at 835 nm and 100 mW at 1020 nm, respectively, directly into the active fiber core. In all simulations coupling efficiencies of 100 % have been assumed on both sides, thus these values will be smaller in a real setup.
The GSA and ESA cross sections of praseodymium-doped ZBLAN glass used in the simulation and the respective emission cross section have already been presented in Figures 4.16, 4.17 and 4.18. All corresponding cross sections for the complementary transitions have been calculated using the McCumber theory (see section 4.3.3) with the wavenumber differences listed in [15]. Radiative transition rates of Pr^{3+} listed in [15] have been used for all simulations.
Red, orange and blue laser characteristics will be simulated for the optimum mirror reflectivity and fiber length in order to obtain maximum output power. The performance of the four-level lasers (red and orange lasers) will be compared to the three-level laser (blue laser). In all simulations with Pr^{3+}-doped fiber lasers all twelve levels of praseodymium-doped ZBLAN glass have been considered (see Figure 3.4) and a Stark offset of 50000 m^{-1} has been assumed. However, it should be mentioned that by varying the fiber length and suppressing all emissions except for the green mirror reflectivity no green laser has been lasing for the chosen simulation parameters. Of course, the green fluorescence is weaker than the red and blue ones in the emission cross section of Pr^{3+} (see Figure 4.18) but then also no orange laser should be achievable since the emission cross section of the orange transition is on the same order as for the green transition. It turned out that the green laser behaves very sensitive with regard to the $^3P_1$ population which depends on a number of unknown parameters such as the exact energy gap to the lower $^3P_0$ level. Nevertheless, the green laser lases by increasing pump power and changing the Boltzmann distribution in the way that the occupation of the $^3P_1$ level becomes more probable. Of course, this is physically not correct but is only an indication that the exact distribution of the upper energy levels of Pr^{3+} is not known. In practice, a green laser can be easily achieved [14].
The same behavior for the green laser has also been observed for the Pr^{3+}/Yb^{3+}-doped ZBLAN fiber laser which will be simulated in section 5.7. Thus, only red, orange and blue lasers will be simulated in this work.

Red laser

The optimum fiber length of the Pr^{3+}:ZBLAN fiber turned out to be about 3.5 m since for this active fiber length both pump powers have been absorbed by more than 90 %.
In the left part of Figure 5.8 the output power is plotted against the output coupling factor showing that for an output coupling factor of 90 % a maximum output power of 109 mW is obtained. The emission wavelength is 633 nm and a maximum power of -12 dBm/nm has

reached the right fiber end. Only 9.8 and 6.4 mW of the pump powers are left at that end. Hence, a mirror reflectivity of 10 % leads to maximum output power and thus is used for all following calculations.
As the simulations turned out, for no reflection of the output mirror (i.e. no laser resonator for 100 % output coupling is available) almost 86 mW output power is obtained (-19 dBm/nm). Single-pass amplification of spontaneously emitted photons without an optical resonator results in a superfluorescence source. The excited ions produce a spontaneous emission, and part of it is captured by the fiber core in both the forward and the backward direction. The forward and backward spontaneous photons are amplified as they travel along the fiber and produce ASE with an intensity which saturates the gain. The output power is therefore comparable to that of a laser resonator. This ASE operation is sometimes referred to as mirror-less lasing because it does not involve an optical resonator. The emitted signals are free from the longitudinal mode structure typical for fiber lasers. In addition, unlike most laser sources, the output signal can exhibit a broad optical spectrum, even at high power levels.
The spectral output power is shown in the right part of Figure 5.8 for the case of the superfluorescence source and the laser. In case of the former, the FWHM is about 1.7 nm. For the laser a FWHM of about 0.8 nm can be determined. The magnitude of the spectrum is a factor of roughly 5 larger for the laser than for the superfluorescence source. The output bandwidth is one of the important parameters of a superfluorescence light source. Spontaneous emission is preferentially amplified at the peak of the gain curve, causing the spectrum to narrow as the gain is increased. The attraction of the superfluorescent emission is that it is spatially coherent, but has a broadband emission and thus a very short coherence length. A fiber-based superfluorescence light source is a promising broadband light source in fiber sensor applications.
Let us go back to the case of the maximum output power for the red laser where a reflectivity of 10 % has been determined as optimum value for the output mirror. In the left part of Figure 5.9 the spatial distribution of signal and pump powers is shown. Both pump powers are almost completely absorbed as they reach the right fiber end. Forward and backward photon fluxes both increase as they propagate along the fiber showing a monotonous increase in gain. The fraction of power coupled out through the output mirror is given by the difference in the power levels of the fluxes in both directions.
While the data from the left part of Figure 5.9 in principle could also be obtained by measurements, the distribution of the relative occupation numbers of all energy levels along the fiber, as shown in the right part of this figure, are accessible only in the simulation. The pump power in the active fiber strongly depletes the ground level $^3H_4$ so that more than one third of the dopant ions are excited in the beginning. In the fiber the occupation number of the first excited level $^3H_5$ is larger than that of all other excited states including the second excited level $^3H_6$.

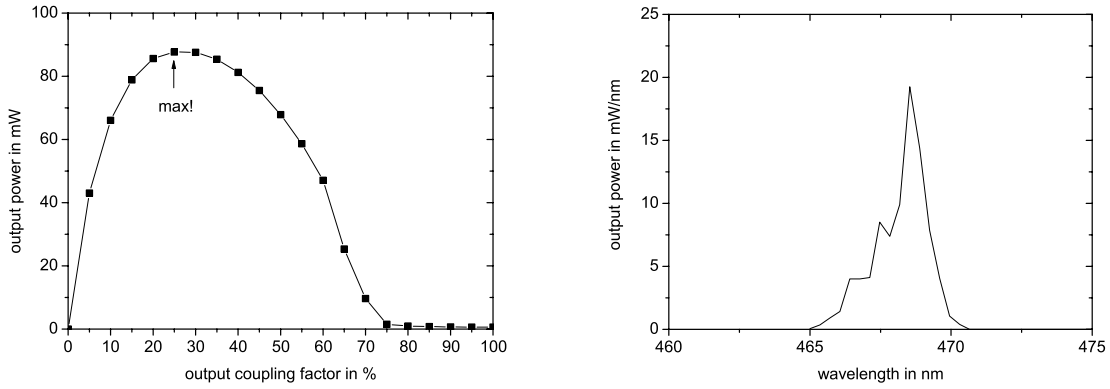

Figure 5.10: Output power at the right fiber end versus output coupling factor (left), and, spectral output power at right fiber end for a pump power of 120 mW and 100 mW at 835 and 1020 nm, respectively (right). The spectral output power is plotted for a mirror reflectivity of 75 % where maximum output power is obtained.

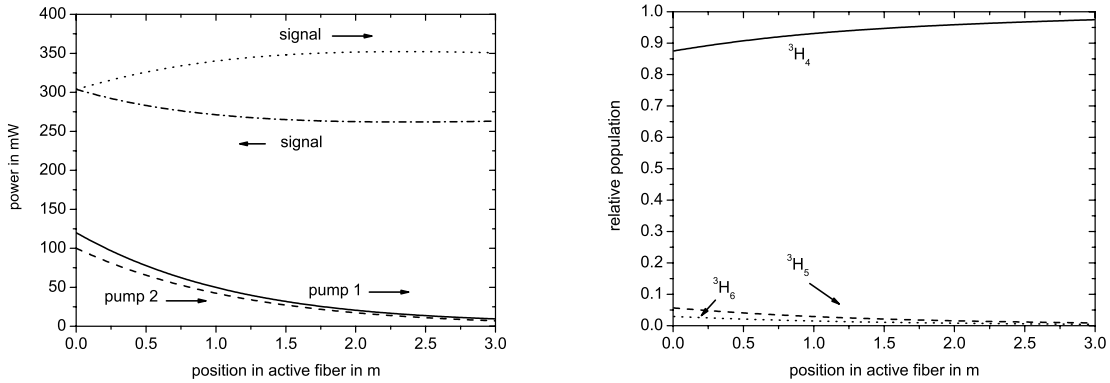

Figure 5.11: Pump powers (solid and dashed lines) and signal powers in forward (dotted line) and backward (dash-dotted line) direction (left), and, relative population (right) of the ground level $^3H_4$ (solid line) and the excited levels $^3H_5$ (dashed line) and $^3H_6$ (dotted line) along the position in the active fiber for the simulated blue Pr^{3+}-doped ZBLAN fiber laser

Blue laser

For the blue laser an optimum fiber length of about 3 m has been determined. The emission wavelength is 468.5 nm and an output coupling factor of 25 % turned out to be the optimum value as shown in the left part of Figure 5.10.
87.7 mW output power has been obtained for a mirror reflectivity of 75 % and the pump

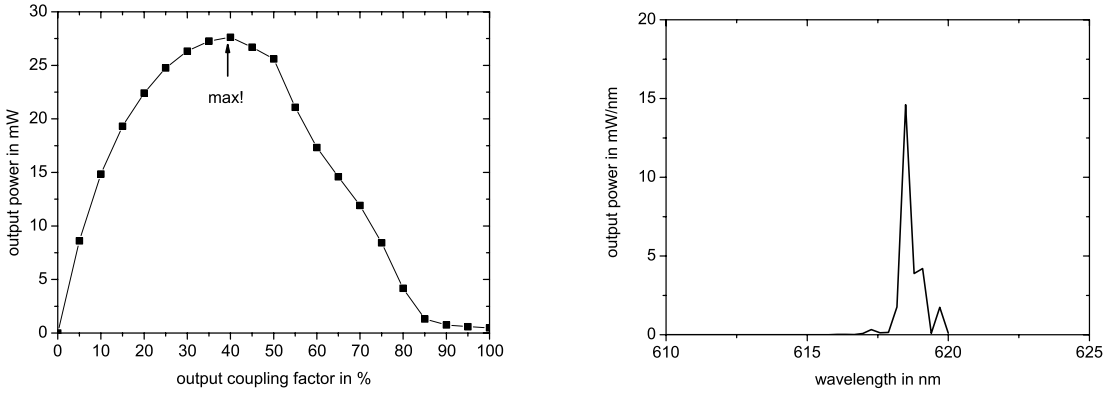

Figure 5.12: Output power at the right fiber end versus output coupling factor (left), and, spectral output power at right fiber end for a pump power of 120 mW and 100 mW at 835 and 1020 nm, respectively (right). The spectral output power is plotted for a mirror reflectivity of 60 % where maximum output power is obtained.

powers at the right fiber end amount to 9.5 and 7 mW, respectively. For larger values than 75 % output coupling almost no output power is obtained. The spectral power, in the right part of Figure 5.10, shows that a maximum power of -14 dBm/nm has reached the right fiber end.
Signal and pump powers in case of the blue laser are shown in the left part of Figure 5.11. At 3 m almost all of the above mentioned pump powers are absorbed leading to maximum output power. The qualitative behavior of the signal powers is similar to the red laser but showing larger values. This is due to the higher energy of the blue compared to the red emission.
In the right part of Figure 5.11 the relative occupation numbers of some relevant energy levels are shown. The behavior of the $^3H_4$, $^3H_5$ and $^3H_6$ level is qualitatively the same as for the red laser but this time less than 15 % of the dopant ions are excited in the beginning due to the fact that population inversion is less effective in a three-level laser.

Orange laser

In case of the orange laser an optimum fiber length of about 3 m has been determined like for the blue laser. The emission wavelength of the orange laser is 617.3 nm. An output coupling factor of 40 % turned out to be the optimum value as shown in the left part of Figure 5.12.
An output power of 27.6 mW has been obtained for a mirror reflectivity of 60 %. The pump powers at the right fiber end amount to 10.2 and 10.6 mW, respectively. For larger values than 85 % output coupling almost no output power is obtained. The spectral power, in the right part of Figure 5.12, shows a maximum power of -16 dBm/nm.

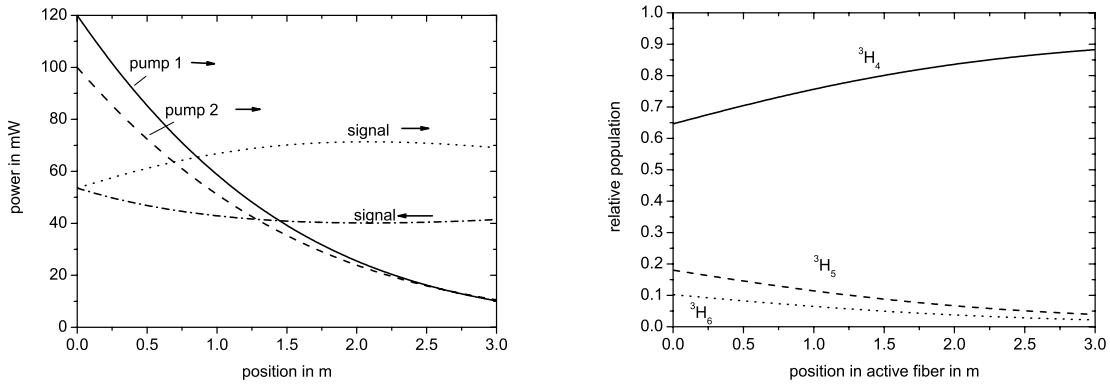

Figure 5.13: Pump powers (solid and dashed lines) and signal powers in forward (dotted line) and backward (dash-dotted line) direction (left), and, relative population (right) of the ground level $^3H_4$ (solid line) and the excited levels $^3H_5$ (dashed line) and $^3H_6$ (dotted line) along the position in the active fiber for the simulated orange Pr^{3+}-doped ZBLAN fiber laser

Signal and pump powers in case of the orange laser are plotted in the left part of Figure 5.13. It can clearly be seen why a fiber length of 3 m is optimum. More than 90 % of the above mentioned pump powers are absorbed. The qualitative behavior of the signal powers is similar to the blue laser but showing smaller values. All these power traces show that for a red laser with optimum fiber length and mirror reflectivities the gain is larger than that of the blue and orange lasers. Of course, this behavior can also be expected from the measured emission cross section spectrum (see Figure 4.18).
In the right part of Figure 5.13 the relative occupation numbers of the relevant energy levels $^3H_4$, $^3H_5$ and $^3H_6$ as a function of position along the active fiber are shown. Qualitatively and nearly quantitatively the same behavior as for the red laser is observed since both lasers are four-level lasers.

Laser characteristics of red, blue and orange lasers

The red, blue and orange laser characteristics of the simulated Pr^{3+}-doped ZBLAN fiber laser are shown in Figure 5.14. The 835 nm pump power has been varied in 10 mW steps in the range of 0 to 120 mW whereas the 1020 nm pump power has been held constant to 100 mW.
It is noted that the output power is plotted over the pump power which has already reached the resonator i.e. the active fiber. The red laser characteristic shows the smallest threshold power of all three lasers. A linear fit to the graph results in a threshold power of 8.7 mW and a slope efficiency of 105 % indicating the high efficiency of the red laser. A maximum output power of 109 mW is achieved for pump powers of 120 mW and 100 mW at both pump

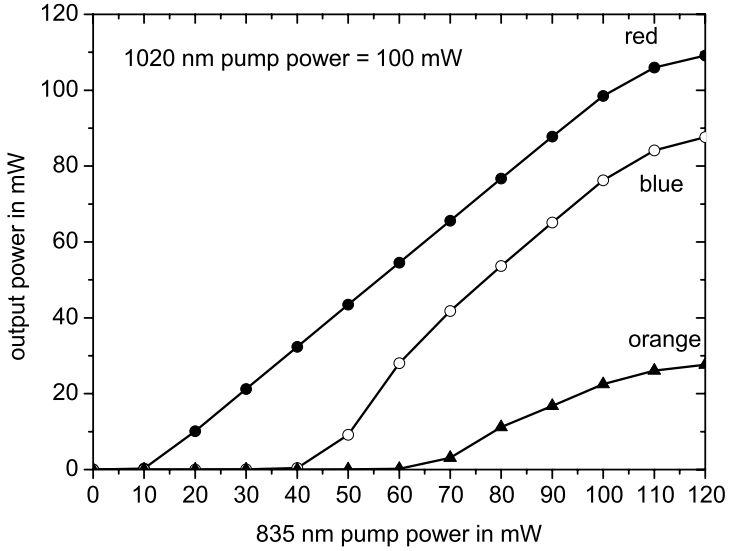

Figure 5.14: Red, blue and orange laser characteristics of the simulated Pr^{3+}-doped ZBLAN fiber laser for varying 835 nm pump power with constant 1020 nm pump power of 100 mW .

wavelengths resulting in a PCE of 49.5 %.
For the blue laser a larger threshold power of about 37 mW is obtained which is more than a factor of four larger than for the red laser. A linear fit to the graph results in a slope efficiency of 116 % which is 11 % larger as for the red laser. A maximum output power of 87.7 mW is achieved for both pump powers resulting in a PCE of about 40 %.
The orange laser shows the largest threshold power of about 59 mW which is a factor of 1.6 larger than for the blue laser. A slope efficiency of 50 % can be extracted from the graph showing a more than twice smaller value compared to the red and blue lasers. 27.6 mW has been obtained as maximum output power resulting in a PCE of about 12.5 %.
In section 5.7 a Pr^{3+}/Yb^{3+}-doped ZBLAN fiber laser is simulated and its results are compared to the results of the praseodymium-doped ZBLAN fiber laser simulated in this section.

5.5.3 Remarks on stationary simulations

Simulations are of great value in the development process of lasers and amplifiers and help to avoid time consuming and expensive measurements in the laboratory. The complicated systems of interfering transitions make a simulation of fiber lasers and amplifiers equally valuable and attractive. Spectroscopic properties of the appropriate rare earth ion(s) play a major role in such a simulation, but not all of these properties may be measured directly or with reasonable effort from bulk glasses or fibers and thus must be calculated.

The simulation model described will act as a helpful tool during the laser and amplifier design process. It will help to understand the processes, which play a role in the lasing or amplification process and finally, it can be used to find out the optimum device parameters and predict the performance of the whole system.
A fiber laser and amplifier stationary simulation model has been described in this chapter allowing for unlimited spectral resolution. It is very useful for the development of cw rare-earth-doped fiber lasers and amplifiers and allows unlimited variations of the parameters to investigate the dependencies between them. Suppressing or increasing the cross section of a specific transition, for instance, is an experiment which is impossible in reality but quite easy in a computer model.
Since the number of parameters is large and their real values in many cases are unknown, one should not expect a quantitative agreement with the measurements in all cases. Of course, the discrepancies between measurement and simulation can be used to gather the correction factors to make the simulations closer to reality. Much more essential is to understand the physical background of laser and amplifier systems and the relationships between different parameters and processes occurring.
The application of the simulation model for an Yb^{3+}-doped and a Pr^{3+}-doped ZBLAN fiber laser has been shown. The insight into the active fiber obtained by the model has been demonstrated which is naturally hardly possible in experiments. The output power has been optimized for both laser systems. A superfluorescence source has been obtained in case of the red Pr^{3+}-doped ZBLAN fiber laser. Red, blue and orange Pr^{3+}-doped fiber lasers have been compared to one another. It has been found that the maximum output power of the red, blue and orange lasers is obtained for an output mirror with a reflectivity of 10 %, 75 % and 60 % in the respective wavelength ranges. The active fiber should be shortened by half a meter in case of the blue and orange lasers. The red laser shows the largest output power and the smallest threshold but the blue laser shows the largest slope efficiency of all three lasers.
In many cases it will be possible to fit the measurements by variation of the unknown parameters [15]. Thus, the simulation will be of great value when measured values of a certain setup are available and the simulation is used to optimize certain values, usually the output power. Besides, the simulation will turn out to be very successful in the interpretation of certain features in laser and amplifier characteristics as e.g. the order in which cascade laser transitions start lasing or the way in which they interact. To sum up, there is a large range of investigations possible with the simulation model at hand.

The remaining part of this chapter deals with cross relaxation processes between two different rare earth ions. This feature will be included in the stationary model and an example for its application will be shown as well.

5.6 Modeling energy transfer processes between different rare earth ions

Simulation of energy transfer processes in rare-earth-doped fiber lasers and amplifiers co-doped with different rare earth ions is an indispensable task. The prediction of the behavior of such kind of lasers and amplifiers plays a significant role in the development process. The presented model for arbitrary lasers and amplifiers in steady-state is extended to cover cross relaxation processes between two different rare earth ions.

5.6.1 Introduction

As mentioned above, several numerical rare-earth-doped fiber laser and amplifier models have already been presented in literature [21, 125, 147–149], mostly for TDFAs, EDFAs, and PDFAs or for TDFLs, EDFLs and PDFLs, based on silica and fluoride glasses, respectively.
In [147] and [148] seven-level models have been presented for EDFLs and EDFAs. In both publications Runge-Kutta methods have been used to find a numerical solution. This is also done in [149] in case of an EDFL based on ZBLAN glass which emits at 3 μm.
Krummrich presented a model of a PDFA [21] which does not take any simplifying assumptions into account and includes modeling of nonlinear effects. This radially resolved model calculates not only the spectral gain but also noise figure.
A black-box model to predict the TDFA performance was shown in [150]. It assumes a three-level homogeneously broadened system. Gain and ASE can be calculated as a function of three spectral functions and gain values for two reference wavelengths. The underlying simplicity is an advantage compared to numerical models, as they often require some parameters which are difficult to obtain. Therefore, this model is quick regarding computing time but does not help to understand the physical background of the amplification process.
Most numerical models presented in the literature are based on rate and gain equations but they significantly differ in their complexity. On the other hand, many analytical models have been developed to find analytical expressions for amplifier and laser parameters [18, 134, 151]. The analytic expressions derived in these publications only apply to the case of specific rare earth ions and comprise a maximum of four relevant energy levels. Zhao presented an analytical model for praseodymium-doped upconversion lasers [18], whereas Whitley derived analytical expressions for gain in PDFAs assuming a four-level system [151]. An analytical model for a three-level ytterbium-doped fiber amplifier was shown with several simplifying assumptions [134].
Modeling of energy transfer processes was also reported in literature [152–154]. Karasek and Yahel presented independently, models of EDFLs co-doped with ytterbium ions and considered energy transfer processes between both kind of ions [152, 153]. In [152] a modified Euler method was used to find a solution. Brunet presented a five-level TDFL emitting at 455 nm and considered energy transfer coefficients in the rate equations [154]. In this model pump and signal have been modeled separately.

Analytical models and general theory for two-, three- and four-level amplifiers and lasers have quite often been presented in literature [136–140]. To the best of the author's knowledge, energy transfer processes have been neglected in finding analytic expressions for rare-earth-doped devices.
In the remaining part of this chapter, the stationary model for arbitrary rare-earth-doped fiber lasers and amplifiers is extended to cover energy transfer processes between two different rare earth ions. Especially when co-dopants are used, energy transfer processes have to be taken into account.
The goal of the remaining part of this chapter is to present a simple numerical model which can be applied to arbitrary rare earth ions to simulate energy transfer processes in cw lasers and amplifiers in a variety of configurations. A general algorithm is presented to consider cross relaxation processes of two different rare earth ions.
To make the theoretical background clear, this section is started with a fundamental description of energy transfer in fiber lasers and amplifiers (section 5.6.2). Moreover, the rate and gain equations for energy transfer processes are presented (section 5.6.3). Furthermore, the discrete mathematical notation for the numerical model and the simulation algorithm will be presented in section 5.6.4. Finally, in section 5.7 the model is applied to simulate the red, orange and blue laser characteristics of a Pr^{3+}/Yb^{3+}-doped ZBLAN fiber laser. The output power of this laser is optimized and the results are compared to the Pr^{3+}-doped ZBLAN fiber laser simulated in section 5.5.2.

5.6.2 Energy transfer

The simulation model described so far does not cover energy transfer processes. Energy transfer (see also section 3.3) is caused by interactions between two dopant ions e.g. via dipole-dipole coupling. First of all, one must distinguish between energy transfers between rare earth ions of the same species and between different ions in case of a co-doped material. The main consequence of the former is concentration quenching (see also section 4.2.7), i.e. the lifetime of energy levels decreases in most cases with increasing dopant concentration. If the distance between ions of the same type is small enough to transfer the excitation energy of one ion to the other, a chain of energy transfer starts. This chain often ends at impurities of the glass matrix where the energy is absorbed by phonons and lost for the laser process. In contrast to the usually unwanted concentration quenching effect, energy transfer between different ions is often used for better performance of fiber lasers and amplifiers. A typical process of this kind is the cross relaxation process between two dopant ions. However, energy transfer is negligible at low dopant concentrations.
The transition rates of such processes are proportional to the occupation number of the initial levels of both interacting transitions. When such terms are inserted in the rate equations, they become non-linear which makes the solution much more difficult. However, the simulation kernel algorithm presented in section 5.4.2 is independent on the method used to solve the rate equations. A straightforward way to implement the important case of a co-dopant is

to fix, at first, the occupation numbers of dopant 2 and then solve the rate equations of dopant 1, which are now linear again. A valid assumption would be that the ground states of the rare earth ions are completely populated before the simulation starts. In the next step these results would be treated as fixed in the rate equations of dopant 2 to solve them. In the third step a better solution for the occupation numbers of dopant 1 are calculated and so forth. This iteration which is very similar to the main loop of the laser and amplifier simulation should converge to an approximation of the correct values after some iteration steps. Of course, such an additional iteration process for each fiber segment would increase the simulation time drastically. Nevertheless, this method turned out to be very efficient and thus it will be described in more detail in the following.

5.6.3 Rate and gain equations for energy transfer processes

Let us concentrate on the very simple Fabry-Perot laser setup shown in Figure 5.1. The fundamental fiber laser and amplifier operation has already been explained in detail in section 5.2. Using the same notation as before, the equations for a system of two rare earth ions including energy transfer processes will be presented. Most equations which have already been presented in section 5.2 have to be written down twice for both ion systems (by replacing the indices i and j by a and b for the second dopant ion). This procedure is very straight-forward. However, to account for accuracy and explicitness, a thorough formulation is given.
The rate equations now show the unknown cross relaxation rates X between ion system 1 and ion system 2 weighted by fixed values e_{c1} and e_{c2} which are given by the ratio of the molar concentrations of both ions:

$$\begin{aligned}\frac{\mathrm{d}n_i}{\mathrm{d}t} = \\ \sum_j \left[A_{ji} + W_{ji} + e_{c1} \sum_{ab} X_{jiab} \cdot n_a(x) + \int f(\lambda) \cdot \left(\phi^+(\lambda, x) + \phi^-(\lambda, x)\right) \cdot \sigma_{ji}(\lambda)\, \mathrm{d}\lambda \right] n_j(x) \\ - \sum_j \left[A_{ij} + W_{ij} + e_{c1} \sum_{ba} X_{ijba} \cdot n_b(x) + \int f(\lambda) \cdot \left(\phi^+(\lambda, x) + \phi^-(\lambda, x)\right) \cdot \sigma_{ij}(\lambda)\, \mathrm{d}\lambda \right] n_i(x)\,.\end{aligned} \tag{5.27}$$

As can be seen from this equation, the unknown cross relaxation rates X_{jiab} and X_{ijba} appear. e_{c1} is defined as $e_{c1} = \frac{c_{mol,dopant2}}{c_{mol,dopant1}}$ for dopant 1 and e_{c2} as $e_{c2} = \frac{c_{mol,dopant1}}{c_{mol,dopant2}}$ in case of dopant 2. The ratio indicates the part of the energy transferred from one ion system to the other one. The same equation has to be written down for the second ion with the indices a and b instead of i and j:

$$\frac{\mathrm{d}n_a}{\mathrm{d}t} =$$

$$\sum_b \left[A_{ba} + W_{ba} + e_{c2} \sum_{ij} X_{baij} \cdot n_i(x) + \int f(\lambda) \cdot \left(\phi^+(\lambda, x) + \phi^-(\lambda, x) \right) \cdot \sigma_{ba}(\lambda) \, \mathrm{d}\lambda \right] n_b(x)$$
$$- \sum_b \left[A_{ab} + W_{ab} + e_{c2} \sum_{ji} X_{abji} \cdot n_j(x) + \int f(\lambda) \cdot \left(\phi^+(\lambda, x) + \phi^-(\lambda, x) \right) \cdot \sigma_{ab}(\lambda) \, \mathrm{d}\lambda \right] n_a(x) . \tag{5.28}$$

Hence, one gets the additional unknown cross relaxation rates X_{baij} and X_{abji} and the equation contains the fixed value e_{c2} instead of e_{c1}. It must be emphasized that the majority of the cross relaxation rates are zero. The double sums for the cross relaxation rates are important and thus they are noted. n_i and n_a are the relative occupation numbers of energy levels i and a in the active material, $\phi(\lambda)$ the photon flux at the wavelength λ, and $\sigma(\lambda)$ the emission or absorption cross section. The variables x and t refer to position along the fiber axis and time, respectively.
A_{ij} and A_{ab} are the radiative emission rate of level i to j and from a to b, respectively, whereas W_{ij} and W_{ab} denote the non-radiative emissions mainly due to multi-phonon emission.
The factor $f(\lambda)$ in equations (5.27) and (5.28) contains the fraction of the total lateral intensity integral, which is interacting with the doped fiber core.
The conversation law for the occupation numbers must be extended for the two ion systems to:

$$\sum_i n_i(x) = 1 \quad \text{and} \quad \sum_a n_a(x) = 1. \tag{5.29}$$

Since both dopant ions can be regarded as a cascade of two systems, one obtains for the gain equations

$$\pm \frac{\mathrm{d}\phi^\pm(\lambda, x)}{\mathrm{dx}} = w(\lambda) \cdot n_\mathrm{I} \cdot \left(\sum_{ij} A_{ij} \cdot g_{ij}(\lambda) \, \mathrm{d}\lambda \cdot n_i(x) + \sum_{ab} A_{ab} \cdot g_{ab}(\lambda) \, \mathrm{d}\lambda \cdot n_a(x) \right)$$
$$+ \left[f(\lambda) \cdot n_I \left(\sum_{ij} \mathrm{sign}(i-j) \cdot \sigma_{ij}(\lambda) \cdot n_i(x) + \sum_{ab} \mathrm{sign}(a-b) \cdot \sigma_{ab}(\lambda) \cdot n_a(x) \right) \right.$$
$$\left. - \alpha(\lambda) \right] \cdot \phi^\pm(\lambda, x) , \tag{5.30}$$

where n_I denotes the density of dopant ions.
The boundary conditions in case of the bidirectionally pumped laser with Fabry-Perot cavity, as shown in Figure 5.1, are already given by equation (5.5). The rate equations (5.27) and (5.28) including the conservation law (5.29) together with the gain equations (5.30) and the boundary conditions (5.5) represent a complex system of coupled ordinary differential equations which can only be solved numerically. It is emphasized that by changing the boundary conditions (5.5), any other laser configuration or any fiber amplifier configuration can easily be modeled as well. In section 5.6.4, an algorithm will be discussed solving this set of equations in the stationary case, i.e. $\frac{\mathrm{d}n_i}{\mathrm{dt}} = 0$ for all i and $\frac{\mathrm{d}n_a}{\mathrm{dt}} = 0$ for all a, to simulate cw fiber lasers and amplifiers doped with two ions and including energy transfer.

5.6.4 Numerical simulation model for cross relaxation processes

All basic parameters which are needed for the simulation have been discussed in detail in section 5.3, thus it is resigned to give a thorough repetition here. $f(\lambda)$, $g_{ij}(\lambda)$ and $w(\lambda)$ have already been explicitly defined in sections 5.4.1 and 5.4.3.
As starting point, the mathematical description in order to find the required output variables such as the relative occupation numbers n_i and n_a and the forward and backward photon fluxes $\Phi^+(\lambda)$ and $\Phi^-(\lambda)$ is presented. So the plain photon flux $\Phi(\lambda)$ instead of its spectral counterpart $\phi(\lambda)$ is introduced. The model simulates the stationary case of an arbitrary laser or amplifier system in a rare-earth-doped fiber.
It is important to note that the indices i, j, a and b are used for the energy level which is already a discrete value, whereas the role of λ and x has not changed. Since only cw fiber lasers and amplifiers are of interest in this context, no change in the occupation number n of any energy level i and a has been assumed, which corresponds to $\frac{\mathrm{d}n_i}{\mathrm{dt}} = 0$ and $\frac{\mathrm{d}n_a}{\mathrm{dt}} = 0$, i.e. $\mathrm{dt} \to \infty$.
Following the discrete numerical formulation in section 5.4.1 for the stationary state, one concludes for the rate equations of level i in fiber segment p which comprise cross relaxation rates now

$$\begin{aligned}\frac{\mathrm{d}n_i}{\mathrm{dt}} = 0 = &\sum_j \left[A_{ji} + W_{ji} + e_{c1} \cdot \sum_{ab} X_{jiab} \cdot n_{ap} + \sum_\lambda f_\lambda \cdot \left(\Phi^+_{\lambda p} + \Phi^-_{\lambda p+1}\right) \cdot \sigma_{ji\lambda} \right] \cdot n_{jp} \\ &- \sum_j \left[A_{ij} + W_{ij} + e_{c1} \cdot \sum_{ba} X_{ijba} \cdot n_{bp} + \sum_\lambda f_\lambda \cdot \left(\Phi^+_{\lambda p} + \Phi^-_{\lambda p+1}\right) \cdot \sigma_{ij\lambda} \right] \cdot n_{ip}, \quad (5.31)\end{aligned}$$

and of level a in fiber segment p

$$\begin{aligned}\frac{\mathrm{d}n_a}{\mathrm{dt}} = 0 = &\sum_b \left[A_{ba} + W_{ba} + e_{c2} \cdot \sum_{ij} X_{baij} \cdot n_{ip} + \sum_\lambda f_\lambda \cdot \left(\Phi^+_{\lambda p} + \Phi^-_{\lambda p+1}\right) \cdot \sigma_{ba\lambda} \right] \cdot n_{bp} \\ &- \sum_b \left[A_{ab} + W_{ab} + e_{c2} \cdot \sum_{ji} X_{abji} \cdot n_{jp} + \sum_\lambda f_\lambda \cdot \left(\Phi^+_{\lambda p} + \Phi^-_{\lambda p+1}\right) \cdot \sigma_{ab\lambda} \right] \cdot n_{ap}. \quad (5.32)\end{aligned}$$

The matrices B^{sp}_{ij} and B^{sp}_{ab} (index sp stands for spontaneous emission) are defined to simplify these equations:

$$B^{sp}_{ij} = \begin{cases} -\sum_{j'} \left(A_{ij'} + W_{ij'}\right) & \text{if } j = i \text{ and} \\ A_{ji} + W_{ji} & \text{otherwise,} \end{cases} \quad (5.33)$$

$$B^{sp}_{ab} = \begin{cases} -\sum_{b'} \left(A_{ab'} + W_{ab'}\right) & \text{if } b = a \text{ and} \\ A_{ba} + W_{ba} & \text{otherwise.} \end{cases} \quad (5.34)$$

An analog definition for the terms of absorption and stimulated emission (index st) is now introduced for both ion systems:

$$B^{st}_{ij\lambda} = \begin{cases} -f_\lambda \cdot \sum_{j'} \sigma_{ij'\lambda} & \text{if } j = i \text{ and} \\ f_\lambda \cdot \sigma_{ji\lambda} & \text{otherwise,} \end{cases} \tag{5.35}$$

$$B^{st}_{ab\lambda} = \begin{cases} -f_\lambda \cdot \sum_{b'} \sigma_{ab'\lambda} & \text{if } b = a \text{ and} \\ f_\lambda \cdot \sigma_{ba\lambda} & \text{otherwise.} \end{cases} \tag{5.36}$$

New matrices for the energy transfer processes (index et) are now defined by:

$$B^{et}_{ija} = \begin{cases} -e_{c1} \cdot \sum_{j'b} X_{ij'ba} & \text{if } j = i \text{ and} \\ e_{c_1} \cdot \sum_b X_{jiab} & \text{otherwise,} \end{cases} \tag{5.37}$$

$$B^{et}_{abi} = \begin{cases} -e_{c2} \cdot \sum_{b'j} X_{ab'ji} & \text{if } b = a \text{ and} \\ e_{c2} \cdot \sum_j X_{baij} & \text{otherwise,} \end{cases} \tag{5.38}$$

with the factors e_{c1} and e_{c2} defined as the ratio of the respective molar concentrations of the two dopant ions.
All elements of all six matrices above are given before the actual simulation starts and thus are calculated outside the simulation kernel.
If one now assumes that the values of the photon fluxes into segment p are already known and defines the matrices B_{ijp} and B_{abp} by

$$\boxed{B_{ijp} = \begin{cases} 1 & \text{for } i = 0 \text{ and} \\ B^{sp}_{ij} + \sum_a B^{et}_{ija} \cdot n_{ap} + \sum_\lambda B^{st}_{ij\lambda} \cdot \left(\Phi^+_{\lambda p} + \Phi^-_{\lambda p+1}\right) & \text{otherwise,} \end{cases}} \tag{5.39}$$

and

$$\boxed{B_{abp} = \begin{cases} 1 & \text{for } a = 0 \text{ and} \\ B^{sp}_{ab} + \sum_i B^{et}_{abi} \cdot n_{ip} + \sum_\lambda B^{st}_{ab\lambda} \cdot \left(\Phi^+_{\lambda p} + \Phi^-_{\lambda p+1}\right) & \text{otherwise,} \end{cases}} \tag{5.40}$$

then the rate equations in the fiber segment p build a set of linear equations, which is solved by matrix inversion to get all relative occupation numbers (in the range between 0 and 1) of all energy levels of both ion systems in the fiber segment. The appropriate equation for level i is

$$\boxed{\sum_j B_{ijp} \cdot n_{jp} = \begin{cases} 1 & \text{for } i = 0 \text{ and} \\ 0 & \text{otherwise,} \end{cases}} \tag{5.41}$$

and for level a

$$\boxed{\sum_b B_{abp} \cdot n_{bp} = \begin{cases} 1 & \text{for } a = 0 \text{ and} \\ 0 & \text{otherwise,} \end{cases}} \tag{5.42}$$

where the special treatment of $i = 0$ and $a = 0$ includes equation (5.29).
After solving the rate equations one obtains the relative occupation of all energy levels which are now the input values for the gain equations (5.30). The photon flux traveling from left to the right can be written down

$$\begin{aligned} \frac{\Phi^+_{\lambda p+1} - \Phi^+_{\lambda p}}{\Delta x_p} &= w_\lambda \cdot n_I \cdot \left(\sum_{ij} A_{ij} \cdot g_{ij\lambda} \cdot n_{ip} + \sum_{ab} A_{ab} \cdot g_{ab\lambda} \cdot n_{ap} \right) \\ &\quad + f_\lambda \cdot n_I \left(\sum_{ij} \operatorname{sign}(i-j) \cdot \sigma_{ij\lambda} \cdot n_{ip} + \sum_{ab} \operatorname{sign}(a-b) \cdot \sigma_{ab\lambda} \cdot n_{ap} \right) \cdot \Phi^+_{\lambda p} \\ &\quad - \alpha_\lambda \cdot \Phi^+_{\lambda p}, \end{aligned} \tag{5.43}$$

and in the opposite direction

$$\begin{aligned} \frac{\Phi^-_{\lambda p} - \Phi^-_{\lambda p+1}}{\Delta x_p} &= w_\lambda \cdot n_I \cdot \left(\sum_{ij} A_{ij} \cdot g_{ij\lambda} \cdot n_{ip} + \sum_{ab} A_{ab} \cdot g_{ab\lambda} \cdot n_{ap} \right) \\ &\quad + f_\lambda \cdot n_I \left(\sum_{ij} \operatorname{sign}(i-j) \cdot \sigma_{ij\lambda} \cdot n_{ip} + \sum_{ab} \operatorname{sign}(a-b) \cdot \sigma_{ab\lambda} \cdot n_{ap} \right) \cdot \Phi^-_{\lambda p+1} \\ &\quad - \alpha_\lambda \cdot \Phi^-_{\lambda p+1}, \end{aligned} \tag{5.44}$$

where Δx_p is the fiber segment's length.
Again, some definitions for matrices containing all data known before the simulation starts are presented. For the term of spontaneous emission (index sp) let us define

$$G^{sp}_{\lambda pi} = n_I \cdot w_\lambda \cdot \Delta x_p \cdot \sum_j A_{ij} \cdot g_{ij\lambda}, \tag{5.45}$$

$$G^{sp}_{\lambda pa} = n_I \cdot w_\lambda \cdot \Delta x_p \cdot \sum_b A_{ab} \cdot g_{ab\lambda}, \tag{5.46}$$

and for the term of absorption and stimulated emission (index st)

$$G^{st}_{\lambda pi} = n_I \cdot f_\lambda \cdot \Delta x_p \cdot \sum_j \operatorname{sign}(i-j) \cdot \sigma_{ij\lambda}, \tag{5.47}$$

$$G^{st}_{\lambda pa} = n_I \cdot f_\lambda \cdot \Delta x_p \cdot \sum_b \operatorname{sign}(a-b) \cdot \sigma_{ab\lambda}. \tag{5.48}$$

The same definition as in section 5.4.1 is used for the background losses (index *att*):

$$G_{\lambda p}^{att} = -\alpha_\lambda \cdot \Delta x_p \quad \text{for } \alpha_\lambda > 0. \tag{5.49}$$

As soon as one knows the values of the relative occupation numbers n_{ip} and n_{ap} in segment p, one can calculate the two new matrices for the cascaded system

$$\boxed{\begin{aligned} G_{\lambda p}^{(1)} &= \sum_i G_{\lambda pi}^{sp} \cdot n_{ip} + \sum_a G_{\lambda pa}^{sp} \cdot n_{ap} \quad \text{and} \\ G_{\lambda p}^{(2)} &= 1 + \sum_i G_{\lambda pi}^{st} \cdot n_{ip} + \sum_a G_{\lambda pa}^{st} \cdot n_{ap} + G_{\lambda p}^{att}, \end{aligned}} \tag{5.50}$$

in order to simplify the expression of the gain equations. Similarly to section 5.4.1, it might be advisable to improve convergence by introducing a denominator for the matrix $G_{\lambda p}^{(2)}$ in equation (5.50). This term may look like $(1 + q_{damp} \cdot (Q - Q_{max}))^2$, where q_{damp} is a dimensionless damping factor usually larger than 1, and the factors Q and Q_{max} define the break criterion for the simulation kernel which will be introduced below. With this term it would follow that if Q equals Q_{max} the matrix $G_{\lambda p}^{(2)}$ would remain unchanged. This would account for undamped oscillations in the photon fluxes between successive iterations (see also section 5.4.1).
The photon flux leaving segment p in the direction of the pump beam and in the opposite direction can now be calculated by

$$\boxed{\begin{aligned} \Phi_{\lambda p+1}^{+} &= G_{\lambda p}^{(1)} + G_{\lambda p}^{(2)} \cdot \Phi_{\lambda p}^{+} \quad \text{and} \\ \Phi_{\lambda p}^{-} &= G_{\lambda p}^{(1)} + G_{\lambda p}^{(2)} \cdot \Phi_{\lambda p+1}^{-}. \end{aligned}} \tag{5.51}$$

Still the gain equations are solved by the FDM.
According to equation (5.5) the fluxes are partially reflected by the mirrors at the fiber ends and fluxes $\Phi_{\lambda,pump}^{fw}$ and $\Phi_{\lambda,pump}^{bw}$ of pump photons are added from both ends, which leads to the equations

$$\boxed{\begin{aligned} \Phi_{\lambda 0}^{+} &= R_\lambda^{in} \cdot \Phi_{\lambda 0}^{-} + T_\lambda^{in} \cdot \Phi_{\lambda,pump}^{fw} \quad \text{and} \\ \Phi_{\lambda m}^{-} &= R_\lambda^{out} \cdot \Phi_{\lambda m}^{+} + T_\lambda^{out} \cdot \Phi_{\lambda,pump}^{bw}, \end{aligned}} \tag{5.52}$$

if the number of fiber segments is m.

The boxed expressions above set up the equations needed for the simulation kernel of the cross relaxation process (see Figure 5.15 for a pseudo-code description of the algorithm used). The algorithm which will be introduced is basically the same as in section 5.4.2 except for the two inner loops which account for cross relaxation between both ions.
For the break criterion the definition in equation (5.24) is taken. The iteration loop is left when Q falls below a certain defined value Q_{max}. An additional break criterion has to be defined for the inner loops in the simulation kernel concerning the cross relaxation processes:

$$Q_{kernel} = \max_\lambda \left(\left| n_{ip} - n_i^0 \right|, \left| n_{ap} - n_a^0 \right| \right) \leq Q_{kernel,max}. \tag{5.53}$$

initial conditions: $\Phi^{\pm}_{\lambda p} = 0$

$\Phi^{+}_{\lambda 0} = T^{in}_{\lambda} \cdot \Phi^{fw}_{\lambda,pump}$

$\Phi^{-}_{\lambda m} = T^{out}_{\lambda} \cdot \Phi^{bw}_{\lambda,pump}$

$n_{jp} = 0$ and $n_{bp} = 0$ for $j,b > 0$

$n_{0p} = 1$ for $j,b = 0$

repeat

  for $p = 0$ **to** $m-1$

    repeat

      calculate n_{jp} and n_{bp} (5.39), (5.41), (5.40), (5.42)

    until (5.53) fulfilled

    calculate $\Phi^{+}_{\lambda p+1}$ (5.50), (5.51)

  $\Phi^{-}_{\lambda m} = R^{out}_{\lambda} \cdot \Phi^{+}_{\lambda m} + T^{out}_{\lambda} \cdot \Phi^{bw}_{\lambda,pump}$ (5.52)

  for $p = m-1$ **to** 0

    repeat

      calculate n_{jp} and n_{bp} (5.39), (5.41), (5.40), (5.42)

    until (5.53) fulfilled

    calculate $\Phi^{-}_{\lambda p}$ (5.50), (5.51)

  $\Phi^{+}_{\lambda 0} = R^{in}_{\lambda} \cdot \Phi^{-}_{\lambda 0} + T^{in}_{\lambda} \cdot \Phi^{fw}_{\lambda,pump}$ (5.52)

until converged

$\Phi^{out,fw}_{\lambda} = T^{out}_{\lambda} \cdot \Phi^{+}_{\lambda m}$

$\Phi^{out,bw}_{\lambda} = T^{in}_{\lambda} \cdot \Phi^{-}_{\lambda 0}$

Figure 5.15: Algorithm of the simulation kernel in pseudo-code of cross relaxation processes between two rare earth ions with the appropriate equations indicated

In equation (5.53) the absolute deviation of the occupation numbers of both ion systems is compared (n_i^0 and n_a^0 are the relative occupation numbers from the last iteration step) and if it is below a certain defined value $Q_{kernel,max}$, the algorithm proceeds. Therefore, the simulation slows down at calculation steps where cross relaxation occurs ($X \neq 0$). Since the value of the cross relaxation rates X is unknown, its value has to be estimated. It must be at least on the order of the sum of radiative and non-radiative transition rates of the respective transitions to have a significant effect. Of course, the value of X strongly depends on the ion concentration in the fiber core.

5.7 Pr^{3+}/Yb^{3+}-doped fiber laser simulation

Extensive studies for the cross relaxation rates have been performed and the following values have been extracted:

For the parameter X_{1006} which represents the transition

$$Yb^{3+} \quad (^2F_{5/2}), \quad Pr^{3+} \quad (^3H_4) \rightarrow Yb^{3+} \quad (^2F_{7/2}), \quad Pr^{3+} \quad (^1G_4),$$

a value of 20000 s^{-1}, and for X_{0196} representing the transition

$$Pr^{3+} \quad (^3P_J), \quad Yb^{3+} \quad (^2F_{7/2}) \rightarrow Pr^{3+} \quad (^1G_4), \quad Yb^{3+} \quad (^2F_{5/2}),$$

a value of 500000 s^{-1} have been obtained. These studies had the intention to obtain a good qualitative agreement with experiments performed by Baraniecki [14] for Pr^{3+}/Yb^{3+}-doped ZBLAN fiber lasers. All other possible cross relaxation rates have been assumed to be zero. It must be mentioned that X_{0196} can also be extracted from lifetime experiments which have been performed and described in detail in section 4.2. There, a lifetime of about 39 μs has been measured for a 0.3 mol% Pr^{3+}-doped ZBLAN glass sample. Co-doping the sample with an amount of 2 mol% Yb^{3+} led to a fluorescent lifetime of about 21 μs (see Figure 4.15). Hence, one could extract an increase in efficiency of exactly 82 % for the energy transfer from Pr^{3+} to Yb^{3+}. A value of 21077 s^{-1} for the cross relaxation rate can be extracted by these measurements since non-radiative transitions and thus the losses are included in the fluorescent lifetime experiments as well. However, a large series of simulations have been carried out with this value and extensive parameter investigations have been performed but no lasing could be achieved with this value and the same set of simulation parameters as in section 5.5.2 and including Yb^{3+} as co-dopant. Even when the active fiber length is chosen to be long enough to completely absorb the 835 nm pump power, no laser is obtained. The reason lies in the fact that the ground states of praseodymium and ytterbium remain fully populated (the $^3H_4$ and the $^2F_{7/2}$ level) and the photon fluxes converge very fast to zero. The cross relaxation rates are highly sensitive parameters and, hence, a discrepancy between experiment and theory is observed in case of Pr^{3+}/Yb^{3+}-doped fiber lasers assuming that both mentioned energy transfers are the dominant transfers occurring which seems to be a reasonable assumption. To sum up, the above mentioned value of 500000 s^{-1} (a factor of 24 larger than the extracted value) led to the best qualitative agreement with the experiments performed by Baraniecki and thus has been used for all Pr^{3+}/Yb^{3+}-doped fiber laser simulations performed in this work.

The same set of simulation parameters as in section 5.5.2 has been chosen for the following simulations of the Pr^{3+}/Yb^{3+}-doped ZBLAN fiber laser. An Yb^{3+} concentration of 20000 ppm has been specified by Le Verre Fluore for the same fiber as in section 5.5.2 but this time with ytterbium ions as co-dopant. This value leads to an ytterbium ion density n_I of $3.68 \cdot 10^{26}$ ions/m^3 in the fiber core. The conventional upconversion pumping scheme is simulated in this section i.e. only a pump wavelength of 835 nm is sufficient to obtain lasing which is an economical advantage compared to purely praseodymium-doped fiber lasers as they need two pump sources. Both Yb^{3+} levels in the transmission window of ZBLAN (see energy level diagram of Figure 3.6) are considered. The Yb^{3+} GSA and its emission have been presented in Figure 5.4. All radiative transition rates have been taken from [15] and for ytterbium the same value as

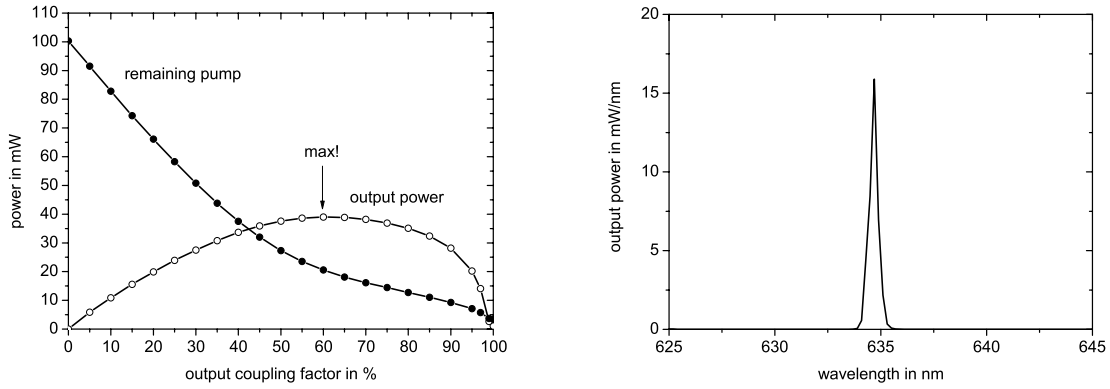

Figure 5.16: Output power and remaining pump power at the right fiber end versus output coupling factor (left), and, spectral output power at right fiber end for a pump power of 120 mW at 835 nm (right). The spectral output power is plotted for a mirror reflectivity of 40 % where maximum output power is obtained.

in section 5.5.1 has been chosen.
The aim of this section is to compare the results for the Pr^{3+}/Yb^{3+}-doped ZBLAN fiber laser to the results of the Pr^{3+}-doped fiber laser simulated in section 5.5.2. Hence, the same pump power of 120 mW at 835 nm is chosen to enter the Fabry-Perot cavity from the left side. It is noted that in case of the Pr^{3+}-doped fiber laser also 100 mW pump power at 1020 nm has been taken additionally to the mentioned amount of pump power at 835 nm.

The active fiber length is chosen to absorb most of the pump power and the output mirror reflectivity is varied in the range of 0 % to 100 % to find the optimum output coupling with regard to maximum output power. It is a well-known fact that in case of the avalanche upconversion scheme the pump power is worse absorbed than in resonant pumping schemes. For the optimum setting red, orange and blue laser characteristics will be simulated.

Red laser

Since the red laser showed a worse convergence of the occupation numbers the precision has been increased from $Q_{max} = 15 \cdot 10^{-2}$ to $5 \cdot 10^{-2}$ in this case. The optimum fiber length of the Pr^{3+}/Yb^{3+}:ZBLAN fiber turned out to be about 1 m which is 2.5 m less than the active fiber length of the red praseodymium-doped fiber laser.
In the left part of Figure 5.16 the output power and the remaining pump power is plotted against the output coupling factor showing that for an output coupling factor of 60 % maximum output power of 39 mW is obtained. The emission wavelength is 633 nm and a maximum power of -16 dBm/nm has reached the right fiber end which is about 4 dBm/nm smaller than the value for the red praseodymium-doped fiber laser. For no reflection a weak superfluorescence source of about 1 mW output power is obtained which is considerably weaker

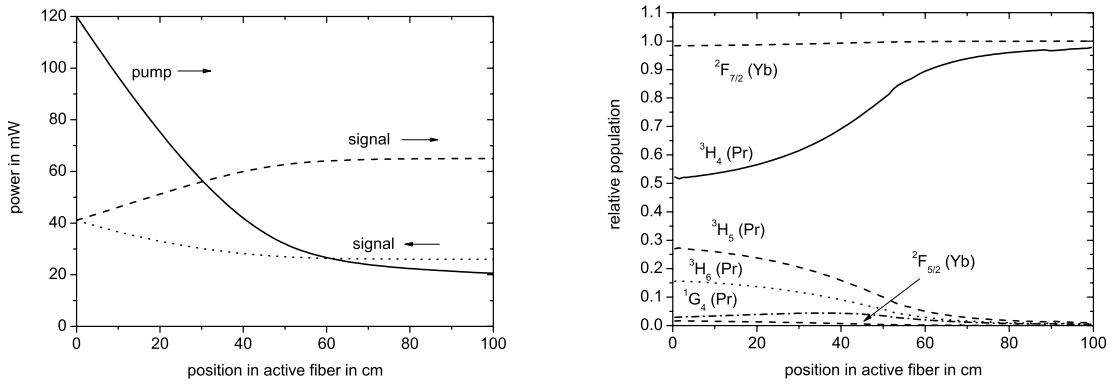

Figure 5.17: Pump power (solid line) and signal powers in forward (dashed line) and backward (dotted line) direction (left), and, relative population (right) of the ground level $^3H_4$ (solid line) and the excited levels $^3H_5$ (dashed line), $^3H_6$ (dotted line) and $^1G_4$ (dash-dotted line) of praseodymium and both ytterbium energy levels (dashed lines) along the position in the active fiber for the simulated red Pr^{3+}/Yb^{3+}-doped ZBLAN fiber laser

than in case of the purely Pr^{3+}-doped ZBLAN fiber. The pump power absorption increases monotonously with increasing output coupling factor. 20.6 mW of the 835 nm pump power is left at the right fiber end for the maximum output power which represents a pump absorption of about 83 %. Therefore, a mirror reflectivity of 40 % has to be chosen. All following calculations will be done with this value.

The spectral output power is shown in the right part of Figure 5.16 indicating the same emission wavelength as for the red praseodymium-doped fiber laser, namely 633 nm, but smaller output power. Signal and pump powers are shown in the left part of Figure 5.17. As one can see the pump power at the right fiber is absorbed by a high degree but a better absorption is not possible in case of the avalanche upconversion pumping scheme. By increasing the fiber length to about 3.5 m a significantly different behavior of the pump power evolution has been observed. In the first half meter of the fiber the pump power drops to roughly 25 % of its former value and in the remaining 3 m to the fiber end only a slight decrease can be observed. However, this is not the optimum fiber length and as already stated above, a value of about 1 m turned out to be optimum. This behavior is in close relation to the relative occupation numbers which are shown in the right part of Figure 5.17. Forward and backward signal both increase along the position in the active fiber.

The distribution of the relative occupation numbers of all relevant energy levels along the fiber are shown in the right part of this figure. The pump power in the active fiber strongly depletes the ground level $^3H_4$ so that about half of the dopant ions are excited at the beginning of the fiber. Towards the end of the active fiber this number decreases to almost zero so that all ions occupy the ground states of praseodymium and ytterbium. In the fiber the

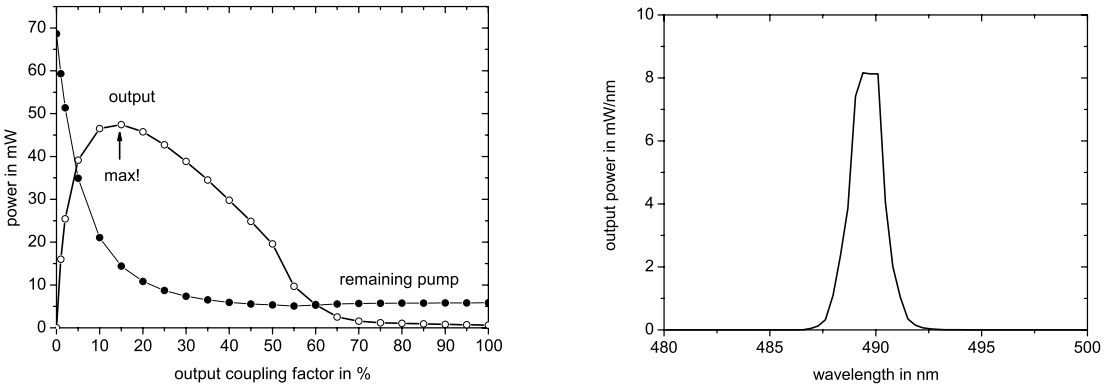

Figure 5.18: Output power and remaining pump power at the right fiber end versus output coupling factor (left), and, spectral output power at right fiber end for a pump power of 120 mW at 835 nm (right). The spectral output power is plotted for a mirror reflectivity of 85 % where maximum output power is obtained.

occupation number of the first excited level $^3H_5$ is larger than that of all other excited states including the second excited level $^3H_6$ and the $^1G_4$ level. The occupation of the $^1G_4$ level plays also a role in the avalanche upconversion pumping scheme. However, as can be concluded from the behavior of the Pr^{3+} occupation numbers, energy transfer in case of the red laser is very effective due to the low occupance of the $^1G_4$ level. After passing about 70 cm of the active fiber nearly all ions are in the ground states of Pr^{3+} and Yb^{3+} showing that a laser is lasing. For Yb^{3+} the behavior is much simpler since along the whole fiber length the ground level $^2F_{7/2}$ is almost completely populated whereas the occupation of the excited level $^2F_{7/2}$ is nearly zero. The ratio of the Yb^{3+} occupation numbers is more or less constant along the fiber.

Blue laser

For the blue laser an optimum fiber length of about 15 cm has been determined which represents an enormous reduction of 85 % in active fiber length compared to the red laser. Compared to the blue praseodymium-doped fiber laser it is also an enormous reduction from 3 m to the obtained 15 cm. The emission wavelength is shifted to the longer wavelength 489.4 nm compared to the 468.5 nm for the blue praseodymium-doped fiber laser. An output coupling factor of 15 % turned out to be the optimum value as shown in the left part of Figure 5.18.
An output power of 47.5 mW has been obtained for a mirror reflectivity of 85 % which is a larger power value than that for the red laser. The pump power at the right fiber end amounts 14.4 mW indicating a pump absorption of 88 %. Pump power absorption increases monotonously with increasing output coupling factor but after reaching 50 % the remaining pump power stays constant to about 6 mW. For larger values than 65 % output coupling al-

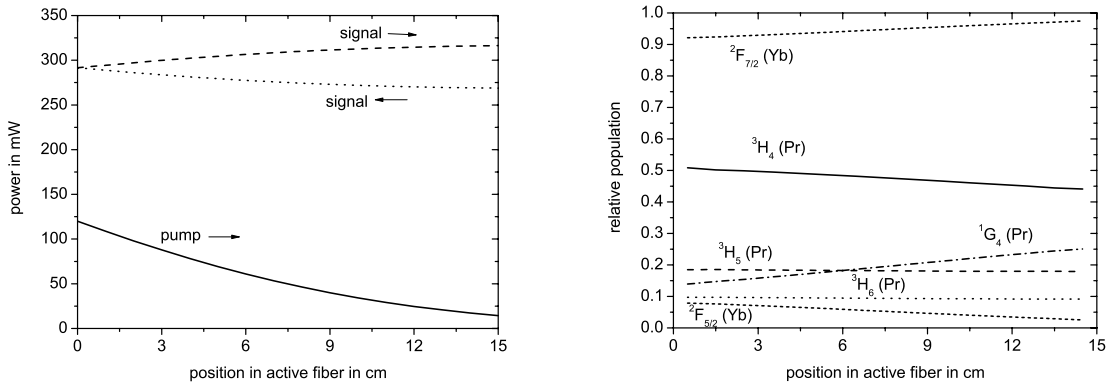

Figure 5.19: Pump power (solid line) and signal powers in forward (dashed line) and backward (dotted line) direction (left), and, relative population (right) of the ground level $^3H_4$ (solid line) and the excited levels $^3H_5$ (dashed line), $^3H_6$ (dotted line) and $^1G_4$ (dash-dotted line) of praseodymium and both ytterbium energy levels (dashed lines) along the position in the active fiber for the simulated blue Pr^{3+}/Yb^{3+}-doped ZBLAN fiber laser

most no output power is obtained. The spectral power, in the right part of Figure 5.18, shows the case for 85 % reflection (maximum output power). A maximum power of -18 dBm/nm has reached the right fiber end for the optimum mirror reflection.
In the left part of Figure 5.19 signal and pump powers in case of the blue laser are plotted. At 15 cm almost 90 % of the pump power is absorbed leading to maximum output power. The qualitative and to a high degree also the quantitative behavior of the signal powers is similar to the blue praseodymium-doped laser. The large signal powers in the resonator are due to the high energy of the blue emission.
In the right part of Figure 5.19 the relative occupation numbers of all relevant energy levels of praseodymium and ytterbium are shown. The behavior of the $^3H_4$, $^3H_5$ and $^3H_6$ level is different to all lasers simulated so far. Again about half of the dopant ions are excited at the beginning of the active fiber but their number increases slightly to about 55 % towards the active fiber end. The ratio of the $^3H_5$ and $^3H_6$ occupation number is almost constant as their traces run nearly parallel. However, these values also slightly decrease to the end of the fiber. The reason lies in the occupation of the $^1G_4$ level which increases linearly from 15 % to about 25 % along the position indicating the major role of this level for the energy transfer in this blue three-level laser. At 6 cm the $^1G_4$ occupation crosses the value of the $^3H_5$ level and becomes larger. As expected the ground energy level of ytterbium is almost completely populated along the whole fiber length.

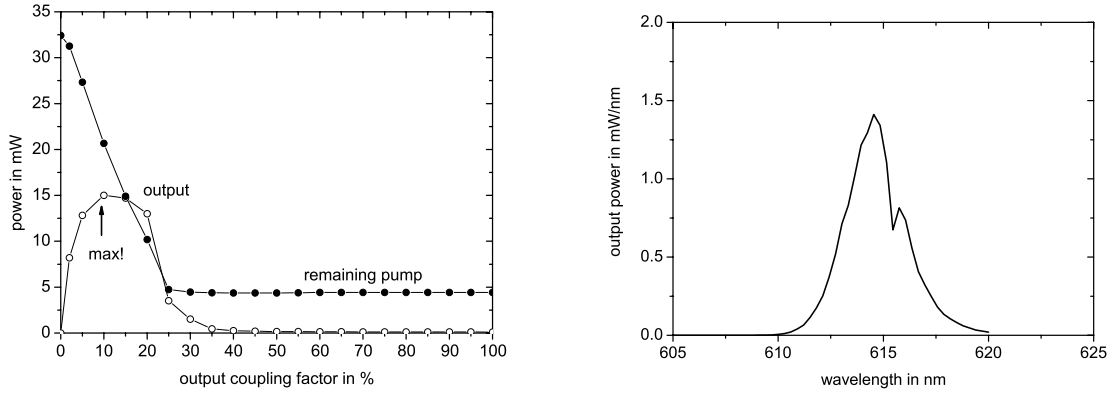

Figure 5.20: Output power at the right fiber end and remaining pump power versus output coupling factor (left), and, spectral output power at right fiber end for a pump power of 120 mW at 835 nm (right). The spectral output power is plotted for a mirror reflectivity of 90 % where maximum output power is obtained.

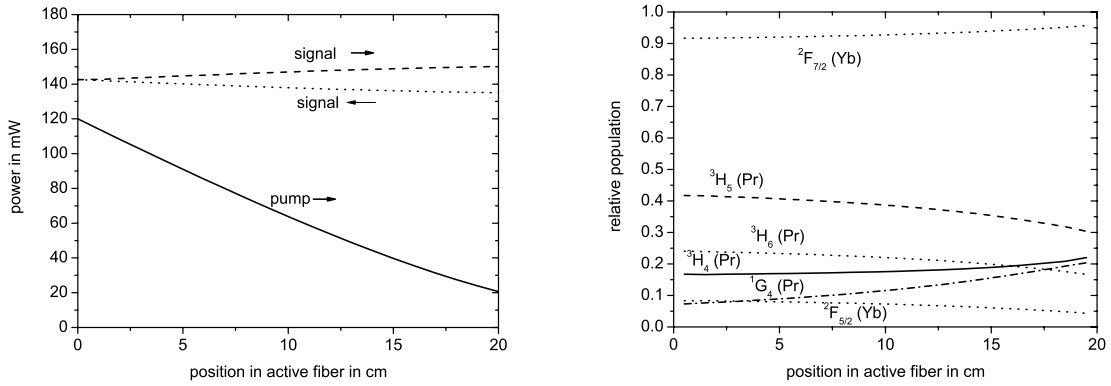

Figure 5.21: Pump power (solid line) and signal powers in forward (dashed line) and backward (dotted line) direction (left), and, relative population (right) of the ground level $^3H_4$ (solid line) and the excited levels $^3H_5$ (dashed line), $^3H_6$ (dotted line) and $^1G_4$ (dash-dotted line) of praseodymium and both ytterbium energy levels (dashed lines) along the position in the active fiber for the simulated orange Pr^{3+}/Yb^{3+}-doped ZBLAN fiber laser

Orange laser

In case of the orange laser an optimum fiber length of about 20 cm has been determined which is only slightly larger as for the blue laser but, on the other hand, significantly smaller than for the orange Pr^{3+}-doped ZBLAN fiber laser. The emission wavelength of the orange laser is 613 nm which is slightly smaller than the 617.3 nm for the orange praseodymium-doped

fiber laser. An output coupling factor of 10 % turned out to be the optimum value as shown in the left part of Figure 5.20.
A maximum output power of 15 mW has been obtained for a mirror reflectivity of 90 %. The pump power at the right fiber end amounts to 20.7 mW in this case indicating a pump absorption of about 83 % which is not the minimum value since for output coupling factors larger than 25 % nearly 95 % pump absorption is obtained. However, choosing such output coupling factors would drastically reduce the output power since for larger values than 35 % output coupling almost no output power is obtained. Hence, this behavior shows that the orange laser is highly sensitive with regard to mirror reflectivity. The spectral power, in the right part of Figure 5.20, shows that a maximum power of -26 dBm/nm has reached the right fiber end and, as already mentioned, the emission wavelength is 613 nm.
Signal and pump powers in case of the orange laser are shown in the left part of Figure 5.21. It can be seen why a fiber length of 20 cm is optimum. The qualitative behavior of the signal powers is similar to the blue laser but showing smaller values. However, these signal values are larger than for the red laser and also the respective values for the orange praseodymium-doped fiber laser. But the gain is smaller than for the red and blue lasers as was also the case for the Pr^{3+}-doped fiber laser.
In the right part of Figure 5.21 the relative occupation numbers of the energy levels $^3H_4$, $^3H_5$, $^3H_6$ and $^1G_4$ of praseodymium and both energy levels of ytterbium are shown as a function of position along the active fiber. Qualitatively the same behavior as for the blue laser is observed.
This time almost 85 % of the dopant ions are excited at the beginning of the active fiber and their number decreases slightly to about 78 % towards the end of the active fiber. These numbers are larger than for the blue laser as it is a four-level laser. The ratio of the $^3H_5$ and $^3H_6$ occupation numbers is almost constant as their traces run nearly parallel. However, these values also slightly decrease to the end of the fiber as for the blue laser. Again the occupation of the $^1G_4$ level is responsible for this behavior. It increases but this time non-linearly from 7 % to about 20 %. At about 17.5 cm the $^1G_4$ occupation crosses the value of the $^3H_6$ level. The same quantitative behavior of the ytterbium occupation numbers as for the red and blue lasers is observable.

Laser characteristics of red, blue and orange lasers

The red, blue and orange laser characteristics of the simulated Pr^{3+}/Yb^{3+}-doped ZBLAN fiber laser are shown in Figure 5.22. The 835 nm pump power has been varied in 10 mW steps in the range of 0 to 120 mW.
The red laser characteristic shows the smallest threshold power of all three lasers. A linear fit to the graph results in a threshold power of 28.5 mW and a slope efficiency of 43 % indicating the lower efficiency of the avalanche upconversion pumping scheme compared to a resonant pumping scheme. A maximum output power of 39 mW is achieved for a pump power of 120 mW at 835 nm resulting in a PCE of 32.5 %.

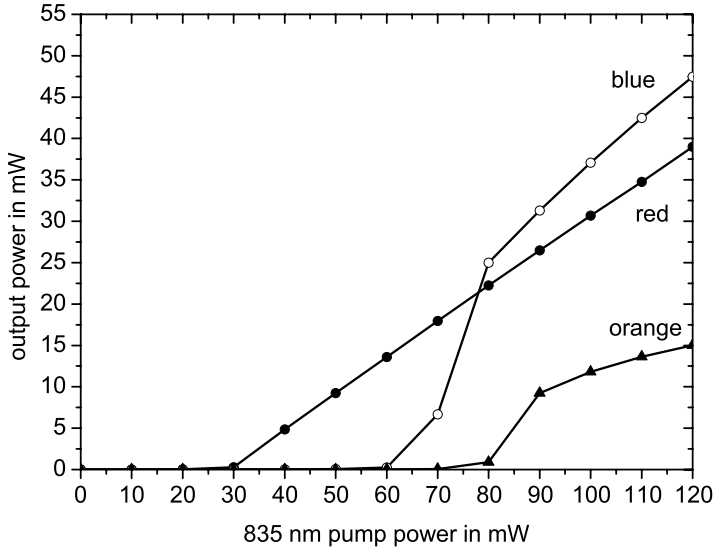

Figure 5.22: Red, blue and orange laser characteristics of the simulated Pr^{3+}/Yb^{3+}-doped ZBLAN fiber laser for varying 835 nm pump power.

For the blue laser a larger threshold power of about 57 mW is obtained which is a factor of two larger than for the red laser. A linear fit to the graph results in a slope efficiency of 80 % which is 37 % larger than for the red laser. A maximum output power of 47.5 mW is achieved. This results in a PCE of about 40 % which is the same value as for the blue praseodymium-doped fiber laser.
The orange laser shows the largest threshold power of 69.4 mW which is a factor of 1.2 larger than for the blue one. A slope efficiency of 33 % can be extracted from the graph. 15 mW has been obtained as maximum output power resulting in a PCE of 12.5 % which again is the same value as for the orange praseodymium-doped fiber laser.
To sum up, slope efficiency and maximum output power of the blue laser is the largest of all three lasers. But the red laser shows the smallest threshold power.

Comparison to the praseodymium-doped ZBLAN fiber laser

The application of the extended simulation model for a Pr^{3+}/Yb^{3+}-doped ZBLAN fiber laser has been shown. The simulations have approved the qualitative behavior of such avalanche upconversion fiber lasers. All simulated lasers have been optimized to absorb roughly 90 % of the pump power(s) and the optimum mirror reflectivity and fiber length have been determined to obtain maximum output power.
A strong red superfluorescence source has been obtained in case of the Pr^{3+}-doped ZBLAN

fiber. Red, blue and orange Pr^{3+}-doped fiber lasers have been compared to one another. It has been found that the maximum output power of the red, blue and orange lasers is obtained for an output mirror with a reflectivity of 10 %, 75 % and 60 % in the respective wavelength ranges. The active fiber should be shortened by half a meter in case of the blue and orange lasers.
In case of the Pr^{3+}/Yb^{3+}-doped ZBLAN fiber laser the output mirror should show a reflectivity of 40 %, 85 % and 90 % in the respective wavelength ranges of the red, blue and orange lasers. In case of the red laser an optimum length of 1 m instead of 3.5 m as for the red praseodymium-doped fiber laser led to maximum output power. After 50 cm only 72 % of the pump power is absorbed. It must be mentioned that a reduction of fiber length to 50 cm led only to an output power of 35 mW (compared to the obtained 39 mW for the 1 m long fiber) and to a worse pump absorption since about 34 mW of the pump is left at the right fiber end of the 50 cm long active fiber. However, an enormous reduction of active fiber length has also been observed in case of the orange and blue lasers. The active fiber can be shortened from 3 m to about 20 cm and 15 cm, respectively, which means that by co-doping the Pr^{3+}-doped fiber with ytterbium ions, the optimum fiber length will be significantly less. Qualitatively the same behavior has been observed by laser experiments performed by Baraniecki [14]. The reduction of fiber length in case of all three lasers is also an economical advantage due to the high price of rare-earth-doped fluoride fibers.
Obviously, energy transfer between praseodymium and ytterbium results in less pump absorption but to an effective decrease of active fiber length needed to obtain maximum output power. However, the results showed that the Pr^{3+}/Yb^{3+}-doped ZBLAN fiber laser is more sensitive with regard to pump power, mirror reflectivity and fiber length and thus is more difficult to optimize than the Pr^{3+}-doped ZBLAN fiber laser.
Of course, the advantage of the Pr^{3+}/Yb^{3+}-doped fiber laser is that it only needs one pump source whereas the purely praseodymium-doped fiber laser needs two (the additional 1020 nm pump). Nevertheless, praseodymium-doped fiber lasers are more effective due to the resonant pumping scheme and one obtains larger output powers. On the other hand, the economical disadvantage of two pump sources is rather low since cheap 1020 nm ytterbium pump lasers can be bought, nowadays. However, the avalanche upconversion pumping scheme is still of interest but high slope efficiencies as for Pr^{3+}-doped fiber lasers are not expected although different fiber parameters can still be optimized to improve its efficiency.
Regarding the red, blue and orange laser characteristics of both lasers the Pr^{3+}/Yb^{3+}-doped fiber laser always shows a larger threshold power and a smaller slope efficiency than the Pr^{3+}-doped fiber laser for the same 835 nm pump power. In all cases, the maximum output power is smaller. Let us summarize the following results:
In case of the red laser the threshold power increases from 8.7 to 28.5 mW and slope efficiency decreases from 105 % to 43 %. A maximum output power of 39 mW compared to 109 mW, and, a PCE of 32.5 % compared to 49.5 % is obtained.
For the blue laser the threshold power increases from 37 to 57 mW and slope efficiency decreases from 116 % to 80 %. A maximum output power of 47.5 mW compared to 87.7 mW is

obtained. In both cases, a PCE of about 40 % is achieved.
Finally, in case of the orange laser the threshold power increases from 59 to 69.4 mW and slope efficiency decreases from 50 % to 33 %. A maximum output power of 15 mW compared to 27.6 mW is obtained. PCE amounts to 12.5 % in both cases.

5.8 Summary

The stationary fiber laser and amplifier simulation model from section 5.4 has been extended in section 5.6.4 to take energy transfer processes between two ions into account. It allows for unlimited spectral resolution and will be very useful in the development process of cw rare-earth-doped fiber lasers and amplifiers in case of co-dopants.
The application of the extended model for a Pr^{3+}/Yb^{3+}-doped ZBLAN fiber laser has been demonstrated. The qualitative impact of the avalanche upconversion process on laser performance has been shown. Red, orange and blue lasers have been optimized and compared to the Pr^{3+}-doped ZBLAN fiber laser simulated in section 5.5.2.
All examples shown underline the enormous saving of expenses by using the simulation model rather than building all lasers in the laboratory. As has already been mentioned, discrepancies of the total power between measurement and simulation can be used to gather the correction factors, which makes the simulations more close to reality. But this was not the aim of this work. In fact, different laser systems have been optimized with regard to output power and their characteristics have been compared to one another resembling the typical approach of system designers. Nevertheless, it is very important to understand the physical background of different lasers and the relationships between different parameters and processes occurring in them. Due to time reasons, this could unfortunately not done within the frame of this work. However, the author hopes that the extension of the stationary model to cover cross relaxation processes will be used by researchers in this field to optimize avalanche upconversion lasers, and, an even more essential point, to investigate different physical relations accurately.
The model can be modified to include radial resolution in the active fiber and to include multi-mode operation as well. It is the author's hope that the presented model described in this chapter will be applied to simulate arbitrary rare-earth-doped fiber lasers and amplifiers in steady-state and its extension will be applied to simulate energy transfer processes between two dopant ions in such lasers and amplifiers.

6 Dynamic model for rare-earth-doped fiber lasers and amplifiers

In this chapter, a novel dynamic model for the simulation of arbitrary rare-earth-doped fiber lasers and amplifiers is presented. A model for a single rare earth ion is presented and then it is extended to model energy transfer processes in lasers and amplifiers doped with two rare earth ions. The model is applied to simulate the dynamics of ytterbium-doped, praseodymium-doped and Pr^{3+}/Yb^{3+}-doped ZBLAN fiber lasers. Relaxation oscillations of the output power have been observed which are typical for such devices.

6.1 Introduction

Several dynamic numerical rare-earth-doped fiber laser and amplifier models have already been presented [123, 124, 148, 155–158], mostly for erbium- or thulium-doped fiber amplifiers (EDFA or TDFA) or lasers (EDFL or TDFL) based on silica and fluoride glasses, respectively. Wu [155] has presented a very simple dynamic two-level model for an EDFA where he introduced artificial delay lines to improve computing speed for multi-wavelength analysis. In 1996, Tellert presented a dynamic fiber laser model for an EDFL co-doped with ytterbium ions where he considered energy transfer between both rare earth ions [156]. Since propagation along the fiber axis is neglected in this model, it is too simplified to build the basics for a general dynamic fiber laser model. Besides, Tellert assumed an exponentially decaying pump power along the position in the active fiber which in most cases is an invalid assumption. A numerical solution of the initial value problem (IVP) has been found by using the method of finite differences (FDM).
A numerical model for an EDFA based on ZBLAN fiber and operating at 3 μm was introduced in [148]. Seven energy levels were considered and two flux equations for the forward and backward propagating fluxes. Moreover, pumping rates were included in the model and a numerical solution was found by applying Runge-Kutta methods. Relaxation oscillations had been observed but a thorough time-space description is missing.
The model in [123] is a simplified monochromatic model of a four-level TDFA simulating stationary and transient states. A model for transient TDFA behavior was also presented in [157] based on some simplifying assumptions. [124] also presents a model for the stationary and dynamic simulation of TDFAs merely considering three energy levels. Runge-Kutta methods are used to find a numerical solution.
Maciuc developed a time dependent numerical model for an EDFL operating at 3 μm where he took seven energy levels into account [158]. An adaptive Runge-Kutta method of 4^{th} order was applied to find a solution.
Most numerical models presented in the literature are based on rate and gain equations but

they significantly differ in their complexity. For some models the gain equations are replaced by propagation or complex field equations. To shorten the computing time, some models neglect the ASE or do not consider the ESA.
On the other hand, many analytical models have been developed to find analytical expressions for amplifier or laser parameters [18, 131–133]. All of them apply to the case of specific rare earth ions and consider a maximum of four relevant energy levels. An analytical model for a three-level ytterbium-doped fiber amplifier was developed in 2002 [134] with several simplifying assumptions.
As already mentioned in chapter 5, modeling of energy transfer processes was also reported in literature [152–154, 156]. In all cases many energy levels of the rare earth ions in their respective glass hosts have been neglected. None of these publications presented general numerical models for arbitrary rare-earth-doped fiber lasers and amplifiers. Many assumptions have been made and some of these models have been drastically simplified and thus cannot accurately simulate specific features of lasers or amplifiers.
Analytical models and general theory for two-, three- and four-level amplifiers and lasers have quite often been presented in the literature [136–140]. Obviously, analytical expressions are only intended to describe steady-state behavior of rare-earth-doped devices.
The goal of this chapter is to present a simple numerical model which can be applied to arbitrary rare earth ions to simulate the dynamics of lasers and amplifiers in a variety of configurations. Moreover, a general algorithm is presented to consider cross relaxation processes of two different rare earth ions as well. The model is based on the model presented in chapter 5 and uses the same mathematical notation. It will turn out that this model, which will be described in this chapter, comprises both transient and stationary states, and thus the model described in chapter 5 has to be regarded as being a special case of this model.
This chapter starts with a section about general fiber laser and amplifier operation in transient state to make the practical and theoretical background clear. The discrete mathematical notation for the numerical model and the simulation algorithm will be presented in sections 6.3.1 and 6.3.2. In section 6.4 the developed model will be extended to model cross relaxation processes between two different rare earth ions. Finally, in sections 6.7.1, 6.7.2 and 6.7.3 the simulation model developed is applied to ytterbium-doped, praseodymium-doped and Pr^{3+}/Yb^{3+}-doped ZBLAN fiber lasers.

6.2 Dynamic fiber laser and amplifier operation

For the sake of clarity, let us still concentrate on lasers and on the very simple Fabry-Perot setup shown in Figure 5.1. Amplifiers are in fact not significantly different to model as already mentioned in chapter 5.

Fundamental fiber laser and amplifier operation has already been presented in section 5.2. There, a mathematical description has been deduced which is of fundamental importance for

fiber laser and amplifier operation:

$$\pm\frac{\mathrm{d}n_i(t)}{\mathrm{dt}} = \sigma(\lambda)\cdot n_i(t)\cdot\Phi(\lambda,t) = \pm\frac{1}{n_I}\cdot\frac{\mathrm{d}\Phi(\lambda,t)}{\mathrm{dx}}, \tag{6.1}$$

$n_i(t)$ being the time dependent relative occupation number of energy level i in the active material, n_I the density of dopant ions, $\Phi(\lambda,t)$ the time dependent photon flux at the wavelength λ, and $\sigma(\lambda)$ the emission or absorption cross section where the cross section is the coupling constant of the interaction between radiation and matter. The variables x and t refer to position along the fiber axis and time, respectively. Depending on the choice of signs and the type of cross section used, this double equation describes the fundamental process of absorption and stimulated emission in laser materials. The left part (matter) can be expanded into a system of rate equations and the right part (radiation) into the gain equations.
As a more general expansion to the rate equation of level i in segment p for an unlimited system of states the following expression is used

$$\begin{aligned}\frac{\mathrm{d}n_i(t)}{\mathrm{dt}} = &\sum_j\left[A_{ji}+W_{ji}+\int f(\lambda)\cdot\left(\phi^+(\lambda,x,t)+\phi^-(\lambda,x,t)\right)\cdot\sigma_{ji}(\lambda)\,\mathrm{d}\lambda\right]\cdot n_j(x,t)\\ &-\sum_j\left[A_{ij}+W_{ij}+\int f(\lambda)\cdot\left(\phi^+(\lambda,x,t)+\phi^-(\lambda,x,t)\right)\cdot\sigma_{ij}(\lambda)\,\mathrm{d}\lambda\right]\cdot n_i(x,t)\,.\end{aligned} \tag{6.2}$$

The equation is describing the temporal development of the relative occupation number n_i of level i and consists of two sums running over all levels j of the dopant ion (see also section 5.2). A_{ij} is the radiative emission rate of level i to j, whereas W_{ij} denotes the non-radiative emissions mainly due to multi-phonon emission.
The flux of photons is replaced by its spectral counterpart $\phi = \frac{\mathrm{d}\Phi}{\mathrm{d}\lambda}$ and separated in two parts ϕ^+ and ϕ^- where the sign denotes the direction of propagation. The position variable along the fiber axis is x and the integral over λ spans the full absorption or emission line. The time variable is t.
For a system of N energy levels N rate equations (equation (6.2)) exist like in case of the stationary model (see chapter 5). One of the equations is replaced by the following one to fix the relative occupation numbers at any points in time:

$$\sum_i n_i(x,t) = 1. \tag{6.3}$$

The right-hand side of equation (6.1) is expanded into a second set of differential equations. There exist two gain equations, one for each direction:

$$\pm\frac{\mathrm{d}\phi^{\pm}(\lambda,x,t)}{\mathrm{dx}} = w(\lambda)\cdot n_{\mathrm{I}}\cdot\sum_{ij}A_{ij}\cdot g_{ij}(\lambda)\,\mathrm{d}\lambda\cdot n_i(x,t)$$

$$+ f(\lambda) \sum_{ij} \operatorname{sign}(i-j) \cdot \sigma_{ij}(\lambda) \cdot n_I \cdot n_i(x,t) \cdot \phi^{\pm}(\lambda,x,t) - \alpha(\lambda) \cdot \phi^{\pm}(\lambda,x,t). \tag{6.4}$$

The parameters of equation (6.4) have already been described in section 5.2.
At both fiber ends of the Fabry-Perot setup shown in Figure 5.1, i.e. at $x = 0$ and $x = L$, the mirrors reflect the co- and counter-propagating photon fluxes into each other. Let us again consider the case where the active fiber is bidirectionally pumped. Denoting the reflectivity of input and output mirror by $R^{in}(\lambda)$ and $R^{out}(\lambda)$, one gets the following boundary conditions:

$$\begin{aligned} \phi^{+}(\lambda,0,t) &= R^{in}(\lambda) \cdot \phi^{-}(\lambda,0,t) + T^{in}(\lambda) \cdot \phi^{fw}_{pump}(\lambda,t) \quad \text{and} \\ \phi^{-}(\lambda,L,t) &= R^{out}(\lambda) \cdot \phi^{+}(\lambda,L,t) + T^{out}(\lambda) \cdot \phi^{bw}_{pump}(\lambda,t), \end{aligned} \tag{6.5}$$

where the flux of pump photons pumping from the left side $\phi^{fw}_{pump}(\lambda,t)$ (index fw stands for forward) and from the right side $\phi^{bw}_{pump}(\lambda,t)$ (index bw stands for backward) with transmission factor $T^{in}(\lambda)$ and $T^{out}(\lambda)$ for input and output mirror have already been included.
The temporal evolution of the pump powers are modeled as step functions which jump to a constant power level at an initial time t_0. Of course, any other temporal evolution of the pump powers can be assumed.
The rate equations (6.2) and (6.3) together with the gain equations (6.4) and the boundary conditions (6.5) represent a complex system of coupled ordinary differential equations which can only be solved numerically. Regarding energy transfer processes, as will be done in section 6.4, the rate equations will become nonlinear. In this case one will obtain nonlinear coupled ordinary differential equations in a finite interval. Sterke [159] proposed to solve such a problem by integrating along the characteristics to find a numerical solution for the deducible partial differential equations (PDEs). The Runge-Kutta method of 4^{th} order was introduced which can always be used as long as there are two counter-propagating waves [159]. However, a way will be presented, in which there is no need to deduce PDEs and thus to integrate along the characteristics. The model presented in chapter 5 will be merely extended to the transient case and a solution will be found by applying a step-by-step algorithm using FDM.
It is worth noting that by changing the boundary conditions (6.5), any other laser configuration or any fiber amplifier configuration can be easily modeled as well. The temporal evolution of the pump powers have to be preset for the simulation. In section 6.3.2, an algorithm solving this set of equations in the transient case will be discussed to simulate the dynamics of fiber lasers and amplifiers.

6.3 Numerical simulation model

All parameters needed for the simulation have already been discussed in detail in section 5.3. The radiative transition rates A_{ij} and other radiative properties of triply ionized praseodymium, erbium and thulium ions in ZBLAN glass have been calculated by Caspary [15]. Due

to the fact that values for most non-radiative transition rates W_{ij} are difficult to obtain an approach to fix these values has been presented in section 5.3.2. A specific solution has been found which solves the rate equations in steady-state. It must be emphasized that these values can be regarded as fixed regardless the transient or stationary case. It must be noted that $f(\lambda)$, $g_{ij}(\lambda)$ and $w(\lambda)$ are dimensionless quantities.
Since all input parameters are given, a mathematical description is presented in order to find the required output variables for all positions and points in time such as the relative occupation numbers n_i and the forward and backward photon fluxes $\Phi^+(\lambda)$ and $\Phi^-(\lambda)$.

6.3.1 Model description

The model covers the dynamics of an arbitrary laser or amplifier system in a rare-earth-doped fiber. Especially when co-dopants are used, energy transfer processes have to be taken into account. A way to implement this feature is shown in section 6.4. The simulation model for fiber lasers and amplifiers is based on powers rather than complex field components and thus does not account for longitudinal modes or phenomena such as spacial holeburning effects (as in chapter 5). Spectral holeburning effects are not considered either since the homogenous linewidth of a transition is not taken into account.
Since the laser and amplifier are simulated numerically, the general equations describing its performance (see section 6.2) have to be given in their discrete form and one has to find an algorithm to solve the resulting equations. The calculations have to be performed in four dimensions: energy levels, wavelengths, spatial position, and time. In other words, the active fiber is divided in m segments (see Figure 5.2: the time dependency is neglected there), for which the occupation numbers of energy levels are calculated and the change in absorption and/or emission is evaluated. It is important to note that the indices i and j are used for the energy level which is already a discrete value, λ is the index corresponding to the wavelength of the radiation field, x denotes the position along the active fiber for which the index p is used, and t is the index corresponding to time. The fiber has to be split in certain pieces which in this case must be of equal length.
Let us now assume that time $\mathrm{d}t$ passes as light propagates along the fiber axis from the position x to $x + \mathrm{d}x$. A time step Δt is given by the relation

$$\Delta t = \Delta x_p / v_g,$$

where v_g denotes the group velocity, i.e. $v_g = c_0/n_g$. c_0 and n_g are the speed of light in vacuum and the group index of the active fiber, respectively. Δx_p denotes the fiber segment's length and defines the spatial and temporal resolution in case of equidistant splitting of the fiber. Alternatively, the group velocity can be calculated from the resonator round-trip time T_r to be $v_g = 2L/T_r$. Concluding, the assumption introduced couples a position step to a time step which is reasonable.
Though the mathematical notation, which will be given now, follows the notation in chapter 5, for sake of completeness and clarity, a thorough formulation is presented:

When converting the integral in the rate equations (6.2) to a sum, it seems convenient to introduce the plain photon flux again

$$\Phi(\lambda, t) = \int_{\lambda}^{\lambda+\mathrm{d}\lambda} \phi\left(\lambda', t\right) \mathrm{d}\lambda',$$

which is defined as the number of photons per unit area and per unit time interval. This leads to the following discrete form of the rate equation of level i in fiber segment p at any point in time t:

$$\begin{aligned}\frac{\mathrm{d}n_{ipt}}{\mathrm{dt}} = &\sum_{j}\left[A_{ji} + W_{ji} + \sum_{\lambda} f_{\lambda}\cdot\left(\Phi^{+}_{\lambda pt} + \Phi^{-}_{\lambda p+1t}\right)\cdot\sigma_{ji\lambda}\right]\cdot n_{jpt} \\ &- \sum_{j}\left[A_{ij} + W_{ij} + \sum_{\lambda} f_{\lambda}\cdot\left(\Phi^{+}_{\lambda pt} + \Phi^{-}_{\lambda p+1t}\right)\cdot\sigma_{ij\lambda}\right]\cdot n_{ipt},\end{aligned} \tag{6.6}$$

where the index $p+1$ of Φ^{-} should be noted. It is necessary since the photon flux between the fiber segments $p-1$ and p is denoted by $\Phi^{\pm}_{\lambda p}$. Thus $\Phi^{-}_{\lambda p}$ is the flux leaving the segment p towards segment $p-1$ (see Figure 5.2). To further simplify the form of this equation, the matrix B^{sp}_{ij} (index sp stands for spontaneous emission) is introduced by the definition

$$B^{sp}_{ij} = \begin{cases} -\sum_{j'}\left(A_{ij'} + W_{ij'}\right) & \text{if } j = i \text{ and} \\ A_{ji} + W_{ji} & \text{otherwise,}\end{cases} \tag{6.7}$$

and the analog definition of the matrix $B^{st}_{ij\lambda}$ for the terms of absorption and stimulated emission (index st)

$$B^{st}_{ij\lambda} = \begin{cases} -f_{\lambda}\cdot\sum_{j'}\sigma_{ij'\lambda} & \text{if } j = i \text{ and} \\ f_{\lambda}\cdot\sigma_{ji\lambda} & \text{otherwise.}\end{cases} \tag{6.8}$$

All elements of both matrices above are given before the actual simulation starts and are therefore calculated outside the simulation kernel.
Let us now assume that the value of the photon fluxes into segment p is already known and define the matrix B_{ijpt} by

$$\boxed{B_{ijpt} = \begin{cases} 1 & \text{for } i = 0 \text{ and} \\ B^{sp}_{ij} + \sum_{\lambda} B^{st}_{ij\lambda}\cdot\left(\Phi^{+}_{\lambda pt} + \Phi^{-}_{\lambda p+1t}\right) & \text{otherwise,}\end{cases}} \tag{6.9}$$

then the rate equations in the fiber segment p build a set of linear equations, which is solved by FDM to get the relative occupation numbers (all in the range between 0 and 1) of all energy levels in the fiber segment. Alternatively, Runge-Kutta methods can be applied. Since

the gain equations will be solved by FDM as well, the same method will be used for the rate equations presented here. The appropriate equation for level i is

$$\sum_j B_{ijpt} \cdot n_{jpt} = \begin{cases} 1 & \text{for } i = 0 \text{ and} \\ \frac{\mathrm{d}n_{ipt}}{\mathrm{dt}} & \text{otherwise,} \end{cases} \tag{6.10}$$

and the special treatment of $i = 0$ includes equation (6.3). Rearranging equation (6.10), one finds the more appropriate equation for implementing the FDM:

$$\boxed{\begin{aligned} n_{jpt+1} &= n_{ipt} + \Delta t \cdot \sum_j B_{ijpt} \cdot n_{jpt} \quad \text{and} \\ n_{0pt+1} &= 1 - \sum_j n_{jpt+1} \quad \text{for } j \geq 1. \end{aligned}} \tag{6.11}$$

Solving the rate equations one obtains the relative occupation of the energy levels, which are the input values for the gain equations (6.4). Now the photon flux traveling from left to the right can be written down in a discrete form:

$$\frac{\Phi^+_{\lambda p+1t} - \Phi^+_{\lambda pt}}{\Delta x_p} = w_\lambda \cdot n_I \cdot \sum_{ij} A_{ij} \cdot g_{ij\lambda} \cdot n_{ipt} + f_\lambda \sum_{ij} \operatorname{sign}(i-j) \cdot \sigma_{ij\lambda} \cdot n_I \cdot n_{ipt} \cdot \Phi^+_{\lambda pt} - \alpha_\lambda \cdot \Phi^+_{\lambda pt}, \tag{6.12}$$

and in the opposite direction

$$\frac{\Phi^-_{\lambda pt} - \Phi^-_{\lambda p+1t}}{\Delta x_p} = w_\lambda \cdot n_I \cdot \sum_{ij} A_{ij} \cdot g_{ij\lambda} \cdot n_{ipt} + f_\lambda \sum_{ij} \operatorname{sign}(i-j) \cdot \sigma_{ij\lambda} \cdot n_I \cdot n_{ipt} \cdot \Phi^-_{\lambda p+1t} - \alpha_\lambda \cdot \Phi^-_{\lambda p+1t}, \tag{6.13}$$

where Δx_p is the fiber segment's length and $g_{ij\lambda}$ the normalized lineshape function defined by $\sum_\lambda g_{ij\lambda} = 1$.
Again, some matrices are defined containing all data known before the simulation starts. From the term of spontaneous emission (index sp) let us define:

$$G^{sp}_{\lambda pi} = n_I \cdot w_\lambda \cdot \Delta x_p \cdot \sum_j A_{ij} \cdot g_{ij\lambda}, \tag{6.14}$$

from the term of absorption and stimulated emission (index st)

$$G^{st}_{\lambda pi} = n_I \cdot f_\lambda \cdot \Delta x_p \cdot \sum_j \operatorname{sign}(i-j) \cdot \sigma_{ij\lambda}, \tag{6.15}$$

and from the term of the background losses (index att)

$$G^{att}_{\lambda p} = -\alpha_\lambda \cdot \Delta x_p \quad \text{for } \alpha_\lambda > 0. \tag{6.16}$$

As soon as the values of the relative occupation numbers n_{ip} in segment p are known, one can calculate the two new matrices

$$\boxed{\begin{aligned} G^{(1)}_{\lambda pt} &= \sum_i G^{sp}_{\lambda pi} \cdot n_{ipt} \quad \text{and} \\ G^{(2)}_{\lambda pt} &= 1 + \sum_i G^{st}_{\lambda pi} \cdot n_{ipt} + G^{att}_{\lambda p}, \end{aligned}} \tag{6.17}$$

which again simplify the expression of the gain equation.
The photon flux leaving segment p in the direction of the pump beam and in the opposite direction can now be calculated by

$$\boxed{\begin{aligned} \Phi^{+}_{\lambda p+1t} &= G^{(1)}_{\lambda pt} + G^{(2)}_{\lambda pt} \cdot \Phi^{+}_{\lambda pt} \quad \text{and} \\ \Phi^{-}_{\lambda pt} &= G^{(1)}_{\lambda pt} + G^{(2)}_{\lambda pt} \cdot \Phi^{-}_{\lambda p+1t}. \end{aligned}} \tag{6.18}$$

As has already been mentioned, the gain equations are also solved by FDM. It is advisable to apply the forward difference quotient to solve rate and gain equations. In principle, the method applied in combination with the relation between position and time step is similar to the Euler method.
According to equation (6.5) the fluxes are partially reflected by the mirrors at the fiber ends and fluxes $\Phi^{fw}_{\lambda t,pump}$ and $\Phi^{bw}_{\lambda t,pump}$ of pump photons are added from both ends, which leads to the equations

$$\boxed{\begin{aligned} \Phi^{+}_{\lambda 0t} &= R^{in}_{\lambda} \cdot \Phi^{-}_{\lambda 0t} + T^{in}_{\lambda} \cdot \Phi^{fw}_{\lambda t,pump} \quad \text{and} \\ \Phi^{-}_{\lambda mt} &= R^{out}_{\lambda} \cdot \Phi^{+}_{\lambda mt} + T^{out}_{\lambda} \cdot \Phi^{bw}_{\lambda t,pump}, \end{aligned}} \tag{6.19}$$

if the number of fiber segments is m. The time dependent pump powers $\Phi^{fw}_{\lambda t,pump}$ and $\Phi^{bw}_{\lambda t,pump}$ are modeled as step functions.
The equation converting power values $P(t)$ to photon fluxes $\Phi(t)$ and vice-versa is

$$\Phi(t) = \frac{P(t)}{h \cdot \nu \cdot A_{core}},$$

where h is Planck's constant, ν the optical frequency and $A_{core} = \pi \cdot \frac{d^2_{core}}{4}$ is the area of the fiber core. With $\nu = \frac{c_0}{\lambda}$ this equation leads to

$$\Phi(t) = \frac{P(t) \cdot \lambda}{h \cdot c_0 \cdot A_{core}}, \tag{6.20}$$

where c_0 is the speed of light in vacuum.

initial conditions at $t = t_0$: $\Phi^{\pm}_{\lambda p} = 0$

$\Phi^{+}_{\lambda 0} = T^{in}_{\lambda} \cdot \Phi^{fw}_{\lambda,pump}$

$\Phi^{-}_{\lambda m} = T^{out}_{\lambda} \cdot \Phi^{bw}_{\lambda,pump}$

$n_{jp} = 0 \quad \text{for} \quad j > 0$

$n_{0p} = 1$

for $t = 0$ **to** $l - 1$

  for $p = 0$ **to** $m - 1$

    calculate n_{jpt} (6.9), (6.11)

    calculate $\Phi^{+}_{\lambda p+1t}$ and $\Phi^{-}_{\lambda pt}$ (6.17), (6.18)

  end

boundary conditions: $\Phi^{-}_{\lambda mt} = R^{out}_{\lambda} \cdot \Phi^{+}_{\lambda mt} + T^{out}_{\lambda} \cdot \Phi^{bw}_{\lambda t,pump}$ (6.19)

$\Phi^{+}_{\lambda 0t} = R^{in}_{\lambda} \cdot \Phi^{-}_{\lambda 0t} + T^{in}_{\lambda} \cdot \Phi^{fw}_{\lambda t,pump}$ (6.19)

end

$\Phi^{out,fw}_{\lambda t} = T^{out}_{\lambda} \cdot \Phi^{+}_{\lambda mt}$

$\Phi^{out,bw}_{\lambda t} = T^{in}_{\lambda} \cdot \Phi^{-}_{\lambda 0t}$

Figure 6.1: Algorithm of the simulation kernel in pseudo-code with the appropriate equations indicated

6.3.2 Simulation algorithm

The boxed expressions above are all equations needed for the simulation kernel. The only thing still missing is a suitable algorithm. The initial and boundary conditions used in the presented algorithm (see Figure 6.1) are in fact close to reality, whereas in the stationary case (see chapter 5) unrealistic initial conditions have been assumed. There, the photon fluxes have all been set to zero and only the pump to non-zero and thus iterations have been needed to find a converged solution. In this context, a step-by-step algorithm will be applied to the dynamic problem (see Figure 6.1 for a pseudo-code description). The advantage of this algorithm is that no convergence criterion is needed. One might simulate up to a point in time where the output power level does not significantly change any more, i.e. steady-state condition is achieved. The time steps must be equidistant due to the underlying relation with the segment's length.

It is assumed that all upper energy states are unpopulated i.e. only the ground state is completely populated at the initial time t_0. All fluxes are set to zero except for the fluxes entering segment 0 and $m - 1$ at t_0. Let us suppose that one already knows the values of all n_{ip}, $\Phi^{+}_{\lambda p}$ and $\Phi^{-}_{\lambda p}$ at time $t = t_L = L \cdot \Delta t$. Then, to determine all relevant variables at $t = t_{L+1} = (L + 1) \cdot \Delta t$ the following two steps are needed: First, solve equation (6.11) for each segment p using values of n_{ip}, $\Phi^{+}_{\lambda p}$ and $\Phi^{-}_{\lambda p+1}$ at $t = t_L$. Thus, one obtains the values of n_{ip} at t_{L+1}. Then, subsequently, solve equation (6.18) for each segment p using values of n_{ip} at $t = t_{L+1}$ and the values of $\Phi^{+}_{\lambda p}$ and $\Phi^{-}_{\lambda p+1}$ at $t = t_L$. Therefore, one obtains $\Phi^{+}_{\lambda p+1}$ and $\Phi^{-}_{\lambda p}$

at $t = t_{L+1}$.
The accuracy of the numerical calculation is given by the number of fiber segments, whereas the accuracy of the stationary model is preset by the convergence criterion.
All operations in the simulation kernel are usual matrix operations such as multiplication and addition, which are carried out at high speed by usual program libraries. Most of the computing time is consumed by matrix operations.
Depending on the laser system, usual simulation runs up to the steady-state with a fine time resolution of 50 ps (corresponding to 1 cm space resolution) equivalent to 100 fiber segments of a one meter long active fiber and using 300 wavelengths may take a few hours on low-end computers. However, the rapid progress in computer technology makes this algorithm very attractive and valuable.
In order not to run out of memory one must not save all fluxes and occupation numbers at all positions and points in time. To increase computing speed, the application of the stationary model (see chapter 5) would make sense. This would allow to find the wavelength of maximum emission in less than one minute of computing time. Using only this single value for the dynamic simulation would allow a reduction in computing time. However, it has to be emphasized that the time has to be large enough for the fluxes to reach the fiber end.
A number of 5 fiber segments turned out to be suitable in most cases. Extensive use of the simulation program showed no problems with numerical stability of the algorithm as long as the fiber segments have been chosen to be short enough. It goes without saying that a spatial evolution along the fiber axis corresponds to a temporal evolution because the relation $\Delta x_p = v_g \cdot \Delta t$ has been used. The presented mathematical problem is an IVP but it can easily be extended to a nonlinear IVP. The presented model will be extended to a non-linear IVP in section 6.4.2 to include energy transfer processes between two rare earth ions. In that case, the rate equations will become nonlinear.

6.4 Cross relaxation processes

6.4.1 Extension to model energy transfer processes

As already mentioned, the simulation model developed in section 6.3.1 does not cover energy transfer processes. Energy transfer is caused by interactions between two dopant ions e.g. via dipole-dipole coupling. The basic principle of energy transfer has already been discussed in section 3.3. Let us only concentrate on energy transfer between two different rare earth ions due to the reason that it is often used for better performance of fiber lasers and amplifiers. A typical process of this kind is the cross relaxation process between two dopant ions. The transition rates of such processes are proportional to the occupation number of the initial levels of both interacting transitions. When such terms are inserted in the rate equations, they become non-linear. However, the kernel algorithm (see section 6.3.2) is independent on the method used to solve the rate equations. A straightforward way to implement the important case of a co-dopant is to fix the occupation numbers of dopant 2 and then solve

the rate equations of dopant 1, which are now linear again. A valid assumption would be that the ground states of the rare earth ions are completely populated before the simulation starts. In the next position step these results would be treated as fixed in the rate equations of dopant 2 to solve them. After calculating all occupation numbers and fluxes in all segments p, the step-by-step algorithm proceeds with the next point in time and so on until the final point in time is reached. However, in the kernel algorithm presented in section 6.3.2 the implementation of such cross relaxation processes is quite easy. The simulation kernel of cross relaxation processes will be presented in section 6.4.2. The method described is very efficient and thus let us go into more detail in the following.
Using the same notation as in section 6.2, the equations for a system of two rare earth ions with energy transfer processes between them are now presented. Most equations have to be written down twice for both ion systems (by replacing the indices i and j by a and b for the second dopant ion). This procedure is very straight-forward. However, to account for completeness, let us continue to give a thorough formulation.
Equation (6.2) now shows the unknown cross relaxation rates X between ion system 1 and ion system 2 weighted by fixed values e_{c1} and e_{c2} which are given by the ratio of the molar concentrations of both ions:

$$\begin{aligned}\frac{\mathrm{d}n_i(t)}{\mathrm{dt}} = \sum_j \Bigg[& A_{ji} + W_{ji} + e_{c1} \cdot \sum_{ab} X_{jiab} \cdot n_a(x,t) + \\ & \int f(\lambda) \cdot \left(\phi^+(\lambda,x,t) + \phi^-(\lambda,x,t)\right) \cdot \sigma_{ji}(\lambda)\,\mathrm{d}\lambda \Bigg] \cdot n_j(x,t) \\ - \sum_j \Bigg[& A_{ij} + W_{ij} + e_{c1} \cdot \sum_{ba} X_{ijba} \cdot n_b(x,t) + \\ & \int f(\lambda) \cdot \left(\phi^+(\lambda,x,t) + \phi^-(\lambda,x,t)\right) \cdot \sigma_{ij}(\lambda)\,\mathrm{d}\lambda \Bigg] \cdot n_i(x,t)\,. \end{aligned} \tag{6.21}$$

As can be seen from this equation, the unknown cross relaxation rates X_{jiab} and X_{ijba} appear. The same equation has to be written down for the second ion with the indices a and b instead of i and j:

$$\begin{aligned}\frac{\mathrm{d}n_a(t)}{\mathrm{dt}} = \sum_b \Bigg[& A_{ba} + W_{ba} + e_{c2} \cdot \sum_{ij} X_{baij} \cdot n_i(x,t) + \\ & \int f(\lambda) \cdot \left(\phi^+(\lambda,x,t) + \phi^-(\lambda,x,t)\right) \cdot \sigma_{ba}(\lambda)\,\mathrm{d}\lambda \Bigg] \cdot n_b(x,t) \\ - \sum_b \Bigg[& A_{ab} + W_{ab} + e_{c2} \cdot \sum_{ji} X_{abji} \cdot n_j(x,t) + \\ & \int f(\lambda) \cdot \left(\phi^+(\lambda,x,t) + \phi^-(\lambda,x,t)\right) \cdot \sigma_{ab}(\lambda)\,\mathrm{d}\lambda \Bigg] \cdot n_a(x,t)\,. \end{aligned} \tag{6.22}$$

Hence, one gets the additional unknown cross relaxation rates X_{baij} and X_{abji} and the equation contains the fixed value e_{c2} instead of e_{c1}. The double sums for the cross relaxation rates must be emphasized and also that most of the cross relaxation rates are zero.
Equation (6.3) must be extended to:

$$\sum_i n_i(x,t) = 1 \quad \text{and} \quad \sum_a n_a(x,t) = 1, \tag{6.23}$$

for all points in time. Since both dopant ions can be regarded as a cascade of two systems (cf. section 5.6.3), equation (6.4) now yields

$$\begin{aligned} \pm\frac{\mathrm{d}\phi^{\pm}(\lambda,x,t)}{\mathrm{dx}} &= w(\lambda)\cdot n_{\mathrm{I}}\cdot\left(\sum_{ij} A_{ij}\cdot g_{ij}(\lambda)\,\mathrm{d}\lambda\cdot n_i(x,t) + \sum_{ab} A_{ab}\cdot g_{ab}(\lambda)\,\mathrm{d}\lambda\cdot n_a(x,t)\right) \\ &+ \left[f(\lambda)\cdot n_I\left(\sum_{ij}\operatorname{sign}(i-j)\cdot\sigma_{ij}(\lambda)\cdot n_i(x,t)\right.\right. \\ &+ \left.\left.\sum_{ab}\operatorname{sign}(a-b)\cdot\sigma_{ab}(\lambda)\cdot n_a(x,t)\right) - \alpha(\lambda)\right]\cdot\phi^{\pm}(\lambda,x,t), \end{aligned} \tag{6.24}$$

which means that both ion systems can contribute independently to the laser or amplifier operation. The boundary conditions (equation (6.5)) remain completely unchanged in case of the bidirectionally pumped laser with Fabry-Perot cavity. Any reasonable temporal model for the pump powers can be assumed. It is emphasized that not only the turn-on behavior of rare earth devices can be simulated but also the turn-off behavior by modeling the input pump power properly.

6.4.2 Model description

Following the discrete numerical formulation in section 6.3.1 for the transient case, one concludes that equation (6.6) has to be doubled but this time comprising the cross relaxation rates:

$$\begin{aligned} \frac{\mathrm{d}n_{ipt}}{\mathrm{dt}} &= \sum_j\left[A_{ji} + W_{ji} + e_{c1}\cdot\sum_{ab} X_{jiab}\cdot n_{apt} + \sum_\lambda f_\lambda\cdot\left(\Phi^+_{\lambda pt} + \Phi^-_{\lambda p+1t}\right)\cdot\sigma_{ji\lambda}\right]\cdot n_{jpt} \\ &- \sum_j\left[A_{ij} + W_{ij} + e_{c1}\cdot\sum_{ba} X_{ijba}\cdot n_{bpt} + \sum_\lambda f_\lambda\cdot\left(\Phi^+_{\lambda pt} + \Phi^-_{\lambda p+1t}\right)\cdot\sigma_{ij\lambda}\right]\cdot n_{ipt}, \end{aligned} \tag{6.25}$$

and

$$\frac{\mathrm{d}n_{apt}}{\mathrm{dt}} = \sum_b\left[A_{ba} + W_{ba} + e_{c2}\cdot\sum_{ij} X_{baij}\cdot n_{ipt} + \sum_\lambda f_\lambda\cdot\left(\Phi^+_{\lambda pt} + \Phi^-_{\lambda p+1t}\right)\cdot\sigma_{ba\lambda}\right]\cdot n_{bpt}$$

$$-\sum_b \left[A_{ab} + W_{ab} + e_{c2} \cdot \sum_{ji} X_{abji} \cdot n_{jpt} + \sum_\lambda f_\lambda \cdot \left(\Phi^+_{\lambda pt} + \Phi^-_{\lambda p+1t} \right) \cdot \sigma_{ab\lambda} \right] \cdot n_{apt}. \quad (6.26)$$

Equations (6.7) and (6.8) have to be written down for both ions:

$$B^{sp}_{ij} = \begin{cases} -\sum_{j'} \left(A_{ij'} + W_{ij'} \right) & \text{if } j = i \text{ and} \\ A_{ji} + W_{ji} & \text{otherwise,} \end{cases} \quad (6.27)$$

$$B^{sp}_{ab} = \begin{cases} -\sum_{b'} \left(A_{ab'} + W_{ab'} \right) & \text{if } b = a \text{ and} \\ A_{ba} + W_{ba} & \text{otherwise,} \end{cases} \quad (6.28)$$

and

$$B^{st}_{ij\lambda} = \begin{cases} -f_\lambda \cdot \sum_{j'} \sigma_{ij'\lambda} & \text{if } j = i \text{ and} \\ f_\lambda \cdot \sigma_{ji\lambda} & \text{otherwise,} \end{cases} \quad (6.29)$$

$$B^{st}_{ab\lambda} = \begin{cases} -f_\lambda \cdot \sum_{b'} \sigma_{ab'\lambda} & \text{if } b = a \text{ and} \\ f_\lambda \cdot \sigma_{ba\lambda} & \text{otherwise.} \end{cases} \quad (6.30)$$

New matrices for the energy transfer processes (index et) are now defined by:

$$B^{et}_{ija} = \begin{cases} -e_{c1} \cdot \sum_{j'b} X_{ij'ba} & \text{if } j = i \text{ and} \\ e_{c_1} \cdot \sum_b X_{jiab} & \text{otherwise,} \end{cases} \quad (6.31)$$

$$B^{et}_{abi} = \begin{cases} -e_{c2} \cdot \sum_{b'j} X_{ab'ji} & \text{if } b = a \text{ and} \\ e_{c2} \cdot \sum_j X_{baij} & \text{otherwise,} \end{cases} \quad (6.32)$$

with the factors e_{c1} and e_{c2} defined as the ratio of the respective molar concentrations of the two dopant ions: $e_{c1} = \frac{c_{mol,dopant2}}{c_{mol,dopant1}}$ for dopant 1 and $e_{c2} = \frac{c_{mol,dopant1}}{c_{mol,dopant2}}$ in case of dopant 2 (see also chapter 5).
Equations (6.9) now becomes

$$\boxed{B_{ijpt} = \begin{cases} 1 & \text{for } i = 0 \text{ and} \\ B^{sp}_{ij} + \sum_a B^{et}_{ija} \cdot n_{apt} + \sum_\lambda B^{st}_{ij\lambda} \cdot \left(\Phi^+_{\lambda pt} + \Phi^-_{\lambda p+1t} \right) & \text{otherwise,} \end{cases}} \quad (6.33)$$

and

$$\boxed{B_{abpt} = \begin{cases} 1 & \text{for } a = 0 \text{ and} \\ B^{sp}_{ab} + \sum_i B^{et}_{abi} \cdot n_{ipt} + \sum_\lambda B^{st}_{ab\lambda} \cdot \left(\Phi^+_{\lambda pt} + \Phi^-_{\lambda p+1t} \right) & \text{otherwise.} \end{cases}} \quad (6.34)$$

Equation (6.10) is now indicated for the first ion:

$$\sum_j B_{ijpt} \cdot n_{jpt} = \begin{cases} 1 & \text{for } i = 0 \text{ and} \\ \frac{\mathrm{d}n_{ipt}}{\mathrm{dt}} & \text{otherwise.} \end{cases} \tag{6.35}$$

For the implementation of the FDM the following notation is advisable:

$$\boxed{\begin{aligned} &n_{jpt+1} = n_{ipt} + \Delta t \cdot \sum_j B_{ijpt} \cdot n_{jpt} \quad \text{and} \\ &n_{0pt+1} = 1 - \sum_j n_{jpt+1} \quad \text{for } j \geq 1. \end{aligned}} \tag{6.36}$$

For the second ion equation (6.10) yields:

$$\sum_b B_{abpt} \cdot n_{bpt} = \begin{cases} 1 & \text{for } a = 0 \text{ and} \\ \frac{\mathrm{d}n_{apt}}{\mathrm{dt}} & \text{otherwise,} \end{cases} \tag{6.37}$$

and again it will be implemented in the following way:

$$\boxed{\begin{aligned} &n_{bpt+1} = n_{apt} + \Delta t \cdot \sum_b B_{abpt} \cdot n_{bpt} \quad \text{and} \\ &n_{0pt+1} = 1 - \sum_b n_{bpt+1} \quad \text{for } b \geq 1. \end{aligned}} \tag{6.38}$$

Equations (6.12) and (6.13) now become

$$\begin{aligned} \frac{\Phi^+_{\lambda p+1t} - \Phi^+_{\lambda pt}}{\Delta x_p} &= w_\lambda \cdot n_I \cdot \left(\sum_{ij} A_{ij} \cdot g_{ij\lambda} \cdot n_{ipt} + \sum_{ab} A_{ab} \cdot g_{ab\lambda} \cdot n_{apt} \right) \\ &+ \left[f_\lambda \cdot n_I \left(\sum_{ij} \operatorname{sign}(i-j) \cdot \sigma_{ij\lambda} \cdot n_{ipt} + \sum_{ab} \operatorname{sign}(a-b) \cdot \sigma_{ab\lambda} \cdot n_{apt} \right) \right. \\ &\left. -\alpha_\lambda \right] \cdot \Phi^+_{\lambda pt}, \end{aligned} \tag{6.39}$$

and

$$\begin{aligned} \frac{\Phi^-_{\lambda pt} - \Phi^-_{\lambda p+1t}}{\Delta x_p} &= w_\lambda \cdot n_I \cdot \left(\sum_{ij} A_{ij} \cdot g_{ij\lambda} \cdot n_{ipt} + \sum_{ab} A_{ab} \cdot g_{ab\lambda} \cdot n_{apt} \right) \\ &+ \left[f_\lambda \cdot n_I \left(\sum_{ij} \operatorname{sign}(i-j) \cdot \sigma_{ij\lambda} \cdot n_{ipt} + \sum_{ab} \operatorname{sign}(a-b) \cdot \sigma_{ab\lambda} \cdot n_{apt} \right) \right. \end{aligned}$$

$$-\alpha_\lambda] \cdot \Phi^{-}_{\lambda p+1t}. \tag{6.40}$$

From equations (6.14) and (6.15) one gets:

$$G^{sp}_{\lambda pi} = n_I \cdot w_\lambda \cdot \Delta x_p \cdot \sum_j A_{ij} \cdot g_{ij\lambda}, \tag{6.41}$$

$$G^{sp}_{\lambda pa} = n_I \cdot w_\lambda \cdot \Delta x_p \cdot \sum_b A_{ab} \cdot g_{ab\lambda}, \tag{6.42}$$

and

$$G^{st}_{\lambda pi} = n_I \cdot f_\lambda \cdot \Delta x_p \cdot \sum_j \text{sign}\,(i-j) \cdot \sigma_{ij\lambda}, \tag{6.43}$$

$$G^{st}_{\lambda pa} = n_I \cdot f_\lambda \cdot \Delta x_p \cdot \sum_b \text{sign}\,(a-b) \cdot \sigma_{ab\lambda}, \tag{6.44}$$

whereas equation (6.16) for the matrix $G^{att}_{\lambda p}$ remains unchanged.
The definitions of the matrices in equations (6.17) have to be extended for the cascaded system:

$$\boxed{\begin{aligned} G^{(1)}_{\lambda pt} &= \sum_i G^{sp}_{\lambda pi} \cdot n_{ipt} + \sum_a G^{sp}_{\lambda pa} \cdot n_{apt} \quad \text{and} \\ G^{(2)}_{\lambda pt} &= 1 + \sum_i G^{st}_{\lambda pi} \cdot n_{ipt} + \sum_a G^{st}_{\lambda pa} \cdot n_{apt} + G^{att}_{\lambda p}. \end{aligned}} \tag{6.45}$$

The boxed expressions in this section, the boxed equations (6.18) as gain equations and equations (6.19) as boundary conditions in section 6.3.1 set up the simulation kernel for the cross relaxation process (see Figure 6.2 for a pseudo-code description of the algorithm used). Since the value of the cross relaxation rates X is unknown, its value has to be estimated. The value of X strongly depends on the ion concentration in the fiber core. It must be on the order of the sum of radiative and non-radiative transition rates to have a significant effect (see also section 5.6.4).

6.5 Remarks on computing speed

An alternative to the FDM is to implement a Runge-Kutta solver which might increase computing speed. However, to significantly increase computing speed one needs an alternative algorithm. In contrast to the step-by-step algorithm presented in this chapter, the new algorithm should be chosen such that a parallelization of the simulation code would become possible. Hence, using a supercomputer for a parallelized code would increase computing speed significantly. Nevertheless, the step-by-step algorithm works well and thus one has to find a compromise which is not that expensive. This could be the use of programming languages such

initial conditions at $t = t_0$: $\Phi^{\pm}_{\lambda p} = 0$

$\Phi^{+}_{\lambda 0} = T^{in}_{\lambda} \cdot \Phi^{fw}_{\lambda,pump}$

$\Phi^{-}_{\lambda m} = T^{out}_{\lambda} \cdot \Phi^{bw}_{\lambda,pump}$

$n_{jp} = 0$ and $n_{bp} = 0$ for $j,b > 0$

$n_{0p} = 1$ for $j,b = 0$

for $t = 0$ **to** $l-1$

for $p = 0$ **to** $m-1$

calculate n_{jpt} and n_{bpt} (6.33), (6.36), (6.34), (6.38)

calculate $\Phi^{+}_{\lambda p+1t}$ and $\Phi^{-}_{\lambda pt}$ (6.45), (6.18)

end

boundary conditions: $\Phi^{-}_{\lambda mt} = R^{out}_{\lambda} \cdot \Phi^{+}_{\lambda mt} + T^{out}_{\lambda} \cdot \Phi^{bw}_{\lambda t,pump}$ (6.19)

$\Phi^{+}_{\lambda 0t} = R^{in}_{\lambda} \cdot \Phi^{-}_{\lambda 0t} + T^{in}_{\lambda} \cdot \Phi^{fw}_{\lambda t,pump}$ (6.19)

end

$\Phi^{out,fw}_{\lambda t} = T^{out}_{\lambda} \cdot \Phi^{+}_{\lambda mt}$

$\Phi^{out,bw}_{\lambda t} = T^{in}_{\lambda} \cdot \Phi^{-}_{\lambda 0t}$

Figure 6.2: Algorithm of the simulation kernel in pseudo-code of cross relaxation processes between two rare earth ions with the appropriate equations indicated

as Fortran or C. In case of interpreter languages like Matlab one could compile the code with the mex-function which allows an increase in speed. However, also with such programming languages or other alternatives one would not come into the range of a few seconds to one minute like in case of the stationary model (see chapter 5). A maximum increase of a factor of 10 in the computing speed is expected if Fortran or C in contrast to interpreter languages like Matlab will be used.

6.6 Relaxation oscillations

Laser devices very often show severe stability problems which may be associated with optical damage problems, mechanical vibrations, acoustic noise and other sources of a so-called *technical noise*. Relaxation oscillations are the most predominant mechanisms causing fluctuation in the output of a solid-state laser. Hence, this effect is described in more detail.
The laser output is a highly irregular function of time. The output consists of individual bursts with random amplitudes, durations and separations. This is termed *spiking* in the output [3].
When the laser pump source is switched on, there is a negligible number of photons at the appropriate frequency. The pump radiation causes a linear buildup of excited atoms, and the population is inverted. Although under steady-state oscillation conditions, the upper-state

population can never exceed the threshold population, under transient conditions, the pump can raise it above the threshold level because no laser oscillation has yet been built up and no radiation exists in the cavity to pull the upper-state population back down by stimulated emission.
The laser oscillation does not build up until after the upper-state population passes the threshold population, so that the net round-trip gain in the laser exceeds unity. Then, however, because the upper-state lifetime is considerably in excess of the threshold population, the oscillation level will actually build up very rapidly to a certain value. This value corresponds to the value of the photon flux which will be substantially in excess of the steady-state value for the particular pumping level. But, when the photon flux becomes larger, the rate of depletion of the upper-level atoms due to stimulated emission becomes correspondingly large, in fact considerably larger than the pumping rate. As a result, the upper-level population as a function of time passes through a maximum and begins to decrease rapidly, driven downward by the large radiation density. The upper-state population is driven back below the threshold level and the net gain in the laser cavity becomes less than unity. So the existing oscillation in the laser cavity begins to die out.
To complete the cycle of this relaxation process, once the radiation level has decreased below the proper steady-state level, the stimulated emission rate again becomes small. At this point the pumping process can begin to build the upper-state population level back toward and beyond the threshold value again. This causes the generation of another burst of laser action, and the system can again go through a repeated, similar cycle. As time passes, the peaks become smaller and the curve becomes damped sinusoidally as will be described in section 6.7.1. The output power shows a sequence of peaks (or laser spikes) of decreasing amplitude. This aspect of regular oscillations for the output power is usually referred to as relaxation oscillations.
However, most lasers show completely irregular, undamped spikes. This discrepancy between theory and experiment is due to the fact that the spiking behavior dies out very slowly. In cw-pumped lasers the relaxation oscillations are weak and usually consist of damped sinusoidal oscillations around the steady-state value. However, any kind of small perturbation, such as a sudden change in pumping rate, fluctuation in gain, cavity loss, or cavity alignment will trigger a transient relaxation oscillation of the same general character which will again die out exponentially in the same oscillatory fashion.
The relaxation oscillations are due to a coupling of the cavity lifetimes τ_{cav} and the lifetime of the upper level laser level τ_2. Its frequency is given by [24]:

$$\nu_{ro} = \frac{1}{2\pi} \cdot \sqrt{(r-1) \cdot \frac{1}{\tau_2 \cdot \tau_{cav}}}, \tag{6.46}$$

with the pump rate r given by the ratio of the pump power to the pump power at laser threshold. The cavity lifetimes can be estimated as [24]:

$$\tau_{cav} = \frac{2 \cdot n \cdot L}{c_0 \cdot \alpha_{rt}}, \tag{6.47}$$

with the fiber length L, the refractive index n and the round-trip losses α_{rt}.
According to equation (6.46) the oscillation frequency increases with increasing pump power. The relaxation oscillations are in the range of a few hundred kilohertz depending on the laser as the simulations turned out. This is in excellent agreement with measurements in [14].
In general, relaxation oscillations are more a troublesome than a useful phenomenon. Nevertheless, measurements of relaxation oscillations normally are used to calculate the losses in fiber laser cavities.
In the following some examples will be presented which show relaxation oscillations. The aim is to apply the presented model to simulate the turn-on behavior of different rare-earth-doped fiber lasers and to show the validity of the underlying rate and gain equations theory.

6.7 Fiber laser simulation

As has already been described in chapter 5, the qualitative and not the quantitative analysis of fiber lasers is the aim of this work. The dynamics of Yb^{3+}-, Pr^{3+}- and Pr^{3+}/Yb^{3+}-doped ZBLAN fiber lasers will be simulated in the following.
In all three examples the pump laser is switched on at the initial time $t_0 = 0$ s. A step function for the pump power has been assumed i.e. at t_0 the end power is reached and remains constant. All simulations have been carried out in the wavelength range between 470 to 1090 nm, except for the Yb^{3+}-doped fiber laser for which a start wavelength of 845 nm has been chosen. The output power of the above mentioned lasers will be simulated up to the steady-state.

6.7.1 Yb^{3+}-doped fiber laser

In this example the dynamics of an ytterbium-doped fiber laser with Fabry-Perot cavity is simulated. The Yb^{3+}-doped ZBLAN fiber laser consists of two laser mirrors which show reflectivities of 80 % for the emission wavelength at input and output, respectively. Both mirrors are assumed to be fully transparent for the pump wavelength. The configuration is pumped from the left side with a pump power of 200 mW directly into the active fiber core and the pump wavelength is 975 nm.
In this simulation the two levels $^2F_{7/2}$ and $^2F_{5/2}$ of ytterbium-doped ZBLAN glass are considered, thus Stark splitting is neglected.
The absorption cross section used in the simulation has already been presented in Figure 5.4. The respective emission cross section of this two-level system has been calculated using the McCumber theory [114, 115] with a wavenumber difference Δk of 10345 cm^{-1} [15]. It is also displayed in Figure 5.4. The value of the radiative transition rate from the excited level $^2F_{5/2}$ to the ground level $^2F_{7/2}$ has been chosen to be $A_{21} = 1000$ s^{-1} in agreement with [88, 146].
The Yb^{3+}-doped ZBLAN fiber shows the following parameters: an NA of 0.2, a core diameter of 2.4 μm, a length of 25 cm and background losses of 0.3 dB/km. The fiber core is doped with a concentration of 1000 ppm of ytterbium ions which corresponds to an ion density n_I of about $1.85 \cdot 10^{25}$ ions/m^3. The fiber is split into 25 pieces of equal length ($\Delta x_p = 1$ cm)

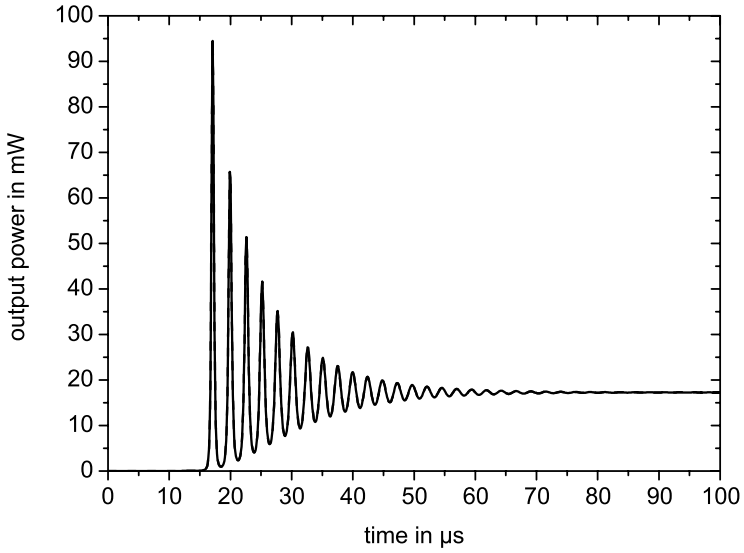

Figure 6.3: Temporal evolution of the output power at both fiber ends for the simulated Yb^{3+}-doped ZBLAN fiber laser

equivalent to a time resolution of 50 ps.
At t_0 the end pump power of 200 mW is reached and remains constant. Relaxation oscillations of the output power at both fiber ends have been found. They begin at approximately $t = 16$ μs (see Figure 6.3) and steady-state is reached after approximately $t = 80$ μs. Two million steps have been carried out to simulate up to 100 μs with the preset time resolution. Since a symmetric setup has been assumed, both output powers are equal except for a small time delay of 1.25 ns. This is the time which light needs to propagate from one fiber end to the other. The output power at both fiber ends is illustrated in Figure 6.3. As shown by stationary simulations, the remaining pump power at the right fiber end is around 163 mW. The power value obtained by transient simulations for steady-state (for $t > 80$ μs) is the same with the value obtained when applying the stationary model to the ytterbium-doped fiber laser.
The laser shows an emission wavelength of about 1007 nm. The output power is 17.24 mW at one end once steady-state is reached. Before reaching steady-state, the laser power output oscillates around the mean laser output power like a exponentially decaying quasi-sinusoidal function (see Figure 6.3) [3]. When the laser starts lasing power values up to 95 mW are reached. It must be emphasized that the output power at both fiber ends is plotted over the pump power which has already reached the resonator i.e. the active fiber.
The nature of the relaxation oscillations depends on several factors such as the populations

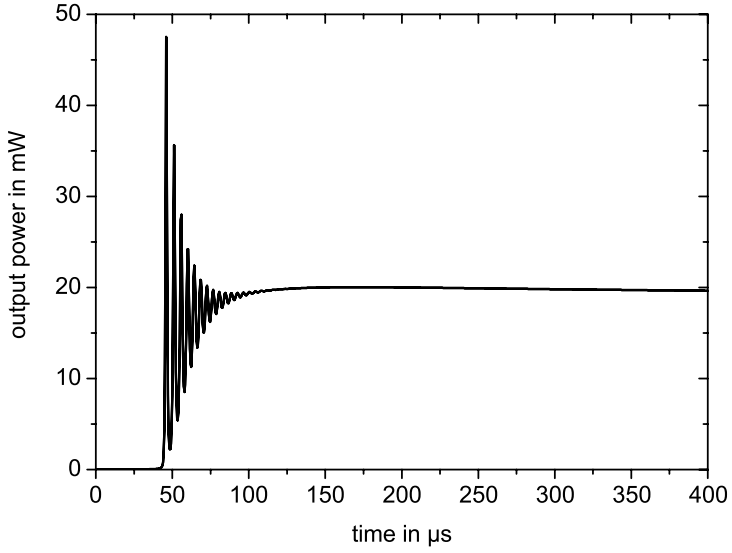

Figure 6.4: Temporal evolution of the output power at both fiber ends for the simulated red Pr^{3+}-doped ZBLAN fiber laser

of the different energy levels, pump power, cavity loss, upper state lifetime etc. [160]. The relaxation parameters can be obtained by fitting the output power with the following function

$$P_{out}(t) = P_{ss} + \hat{P} \cdot \exp(-\epsilon_{ro} \cdot t) \cdot \cos(\omega_{ro} \cdot t - \psi), \tag{6.48}$$

where P_{ss} denotes the steady-state power, ϵ_{ro} gives the decay rate with which the relaxation-oscillation behavior (index ro) dies out and ω_{ro} is the relaxation-oscillation frequency of the laser. $\hat{P}$ is the peak value of the exponentially damped cosine function and ψ denotes merely a constant phase. The relative occupation numbers will have similar damped sinusoidal fluctuations about its steady-state value [3]. By fitting the simulated output power with the above function, for the relaxation-oscillation frequency $f_{ro} = \frac{\omega_{ro}}{2\pi}$ a value of about 383 kHz has been found. One can define a Q factor for the relaxation oscillations given by $Q_{ro} = \omega_{ro}/\epsilon_{ro}$ which is usually in the range between 10 and 100 [3]. In this example, Q_{ro} amounts about 22.5. Stable mechanical design and power supply stabilization are the keys to avoiding recurrent relaxation oscillations.

6.7.2 Pr^{3+}-doped fiber laser

A red praseodymium-doped fiber laser with Fabry-Perot cavity as shown in Figure 5.1 is simulated in this section. It consists of two laser mirrors which show reflectivities of 90 % for

the emission wavelength at input and output, respectively. Both mirrors are assumed to be fully transparent for both IR pump wavelengths. The configuration is pumped from the left side with pump powers of 500 mW and 100 mW directly into the active fiber core and the pump wavelengths are 835 and 1020 nm, respectively.
In this simulation all twelve levels of Pr^{3+} in the transmission window of ZBLAN (see Figure 3.4) are considered.
The absorption cross section of the ground state and the excited state and the emission cross section of Pr^{3+} in ZBLAN glass used in the simulation have already been presented in Figures 4.16, 4.17 and 4.18. All corresponding cross sections for the complementary transitions have been calculated using the McCumber theory (see section 4.3.3) with the wavenumber differences listed in [15]. All radiative transition rates have also been taken from [15]. For the Stark offset a value of $k_{Stark} = 50000$ m^{-1} has been assumed.
The Pr^{3+}:ZBLAN fiber shows the following parameters: an NA of 0.15, a core diameter of 12 μm, a length of 60 cm and background losses of 0.3 dB/km. The fiber core is doped with a concentration of 1200 ppm of Pr^{3+} ions which corresponds to an ion density n_I of about $2.21 \cdot 10^{25}$ ions/m^3. The fiber is split into 15 pieces of equal length ($\Delta x_p = 4$ cm) equivalent to a time resolution of 200 ps.
At t_0 the end pump powers of 500 and 100 mW are reached and remain constant. Relaxation oscillations of the output power at both fiber ends have been found beginning at approximately $t = 44$ μs (see Figure 6.4). The steady-state is reached after approximately $t = 120$ μs. Two million steps have been carried out to simulate up to 400 μs with the preset time resolution. Since a symmetric setup has been assumed, both output powers are equal except for a small time delay of 3 ns which is the time light needs to propagate from one fiber end to the other end. The output power at both fiber ends is illustrated in Figure 6.4. The remaining pump power at the right fiber end is around 454 mW at 835 nm and 61 mW at 1020 nm. The power value in steady-state (for $t > 120$ μs) is the same with the value obtained when applying the stationary model of chapter 5.
The laser shows an emission wavelength of about 633 nm (red laser) for which a maximum power of -16 dBm/nm has been reached at both fiber ends. The output power is about 19.8 mW at one end once steady-state is reached. Before reaching steady-state, the laser power output oscillates around the mean laser output power like a exponentially decaying quasi-sinusoidal function as indicated in equation (6.48). When the laser starts lasing power values up to 46 mW are reached.
The relaxation parameters can be obtained by fitting the output power to equation (6.48). For the relaxation-oscillation frequency f_{ro} a value of about 421 kHz, and, for the Q_{ro} factor a value of 32.8 have been found. Both values are larger than the values extracted for the simulated Yb^{3+}-doped ZBLAN fiber laser in section 6.7.1.
It should be emphasized that with exactly the same simulation parameters but only with a mirror reflectivity of 70 % instead of 90 % no relaxation oscillations have been observed. In addition, by only increasing attenuation the damped oscillations do not occur any more. The dependence of relaxation oscillations on different parameters has been quantitatively

described in section 6.6.

6.7.3 Pr^{3+}/Yb^{3+}-doped fiber laser

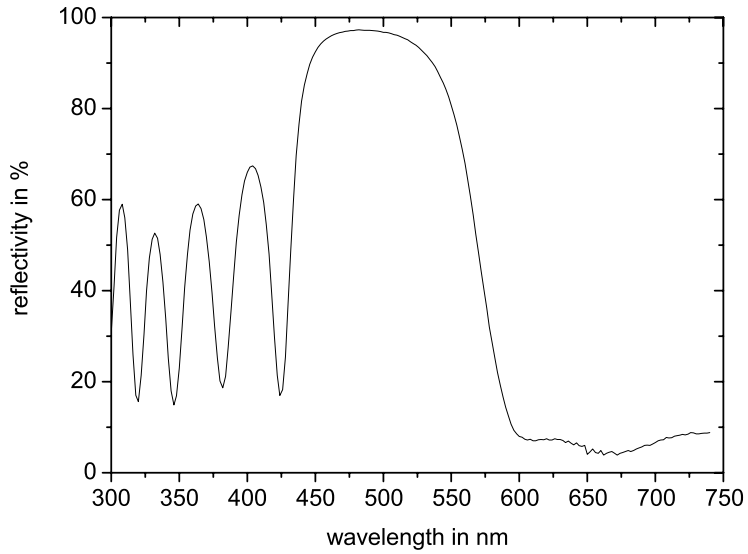

Figure 6.5: Reflectivity versus wavelength for a blue-green laser mirror [14]

The dynamics of a blue Pr^{3+}/Yb^{3+}-doped fiber laser with Fabry-Perot cavity is simulated now. It consists of two laser mirrors which show reflectivities like the mirrors illustrated in Figure 6.5, i.e. they show about 95 % reflectivity for the blue emission wavelength at input and output, respectively. It is easy to obtain a red laser due to the fact that the red fluorescence in praseodymium-doped ZBLAN glasses is very large (see chapter 4) and thus even small Fresnel reflections from the fiber end are sufficient to excite a red laser. This property is very helpful for designing a setup for red emissions. On the other hand, when other than red emissions are required, it is troublesome to suppress the red emission and one has to be very careful in selecting proper laser mirrors. The reflections of these mirrors for red light should be as small as possible, otherwise the threshold of the red laser will be lower than that of the desired laser. The reflectivity of the mirror for a blue-green laser as a function of the wavelength is shown in Figure 6.5.
This mirror provides a high reflection of 95 % for the green (520 nm) and blue emission (490 nm). The reflection of around 5 % for the red transition at 635 nm is very small. This mirror shows also a good transmission at the pump wavelength. Two such mirrors butt-

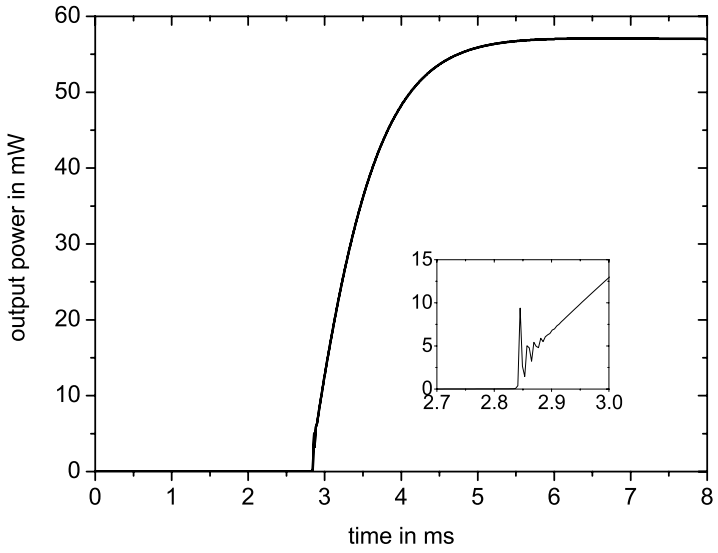

Figure 6.6: Temporal evolution of the output power at both fiber ends for the simulated blue Pr^{3+}/Yb^{3+}-doped ZBLAN fiber laser

coupled to the fiber ends present the Fabry-Perot cavity as shown in Figure 5.1.

The configuration is pumped from the left side with a pump power of 500 mW directly into the active fiber core and the pump wavelength is 835 nm.

In this simulation all twelve levels of Pr^{3+} and both Yb^{3+} levels are considered in the transmission window of ZBLAN (see Figure 3.6). All relevant spectroscopic data for both ions have been introduced in this work and used for the simulation. The cross relaxation rate values of the respective transitions have been extracted by extensive parameter studies to obtain a good qualitative agreement with steady-state laser experiments performed by Baraniecki [14] (see also chapter 5). For the parameter X_{1006} a value of 20000 s^{-1}, and for X_{0196} a value of 500000 s^{-1} has been obtained. All other possible cross relaxation rates have been set to zero. The Pr^{3+}/Yb^{3+}:ZBLAN fiber shows the following parameters: an NA of 0.26, a core diameter of 2.4 μm, a length of 1 m and background losses of 0.3 dB/km. The fiber core is doped with a concentration of 3000 ppm and 20000 ppm of Pr^{3+} and Yb^{3+} ions, respectively. This corresponds to an ion density n_I of about $5.52 \cdot 10^{25}$ and $3.68 \cdot 10^{26}$ ions/m^3 for Pr^{3+} and Yb^{3+} ions, respectively. The fiber is split into 5 pieces of equal length ($\Delta x_p = 20$ cm) equivalent to a time resolution of 1 ns.

At t_0 the end power of 500 mW is reached and remains constant. Only slight relaxation oscillations of the output power at both fiber ends have been found beginning at approximately $t = 2.7$ ms and ending at $t = 3$ ms (see inset of Figure 6.6). After 3 ms the output power

still increases without oscillating until steady-state is reached which is the case approximately after $t = 5.6$ ms. Eight million steps have been carried out to simulate up to 8 ms with the preset time resolution. Since a symmetric setup has been assumed, both output powers are equal except for a small time delay of 5 ns which is the time light needs to propagate from one fiber end to the other end. The temporal evolution of the output power at both fiber ends is shown in Figure 6.6. The remaining pump power at the right fiber end is around 338 mW at 835 nm. The power value in steady-state (for $t > 5.6$ μs) is the same as the value obtained when applying the stationary model of chapter 5.
The laser shows an emission wavelength of 470 nm (blue laser). A maximum power of -9 dBm/nm has been reached at both fiber ends. The output power is about 57 mW at one end once steady-state is reached. Since there are many unknown parameters (such as the non-radiative transition rates and the cross relaxation rates), it is very difficult to extract whether this slight relaxation oscillations come from Pr^{3+} or Yb^{3+}. Only extensive simulations and a comparison to measurement results would help to get an accurate answer but this is not the aim of this work, as has already been described in chapter 5.
The relaxation parameters can be obtained by fitting the output power to equation (6.48) in the range of 2.7 to 3 ms. For the relaxation-oscillation frequency f_{ro} a value of about 417 Hz has been found which is three orders of magnitude smaller than the one obtained for the Pr^{3+}-doped ZBLAN fiber laser in section 6.7.2. However, as can be seen from Figure 6.6 almost no relaxation oscillations like for the Pr^{3+}-doped fiber laser occurs. For the Q_{ro} factor a value of 12.9 has been found.
In case of the blue laser a stable population inversion will be difficult to obtain because it acts as a three-level laser. Hence, a large amount of noise has been observed by experiments [14]. It is noted that with exactly the same simulation parameters but only increasing the attenuation parameter the slight oscillations, which can be seen in the inset of Figure 6.6, do not occur any more and the red laser dominates the blue one.

6.8 Summary

A novel fiber laser and amplifier dynamic simulation model has been developed in this chapter allowing for unlimited spectral resolution. It is very useful to study the transient behavior of rare-earth-doped fiber lasers and amplifiers. One advantage of the model is that it uses the same mathematical notation as has already been presented in chapter 5 for the stationary case. It is worth noting that the stationary model, which has been described in chapter 5, is a special case of the dynamic model described in this chapter due to the fact that the dynamic model also comprises the steady-state behavior of rare-earth-doped devices. The dynamic model has also been extended to simulate energy transfer processes between two dopant ions in rare-earth-doped devices. A step-by-step algorithm which does not need any convergence criterion has been used to find a numerical solution.
The application of the developed simulation model to an ytterbium-doped, a praseodymium-doped and a Pr^{3+}/Yb^{3+}-doped ZBLAN fiber laser has been shown. Relaxation oscillations

have been observed in the laser output power. The difference of the Pr^{3+}/Yb^{3+}-doped fiber laser to the single dopant lasers is that the on-switching behavior takes place in the millisecond instead of the microsecond range.
For a stable laser design the goal must be to suppress relaxation oscillations or, at least, to make them as small as possible. However, they provide a convenient illustration of the validity of the presented rate and gain equations theory for fiber lasers and amplifiers.
An enormous range of investigations is possible with the simulation model at hand. The model can be modified to simulate gain switching behavior typical to solid-state lasers and amplifiers. For this purpose, power dependent mirror reflectivities have to be assumed and so the behavior of a saturable absorber can be simulated. It is the author's hope that the model will be helpful to scientists and system designers, and will be applied to simulate the dynamic behavior of arbitrary rare-earth-doped fiber lasers and amplifiers in a variety of configurations.

Conclusions

This work started with the goal to determine different parameters of rare-earth-doped fibers and glasses for laser and amplifier applications. Furthermore, a numerical simulation model applicable for arbitrary rare-earth-doped fiber lasers and amplifiers in a variety of configurations had to be developed. The model should simulate steady-state and transient behavior of rare-earth-doped devices. In the preceding chapters both goals were attained. Good or even excellent agreement was achieved when measurement and simulation results were compared to literature results. It is the author's hope that this thesis provides its reader a useful introduction to this subject. Let us now recall the whole survey of this work in brief and remind us of important results.

General laser theory and an overview of some selected solid-state and semiconductor laser systems was given at the beginning of this work. Moreover, properties of rare-earth-doped materials and glass hosts have been discussed. Emphasis was put on Pr^{3+}/Yb^{3+}-doped fluoride fiber lasers and on the underlying avalanche upconversion process.

Then, a coherent optical frequency-domain reflectometry setup was developed and used to characterize thulium-doped fluoride fiber amplifiers. It turned out that highly thulium-doped fluoride fibers are more efficient and offer a larger fiber gain and gain-length ratio. Furthermore, a frequency transfer function method was introduced to determine fluorescent lifetimes of arbitrary rare-earth-doped glasses and fibers. The method was applied to determine the fluorescent lifetimes of praseodymium-doped fluoride glasses, some of them co-doped with ytterbium. Two heavy metal fluoride glasses, namely ZBLAN and IBZP, were investigated and it was found that both glasses show similar characteristics. The concentration quenching effect was observed for highly praseodymium-doped samples. Moreover, all relevant spectroscopic parameters of Pr^{3+}- and Yb^{3+}-doped ZBLAN glasses were presented.

These parameters were used in the simulation model developed in the last two chapters. The stationary model included cross relaxation processes between two different rare earth ions and a novel approach to fix the usually unknown values of non-radiative transitions as well. The model was successfully applied to simulate the behavior of Yb^{3+}-, Pr^{3+}, and Pr^{3+}/Yb^{3+}-doped ZBLAN fiber lasers. In case of the latter the dominant role of the avalanche upconversion process was proven.

Finally, a dynamic simulation model with the same mathematical concept used for the stationary model was developed. It was also extended to cover cross relaxation processes between two different rare earth ions and was successfully applied to simulate the transient behavior of Yb^{3+}-, Pr^{3+}, and Pr^{3+}/Yb^{3+}-doped ZBLAN fiber lasers. Relaxation oscillations typical for solid-state lasers were observed underlining the validity of the presented rate and gain equations theory. The model allows for unlimited spectral resolution and the insights into the active fiber obtained by the simulation model were demonstrated.

All in all, the way from the development of special measurement setups to characterize fiber amplifiers and to determine spectroscopic parameters of rare-earth-doped glasses in conjunction with the presentation of a fundamental theory to the final simulation models for arbitrary lasers and amplifiers in stationary and dynamic states turned out to be very successful.

It is the author's belief that especially the simulation model will be useful to researchers working in the field of rare-earth-doped fiber lasers and amplifiers.

Appendix A

OFDR - Analytical expressions for measurement sensitivity

In this appendix, analytical expressions for phase noise and RBS levels in OFDR experiments are derived. The signal spectral density and the respective noise spectral densities will be calculated. With these expressions the minimum detectable reflection strengths in case of the dominance of the respective noise source can be derived. Moreover, the maximum arm-difference length for RBS level measurements in the presence of phase noise can be calculated by these expressions. This rule of thumb has already been presented in section 4.1.5. There, it has been described that phase noise limits the dynamic range from 50 dB to 80 dB regardless of strong or weak discrete and distributed reflectors.

A.1 Signal spectral density

In this section an expression for the one-sided spectral density of the measurement signal in the OFDR setup used will be deduced.

Figure A.1 shows the DUT interferometer of the OFDR setup used. The input power is $P_{\mathrm{in}}/2$

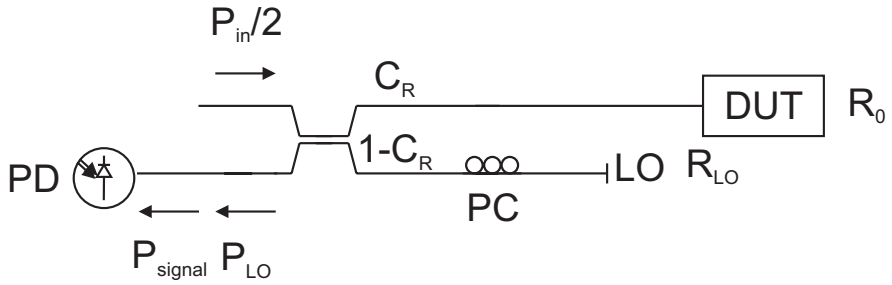

Figure A.1: DUT (device under test) interferometer of the OFDR setup. The abbreviations are: PD: InGaAs photodiode, PC: polarization controller, and LO: reflector acting as local oscillator.

because the adjusted TLS power P_{in} is split by exactly the same amount to the DUT and the auxiliary interferometer (not shown in Figure A.1). This has been done by using a 3 dB coupler as a splitter in front of both interferometers.
The AC part of the signal current is given by [6]:

$$i_{\mathrm{s}}(t) = \Re \cdot 2\sqrt{P_{\mathrm{signal}} \cdot P_{\mathrm{LO}}} \cdot \cos\left(2\pi \cdot f_0 \cdot t\right), \tag{A.1}$$

where P_{signal} is the power from the signal arm of the DUT interferometer, P_{LO} the power from

the local oscillator (LO) arm and f_0 the beat frequency of a single reflector with the power reflection factor R_0 in the DUT arm and R_{LO} in the LO arm.
$\Re$ denotes the responsivity of the detector and is given by

$$\Re = \frac{\eta \cdot q}{h \cdot \nu}, \tag{A.2}$$

where η ($0 < \eta \leq 1$) is the detector quantum efficiency, a measure of the conversion efficiency of incident photons into electrical charge. The parameters q and $h \cdot \nu$ are electronic charge ($1.6 \cdot 10^{-19}$ C) and photon energy ($h = 6.6 \cdot 10^{-34}$ J, Planck constant), respectively. Usually $\Re$ is about 1 $\frac{\mathrm{A}}{\mathrm{W}}$ for optical frequencies around 1550 nm. The detector responsivity (New Focus 2011) at a center wavelength of 1470 nm amounts $\Re \approx 0.84$.
The optical powers P_{LO} and P_{signal} are given by the properties of the fiber couplers used in the setup (cf. Figure A.1), and the reflections from LO and DUT:

$$P_{\mathrm{LO}} = \frac{P_{\mathrm{in}}}{2} \cdot R_{\mathrm{LO}} \cdot C_{\mathrm{R}} \cdot (1 - C_{\mathrm{R}}) \tag{A.3}$$

and

$$P_{\mathrm{signal}} = \frac{P_{\mathrm{in}}}{2} \cdot R_0 \cdot C_{\mathrm{R}} \cdot (1 - C_{\mathrm{R}}), \tag{A.4}$$

with C_{R} as coupled part of light into the DUT arm.
Therefore, equation (A.1) can be written as:

$$i_{\mathrm{s}}(t) = \hat{i_{\mathrm{s}}} \cdot \cos(2\pi \cdot f_0 \cdot t), \tag{A.5}$$

with

$$\hat{i_{\mathrm{s}}} = \Re \cdot P_{\mathrm{in}} \cdot C_{\mathrm{R}} (1 - C_{\mathrm{R}}) \cdot \sqrt{R_0 \cdot R_{\mathrm{LO}}}. \tag{A.6}$$

Since $i_{\mathrm{s}}(t)$ is only defined in the interval $-\frac{T_{\mathrm{s}}}{2} \leq t \leq \frac{T_{\mathrm{s}}}{2}$ with T_{s} as measurement time, Fourier transformation of equation (A.5) yields:

$$I_{\mathrm{s}}(f) = \int_{-\frac{T_{\mathrm{s}}}{2}}^{\frac{T_{\mathrm{s}}}{2}} \hat{i_{\mathrm{s}}} \cdot \frac{1}{2} \cdot \left(e^{j \cdot 2\pi \cdot f_0 \cdot t} + e^{-j \cdot 2\pi \cdot f_0 \cdot t}\right) \cdot e^{-j \cdot 2\pi \cdot f \cdot t} \mathrm{d}t. \tag{A.7}$$

One is only interested in the *one-sided* spectral density of the signal current, i.e. only positive frequencies $f \geq 0$ are evaluated, and after a few mathematical steps, one obtains the one-sided Fourier spectrum of the signal current:

$$I_{\mathrm{s}}^{+}(f) = \frac{\hat{i_{\mathrm{s}}} \cdot T_{\mathrm{s}}}{2} \cdot \mathrm{sinc}((f - f_0) \cdot T_{\mathrm{s}}), \tag{A.8}$$

where T_{s} is given by the frequency resolution

$$\Delta f = \frac{f_{\mathrm{s}}}{N} = \frac{1}{T_{\mathrm{s}}}, \tag{A.9}$$

with f_s as sampling rate and N as the number of recorded data points.
The sinc function is defined as $\frac{\sin(\pi x)}{\pi x}$.
The *one-sided spectral density of the signal* is proportional to the square magnitude of $I_s^+(f)$ and is given by [48]:

$$S_{\text{signal}}(f) = \frac{2}{T_s} \cdot \left|I_s^+(f)\right|^2 = \frac{\hat{i_s}^2 \cdot T_s}{2} \cdot \text{sinc}^2\left((f - f_0) \cdot T_s\right). \tag{A.10}$$

To calculate the FWHM of the signal reflection, the argument of the sinc^2 line shape of the signal must be expressed in distances:

$$(f - f_0) \cdot T_s = \frac{2 \cdot \gamma \cdot n_g}{c_0} (L - L_0) \cdot T_s, \tag{A.11}$$

where γ is the TLS frequency sweep speed. Substituting the swept frequency $\Delta\nu$ by the swept wavelength $\Delta\lambda$ using

$$\gamma \cdot T_s = \Delta\nu = \frac{c_0}{\lambda_0^2} \cdot \Delta\lambda, \tag{A.12}$$

with the center wavelength λ_0, we get

$$(f - f_0) \cdot T_s = \frac{2 \cdot n_g \cdot \Delta\lambda}{\lambda_0^2} (L - L_0). \tag{A.13}$$

The FWHM is $\Delta z = 2(L - L_0)$ and since $\text{sinc}^2(0.44) = 0.5$, we get

$$\Delta z = 0.88 \cdot \frac{\lambda_0^2}{2 \cdot n_g \cdot \Delta\lambda}. \tag{A.14}$$

Inserting the typical values $\lambda_0 = 1470$ nm, $n_g = 1.467$, $\Delta\lambda = 12$ nm/s $\cdot$ 1.25 s, we find a typical spatial resolution of $\Delta z = 43$ μm.
The peak value of the signal spectral density is located at the beat frequency f_0 which corresponds to the reflector location:

$$\hat{S}_{\text{signal}} = S_{\text{signal}}(f_0) = \frac{\hat{i_s^2} \cdot T_s}{2}. \tag{A.15}$$

With equation (A.6) one obtains for equation (A.15):

$$\hat{S}_{\text{signal}} = \frac{R_{\text{LO}} R_0 \cdot C_R^2 \cdot (1 - C_R)^2}{2 \cdot \Delta f} \cdot (\Re P_{\text{in}})^2. \tag{A.16}$$

The DUT interferometer contains a 80:20 coupler ($C_R = 0.8$) which means that 80 % of the incident power is going to the DUT arm and 20 % to the LO arm of the DUT interferometer. A fiber end which is cut straightly (Fresnel reflector) has been used as LO reflector ($R_{\text{LO}} = 0.04$).

A.2 Phase noise spectral density and minimum detectable reflection strength

In this section, the major cause for the limitation of sensitivity in the OFDR setup used is described: *phase noise*. A formula for the minimum detectable reflection strength due to phase noise is developed.

A slight phase jitter (random fluctuating optical phase $\varepsilon(t)$) of the light source leads to a variation of the emitted frequency and due to the beat signal behavior of C-OFDR to intensity fluctuations (noise).
The one-sided spectral density of phase noise is given by [58]:

$$S_\Phi(f) = 4 \cdot R_0 \cdot C_\mathrm{R} \cdot (1 - C_\mathrm{R}) \cdot \frac{\tau_0^2}{\tau_c} \cdot \mathrm{sinc}^2\left((f - f_0)\ \tau_0\right) \cdot \left(\Re\, P_\mathrm{in}\right)^2, \tag{A.17}$$

where R_0 is the power reflection factor of the signal, τ_0 the time delay to the reflection location L_0 ($\tau_0 = \frac{2 \cdot L_0}{c_0} \cdot n_\mathrm{g}$), $f_0 = \gamma \cdot \tau_0$ the beat frequency (γ is the TLS frequency sweep rate), $\Re$ the detector responsivity and P_in the optical input power. In [58] a 3 dB coupler was used to derive an analytical expression, thus formula (A.17) has been applied to the setup used.
τ_c denotes the coherence time which is determined by the laser linewidth $\Delta\nu_\mathrm{source}$:

$$\tau_\mathrm{c} = \frac{1}{\pi \cdot \Delta\nu_\mathrm{source}}. \tag{A.18}$$

The TLS used (GN Nettest, Tunics Reference ES) shows a linewidth of 150 kHz and thus a coherence time τ_c of 2.12 μs.
The minimum detectable reflection strength due to phase noise R^Φ_min can be derived when demanding $\hat{S}_\mathrm{signal} = S_\Phi$ (cf. section A.1):

$$R^\Phi_\mathrm{min}(f) = 8 \cdot \frac{R_0}{R_\mathrm{LO}} \cdot \frac{\tau_0^2}{\tau_c} \cdot \frac{1}{C_\mathrm{R} \cdot (1 - C_\mathrm{R})} \cdot \Delta f \cdot \mathrm{sinc}^2\left((f - f_0)\,\tau_0\right), \tag{A.19}$$

where Δf denotes the frequency resolution and R_LO denotes the reflectivity of the LO arm.
It is worth noting that R^Φ_min is a function of frequency and has its maximum at the beat frequency of the regarded reflector ($f = f_0$). To calculate the spatial behavior of (A.19) given by the sinc^2 factor, we must express the argument of sinc^2 in distances:

$$(f - f_0) \cdot \tau_0 = \frac{2 \cdot \gamma \cdot n_\mathrm{g}}{c_0} \cdot (L - L_O) \cdot \frac{2 \cdot n_\mathrm{g}}{c_0} L_0. \tag{A.20}$$

If we substitute the frequency sweep speed γ by the wavelength sweep speed σ using

$$\gamma = \frac{c_0}{\lambda_0^2}\sigma, \tag{A.21}$$

we end up with the argument

$$(f - f_0) \cdot \tau_0 = \frac{4 \cdot \sigma \cdot n_\mathrm{g}^2}{c_0 \cdot \lambda_0^2} \cdot (L - L_O)\, L_0. \tag{A.22}$$

When we insert the typical values $\sigma = 12$ nm/s, $n_\mathrm{g} = 1.467$, $\lambda_0 = 1470$ nm and even the rather large value $L_0 = 10$ m, we still find a distance $\Delta L = L - L_0 = 34$ m until which the sinc^2 factor is larger than 0.99. Since this is far outside the range of all measurements in this work, it means that in any usual case we can set the sinc^2 factor to one. Hence, the more simplified expression

$$R_\mathrm{min}^\Phi \approx 8 \cdot \frac{R_0}{R_\mathrm{LO}} \cdot \frac{\tau_0^2}{\tau_c} \cdot \frac{1}{C_\mathrm{R} \cdot (1 - C_\mathrm{R})} \cdot \Delta f \tag{A.23}$$

is used for further calculations. A strong reflection increases noise floor in the whole measurement range. So dynamic range and measurement sensitivity, respectively, in case of phase noise are fully given by the strongest reflection in the measurement range.
Formula (A.23) shows that with a decreasing reflection strength of the DUT R_0 and with a decreasing arm-difference length of the DUT interferometer the dynamic range would increase and thus improve sensitivity.

A.3 RBS spectral density and minimum detectable reflection strength

In this section, Rayleigh backscattering (RBS) is described and expressions for the one-sided spectral density of RBS and the minimum detectable reflection strength due to RBS will be derived.

RBS arises due to scattering at fiber inhomogeneities which result in submicroscopic refractive index differences. Parts of this scattered power propagate in opposite direction to the signal and interfere with the LO signal and thus can be detected. RBS represents the case when in the DUT interferometer a certain amount of backscattered light and the location dependent attenuation from the active fluoride fiber and the optical waveguide (in this case standard single mode fiber, SMF) is available. Due to elastic scattering processes inside the fiber a part of the incident light is backscattered and guided by the fiber. Hence, RBS represents distributed reflections along the fiber length. In the OFDR spectra an increasing noise floor level would arise along the fiber parts with large backscattering values.
The effective reflection factor along the fiber length corresponds to the power guided in the opposite direction of the signal and can be calculated by

$$R_\mathrm{eff} = S \cdot \alpha_s \cdot \Delta L, \tag{A.24}$$

where S is the so-called *capture fraction* which describes the part of light which is backscattered from the fiber and will be guided, α_s is the scattering attenuation coefficient (loss constant) and ΔL is the fiber length for which the effective reflectivity should be calculated.

α_s is not only due to Rayleigh scattering but also due to IR and UV absorption and OH^{-1} impurities.
The one-sided spectral density of RBS can be derived when regarding the mean square of the RBS noise current (cf. equations (A.5) and (A.6))

$$\overline{i_{\mathrm{RBS}}^2} = R_{\mathrm{eff}} \cdot R_{\mathrm{LO}} \cdot \left(C_{\mathrm{R}} \cdot (1 - C_{\mathrm{R}})\, \Re \cdot P_{\mathrm{in}}\right)^2 \cdot \overline{\cos^2\left(2\pi \cdot f_0 \cdot t\right)}, \tag{A.25}$$

where the mean value of the cosine square term is $\frac{1}{2}$.
The relation of the RBS noise current to the one-sided spectral density of RBS is given by the following equation [48]:

$$\overline{i_{\mathrm{RBS}}^2} = \int_0^\infty S_{\mathrm{RBS}}(f)\mathrm{d}f = \int_0^\infty \frac{2}{T_{\mathrm{s}}} \cdot \left|I_{\mathrm{RBS}}(f)\right|^2 \mathrm{d}f = S_{\mathrm{RBS}}(f) \cdot f_{\mathrm{N}}, \tag{A.26}$$

with the Nyquist frequency f_{N} which is the maximum frequency appearing in the OFDR spectrum. f_{N} corresponds to the total fiber length (time delay $\Delta\tau$)::

$$f_{\mathrm{N}} = \gamma \cdot \Delta\tau = \gamma \cdot \frac{2 \cdot \Delta L}{c_0} \cdot n_{\mathrm{g}}, \tag{A.27}$$

where γ denotes the TLS frequency sweep speed, n_{g} the group index of the medium and c_0 the speed of light in vacuum. The factor 2 arises from the fact that light travels bidirectionally.
Equating (A.25) and (A.26), rearranging (A.27) for ΔL and inserting this in combination with (A.24), one finally obtains for the *one-sided spectral density of RBS*:

$$S_{\mathrm{RBS}} = \frac{R_{\mathrm{LO}} \cdot S \cdot \alpha_S \cdot c_0 \cdot C_{\mathrm{R}}^2 \cdot (1 - C_{\mathrm{R}})^2}{4 \cdot \gamma \cdot n_{\mathrm{g}}} \cdot \left(\Re\, P_{\mathrm{in}}\right)^2. \tag{A.28}$$

The minimum detectable reflection strength due to RBS $R_{\mathrm{min}}^{\mathrm{RBS}}$ can be derived when demanding $\hat{S}_{\mathrm{signal}} = S_{\mathrm{RBS}}$ and with the relation $\gamma \approx \sigma \cdot \frac{c_0}{\lambda_0^2}$ in which σ represents the wavelength sweep speed, this yields:

$$R_{\mathrm{min}}^{\mathrm{RBS}} = \frac{\lambda_0^2 \cdot S \cdot \alpha_s}{2 \cdot \sigma \cdot n_{\mathrm{g}}} \cdot \Delta f. \tag{A.29}$$

Equation (A.29) is equivalent to the mean backscattered power $S \cdot \alpha_S \cdot \Delta z$ [58], where Δz denotes the two-point spatial resolution. RBS is therefore proportional to the inverse sweep speed. Hence, with decreasing sweep speed the RBS power increases. It is noted that a decrease of sweep speed corresponds to a decrease in the swept wavelength range according to the relation $\Delta\lambda = \sigma \cdot T_{\mathrm{S}}$. In conclusion, one may better observe the effect of RBS when decreasing the swept wavelength range, which is equivalent to a decrease of spatial resolution.

Appendix B

FTF method - Alternatives to determine fluorescent lifetimes

The introduced concept for acquiring the phase and modeling the complex FTF to gain the model parameter (see section 4.2) is in principle only one possible realization to determine fluorescent lifetimes in frequency-domain. A first alternative would be to measure magnitudes and phases up to high modulation frequencies and then to perform the inverse Fourier transform of the measured FTF to obtain the impulse response. The integration of the impulse response over time yields the step response which can e.g. be modeled as a superposition of several exponential functions or in the way indicated in equation (4.32). This function can be used as fit function to determine the respective lifetimes. The advantage of this method is that one does not need any knowledge about the complex FTF. A second alternative is to measure the magnitude of the FTF and to determine the fluorescent lifetimes by fitting the magnitude. The only prerequisite is that for sufficiently large modulation frequencies the magnitude has still to be measurable. In this appendix, the latter alternative is considered and two cases are distinguished: the pump power is negligible or has to be considered at the signal wavelength. Both cases have also been distinguished as the phase of the complex FTF has been determined in section 4.2.4.

B.1 Extracting lifetimes from the magnitude of the complex FTF

For high modulation frequencies the signal magnitude might decrease so drastically that it becomes hardly possible to determine the exact magnitude. This is by far better for the signal phases. However, in this section an alternative to determine the lifetimes is shown by fitting the signal magnitudes. This might become interesting for low modulation frequencies. One has to be aware that a distortion of the ratio of pump and signal power can be observed for measurements with bulk glasses due to the different imaging of pump and signal power. Hence, this behavior of the measurement setup must be considered in the FTF by means of the constant factor C introduced in section 4.2.4. C had no influence on the measured phases but will have an influence on the signal magnitude. In addition, the unknown absorption probabilities and the quantum efficiency lead to an unknown constant which is absorbed in the same constant C.
The complex FTF is given by

$$H_N(j\omega) = \sum_{i=1}^{N} \left(\frac{a_i \left(1 - j\omega\tau_i\right) \prod_{j=1, j\neq i}^{N} \left(1 + (\omega\tau_j)^2\right)}{\prod_{j=1}^{N} \left(1 + (\omega\tau_j)^2\right)} \right). \tag{B.1}$$

The argument of equation (B.1) leads to the phase of the total system indicated in equation (4.34). The magnitude of equation (B.1) can be calculated to be

$$\boxed{|H_N(j\omega)| = \frac{\sqrt{K+L}}{\prod_{j=1}^{N}\left(1+(\omega\tau_j)^2\right)}}, \tag{B.2}$$

with the factors K and L defined by

$$K = \omega^2 \left[\sum_{i=1}^{N}\left(a_i\tau_i \prod_{j=1,j\neq 1}^{N}\left(1+(\omega\tau_j)^2\right)\right)\right]^2, \tag{B.3}$$

and

$$L = \left[\sum_{i=1}^{N}\left(a_i \prod_{j=1,j\neq 1}^{N}\left(1+(\omega\tau_j)^2\right)\right)\right]^2. \tag{B.4}$$

In case of considering the pump power the magnitude of the FTF becomes:

$$\boxed{|H_N^{wp}(j\omega)| = \frac{\sqrt{K+M}}{\prod_{j=1}^{N}\left(1+(\omega\tau_j)^2\right)}}, \tag{B.5}$$

where K has already been defined above and M is a new factor defined by

$$M = \left[\sum_{i=0}^{N}\left(a_i \prod_{j=1,j\neq 1}^{N}\left(1+(\omega\tau_j)^2\right)\right)\right]^2. \tag{B.6}$$

The only difference to the factor L is that M starts with the index $i = 0$.
Both boxed expressions can be used to fit the measured magnitude of the FTF. It is noted that a multiplication of the magnitude with a constant factor will affect every a_i and thus not distort the result. For instance, it is possible to normalize to $H_N(0) = 1$ or $H_N^{wp}(0) = 1$, respectively, by dividing the magnitude with the sum of all a_i (including a_0 in case of equation (B.5)).
All relevant models for determining the fluorescent lifetimes of rare-earth-doped glasses and fibers in frequency-domain are thus found. In all cases one can list all fit parameters in a table. If for a transition with τ_i the function $p_i(\lambda)$ has been determined over the whole spectral range of the emission by continued excitation, then the product of emission spectrum and $p_i(\lambda)$ gives the emission from state i. Further, the temporal output response $g(t)$ can be obtained by equation (4.32) and be used for a direct comparison with a time-domain measurement.
It must be noted that all models are only valid in case of neglected stimulated emission which is a good approximation. In case of the upper levels of praseodymium equation (4.27) has been used since only one lifetime is relevant. All upper levels are thermally coupled so that no difference has been observed when determining the lifetimes by fitting the recorded phase for the red, orange, green or blue transition (see Figure 4.10), respectively. The pump power at the signal wavelength has been negligible since glass samples have been measured and not fibers.

Appendix C

Spectroscopy

In this appendix, a special Gauss fit technique to separate more than two transitions in measured cross section spectra is presented [15]. Only separated transitions are inserted into the simulation model presented in chapters 5 and 6. In addition, the Ladenburg-Fuchtbauer relation in frequency-, wavenumber- and wavelength-domain is indicated, so that one can choose in which domain all input parameters for the simulation model should be given. In this work the wavelength is chosen for parametrization, however, any of the above quantities can be chosen.

C.1 Gauss fits for measured cross sections

If several absorption or emission lines overlap, difficulties with the implementation of the results of cross section measurements in the simulation model arise. In these cases the absorption or emission lines have to be split by a special technique.
First of all, a fit with several Gauss functions has been applied to the spectrum of the group of lines, one or more Gauss functions for each line. For praseodymium GSA cross sections, it has been found that for N transitions $N + 1$ Gauss fits are sufficient to split the absorption lines. However, it should be noted that there is no general rule of thumb as each rare earth ion may show different behavior. Moreover, it should be emphasized that the application of the presented technique is independent to the wavelength-, wavenumber- or frequency-domain.
For the sake of simplicity, it is assumed that measured cross section spectra in wavelength-domain are available. Further, it is assumed that in the measured spectrum $\sigma(\lambda)$ two transitions A and B overlap. A Gauss fit with e.g. three Gauss functions $G_1(\lambda)$, $G_2(\lambda)$ and $G_3(\lambda)$ is performed, so that the sum of the fitted functions is in good agreement with the measured spectrum $\sigma(\lambda)$. However, the sum is usually different from the actual cross section spectrum because the real shape of the individual lines is normally not just a Gauss function.
Dependent on the special rare earth ion and its respective transition, one assigns e.g. the Gauss functions $G_1(\lambda)$ and $G_2(\lambda)$ to the transition A and the Gauss function $G_3(\lambda)$ to the transition B:

$$G_A(\lambda) = G_1(\lambda) + G_2(\lambda) \quad \text{and} \tag{C.1}$$

$$G_B(\lambda) = G_3(\lambda). \tag{C.2}$$

The sum of all lines must be equal to the measured cross section spectrum and thus the fit functions in the next step have only been used as weight functions. More precisely, the measured spectrum $\sigma(\lambda)$ is split into two spectra $\sigma_A(\lambda)$ and $\sigma_B(\lambda)$ of transitions A and B, i.e.:

$$\sigma(\lambda) = \sigma_A(\lambda) + \sigma_B(\lambda). \tag{C.3}$$

The spectra $\sigma_A(\lambda)$ and $\sigma_B(\lambda)$ are approximated by using the spectra $\tilde{\sigma_A}(\lambda)$ and $\tilde{\sigma_B}(\lambda)$ which can be calculated by the following relations:

$$\tilde{\sigma_A}(\lambda) = \sigma(\lambda) \cdot \frac{G_A(\lambda)}{G_A(\lambda) + G_B(\lambda)} \quad \text{and} \tag{C.4}$$

$$\tilde{\sigma_B}(\lambda) = \sigma(\lambda) \cdot \frac{G_B(\lambda)}{G_A(\lambda) + G_B(\lambda)}. \tag{C.5}$$

This means, that the Gauss fits are only used as weight factors. Additionally, the following relation is valid:

$$\sigma(\lambda) = \tilde{\sigma_A}(\lambda) + \tilde{\sigma_B}(\lambda). \tag{C.6}$$

Thus, $\tilde{\sigma_A}(\lambda)$ and $\tilde{\sigma_B}(\lambda)$ are for sure better approximations for $\sigma_A(\lambda)$ and $\sigma_B(\lambda)$ than the pure Gauss fits $G_A(\lambda)$ and $G_B(\lambda)$. Hence, at each wavelength the measured cross section is distributed among all lines according to the value of their respective Gauss function(s) and it is assured that at each wavelength the sum of all lines is exactly the measured cross section. Care must be taken in case of overlapping emission lines, which must be separated before the Ladenburg-Fuchtbauer equation (see section 4.3.3) is applied to each component separately. The application of this formula to the combined spectrum using the sum of the A_{21}'s of all lines contained in the spectrum would lead to completely wrong results.

C.2 Ladenburg-Fuchtbauer equation in frequency-, wavenumber- and wavelength-domain

The emission cross section $\sigma_{21}(\nu)$ is calculated by the measured lineshape $g_{21}(\nu)$ with the Ladenburg-Fuchtbauer equation:

$$\sigma_{21}(\nu) = \frac{c_0^2}{8\pi \cdot n^2 \cdot \nu_0^2} \cdot A_{21} \cdot g_{21}(\nu), \tag{C.7}$$

where c_0 denotes the speed of light in vacuum, n is the refractive index of the medium, ν_0 the optical center frequency and A_{21} the calculated radiative transition rate. The lineshape is normalized by the relation $\int g_{21}(\nu)\mathrm{d}\nu = 1$.
Converting this formula from frequency- to wavenumber-domain yields:

$$\sigma_{21}(k) = \frac{1}{8\pi \cdot c_0 \cdot k_{cm}^2 \cdot n^2} \cdot A_{21} \cdot g_{21}(k), \tag{C.8}$$

where the frequency ν has been replaced by the wavenumber $k = \nu/c_0$, and the lineshape $g_{21}(k)$, due to the different normalization $\int g_{21}(k)\mathrm{d}k = 1$, has the dimension of an inverse wavenumber in contrast to $g_{21}(\nu)$. Therefore, a factor c_0 is introduced. k_{cm} is the center of mass wavenumber defined in section 4.3.6.

Now, if one wants to have the respective formula in wavelength-domain, one can convert either of the previous expressions with the relation $\lambda = c_0/\nu = 1/k$ and thus obtain:

$$\sigma_{21}(\lambda) = \frac{\lambda_0^4}{8\pi \cdot c_0 \cdot n^2} \cdot A_{21} \cdot g_{21}(\lambda), \tag{C.9}$$

with the normalized lineshape $\int g_{21}(\lambda)\mathrm{d}\lambda = 1$ and the center wavelength λ_0.

References

[1] T.H. Maiman, "Stimulated optical radiation in ruby," Nature, vol. 187, no. 4736, pp. 493-494, Aug. 1960

[2] O. Svelto, *Principles of Lasers,* 4^{th} edition, Plenum Press, ISBN 0-306-45748-2, 1998

[3] A.E. Siegman, *Lasers,* University Science Books, ISBN 0-935702-11-5, 1986

[4] B.E.A. Saleh and M.C. Teich, *Fundamentals of Photonics,* Wiley-Interscience, ISBN 0-471-83965-5, 1991

[5] M.J.F. Digonett (Editor), *Rare-earth-doped fiber lasers and amplifiers,* Second Edition, Marcel Dekker Inc., ISBN 0-8247-0458-4, 2001

[6] D. Derickson (Editor), *Fiber Optic Test and Measurement,* Prentice Hall, ISBN 0-13-534330-5, 1998

[7] S. Sudo (Editor), *Optical Fiber Amplifiers: Materials, Devices and Applications,* Artech House Inc., ISBN 0-89006-809-7, 1997

[8] P.C. Becker, N.A. Olsson, and J.R. Simpson, *Erbium-doped fiber amplifiers- fundamentals and technology,* Academic Press, ISBN 0-12-084590-3, 1999

[9] M.F. Joubert, "Photon avalanche upconversion in rare earth laser materials," Opt. Mater., vol. 11, no. 2-3, pp. 181-203, 1999

[10] W. Lenth and R.M. MacFarlane, "Upconversion lasers," Opt. Phot. News, vol. 3, no. 3, pp. 8-15, 1992

[11] J.Y. Allain, M. Monerie, and H. Poignant, "Tunable cw lasing around 610, 635, 695, 715, 885 and 910 nm in praseodymium-doped fluorozirconate fibre," Electron. Lett., vol. 27, no. 2, pp. 189-191, 1991

[12] J.L. Adam and W.A. Sibley, "Optical transitions of Pr^{3+} ions in fluorozirconate glass," Journal of Non-Crystalline Solids, 76, pp. 267-279, 1985

[13] R.M. Percival, M.W. Philips, D.C. Hanna, and A.C. Tropper, "Characterization of spontaneous and stimulated emission from praseodymium (Pr^{3+}) ions doped into a silica-based monomode optical fiber," IEEE J. Quantum Electron., vol. QE-25, no. 10, pp. 2119-2123, 1989

[14] T.P. Baraniecki, *Praseodymium doped fluoride fiber lasers,* Doctoral dissertation, Gemeinsame Fakultät für Maschinenbau und Elektrotechnik der Technischen Universität Braunschweig, 2006

[15] R. Caspary, *Applied rare-earth spectroscopy for fiber laser optimization,* Doctoral dissertation, Gemeinsame Fakultät für Maschinenbau und Elektrotechnik der Technischen Universität Braunschweig, 2001

[16] Y. Zhao and S. Fleming, "Theory of Pr^{3+}-doped fluoride fiber upconversion lasers," IEEE J. Quantum Electron., vol. 33, no. 6, pp. 905-915, 1997

[17] R.G. Smart et al., "CW room temperature upconversion lasing at blue, green and red wavelengths in infrared-pumped Pr^{3+}-doped fluoride fibre," Electron. Lett., vol. 27, no. 14, pp. 1307-1309, 1991

[18] Y. Zhao, "An analytical model for Pr^{3+}-doped fluoride fibre upconversion lasers," Opt. Commun., vol. 134, no. 1-6, pp. 470-478, Jan. 1997

[19] R.S. Quimby and B. Zheng, "New excited-state absoprtion measurement technique and application to Pr^{3+} doped fluorozirconate glass," Appl. Phys. Lett., vol. 60, no. 9, pp. 1055-1057, 1992

[20] R.G. Smart et al., "CW room temperature operation of praseodymium-doped fluorozirconate glass fibre lasers in the blue-green, green and red spectral regions," Opt. Comm., vol. 86, no. 3-4, pp. 337-340, 1991

[21] P. Krummrich, *Praseodym-dotierte Faserverstärker für den Wellenlängenbereich um 1,3 μm (English: Praseodymium-doped fiber amplifier for the wavelength region around 1.3 μm),* Doctoral dissertation, Gemeinsame Fakultät für Maschinenbau und Elektrotechnik der Technischen Universität Braunschweig, 1995

[22] P.M. Krummrich, "Experimental determination of the emission cross-section spectrum of the pump transition of praseodymium," IEEE Photon. Technol. Lett., vol. 7, no. 1, pp. 62-64, Jan. 1995

[23] J.Y. Allain, M. Monerie, and H. Poignant, "Red upconversion Yb-sensitised Pr fluoride fibre laser pumped in 0.8 μm region," Electron. Lett., vol. 27, no. 13, pp. 1156-1157, 1991

[24] H. Zellmer, P. Riedel, and A. Tunnermann, "Visible upconversion lasers in praseodymium-ytterbium-doped fibers," Appl. Phys. B, vol. 69, no. 5-6, pp. 417-421, 1999

[25] J.Y. Allain, M. Monerie, H. Poignant, and T. Georges, "High-efficiency ytterbium-doped fluoride fibre laser," J. Non-Cryst. Solids, vol. 161, pp. 270-273, 1993

[26] M.C. Brierley et al., "Visible fibre lasers," J. Br. Telecom. Technol., vol. 11, no. 2, pp. 128-136, 1993

[27] J.Y. Allain, M. Monerie, and H. Poignant, "Energy transfer in Pr^{3+}/Yb^{3+}-doped fluorozirconate fibres," Electron. Lett., vol. 27, no. 12, pp. 1012-1014, 1991

[28] G. Huber, E. Heumann, T. Sandrock, and K. Petermann, "Up-conversion processes in laser crystals," J. Lumin., vol. 72-74, pp. 1-3, 1997

[29] T. Sandrock, H. Scheife, E. Heumann, and G. Huber, "High-power continuous-wave upconversion fiber laser at room temperature," Opt. Lett., vol. 22, no. 11, pp. 808-810, 1997

[30] T.R. Gosnell, "Avalanche assisted upconversion in Pr^{3+}/Yb^{3+}-doped ZBLAN glass," Electron. Lett., vol. 33, no. 5, pp. 411-413, 1997

[31] M.M. Kozak, D. Goebel, W. Kowalsky, and R. Caspary, "Excited state absorption spectroscopy for thulium-doped zirconium fluoride fiber," Optics Communications, 259 (1), pp. 154-157, 2005

[32] W. Blanc, P. Peterka, B. Faure, B. Dussardier, G. Monnom, I. Kasik, J. Kanka, D. Simpson, and G. Baxter, "Characterization of a thulium-doped silica-based optical fibre for S-band amplification," Proceedings of SPIE, vol. 6180, Photonics, Devices, and Systems III, April 18, 2006

[33] M.M. Kozak, *Development of thulium-doped fluoride fiber amplifiers,* Doctoral dissertation, Gemeinsame Fakultät für Maschinenbau und Elektrotechnik der Technischen Universität Braunschweig, 2005

[34] M.B. Costa e Silva, M.T. Carvalho, M.L. Sundheimer, A.S.L. Gomes, J.P. von der Weid, W. Margulis, and F. Carlsson, "Distributed-gain measurements in S-band TDFA by coherent optical frequency domain reflectometry," Electronics Letters, vol. 38, no. 14, pp. 729-730, July 2002

[35] A.S.L. Gomes, M.T. Carvalho, and M.L. Sundheimer, "Comparison of distributed gain in two dual-wavelength pumping schemes for thulium-doped fibre amplifiers," Electronics Letters, vol. 39, no. 8, pp. 647-648, April 2003

[36] M.M. Kozak, D. Goebel, R. Caspary, and W. Kowalsky, "Systematic investigation of the avalanche effect in highly thulium-doped fiber amplifiers," Appl. Phys. B, vol. 86, no. 1, pp. 55-59, Jan. 2007

[37] M. Wegmüller, P. Oberson, J.P. von der Weid, O. Guinnard, L. Guinnard, C. Vinegoni, M. Legre, and N. Gisin, "Overview of coherent reflectometry techniques: characterization of components and small systems," Proceedings of Symposium on Optical Fiber Measurements, Boulder, CO, USA, pp. 155-160, 26-28 Sept. 2000

[38] H. Barfuss and E. Brinkmeyer, "Modified optical frequency domain reflectometry with high spatial resolution for components of integrated optic systems," J. Lightwave Technol., vol. 7, no. 1, pp. 3-10, Jan. 1989

[39] H. Rosenfeldt, Ch. Knothe, J. Cierullies, and E. Brinkmeyer, "Evolution of amplitude and dispersion spectra during fiber Bragg grating fabrication," in *OSA Technical Digest: Conference on Bragg Gratings, Photosensitivity and Poling in Glass Waveguides*, Stresa, Italy, BWA4, July 2001

[40] S. Kieckbusch, Ch. Knothe, and E. Brinkmeyer, "Fast and accurate characterization of fiber Bragg gratings with high spatial and spectral resolution," in *OFC 2003*, 1, WL2, 379-381, March 2003

[41] C. Knothe, *Holographisches Herstellungsverfahren für Bragg-Gitter in UV-sensitiven Wellenleitern (English: Holographic manufacturing technology for Bragg gratings in UV sensitive waveguides),* Doctoral dissertation, VDI, ISBN 3-18-375410-X, Technische Universität Hamburg-Harburg, 2004

[42] K. Takada, K. Yukimatsu, M. Kobayashi, and J. Noda, "Rayleigh backscattering measurement of single-mode fibers by low coherence optical time-domain reflectometer with 14 μm spatial resolution," Appl. Phys. Lett., vol. 59, no. 2, pp. 143-145, July 1991

[43] U. Glombitza, *Frequenz- und Kohärenzbereichsreflektometrie: Optische Messverfahren zur Charakterisierung passiver und aktiver Wellenleiter (English: Frequency- and coherence-domain reflectometry: optical measurement procedures to characterize passive and active waveguides),* Doctoral dissertation, Technische Universität Hamburg-Harburg, 1993

[44] A. Kohlhaas, C. Frömchen, and E. Brinkmeyer, "High-resolution OCDR for testing integrated-optical waveguides: Dispersion-corrupted experimental data corrected by a numerical algorithm," J. Lightwave Technol., vol. 9, no. 11, pp. 1493-1502, Nov. 1991

[45] W.V. Sorin and D.M. Baney, "Measurement of Rayleigh backscattering at 1.55 μm with 32 μm spatial resolution," IEEE Photon. Technol. Lett., vol. 4, no. 4, pp. 374-376, April 1992

[46] K. Takada, M. Oguma, H. Yamada, S. Mitachi, and M. Golling, "Gain distribution measurement of an erbium-doped silica-based waveguide amplifier using a complex OLCR," IEEE Photon. Technol. Lett., vol. 9, no. 8, pp. 1102-1103, Aug. 1997

[47] W. Eickhoff and R. Ulrich, "Optical frequency domain reflectometry in single-mode fiber," Appl. Phys. Lett., vol. 39, no. 9, pp. 693-695, Nov. 1981

[48] H. Shalibeik, "Coherent optical frequency domain reflectometry for characterization of optical devices and components," Diploma thesis, Technische Universität Hamburg-Harburg, Oct. 2003

[49] P. Oberson, B. Huttner, O. Guinnard, L. Guinnard, G. Ribordy, and N. Gisin, "Optical frequency domain reflectometry with a narrow linewidth fiber laser," IEEE Photon. Technol. Lett., vol. 12, no. 7, pp. 867-869, July 2000

[50] J. Geng, C. Spiegelberg, and S. Jiang, "Narrow linewidth fiber laser for 100 km optical frequency domain reflectometry," IEEE Photon. Technol. Lett., vol. 17, no. 9, pp. 1827-1829, Sept. 2005

[51] Myoung Sook Oh, Hee Su Park, and Byoung Yoon Kim, "Optical frequency-domain reflectometry based on wavelength-swept mode-locked fiber laser," IEEE Photon. Technol. Lett., vol. 15, no. 2, pp. 266-268, Feb. 2003

[52] S.H. Yun, G.J. Tearney, J.F. de Boer, N. Iftima, and B.E. Bouma, "High-speed optical frequency-domain imaging," Optics Express, vol. 11, no. 22, pp. 2953-2963, Nov. 2003

[53] H. Shalibeik, A. Behrends, M.M. Kozak, W. Kowalsky, and R. Caspary, "Characterization of 1050 nm pumped S-band TDFA with different dopant concentrations by coherent optical frequency-domain reflectometry," IEEE Photon. Technol. Lett., vol. 19, no. 4, pp. 188-190, Feb. 2007

[54] R. Passy, N. Gisin, J.P. von der Weid, and H.H. Gilgen, "Experimental and theoretical investigations of coherent OFDR with semiconductor laser sources," J. Lightwave Technol., vol. 12, no. 9, pp. 1622-1630, Sept. 1994

[55] U. Glombitza and E. Brinkmeyer, "Coherent frequency-domain reflectometry for characterization of single-mode integrated-optical waveguides," J. Lightwave Technol., vol. 11, no. 8, pp. 1377-1384, Aug. 1993

[56] J.P. von der Weid, R. Passy, G. Mussi, and N. Gisin, "On the characterization of optical fiber network components with optical frequency domain reflectometry," J. Lightwave Technol., vol. 15, no. 7, pp. 1131-1141, July 1997

[57] G. Mussi, P. Stamp, N. Gisin, R. Passy, and J.P. von der Weid, "Polarization effects in coherent optical frequency-domain reflectometry," IEEE Photon. Technol. Lett., vol. 8, no. 11, pp. 1513-1515, Nov. 1996

[58] S. Venkatesh and W.V. Sorin, "Phase noise considerations in coherent optical FMCW reflectometry," J. Lightwave Technol., vol. 11, no. 10, pp. 1694-1700, Oct. 1993

[59] R. Passy, N. Gisin, and J.P. von der Weid, "High-sensitivity-coherent optical frequency-domain reflectometry for characterization of fiber-optic network components," IEEE Photon. Technol. Lett., vol. 7, no. 6, pp. 667-669, June 1995

[60] A. Behrends, "Optische Frequenzbereichsreflektometrie zur Charakterisierung Thulium-dotierter Fluoridglasfaserverstärker" (English: Optical frequency domain reflectometry for characterization of thulium-doped fluoride fiber amplifiers), Diploma thesis, Technische Universität Braunschweig, Dec. 2006

[61] E. Brinkmeyer, "Analysis of the backscattering method for single-mode optical fibers," J. Opt. Soc. Am., vol. 70, no. 8, pp. 1010-1012, Aug. 1980

[62] E. Voges and K. Petermann (Hrsg.), *Optische Kommunikationstechnik. Handbuch für Wissenschaft und Industrie (English: Optical communication technology - Handbook for science and industry)*, Springer, ISBN 3-540-67213-3, 2002

[63] S. Aozasa, H. Masuda, I. Sakamoto, K. Shikano, and M. Shimizu, "Gain-shifted TDFA employing high concentration doping technique with high internal power conversion efficiency of 70%," Electronics Letters, vol. 38, no. 8, pp. 361-363, April 2002

[64] J.P. von der Weid, R. Passy, and N. Gisin, "Coherent reflectometry of optical fiber amplifiers," IEEE Photon. Technol. Lett., vol. 9, no. 9, pp. 1253-1255, Sept. 1997

[65] J.P. von der Weid, R. Passy, B. Huttner, O. Guinard, and N. Gisin, "High-resolution distributed-gain measurements in erbium-doped fibers," IEEE Photon. Technol. Lett., vol. 10, no. 7, pp. 949-951, July 1998

[66] M. Wegmuller, P. Oberson, O. Guinnard, B. Huttner, L. Guinnard, C. Vinegoni, and N. Gisin, "Distributed gain measurements in Er-doped fibers with high resolution and accuracy using an optical frequency domain reflectometer," J. Lightwave Technol., vol. 18, no. 12, pp. 2127-2132, Dec. 2000

[67] M.B. Costa e Silva, J.P. von der Weid, and W. Margulis, "Optimising erbium doped L-band amplifiers with Bragg gratings using tuneable coherent reflectometry," 28$^{\text{th}}$ European Conference on Optical Communication, ECOC 2002, p. 2 pp., vol. 4, Copenhagen, Denmark, 8-12 Sept. 2002

[68] J.F. Martins-Filho, C.J.A. Bastos-Filho, M.T. Carvalho, M.L. Sundheimer, and A.S.L. Gomes, "Dual-wavelength (1050 nm + 1550 nm) pumped thulium-doped fiber amplifier characterization by optical frequency-domain reflectometry," IEEE Photon. Technol. Lett., vol. 15, no. 1, pp. 24-26, Jan. 2003

[69] A.S.L. Gomes, M.T. Carvalho, M.L. Sundheimer, C.J.A. Bastos-Filho, J.F. Martins-Filho, M.B. Costa e Silva, J.P. von der Weid, and W. Margulis, "Characterization of

efficient dual-wavelength (1050 + 800 nm) pumping scheme for thulium-doped fiber amplifiers," IEEE Photon. Technol. Lett., vol. 15, no. 2, pp. 200-202, Feb. 2003

[70] S.S.H. Yam, Y. Akasaka, Y. Kubota, H. Inoue, and K. Parameswaran, "Novel pumping schemes for fluoride-based thulium-doped fiber amplifier at 690 and 1050 nm (or 1400 nm)," IEEE Photon. Technol. Lett., vol. 17, no. 5, pp. 1001-1003, May 2005

[71] C. Floridia, M.T. Carvalho, S.R. Lüthi, and A.S.L. Gomes, "Modeling the distributed gain of single- (1050 or 1410 nm) and dual- wavelength- (800 + 1050 nm or 800 + 1410 nm) pumped thulium-doped fiber amplifiers," Optics Letters, vol. 29, no. 17, pp. 1983-1985, Sept. 2004

[72] P. Peterka, B. Faure, W. Blanc, M. Karasek, and B. Dussardier, "Theoretical modelling of S-band thulium-doped silica fibre amplifiers," in *Proceedings of 11th International Workshop on Optical Waveguide Theory and Numerical Modelling*, Prague, Czech Republic, 4-5 April 2003

[73] M.M. Kozak, W. Kowalsky, and R. Caspary, "Low-loss glue splicing method to join silica and fluoride fibers," Electronics Letters, vol. 41, no. 16, pp. 897-899, 2005

[74] G. Mussi, N. Gisin, R. Passy, and J.P. von der Weid, "-152.5 dB sensitivity high dynamic-range optical frequency-domain reflectometry," Electronics Letters, vol. 32, no. 10, pp. 926-927, May 1996

[75] B. Bourliaguet, F. Emond, S. Mohrdiek, A.-C. Jacob-Poulin, P.-Y. Cortes, and J. Lauzon, "Thulium-doped fibre amplifier using 1055 nm laser diode pumping configuration," Electronics Letters, vol. 38, no. 10, pp. 447-448, May 2002

[76] A.S.L. Gomes and S.R. Lüthi, "Dual-wavelength pumped TDFAs for S-band optical telecommunication - an evaluation," Optical Fiber Communications Conference Technical Digest, Anaheim, CA, USA, paper JWA13, vol. 3, 6-11 March 2005

[77] H. Shalibeik, P. Görrn, W. Kowalsky, and R. Caspary, "Frequency transfer function method to measure the fluorescent lifetime of praseodymium-doped fluoride glasses," to be published in IEEE Journal of Quantum Electronics, 2007

[78] Y. Ohishi, T. Kanamori, and S. Takahashi, "Concentration quenching in Pr^{3+}-doped fluoride fiber amplifier operating at 1.3 μm," 17$^{\text{th}}$ European Conference on Optical Communication (ECOC) 1991, 8$^{\text{th}}$ International Conference on Integrated Optics and Optical Fibre Communication (IOOC) 1991, Paris, France, pp. 17-20, MoA2-2, 9-12 Sept. 1991

[79] Y. Ohishi, T. Kanamori, T. Nishi, S. Takahashi, and E. Snitzer, "Gain characteristics of Pr^{3+}-Yb^{3+} codoped fluoride fiber for 1.3 μm amplification," IEEE Photon. Technol. Lett., vol. 3, no. 11, pp. 990-992, Nov. 1991

[80] Y. Nishida, M. Yamada, T. Kanamori, K. Kobayashi, J. Temmyo, S. Sudo, and Y. Ohishi, "Development of an efficient praseodymium-doped fiber amplifier," IEEE J. Quantum Electron., vol. 34, no. 8, pp. 1332-1339, Aug. 1998

[81] Y. Ohishi, T. Kanamori, T. Nishi, S. Takahashi, and E. Snitzer, "Concentration effect on gain of Pr^{3+}-doped fluoride fiber for 1.3 μm amplification," IEEE Photon. Technol. Lett., vol. 4, no. 12, pp. 1338-1341, Dec. 1992

[82] P. Xie and T.R. Gosnell, "Efficient sensitisation of praseodymium 1.31 μm fluorescence by optically pumped ytterbium ions in ZBLAN glass," Electron. Lett., vol. 31, no. 3, pp. 191-192, Feb. 1995

[83] W.G. Jordan, A. Jha, M. Lunt, S.T. Davey, R. Wyatt, and W.J. Rothwell, "The optical properties of ZrF_4-based glasses with extended Pr^{3+}: $^1G_4 \rightarrow {}^3H_5$ fluorescence lifetimes," Journal of Non-Crystalline Solids, 184, pp. 5-8, 1995

[84] D. Marchese, G. Kakarantzas, and A. Jha, "$^1G_4$ lifetimes, optical and thermal characteristics of Pr-doped GeS_2-chalcohalide glasses," Journal of Non-Crystalline Solids, 196, pp. 314-319, 1996

[85] T. Sun, Z.Y. Zhang, K.T.V. Grattan, A.W. Palmer, and S.F. Collins, "Temperature dependence of the fluorescence lifetime in Pr^{3+}:ZBLAN glass for fiber optic thermometry," Review of Scientific Instruments, 68 (9), pp. 3447-3451, Sept. 1997

[86] I.R. Mitchell, P.M. Farrell, G.W. Baxter, S.F. Collins, K.T.V. Grattan, and T. Sun, "Analysis of dopant concentration effects in praseodymium-based fluorescent fiber optic temperature sensors," Review of Scientific Instruments, 71 (1), pp. 100-103, Jan. 2000

[87] Y. Hou, Y. Li, X. Chen, G. Zhang, and Y. Wang, "Temperature dependence of upconversion luminescence from Pr^{3+} and Yb^{3+} codoped ZBLAN glass pumped by 960 nm laser diode," Journal of Non-Crystalline Solids, 260, pp. 54-58, 1999

[88] A. Remillieux, B. Jacquir, and H. Poignant, "Cooperative energy transfer in a Yb-Pr doped ZBLAN fiber," Conf. Advanced Solid State Lasers, New Orleans, no. 01-04, paper JWE3, pp. 461-463, 1993

[89] R. Alcala and R. Cases, "Optical properties of Pr^{3+} ions in fluoride glasses," Advanced Materials, vol. 7, no. 2, pp. 190-193, 1995

[90] W. Seeber, E.A. Downing, L. Hesselink, M.M. Fejer, and D. Ehrt, "Pr^{3+}-doped fluoride glasses," Journal of Non-Crystalline Solids, 189, no. 3, pp. 218-226, 1995

[91] B. Peng and Z. Zhou, "Study on optical spectra of praseodymium-doped fluoride and fluorophosphate glasses," Journal of Materials Science Letters, vol. 21, no. 23, pp. 1836-1865, Dec. 2002

[92] E. Meneses-Pacheco, C.B. de Araujo, and Y. Messaddeq, "Energy transfer between Pr^{3+} ions in a fluoroindate glass," Journal of Non-Crystalline Solids, 226, no. 3, pp. 265-272, 1998

[93] A.B. Arauzo, R. Cases, and R. Alcala, "Optical absorption, photoluminescence and cross relaxation of Pr^{3+} ions in some fluoride glasses," Physics and Chemistry of Glasses, vol. 35, no. 5, pp. 202-206, Oct. 1994

[94] T.B. Nguyen, S. Trpkovski, P.M. Farrell, G.W. Baxter, and S.F. Collins, "Dependence of the fluorescence lifetime on dopant concentration and temperature in praseodymium-doped fluoride glass," Optics Communications, vol. 186, no. 4-6, pp. 277-281, 2000

[95] H. Kiriyama, N. Srinivasan, M. Yamanaka, Y. Izawa, T. Yamanaka, and S. Nakai, "Temperature dependence of emission cross-section of Yb:glass," Japanese Journal of Applied Physics, vol. 36, part 2, no. 9 A/B, pp. L1165-L1167, Sept. 1997

[96] S. Sengar, S.J. Dhoble, D.S. Raghuvanshi, and B.P. Chandra, "Temperature dependence of anti-stokes luminescence in ZBLAN:Pr^{3+}," Indian Journal of Pure and Applied Physics, vol. 41, no. 7, pp. 575-577, July 2003

[97] Y. Ohishi, T. Kanamori, T. Nishi, and S. Takahashi, "A high gain, high output saturation power Pr^{3+}-doped fluoride fiber amplifier operating at 1.3 μm," IEEE Photon. Technol. Lett., vol. 3, no. 8, pp. 715-717, Aug. 1991

[98] A. Remillieux, B. Jacquier, C. Linares, C. Lesergent, S. Artigaud, D. Bayard, L. Hamon, and J.L. Beylat, "Upconversion mechanisms of a praseodymium-doped fluoride fibre amplifier," J. Phys. D: Appl. Phys., vol. 29, no. 4, pp. 963-974, April 1996

[99] Y. Ohishi, T. Kanamori, J. Temmyo, M. Wada, M. Yamada, M. Shimizu, K. Yoshino, H. Hanafusa, M. Horiguchi, and S. Takahashi, "Laser diode pumped Pr^{3+}-doped and Pr^{3+}-Yb^{3+}-codoped fluoride fibre amplifiers operating at 1.3 μm," Electron. Lett., vol. 27, no. 22, pp. 1995-1996, Oct. 1991

[100] J. Zhong, L. Zan, L. Huang, Q. Luo, C. Li, and D. Huang, "Thermal and optical properties of Pr^{3+}/Yb^{3+}-codoped ZBLAPN glasses," Journal of Non-Crystalline Solids, 256 & 257, pp. 304-309, 1999

[101] B.R. Judd, "Optical absorption intensities of rare-earth ions," Physical Review, vol. 127, no. 3, pp. 750-761, Aug. 1962

[102] G.S. Ofelt, "Intensities of crystal spectra of rare-earth ions," Journal of Chemical Physics, vol. 37, no. 3, pp. 511-520, Aug. 1962

[103] J.A. Medeiros Neto, D.W. Hewak, and H. Tate, "Application of a modified Judd-Ofelt theory to praseodymium-doped fluoride glasses," Journal of Non-Crystalline Solids, 183, no. 1-2, pp. 201-207, 1995

[104] A. Florez, O.L. Malta, Y. Messaddeq, and M.A. Aegerter, "Judd-Ofelt analysis of Pr^{3+} ions in fluoroindate glasses: influence of odd third order intensity parameters," Journal of Non-Crystalline Solids, 213 & 214, pp. 315-320, 1997

[105] R.S. Quimby and W.J. Miniscalco, "Modified Judd-Ofelt technique and application to optical transitions in Pr^{3+}-doped glass," J. Appl. Phys., vol. 75, no. 1, pp. 613-615, Jan. 1994

[106] P. Goldner and F. Auzel, "Application of standard and modified Judd-Ofelt theories to a praseodymium-doped fluorozirconate glass," J. Appl. Phys., vol. 79, no. 10, pp. 7972-7977, May 1996

[107] P. Görrn, "Spektroskopie von Cr^{3+}-dotierten Gläsern und Glasfasern" (English: Spectroscopy of Cr^{3+}-doped glasses and fibers), Project work, Technische Universität Braunschweig, Sept. 2003

[108] J. Morel, A. Woodtli, and R. Dändliker, "Characterization of the fluorescent lifetime of doped fibers by measuring the frequency transfer function," J. Lightwave Technol., vol. 14, no. 5, pp. 739-742, May 1996

[109] D.L. Dexter, "A theory of sensitized luminescence in solids," Journal of Chemical Physics, vol. 21, no. 5, pp. 836-850, May 1953

[110] L. Wetenkamp, *Charakterisierung von laseraktiv dotierten Schwermetallfluorid-Gläsern und Faserlasern (English: Characterization of laser-actively doped heavy-metal fluoride glasses and fiber lasers),* Doctoral dissertation, Gemeinsame Fakultät für Maschinenbau und Elektrotechnik der Technischen Universität Braunschweig, 1991

[111] R. Rolli, S. Ronchin, M. Montagna, E. Moser, C. Duverger, V.K. Tikhomirov, A. Jha, and M. Ferrari, "Yellow-to-blue frequency upconversion in Pr^{3+}-doped aluminium-fluoride glasses," Journal of Non-Crystalline Solids, 280, pp. 269-276, 2001

[112] B.P. Petreski, P.M. Farrell, and S.F. Collins, "Cross-relaxation in praseodymium-doped fluorozirconate glass," Optics Communications, vol. 132, pp. 89-93, Nov. 1996

[113] M. Braglia, C. Bruschi, G. Dai, J. Kraus, S. Mosso, C. Meneghini, A. Balerna, F. Boscherini, S. Pascarelli, and C. Lamberti, "Local structure of Pr^{3+} in fluorozirconate glasses," Journal of Non-Crystalline Solids, 256 & 257, pp. 83-88, 1999

[114] D.E. McCumber, "Einstein relations connecting broadband emission and absorption spectra," Phys. Rev. A, vol. 136, no. 4, pp. 954-957, Nov. 1964

[115] D.E. McCumber, "Theory of phonon-terminated lasers," Bulletin of the American Physical Society, vol. 9, no. 280, March 1964

[116] H. Hu, F. Lin, G. Yi, B. Guo, and C. Qi, "The spectroscopic and fluorescent properties of Pr^{3+}-doped fluoride glass," Conference on halide glasses, May 1994

[117] M. Eyal, E. Greenberg, R. Reisfeld and N. Spector, "Spectroscopy of praseodymium(III) in zirconium fluoride glass," Chemical Physics Letters, vol. 117, no. 2, pp. 108-114, June 1985

[118] K.S. Naidu and S. Buddhudu, "Fluorescence properties of Pr^{3+}-doped $(NaPO_3)_6$-$BaCl_2$-$ZnCl_2$-RF glasses," Journal of Materials Science Letters, vol. 11, no. 7, pp. 386-389, 1992

[119] Z. Mazurak, W.A. Pisarski, J. Gabrys-Pisarska, and M. Zelechower, "Optical properties and concentration dependence of the luminescence of Pr^{3+} ion in fluoroindate glass," Physica Status Solidi B, Germany, vol. 237, no. 2, pp. 581-591, June 2003

[120] E.S. Moraes, M.M. Opalinska, A.S.L. Gomes, and C.B. Araujo, "Up-conversion fluorescence spectroscopy in Pr^{3+} doped optical fibers," Optics Communications, vol. 84, no. 5,6, pp. 279-282, Aug. 1991

[121] G. Amaranath and S. Buddhudu, "Spectroscopic properties of Pr^{3+}-doped multicomponent fluoride glasses," Mat. Res. Bull., vol. 25, pp. 1317-1323, 1990

[122] E. Bayer, W. Rossner, B.C. Grabmaier, R. Alcala, and G. Blasse, "Time-resolved emission spectroscopy of Pr^{3+} in a fluoride glass," Chemical Physics Letters, vol. 216, no. 1,2, pp. 228-230, Dec. 1993

[123] M. Eichhorn, "Numerical modeling of Tm-doped double-clad fluoride fiber amplifiers," IEEE J. Quantum Electron., vol. 41, no. 12, pp. 1574-1581, Dec. 2005

[124] S.S.-H. Yam and J. Kim, "Ground state absorption in thulium-doped fiber amplifier: experiment and modeling," IEEE J. Sel. Top. Quantum Electron., vol. 12, no. 4, pp. 797-803, July/Aug. 2006

[125] F. Duclos and P. Urquhart, "Thulium-doped ZBLAN blue upconversion fiber laser: theory," J. Opt. Soc. Am. B, vol. 12, no. 4, pp. 709-717, April 1995

[126] A. Escuer, S. Jarabo, and J.M. Alvarez, "Analysis of theoretical models for erbium-doped silica fibre lasers," Opt. Commun., vol. 187, pp. 107-123, Jan. 2001

[127] C.R. Giles and E. Desurvire, "Modeling erbium-doped fiber amplifiers," J. Lightw. Technol., vol. 9, no. 2, pp. 271-283, Feb. 1991

[128] A. Cucinotta, S. Dallargine, S. Selleri, C. Zilioli, and M. Zoboli, "Modeling of erbium doped fiber ring laser," Opt. Commun., vol. 141, pp. 21-24, Aug. 1997

[129] M. Karasek, "Analysis of a tunable Pr^{3+}-doped fluoride fibre ring laser," Pure Appl. Opt., vol. 7, no. 1, pp. 61-69, 1998

[130] P.R. Morkel and R.I. Laming, "Theoretical modeling of erbium-doped fiber amplifiers with excited-state absorption," Opt. Lett., vol. 14, no. 19, pp. 1062–1064, Oct. 1989

[131] J. Chen, X. Zhu, and W. Sibbett, "Rate-equation studies of erbium-doped fiber lasers with common pump and laser energy bands," J. Opt. Soc. Am. B, vol. 9, no. 10, pp. 1876-1882, Oct. 1992

[132] T. Pfeiffer, H. Schmuck, and H. Bülow, "Output power characteristics of erbium-doped fiber ring lasers," IEEE Phot. Technol. Lett., vol. 4, no. 8, pp. 847-849, Aug. 1992

[133] A. Yu and M.J. O'Mahony, "Design and modeling of laser-controlled erbium-doped fiber amplifiers," IEEE J. Sel. Top. Quantum Electron., vol. 3, no. 4, pp. 1013-1018, Aug. 1997

[134] H. Coic, "Analytic modelling of high-gain ytterbium-doped fibre amplifiers," J. Opt. A: Pure Appl. Opt., vol. 4, pp. 120-129, 2002

[135] S. Selvakennedy, M.A. Mahdi, M.K. Abdullah, P. Poopalan, and H. Ahmad, "Erbium-doped fiber ring laser cavity in transient and steady states studied by a numerical approach," J. Opt. Soc. Am. B, vol. 17, no. 6, pp. 914-918, June 2000

[136] J.R. Armitage, "Three-level fiber laser amplifier: a theoretical model," Appl. Opt., vol. 27, no. 23, pp. 4831-4836, Dec. 1988

[137] M.J.F. Digonnet and C.J. Gaeta, "Theoretical analysis of optical fiber laser amplifiers and oscillators," Appl. Opt., vol. 24, no. 3, pp. 333-342, Feb. 1985

[138] M.J.F. Digonnet, "Theory of operation of three- and four-level fiber amplifiers and sources," in *Fiber laser sources and amplifiers*, Proc. SPIE, vol. 1171, pp. 8-26, 1989

[139] Q.H. Wang and H.X. Lian, "Theoretical analysis of a four-level single-mode fiber laser," Microwave Opt. Technol. Lett., vol. 2, no. 1, pp. 34-37, Jan. 1989

[140] C. Barnard, P. Myslinski, J. Chrostowski, and M. Kavehrad, "Analytical model for rare-earth-doped fiber amplifiers and lasers," IEEE J. Quantum Electron., vol. 30, no. 8, pp. 1817-1830, Aug. 1994

[141] G. Calo, A. D'Orazio, M. De Sario, L. Mescia, V. Petruzzelli, and F. Prudenzano, "Genetic algorithms in design and characterization of rare earth doped fiber amplifiers," in *8^{th} International Conference on Transparent Optical Networks*, paper We.A 1.3, ICTON 2006, Nottingham, UK, June 2006

[142] H.G. Unger, *Optische Nachrichtentechnik (English: Optical telecommunication),* Hüthig, Heidelberg, vol. 1, 3rd edition, ISBN 3-7785-2261-2, 1993

[143] C.B. Layne, W.H. Lowdermilk, and M.J. Weber, "Multiphonon relaxation of rare-earth ions in oxide glasses," Phys. Rev. Lett., vol. 16, no. 1, pp. 10-20, July 1977

[144] E.G. Neumann, *Single-mode fibers,* Springer series in Optical Sciences, Springer-Verlag, Berlin, vol. 57, 1988

[145] S. Sujecki, "Modeling of high power semiconductor lasers," in *8th International Conference on Transparent Optical Networks*, paper We.A 1.4, ICTON 2006, Nottingham, UK, June 2006

[146] M.J. Weber, J.E. Lynch, D.H. Blackburn, and D.J. Cronin, "Dependence of the stimulated emission cross section of Yb^{3+} on host glass composition," IEEE J. Quant. Electron., vol. 19, no. 10, pp. 1600-1608, Oct. 1983

[147] F.C. Maciuc, C.I. Stere, and A.R.P. Sterian, "Rate equations for an erbium laser system, a numerical approach," in *Romopto 2000, Sixth Conference on Optics*, Proc. SPIE, vol. 4430, pp. 136-146, 2001

[148] A.R. Sterian and F.C. Maciuc, "Numerical model of an EDFA based on rate equations," Proc. SPIE, vol. 5226, pp. 74-78, 2003

[149] M. Pollnau, "The route toward a diode-pumped 1-W erbium 3-μm fiber laser," IEEE J. Quantum Electron., vol. 33, no. 11, pp. 1982-1990, Nov. 1997

[150] A.A. Rieznik, G.S. Wiederhecker, H.L. Fragnito, M.T. Carvalho, M.L. Sundheimer, A.S.L. Gomes, C.J.A. Bastos-Filho, and J.F. Martins-Filho, "Black box model for thulium doped fiber amplifiers," in *Proceedings of Optical Fiber Communication Conference*, paper FB2, Atlanta, GA, USA, 23–28 March 2003

[151] T. Whitley and R. Wyatt, "Analytic expression for gain in an idealised 4-level doped fibre amplifier," in *OSA technical digest, Optical amplifiers and their applications*, 20–23, 1992

[152] M. Karasek and J. Kanka, "Numerical analysis of Yb^{3+}-sensitised, Er^{3+}-doped, fibre-ring laser," IEE Proc. Optoelectronic., vol. 145, no. 2, pp. 133-137, April 1998

[153] E. Yahel and A. Hardy, "Modeling high-power Er^{3+}-Yb^{3+} codoped fiber lasers," J. Lightw. Technol., vol. 21, no. 9, pp. 2044-2052, Sept. 2003

[154] F. Brunet, P. Laperle, R. Vallee, S. LaRochelle, and L. Pujol, "Modeling of Tm-doped ZBLAN blue upconversion fiber lasers operating at 455 nm," in *Infrared Optical Fibers and Their Applications*, Proc. SPIE, 125–135, Boston, MA, USA, 21–22 Sept. 1999

[155] A.W.T. Wu and A.J. Lowery, "Efficient multiwavelength dynamic model for erbium-doped fiber amplifier," IEEE J. Quantum Electron., vol. 34, no. 8, pp. 1325-1331, Aug. 1998

[156] T. Tellert, F. Di Pasquale, and M. Federighi, "Theoretical analysis of the dynamic behaviour of highly-efficient erbium/ytterbium codoped fiber lasers," IEEE Photon. Technol. Lett., vol. 8, no. 11, pp. 1462-1464, Nov. 1996

[157] J. Kim, S.S.-H. Yam, M.E. Marhic, and L.G. Kazovsky, "Modeling gain dynamics of thulium-doped fiber amplifiers," IEEE Photon. Technol. Lett., vol. 17, no. 5, pp. 998-1000, May 2005

[158] F.C. Maciuc, C.I. Stere, and A.R.P. Sterian, "The time evolution and multiple parameters variations in a time dependent numerical model applied for an Er^{3+} laser system," in *11^{th} International School on Quantum Electronics*, Proc. SPIE, vol. 4397, pp. 84-88, 2001

[159] C.M. de Sterke, K.R. Jackson, and B.D. Robert, "Nonlinear coupled mode equations on a finite interval: a numerical procedure," J. Opt. Soc. Am. B, vol. 8, no. 2, pp. 403-412, Feb. 1991

[160] V. Karthik and G. Stewart, "Experimental and theoretical investigation of fiber ring laser dynamics and transient analysis," in *7^{th} International Conference on Optoelectronics*, Photonics 2004, Kochi, India, Dec. 2004